EXTRINSIC CONTRIBUTIONS TO THE PIEZOELECTRIC RESPONSE OF LEAD-BASED FERROELECTRICS

THÈSE N^{O} 2357 (2001)

PRÉSENTÉE AU DÉPARTEMENT DES MATÉRIAUX

ÉCOLE POLYTECHNIQUE FÉDÉRALE DE LAUSANNE

POUR L'OBTENTION DU GRADE DE DOCTEUR ÈS SCIENCES

PAR

Gilles ROBERT
Ingénieur en science des matériaux diplômé EPF
de nationalité suisse et originaire du Locle (NE)

acceptée sur proposition du jury:

Prof. N. Setter, directrice de thèse
Dr D. Damjanovic, rapporteur
Prof. M. Gijs, rapporteur
Prof. P. Gonnard, rapporteur
Prof. P. Stadelmann, rapporteur
Prof. A. Turik, rapporteur

Lausanne, EPFL
2001

à mon grand-père

Summary

The present study aims at a better understanding of the high piezoelectric properties encountered in lead-based ferroelectrics by focusing on the extrinsic contributions to the response. The main characteristics of these materials are the highly nonlinear character of the electro-mechanical response and the presence of a morphotropic phase boundary (MPB) where properties are reaching a maximum. Thus, our approach was first to develop a new description for the piezoelectric hysteresis and nonlinearities and second to investigate MPB effects on the extrinsic contributions to the piezoelectric response. For these purposes, lead titanate (PT), lead zirconate titanate (PZT), and lead nickel niobate-lead zirconate titanate solid solution (PNN-PZT) were chosen as prototype compositions. The sample preparation was classical for the first two compounds whereas two new synthesis routes of PNN-PZT were developed. The first consists in the preparation of a B-site precursor combining all the perovskite B-site cations before calcination with lead oxide, enhancing chemical homogeneity and insuring good reproducibility in the final properties. The second processing method aimed at more time efficiency: the use of a nickel hydroxy-carbonate instead of nickel oxide permitted to obtain in one single calcination step a pure perovskite phase exhibiting properties as high as those obtained for two firing steps procedures.

The piezoelectric hysteresis and nonlinearity description was undertaken using the Preisach formalism, first developed in ferromagnetism. This approach considers that each hysteretic system satisfying the wiping-out and the congruency properties can be seen as composed of bistable units characterized by distributed coercive and bias fields. In our case, the use of a general expression for the unit parameters distribution function permitted to describe the most significant piezoelectric coefficient nonlinearities such as applied field dependence, saturation or threshold fields. Moreover, a minimal expression describing the piezoelectric nonlinearity in lead-based compounds was derived from experimental determination of the distribution function topography.

Advanced piezoelectric hysteresis modelling was attained by coupling the classical viscous descriptions with Preisach-inspired loops expressions. This allowed to separate piezoelectric losses into viscous and field dependent parts. Moreover, the possibility of extracting distribution function parameters from the loops was established. The versatility of the Preisach hysteresis description was also demonstrated by deriving pinched ferroelectric loops from the supposed microscopical mechanisms in hard-doped ferroelectrics.

Morphotropic phase boundary study started with the derivation of a composition-temperature phase diagram for PNN-PZT using dielectric and pyroelectric measurements along with X-ray diffraction. The MPB of this solid solution was shown to be strongly curved toward the rhombohedral side. Therefore, certain compositions undergo a tetragonal to rhombohedral transition upon cooling. The influence of electric field and thermal history on this morphotropic transition was first investigated in view of optimizing the poling conditions of such materials. Then, the piezoelectric extrinsic contributions at MPB for both PZT and PNN-PZT were studied as a function of composition and temperature. The peak of properties occurring in this region was assigned to intrinsic effects coupled with an extension of the irreversible contributions. Using the developed hysteresis and nonlinearity formalism, this extrinsic contributions increase could be related to an extended response of each defect rather than to an increase in the defects density.

Version Abrégée

Cette étude vise à une meilleure compréhension des propriétés piézoélectriques élevées rencontrées dans les ferroélectriques au plomb, notamment en se concentrant sur les contributions extrinsèques. Les caractéristiques principales de ces matériaux sont un comportement hautement non-linéaire ainsi que la présence d'une frontière morphtropique de phase (MPB) où les propriétés atteignent un maximum. Ainsi, notre approche a donc été premièrement de développer un formalisme de description des hystérèses et non-linéarités piézoélectriques et secondement d'examiner les effets d'une MPB sur les contributions extrinsèques aux propriétés piézoélectriques. Dans cette optique, le titanate de plomb (PT), le zirconate titanate de plomb (PZT) et la solution solide de nickel niobate de plomb et de zirconate titanate de plomb (PNN-PZT) ont été choisis comme compositions prototypiques. L'élaboration des échantillons s'est déroulée de manière classique pour les premiers composés, tandis que deux nouvelles méthodes de synthèse ont été développées pour la synthèse du PNN-PZT. La première consiste à préparer un précurseur contenant tous les cations de site B de la perovskite finale avant la calcination avec l'oxyde de plomb. Cette méthode permet d'obtenir une meilleur homogénéité chimique et assure une bonne reproductibilité des propriétés. Le second procédé vise à augmenter la rapidité de la synthèse. En effet, l'utilisation d'un hydroxy-carbonate de nickel au lieu d'oxyde de nickel a permis d'obtenir une perovskite monophasée en une seule étape de calcination tout en conservant des propriétés comparables à celles obtenues pour le procédé en deux étapes.

La description des hystérèses et des non-linéarités piézoélectriques a été approchée par le formalisme de Preisach, initialement introduit en ferromagnétisme. Dans ce formalisme, tout système hystérètique satisfaisant aux conditions d'effacement et de congruence peut être décrit par un ensemble d'unité bistables dont les champs coercitif et interne sont distribués. Ici, une expression générale de la fonction de distribution de ces paramètres a permis de décrire les principaux comportements piézoélectriques non-linéaires dont la dépendance en champ appliqué, la saturation et le seuil en champ. De plus, une expression minimale pour la description des non-linéarités piézoélectriques dans les composés au plomb a été obtenue par l'étude expérimentale de la topographie des fonctions de distribution.

Une modélisation détaillée des hystérèses piézoélectriques a été obtenue en couplant la description visqueuse classique avec des expressions dérivées du formalisme de Preisach. Un tel modèle a autorisé la séparation des pertes piézoélectriques en parties dépendante en champ et visqueuse. De plus, la possibilité d'extraire les paramètres de distribution directement des boucles d'hystérèses a été démontrée. Finalement, la souplesse descriptive du formalisme de Preisach a été illustrée par la dérivation d'une équation pour les hystérèses pincées à partir d'une fonction de distribution basée sur les mécanismes physiques supposés entrer en oeuvre

dans les ferroélectriques dopés accepteurs.

L'étude de la frontière morphtropique de phase a débuté par la dérivation d'un diagramme de phase composition-température pour le PNN-PZT se basant sur des mesures diélectriques, pyroélectriques et des spectres de diffraction de rayons X. La MPB de cette solution solide présente une forte courbure en direction de la région rhomboédrique. Ceci conduit, pour certaines compositions, à une transition spontanée de la phase tetragonale à la phase rhomboédrique au refroidissement. L'influence de champs électriques et de l'histoire thermique sur cette transition morphtropique a d'abord été traitée en vue d'optimiser les conditions de polarisation de tels matériaux. Puis, les effets de la MPB sur les contributions extrinsèques à la piézoélectricité ont été étudiés en fonction de la composition et de la température pour le PZT et le PNN-PZT. Le pic de propriétés dans cette région a pu être mis en relation avec des effets intrinsèques et extrinsèques. Grâce aux méthodes développées plus haut, il a pu être démonté que cette augmentation des contributions extrinsèques provient d'une extension de la réponse moyenne par défaut contributif plutôt que d'une densité supérieure de défauts.

Table of Contents

Summary i

Version Abrégée iii

Table of Contents v

List of Figures ix

List of Tables xix

INTRODUCTION AND GOALS 1

1.1 HIGH PERFORMANCE PIEZOELECTRICS 2

1.1.1 Lead zirconate titanate (PZT) 2
1.1.2 Relaxor ferroelectric solid solutions 5
1.1.3 State of the art: Relaxor-ferroelectric single crystals 7

1.2 PIEZOELECTRIC NONLINEARITIES AND EXTRINSIC CONTRIBUTIONS 8

1.2.1 Nonlinearity in applications 8
1.2.2 Microscopics of extrinsic contributions 11

1.3 GOALS AND THESIS CONSTRUCTION 13

1.4 REFERENCES 15

MATERIALS PREPARATION 19

2.1 LEAD TITANATE (PTSM) 20

2.2 LEAD ZIRCONATE TITANATE (PZT) 20

2.2.1 Mixed oxide route 20
2.2.2 Samples basic electro-mechanical characterization 26
2.2.3 Conclusion 27

2.3 LEAD NICKEL NIOBATE - LEAD ZIRCONATE TITANATE (PNN-PZT) 28

2.3.1 Lead-based complex perovskite processing 28
2.3.2 B-site precursor route 30
2.3.3 Samples basic electro-mechanical characterization 38

2.3.4 Reactive Ni oxide route 41

2.3.5 Conclusion 46

2.4 REFERENCES 47

PHASES IN PNN - PZT SOLID SOLUTIONS 53

3.1 PHASES IN CLASSICAL AND RELAXOR FERROELECTRIC SYSTEMS 54

3.1.1 Phase coexistence in PZT 54

3.1.2 Relaxor-lead titanate solid solutions 56

3.1.3 Normal to relaxor ferroelectric transition 56

3.2 DIELECTRIC CHARACTERIZATION 57

3.2.1 Experimental 57

3.2.2 Poled samples 58

3.2.3 Unpoled samples 62

3.2.4 Conclusion 64

3.3 PYROELECTRIC CHARACTERIZATION 64

3.3.1 Experimental 64

3.3.2 Pyroelectric transitions 66

3.3.3 Conclusion 69

3.4 XRD CHARACTERIZATION 69

3.4.1 Around the morphotropic transition 70

3.4.2 Around the dielectric peak 71

3.5 PNN-PZT PHASE DIAGRAM AND CURVING MPB 72

3.5.1 Final Phase diagrams for 40% and 50% PNN-PZT 73

3.5.2 Exploring the curving MPB in PNN-PZT 75

3.6 POLING STUDIES 77

3.6.1 Phase stabilization due to electric field 77

3.6.2 Poling method influences on morphotropic phase transition 83

3.7 SUMMARY 85

3.8 REFERENCES 87

PIEZOELECTRIC COEFFICIENT NONLINEARITY 91

4.1 HYSTERESIS AND PREISACH MODELING 92

4.1.1 Piezoelectric nonlinearity: between empirical and physical descriptions 92
4.1.2 The Preisach approach: collections of bistable units 94
4.1.3 Microscopical interpretations: stochastic processes 98

4.2 DISTRIBUTION FUNCTIONS AND PIEZOELECTRIC NONLINEARITY 99

4.2.1 Generalized distribution function 99
4.2.2 Specific distribution functions 102

4.3 VALIDATION OF THE PREISACH APPROACH FOR PIEZOELECTRICS 106

4.3.1 Experimental 106
4.3.2 Wiping-out and congruency 107
4.3.3 Description of experimental d_{33} nonlinearities 110
4.3.4 Experimental determination of distribution functions 114

4.4 SUMMARY 121

4.5 REFERENCES 123

PIEZOELECTRIC RESPONSE HYSTERESIS 127

5.1 PIEZOELECTRIC LOSS DESCRIPTION 128

5.2 HYSTERESIS FITTING AND LOSS SEPARATION 132

5.2.1 Experimental 132
5.2.2 Linear piezoelectric: PTSm 133
5.2.3 Nonlinear Piezoelectrics: PZT & PNN-PZT 137
5.2.4 Loss mechanisms in piezoelectrics 145
5.2.5 Conclusion 146

5.3 ADVANCED PREISACH DESCRIPTION OF HYSTERESIS 147

5.3.1 Fitting hysteresis for distribution parameters 148
5.3.2 Pinched loops description 152

5.4 SUMMARY 155

5.5 REFERENCES 157

PIEZOELECTRIC BEHAVIOR AND CRYSTALLINE STRUCTURE 161

6.1 PIEZOELECTRIC PROPERTIES AT MPB IN FERROELECTRICS 162

6.2 COMPOSITIONAL DEPENDENCE OF PIEZOELECTRICITY IN PZT 163

6.2.1 Experimental 163

6.2.2 Distributions characteristics across MPB 164

6.3 TEMPERATURE DEPENDENCE OF PIEZOELECTRICITY IN PNN-PZT 170

6.3.1 Experimental 170

6.3.2 Nonlinear characteristics across MPB 172

6.4 THE PIEZOELECTRIC RESPONSE ACROSS A MPB 177

6.5 SUMMARY 179

6.6 REFERENCES 180

CONCLUSIONS AND PERSPECTIVES 183

7.1 HIGH PERFORMANCE PIEZOELECTRICS NONLINEARITY AND HYSTERESIS 183

7.2 PIEZOELECTRICITY AROUND THE MORPHOTROPIC PHASE BOUNDARY 184

7.3 PERSPECTIVES 185

Table of Symbols 187

Table of Abbreviations 191

Curriculum Vitae 193

Publications 195

Acknowledgements 197

List of Figures

INTRODUCTION AND GOALS

Figure 1.1: Piezoelectric properties as a function of composition for lead zirconate titanate. 3

Figure 1.2: Phase diagram for lead zirconate titanate exhibiting the cubic (paraelectric), antiferroelectric (AF), tetragonal and rhombohedral high/low temperature states. 4

Figure 1.3: Lattice cells associated with the paraelectric to ferroelectric transition in lead zirconate titanate. 4

Figure 1.4: Typical ternary diagram for relaxor-PZ-PT solid solutions. 6

Figure 1.5: Phase diagram for PZN-PT, MPB is represented by the dashed line. 7

Figure 1.6: Piezoelectric properties as a function of composition and crystal orientation in PZN-PT single crystals. 7

Figure 1.7: Typical converse unipolar hysteresis loop for a multilayer piezoelectric actuator made of PZT. 9

Figure 1.8: Strain hysteresis of a PZN-8%PT crystal poled along [001] direction. 9

Figure 1.9: Typical stress amplitude dependence of the longitudinal piezoelectric coefficient, d_{33} for lead zirconate titanate. 10

Figure 1.10: Contributing defects path under field in a potential typical of weak pinning. X_{rev} and X_{irrev} stand respectively for reversible and irreversible contributive paths. 12

Figure 1.11: Thesis structure. Lines state respectively the goals, the tools, the first level results and the final results of this study. 13

Figure 1.12: Thesis chapter structure. The main achievements of each chapter are summarized below the titles. 14

MATERIALS PREPARATION

Figure 2.1: Flow chart describing the mixed oxide route for synthesis of PZT. (Milling is performed using zirconia balls in isopropanol). 21

Figure 2.2: XRD spectra of PZT calcinated powders as a function of composition.......23

Figure 2.3: XRD spectrum of PZT sintered samples as a function of composition.. 24

Figure 2.4: SEM of 40/60 tetragonal PZT microstructure after etching.........25

Figure 2.5: SEM of 65/35 rhombohedral PZT microstructure after etching.........25

Figure 2.6: General flow chart describing the various precursor routes for synthesis of relaxor-ferroelectric solid solutions.........29

Figure 2.7: Flow chart describing the B-site precursor route for synthesis of PNN-PZT. (Milling is performed using zirconia balls in isopropanol).........31

Figure 2.8: XRD analysis of B-site precursors as a function of ZrO_2 content in 40PNN-60PZT compositions. 32

Figure 2.9: XRD of $ZrTiO_4$ (Pnab) with the B-site precursor for the 40PNN-32PZ-28PT composition.........33

Figure 2.10: XRD analysis of calcinated powders as a function of PZ content in 40PNN-60PZT compositions (sintering was performed at 1200°C - 2h)....33

Figure 2.11: XRD analysis of the final sintered samples as a function of PZ content in 40PNN-60PZT compositions. 34

Figure 2.12: SEM etched microstructure of a rhombohedral 40PNN-32PZ-28PT sintered sample.........35

Figure 2.13: SEM etched microstructure of a tetragonal 40PNN-20PZ-40PT sintered sample.........35

Figure 2.14: XRD analysis of the sintered samples as a function of PZ content in 50PNN-50PZT compositions (sintering was performed at 1200°C - 2h)....36

Figure 2.15: SEM etched microstructure of a rhombohedral 50PNN-18PZ-32PT sintered sample.........37

Figure 2.16: SEM etched microstructure of a tetragonal 50PNN-13PZ-37PT sintered sample.........37

Figure 2.17: Dielectric properties summary for the 40PNN-60PZT compositions as a function of PZ content. 38

Figure 2.18: Piezoelectric properties summary for the 40PNN-60PZT compositions as a function of PZ content. 39

Figure 2.19: Flow chart describing the reactive Ni oxide route for synthesis of PNN-PZT. (Milling is performed using zirconia balls in isopropanol). 42

Figure 2.20: XRD analysis of 34PNN-27PZ-39PT powders as a function of calcination temperature. 42

Figure 2.21: XRD analysis of 34PNN-27PZ-39PT sintered samples as a function of calcination temperature (sintering was performed at 1200°C - 2h). 43

Figure 2.22: Typical SEM etched microstructure of 34PNN-27PZ-29PT sintered sample (in this case calcinated at 850°C). 45

PHASES IN PNN - PZT SOLID SOLUTIONS

Figure 3.1: Dielectric permittivity vs. temperature curves for various poled 40PNN-60PZT compositions. Measurements were performed at 100 Hz (upper curve) and 10 kHz (lower curve) upon heating. 58

Figure 3.2: Dielectric permittivity vs. temperature curve for the poled 40PNN-26PZ-34PT composition. Measurements were performed at 100 Hz, 1 kHz, 10 kHz, and 100 kHz upon heating. 59

Figure 3.3: Dielectric losses and permittivity vs. temperature curve for the poled 40PNN-26PZ-34PT composition. Loss measurements are performed at 1 kHz upon heating. 60

Figure 3.4: Vögel-Fulcher plot for the 40PNN-26PZ-34PT composition. Circles represent inverse experimental (T_m - fitted T_f) and dotted line is a logarithmic fit to data points. 61

Figure 3.5: Dielectric permittivity vs. temperature curve for the poled and unpoled 40PNN-26PZ-34PT composition. Measurements were performed at 100 Hz, 1 kHz, 10 kHz and 100 kHz upon heating. Dotted lines represent the five points derivatives of 1 kHz data. 62

Figure 3.6: Dielectric permittivity vs. temperature upon heating and cooling of the unpoled 40PNN-26PZ-34PT composition. Measurements were performed at 100 Hz, 1 kHz, 10 kHz and 100 kHz. 63

Figure 3.7: Measured pyroelectric currents, I_{pyro} for various 40PNN-60PZT compositions. 66

Figure 3.8: Typical pyroelectric polarization, P_{pyro}, and current density, I_{pyro}, for the 40PNN-26PZ-34PT composition. 67

Figure 3.9: Effect of composition change on the shape of the pyroelectric current, I_{pyro} as a function of PZ content for two 40PNN-60PZT compositions exhibiting a rhombohedral structure at room temperature. 67

Figure 3.10: Comparison of the obtained pyroelectric current, I_{pyro} with the dielectric permittivity, ε^{poled} measurement for 40PNN-26PZ-34PT. 68

Figure 3.11: Comparison of the obtained pyroelectric current, I_{pyro} with the dielectric losses, tg δ measurement for 40PNN-26PZ-34PT. 68

Figure 3.12: Zoom of the (200) and (222) peaks as a function of temperature for 40PNN-26PZ-34PT. 70

Figure 3.13: FWHM of the (220) and (222) peaks for 50PNN-16PZ-34PT as a function of temperature. 71

Figure 3.14: FWHM of the (200) peak for 50PNN-16PZ-34PT as a function of temperature. 72

Figure 3.15: Suggested phase diagram for 40PNN-60PZT in the region of the MPB. The points are derived from dielectric and pyroelectric measurements and phases regions were identified with XRD. 73

Figure 3.16: Suggested phase diagram for 50PNN-50PZT in the region of the MPB. The points are derived from dielectric and pyroelectric measurements and phases regions were identified with XRD 74

Figure 3.17: Pyroelectric current response, I_{pyro} in the morphotropic transition region as a function of poling temperature for 40PNN-24PZ-36PT. 78

Figure 3.18: Pyroelectric polarization, P_{pyro} as a function of temperature for different poling temperatures of 40PNN-24PZ-36PT. 79

Figure 3.19: Pyroelectric polarization, P_{pyro} as a function of poling temperature and thermal history for 40PNN-24PZ-36PT. 80

Figure 3.20: Schematized effects of temperature and electric field on tetragonal phase volume fraction (V_{tetra}) in the MPB region. 82

Figure 3.21: Effect of poling method on the dielectric permittivity, ε^{poled} dependence on temperature for 50PNN-13PZ-37PT (tetragonal symmetry at room temperature). 84

Figure 3.22: Effect of poling method on the dielectric permittivity, ε^{poled} dependence on temperature for 50PNN-16PZ-34PT (rhombohedral symmetry at room temperature). 84

PIEZOELECTRIC COEFFICIENT NONLINEARITY

Figure 4.1: Elementary bistable unit represented as square hysteresis (a) and as energy profile (b). Néel in his microscopic analysis of Rayleigh formulas considered domain walls trapped in energy profiles such as the (b) representation. 94

Figure 4.2: State of the bistable units as a function of their position on the Preisach plane at zero applied field. 96

Figure 4.3: Schematic view of the switched bistable units for an alternating external field without bias ($\mathcal{F}_= = 0$). $\mathcal{F}_{inc}$ and $\mathcal{F}_{dec}$ stand for respectively increasing and decreasing applied field, $\mathcal{F}$. 97

Figure 4.4: Definition of the state line $b(\mathcal{F}_c)$ as a function of the field history since the application of a negative infinite field and subsequent series of local field extrema. 97

Figure 4.5: Free energy profile combining a quadratic behavior with a random walk roughness. 98

Figure 4.6: Portion of the Preisach plane reoriented by a field of amplitude $\mathcal{F}_0$ and offset $\mathcal{F}_=$. 100

Figure 4.7: Calculated loop from Equations (4.8)-(4.10) using a uniform distribution function, $f(\mathcal{F}_i, \mathcal{F}_c) = f_0$ (Rayleigh case). 101

Figure 4.8: Ellipsoidal distribution function based on Equation (4.13). The maximum of this distribution is situated at the Preisach plane origin. 103

Figure 4.9: Conical distribution function based on Equation (4.16). The maximum of this distribution is situated at the Preisach plane origin. 104

Figure 4.10: Roof-like distribution function based on Equation (4.18). The maximum of this distribution is situated at the Preisach plane origin. Intersections of the distribution function with $\mathcal{F}_i$ and $\mathcal{F}_c$ axis correspond to $\pm f_0$ /k and $-f_0$ /g respectively. 105

Figure 4.11: Schematic view of the switched units for the direct piezoelectric characterization technique presented in this section. 107

Figure 4.12: Piezoelectric coefficient, d_{33} dependence on stress amplitude, σ_0 for measurements made with increasing and decreasing field amplitude on a 50PNN-13PZ-37PT sample. 108

Figure 4.13: Different state lines for a decreasing stress amplitude measurement. The grey triangle corresponds to the tested stress amplitude. 109

Figure 4.14: Piezoelectric loops obtained from two distinct decreasing amplitude measurements and one increasing amplitude measurement on a 50PNN-13PZ-37PT sample. 110

Figure 4.15: Various types of piezoelectric coefficient, d_{33} dependence on amplitude of applied stress, σ_0, (a) Nb-doped $Bi_4Ti_3O_{12}$, (b) $Pb(Zr_{0.53},Ti_{0.47})O_3$, (c) Sm doped $PbTiO_3$ and (d) $0.95Bi_4Ti_3O_{12}$-$0.05Bi_3TiO_9$. 111

Figure 4.16: Piezoelectric coefficient d_{33} dependence on amplitude of applied stress, σ_0, for a 40/60 PZT 112

Figure 4.17: Bias stress, $\sigma_=$ dependence of the non-linear behavior of the piezoelectric coefficient, d_{33}, for a 40/60 PZT. 113

Figure 4.18: Principle of distribution function characterization along the internal field axis. 115

Figure 4.19: Bias stress, $\sigma_=$, dependence of the piezoelectric coefficient, d_{33}, nonlinearity for a 60/40 PZT at low stress amplitudes, σ_0. 116

Figure 4.20: Absolute bias stress, $\sigma_=$, dependence of the nonlinear parameter, α, for 60/40 PZT. In the Preisach formalism, the displayed α are proportional to the trace of the distribution function in the $\sigma_c = 0$ plane. 116

Figure 4.21: Bias stress, $\sigma_=$, dependence of the piezoelectric coefficient, d_{33}, nonlinearity for a 60/40 PZT at high stress amplitudes, σ_0. 118

Figure 4.22: Bias stress dependence of the nonlinear parameter, α, for PZT 60/40. 118

Figure 4.23: Bias stress dependence of the quadratic nonlinear parameter, β, for PZT 60/40. 119

Figure 4.24: Schematic view of the corrected roof-like distribution with the extra σ_i-σ_c coupled term. Intersections of the distributions function with σ_i and σ_c correspond to $\pm f_0$ /k and $-f_0$ /g respectively. 120

PIEZOELECTRIC RESPONSE HYSTERESIS

Figure 5.1: Frequency dependence of the piezoelectric coefficient, d_{33}, of a quartz sample. 133

Figure 5.2: Typical charge density, D, vs. stress, σ hysteresis (a) and piezoelectric coefficient, d_{33} vs. stress amplitude, σ_0 (b) dependences obtained for PTSm at 35 Hz. 134

Figure 5.3: Dependence of fitted loop parameters on stress amplitude, σ_0 for PTSm for a purely field-dependent model (Equation (5.11)) and a mixed model (Equation (5.13)). 135

Figure 5.4: Stress amplitude, σ_0, dependence of the viscous loss tangent obtained when fitting PTSm hysteresis with Equation (5.13) and obtained directly from measurements 136

Figure 5.5: Frequency dependence of the measured, fitted with Equation (5.11) and Equation (5.13) converse piezoelectric coefficients for PTSm. 137

Figure 5.6: Typical charge density, D vs. stress, σ hysteresis obtained for PZT 138

Figure 5.7: Piezoelectric coefficient, d_{33} vs. stress amplitude obtained for PZT at 35 Hz. The solid line represents a second order polynomial fit to Equation (5.17) which result is displayed in the graph. 138

Figure 5.8: Piezoelectric coefficient, d_{33} vs. stress amplitude, σ_0 obtained for PNN-PZT at 1 Hz. 139

Figure 5.9: Dependence of the Rayleigh parameter, α on stress amplitude, σ_0 for a purely field-dependent model and a mixed model in the case of PZT. 140

Figure 5.10: Dependence of the Rayleigh parameter, α on stress amplitude, σ_0 for purely field-dependent and mixed models in the case of PNN-PZT. 140

Figure 5.11: Stress amplitude, σ_0 dependence of the viscous loss tangent, tg δ_V obtained when fitting half of PZT hysteresis with Equation (5.13). 142

Figure 5.12: Stress amplitude, σ_0 dependence of the viscous loss tangent, tg δ_V obtained when fitting half of PNN-PZT hysteresis with Equation (5.13). 142

Figure 5.13: Stress amplitude, σ_0, dependence of losses, tg δ, obtained from measurements, area integration and Rayleigh loop area calculation for PZT. The difference between actual and calculated losses, tg δ_Δ ,is represented by open circles. 144

Figure 5.14: Stress amplitude, σ_0, dependence of losses, tg δ, obtained from measurements, area integration and Rayleigh loop area calculation for PNN-PZT. The difference between actual and calculated losses, tg δ_Δ ,is represented by open circles. 144

Figure 5.15: Schematic representation of the proposed pinning energy profile, G to account for field dependent losses (large scale roughness) and viscous losses (inset, low scale roughness). 146

Figure 5.16: Example of PZT 60/40 loop fitted with Equation (5.20) and a viscous term with indication of axes intersecting values. 149

Figure 5.17: Generated piezoelectric coefficient, d_{33} vs. stress amplitude, σ_0 (through Equation (5.21)) compared to values measured classically. 150

Figure 5.18: Stress amplitude, σ_0 dependence of the fitted f_0 parameter. 150

Figure 5.19: Stress amplitude, σ_0 dependence of the viscous loss tangent, tg δ_V 151

Figure 5.20: Plot of the proposed polynomial distribution function for a system containing dipolar defects oriented in different directions. 154

Figure 5.21: Plot of the loop obtained using Equation (5.24) with $d_0 = 5$, $c = 1$, $k = 25$ and $\mathcal{F}_0 = 5$. 154

PIEZOELECTRIC BEHAVIOR AND CRYSTALLINE STRUCTURE

Figure 6.1: Dielectric displacement data, D and their fit by Equation (5.20) plus a viscous term for a 45/55 PZT sample at $\sigma_=$ = 3 MPa. 164

Figure 6.2: Compositional dependence of the intrinsic and reversible piezoelectric contributions, d_0 (measured at 1 and 35 Hz). 165

Figure 6.3: Compositional dependence of the f_0 parameter, representing the absolute amplitude of the irreversible extrinsic contributions for PZT at 1 Hz. 166

Figure 6.4: Preisach distribution limits along coercive stress axis: $-f_0/k$, and internal stress axis: $-f_0/g$, as a function of PZT composition. 167

Figure 6.5: Compositional dependence of the j/f_0 ratio, representing the curvature of the distribution function for PZT at 1 Hz. 168

Figure 6.6: Viscous loss tangent as a function of PZT composition for measurements at 1 and 35 Hz. 169

Figure 6.7: Phase diagram for the 50PNN-50PZT compositions with the composition chosen for the temperature dependent measurements. 170

Figure 6.8: Pyroelectric current density for 50PNN-16PZ-34PT poled at 25°C upon heating and cooling through morphotropic phase transition.........................171

Figure 6.9: Typical d_{33} vs. stress amplitude, σ_0 dependence for the 50PNN-16PZ-34PT at 40°C for 1 Hz. The line represents the best linear fit ($d_{33} = d_0 + \alpha\sigma_0$) to the data points. 172

Figure 6.10: Temperature dependence of the intrinsic and reversible piezoelectric contributions, d_0 (measured at 1 Hz) for 50PNN-16PZ-34PT. 173

Figure 6.11: Typical bias stress, $\sigma_=$ dependence of the nonlinear parameter, α for 50PNN-16PZ-34PT at 70°C. 174

Figure 6.12: Temperature dependence of the nonlinear parameter, α (measured at 1 Hz) for a 50PNN-16PZ-34PT for $\sigma_=$ = 2.5 MPa. 175

Figure 6.13: Temperature dependence of the nonlinear parameter, α (measured at 1 Hz, with 2 kV/cm field applied at each temperature change) for 50PNN-16PZ-34PT for $\sigma_=$ = 3.2 MPa. 176

Figure 6.14: Viscous loss tangent as a function of temperature for 50PNN-16PZ-34PT at 1 Hz. 177

List of Tables

INTRODUCTION AND GOALS

Table 1.1: Comparison of the dielectric and piezoelectric properties of undoped PZT and barium titanate. 3

Table 1.2: Comparison of the dielectric and piezoelectric properties of relaxor-PT solutions at MPB and undoped PZT. 6

MATERIALS PREPARATION

Table 2.1: PZT compositions average characteristics after sintering. 24

Table 2.2: PZT compositions average electro-mechanical characteristics. 27

Table 2.3: 50PNN-50PZT compositions average electro-mechanical characteristics (noted PZ/PT). 40

Table 2.4: Electro-mechanical characteristics for 34PNN-27PZ-39PT as a function of calcination temperature. 44

Table 2.5: Comparison of electro-mechanical properties as a function of processing method
for the 34PNN-27PZ-39PT composition. 46

PHASES IN PNN - PZT SOLID SOLUTIONS

Table 2.1: Rhombohedral to tetragonal transition temperatures, T_{rt} at heating as a function of cycling number for the 40PNN-24PZ-36PT composition 81

Table 2.2: Tetragonal to rhombohedral transition temperatures, T_{rt} at cooling as a function of cycling number for the 40PNN-24PZ-36PT composition 82

PIEZOELECTRIC COEFFICIENT NONLINEARITY

Table 4.1: Equivalent distribution parameters values for PZT 60/40. 121

PIEZOELECTRIC RESPONSE HYSTERESIS

Table 5.1: Comparison of stress dependency parameters of the nonlinear coefficient for PZT and PNN-PZT. 141

Table 5.2: Comparison of viscous losses obtained by hysteresis fitting (tg δ_V) and by area substraction of Rayleigh-like contributions (tg δ_Δ). 143

Table 5.3: Comparison of the equivalent distribution parameters obtained by loop fitting and by varying bias stress measurements. 151

PIEZOELECTRIC BEHAVIOR AND CRYSTALLINE STRUCTURE

Table 6.1: Compositional dependence of the equivalent corrected roof distribution parameters (average of 1 Hz and 35 Hz values). 165

CHAPTER I
INTRODUCTION AND GOALS

Piezoelectricity describes either a variation of the dielectric displacement due to a stress (direct effect) or a deformation due to an electric field (converse effect). Today, piezoelectrics are widely used in actuators, sensors, transducers and transformers. At first, the piezoelectric effect was observed in single crystals only, since its discovery by J. and P. Curie in 1880 until the end of World War II. At that point, the uncovering of ferroelectricity in barium titanate ($BaTiO_3$ or BT) [1] really triggered the wide application of piezoelectricity, as this ferroelectric character enabled the first implementation of poling [2] which permitted to obtain piezoelectric properties in a poly-crystalline material. The path was then wide open for chemical variations of barium titanate and synthesis of new materials. The search for new ferroelectric compositions yielded the most widely used piezoelectric material up to now: the lead zirconate titanate ($Pb(Zr,Ti)O_3$ or PZT) solid solution [3]. Based on this success, complex lead-based perovskite materials were then systematically investigated leading to the first observation of a relaxor behavior in lead magnesium niobate and lead nickel niobate compounds [4]. These new compounds were exhibiting very high values of the dielectric constant with a pronounced frequency dispersion. In parallel, doping lead zirconate titanate with acceptor or donor species was shown to significantly improve its properties, leading to hard (high stability) and soft (high response) ferroelectrics. However, high doping levels compromise the chemical and crystalline stability of PZT. These concerns naturally lead to the introduction of compensated doping (i.e. simultaneous acceptor and donor doping) that is equivalent to the dissolution of relaxors in lead zirconate titanate. Thus, a flourishing variety of relaxor-ferroelectric-based compositions exhibiting very high properties appeared in the mid 1960's. With Curie temperatures close to room temperature, they exhibited properties alike the donor-doped materials with even higher dielectric permittivities and piezoelectric modulus. The next significant improvement was obtained in single crystals of such compositions poled in special directions and hence possessing a particular domain structure. They were shown to exhibit extremely high piezoelectric properties [5], more than 10 times higher than those of lead zirconate titanate.

The increase in properties obtained for piezoelectric materials during the last 50 years is impressive. However, it has been mostly reached by empirical methods as the mechanisms leading to such improvements in soft ferroelectrics are today still under discussion. Moreover, such high properties are often accompanied by strong nonlinearities originating from microscopic mechanisms that are not yet understood. Such mechanisms and their nonlinear consequences are the corner stones of the present study. In this chapter, we will first present the main characteristics of the lead-based compositions exhibiting high piezoelectric performance. Then, extrinsic contributions to the piezoelectric properties in these compositions will be briefly reviewed. In this framework, the goals of the thesis will be finally stated and the structure of the work will be presented.

1.1 HIGH PERFORMANCE PIEZOELECTRICS

High performance piezoelectrics designate the piezoelectrically and dielectrically soft ferroelectrics possessing the highest dielectric and piezoelectric response characteristics. For 40 years, the highest piezoelectric properties were obtained with materials containing lead. Hence, in this section, the characteristics of such lead-based materials will be exposed from the ever-young lead zirconate titanate to the advanced ferroelectric-relaxor single crystals.

1.1.1 Lead zirconate titanate (PZT)

Even though lead zirconate titanate, $Pb(Zr,Ti)O_3$ (PZT), solid solutions were first reported in 1952 [6, 7], real interest in PZT was drawn by the discovery of a peak in the dielectric and piezoelectric properties for compositions close to 52 mol% of $PbZrO_3$ (PZ) by Jaffe, Roth and Marzullo [3], as illustrated for the piezoelectric coefficients in Figure 1.1.

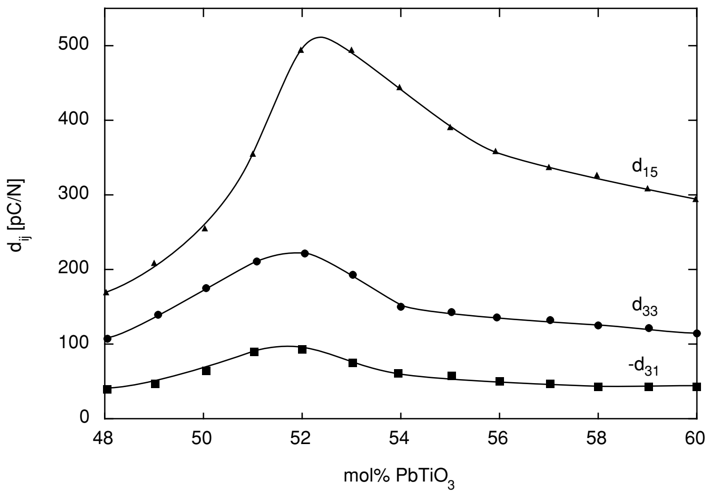

Figure 1.1: *Piezoelectric properties as a function of composition for lead zirconate titanate (reported from Ref. [8]).*

The properties of the undoped 52 mol% PZ composition are compared to those of barium titanate in Table 1.1. Besides the much higher piezoelectric properties of PZT, it also exhibits a higher Curie temperature which is advantageous in applications. Note that the reported properties were obtained for undoped materials. Doping with a few mol% of Nb increases significantly the permittivity and the piezoelectric properties of PZT [9].

Table 1.1: *Comparison of the dielectric and piezoelectric properties of undoped PZT and barium titanate [9].*

	ε	T_C [°C]	d_{33} [pC/N]	k_p
$Pb(Zr_{0.52}, Ti_{0.48})O_3$	1180	386	223	53 %
$BaTiO_3$	1620	120	191	35 %

The chemically localized increase of properties in PZT was immediately related to the structural change from a rhombohedral to a tetragonal symmetry occurring in this compositional region upon increase of the $PbTiO_3$ (PT) concentration. Such a phase transition was designated as "morphotropic" following the nomenclature introduced by Goldschmidt [10] for structural transformations occurring upon a chemical concentration change. Indeed, the PZT phase diagram (see Figure 1.2) presents an almost vertical morphotropic phase boundary (MPB) separating the tetragonal and rhombohedral ferroelectric phases.

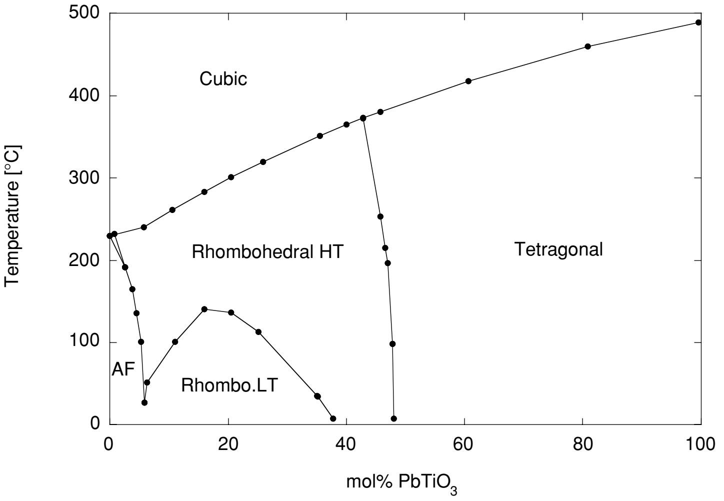

Figure 1.2: *Phase diagram for lead zirconate titanate (reported from Ref. [9]) exhibiting the cubic (paraelectric), antiferroelectric (AF), tetragonal and rhombohedral high/low temperature states.*

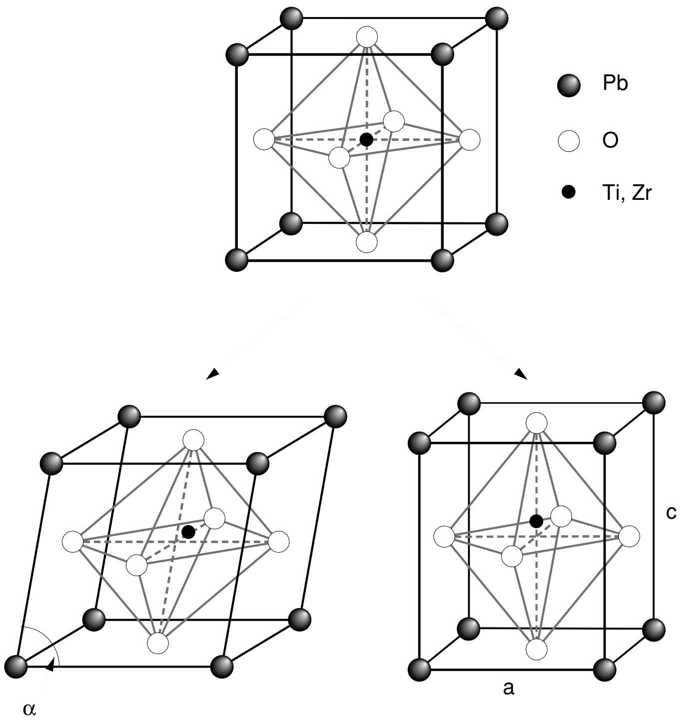

Figure 1.3: *Lattice cells associated with the paraelectric to ferroelectric transition in lead zirconate titanate (from Ref. [11]). Top is cubic, left is rhombohedral HT (with the distortion angle, α) and right is tetragonal (with lattice parameters, a and c).*

The phase diagram presents 3 main regions: the cubic paraelectric state, the antiferroelectric (AF) state around pure PZ and the ferroelectric state consisting in two types of rhombohedral phases (R3m at high temperature, and R3c at low temperature) and one tetragonal (P4mm). These ferroelectric phases are obtained by slight deformations of the prototype perovskite cubic cell, ABO_3 leading to the rhombohedral and the tetragonal symmetries, as represented in Figure 1.3. In such phases, the spontaneous polarization partially arises from the off-center position of the B-site atom (Ti or Zr). Its displacement follows the polarization vector ([111] in R3m and [001] in P4mm). Moreover, there are good indications (see e.g. Ref. [12]) that a lead shift also contributes to the total polarization. The transition between the two rhombohedral phases (HT and LT) is related to a tilt in the oxygen octahedra [13, 14].

As the spontaneous polarization can take 8 different orientations in the rhombohedral state and 6 in the tetragonal one, ferroelectric domains generally form in PZT ceramics cooled below their Curie temperature. In such symmetries, the permissible domain walls can be separated in two groups: pure ferro-electric and ferro-elasto-electric walls. The former is constituted by 180° domain walls (DW) which separate two oppositely polarized domains. The latter implies a change of both direction of polarization and associated strain across the wall. They are hence confined to mechanical twinning planes. In the tetragonal structure, 90° domain walls (i.e. separating two perpendicular polarization domains) are the only ones of this kind and sit on (110) planes. In the rhombohedral structure, there are two types of such walls, the 109° DW and the 71° DW located on (110) and (100) planes respectively. Note that 109° DW seem to be more frequent as their surface energy is significantly lower than 71° DW [15]. In general, those ferro-elasto-electric domain walls are often referred to as non-180° domain walls.

1.1.2 Relaxor ferroelectric solid solutions

The high properties in PZT being related to the presence of a morphotropic phase boundary, it was natural to look for other perovskite compounds exhibiting a similar feature. For instance, solid solutions of lead hafnate titanate were tested and indeed exhibited a MPB with enhanced properties [16] but not sufficiently elevated to compete with PZT. A significant increase in properties came from the mixing of relaxor ferroelectrics (such as $Pb(Mg_{1/3}Nb_{2/3})O_3$ (PMN) or $Pb(Ni_{1/3}Nb_{2/3})O_3$ (PNN)) with normal ferroelectrics such as PT or PZT. These compounds form a solid solution which typically follows the typical ternary diagram presented in Figure 1.4.

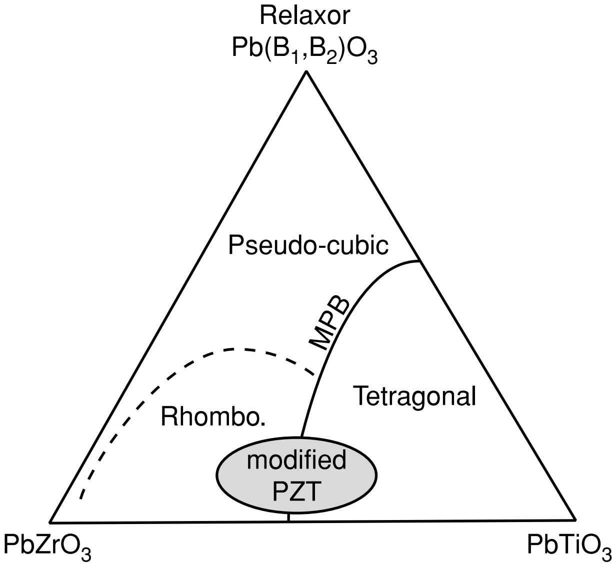

Figure 1.4: *Typical ternary diagram for relaxor-PZ-PT solid solutions (after Ref. [17]).*

Those solid solutions present a MPB which is dependent on the relaxor content. Such MPB compositions, and in particular the binary ones between PT and relaxors, exhibit very high properties as presented in Table 1.2.

Table 1.2: *Comparison of the dielectric and piezoelectric properties of relaxor-PT solutions at MPB* [17, 18] *and undoped PZT* [9].

	ε	T_C [°C]	d_{33} [pC/N]	k_p
52PZ-48PT	1180	386	223	53 %
70PNN-30PT	$3500^\dagger$	120	900	55 %
67PMN-33PT	$3000^\dagger$	160	690	63 %

† Values estimated for room temperature.

Although the Curie temperatures are quite low for the relaxor-ferroelectric solid solutions reported above, their superior dielectric and piezoelectric properties are very attractive. Hence, a compromise is necessary between T_C decrease and properties improvement. Nowadays, these compositions (and their compounds with PZ) are among the most interesting soft ferroelectrics for piezoelectric applications [19].

1.1.3 State of the art: Relaxor-ferroelectric single crystals

The lead-based relaxor-PT solid solutions can be grown as single crystals in lead oxide fluxes. Such crystals also exhibit a MPB as shown in the $Pb(Zn_{1/3}Nb_{2/3})O_3$-$PbTiO_3$ (PZN-PT) phase diagram presented in Figure 1.5. In such a system, a new increase in piezoelectric properties was obtained by Kuwata *et al.* [5] for single crystals of 91PZN-9PT which exhibited a d_{33} as high as 2000 pC/N.

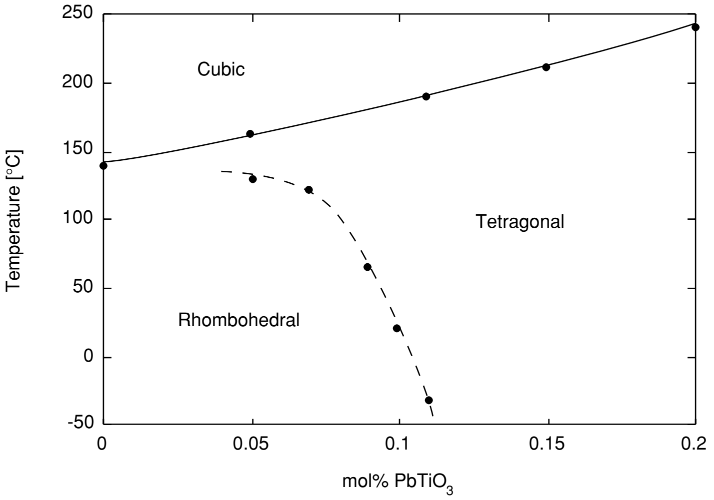

Figure 1.5: *Phase diagram for PZN-PT (reported from Ref. [20]), MPB is represented by the dashed line.*

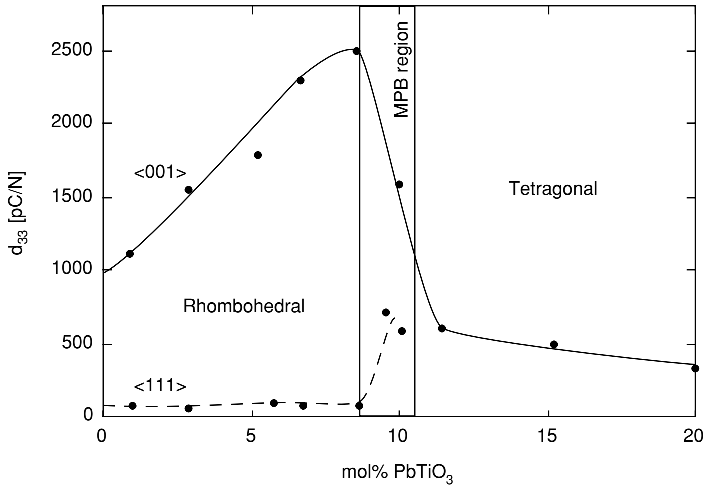

Figure 1.6: *Piezoelectric properties as a function of composition and crystal orientation in PZN-PT single crystals (reported from Ref. [22]).*

However, as illustrated in Figure 1.6, such high properties can only be obtained in rhombohedral compositions oriented and poled along the pseudo-tetragonal axis [001]. This procedure leads to increased properties due to intrinsic crystallographic effects [21] and perhaps also to the engineered domain structure [22]. Again, Figure 1.6 shows that a peak in properties is obtained in the MPB region, alike the pure PZT and the polycrystalline relaxor-ferroelectric solid solutions.

In summary, the high properties in the lead-based piezoelectrics are always related to the presence of a morphotropic phase boundary between the tetragonal and the rhombohedral symmetries. Although important properties enhancements have been obtained by the addition of relaxors to PZT, basic physical mechanisms leading to increased properties at MPB seem to be preserved. Therefore, a better understanding of properties improvements will have to take into account the influence of the crystalline phases on the piezoelectric response.

1.2 PIEZOELECTRIC NONLINEARITIES AND EXTRINSIC CONTRIBUTIONS

Thermodynamically, the piezoelectric effect relates linearly stress and dielectric displacement or electric field and strain. Hence, the piezoelectric coefficient given by the ratio of the response to the applied field should be independent on the applied field conditions. However, besides the existence of MPB, a second characteristic of the high performance piezoelectrics is their nonlinear piezoelectric behavior, i.e. a frequency and field dependence of the piezoelectric coefficient. This is often linked to high losses and hysteresis in the piezoelectric response. Such nonlinearity has consequences on the applications as will be presented in the first part of the next section. Moreover, its origin is not yet understood. Hence, the current hypothesis about the physical mechanisms of such contributions will be reviewed in section 1.2.2.

1.2.1 Nonlinearity in applications

Piezoelectrics are used in three main types of applications: actuators, sensors and high frequency transducers. In each one, piezoelectric nonlinearity is undesired. Let us consider first the actuators. A typical response vs. applied voltage curve is presented in Figure 1.7.

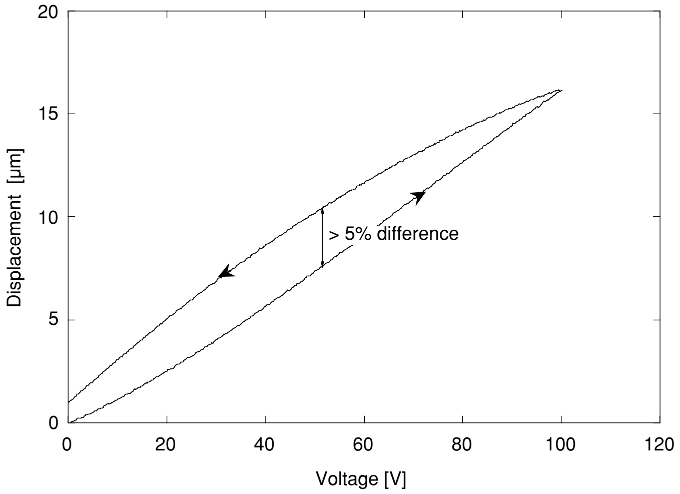

Figure 1.7: *Typical converse unipolar hysteresis loop for a multilayer piezoelectric actuator made of PZT (courtesy of E.L. Colla, Ceramics laboratory, EPFL).*

This figure illustrates how difficult can be the accurate positioning using a piezoelectric device when the actual displacement for a given voltage may vary by more than 5 %, depending on which branch of the hysteresis one sits on. In practice, such response hysteresis can be compensated by a feed-back loop or by some elaborated feed forward algorithms [23-25]. But such procedures either necessitate an extra displacement sensor or large computational facility.

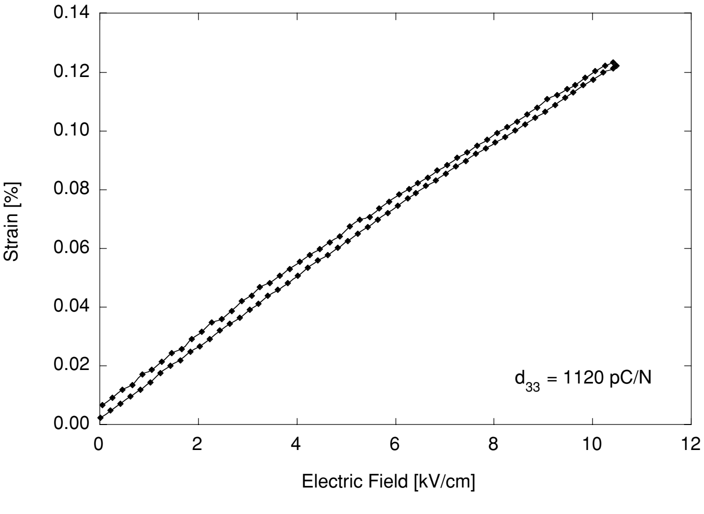

Figure 1.8: *Strain hysteresis of a PZN-8%PT crystal poled along [001] direction (reported from Ref. [22]).*

Regarding nonlinearity, the single crystals presented in the previous section are particular. They exhibit a limited response hysteresis up to quite large displacements [22], as shown in Figure 1.8. Unfortunately, these crystals are quite difficult to obtain in large sizes and hence the range of displacement for a given field is still small. Moreover, at high fields (> 15 kV/cm), a spontaneous transition from rhombohedral to tetragonal occurs leading to a strong hysteresis in deformation [26, 27].

Concerning sensors, high performance piezoelectrics applications are very limited due to their high piezoelectric coefficient nonlinearity. The Figure 1.9 presents a typical dependence of the piezoelectric coefficient on the amplitude of the applied stress. Obviously, an error of almost 100 % on the response factor is not acceptable for stresses differing in amplitude by an order of magnitude, even though the response is more than ten times higher than in linear piezoelectrics such as quartz. Numerous nonlinear models for the piezoelectric coefficient have been proposed [28-31]. However, none is sufficiently precise and general to efficiently compensate for this nonlinear behavior.

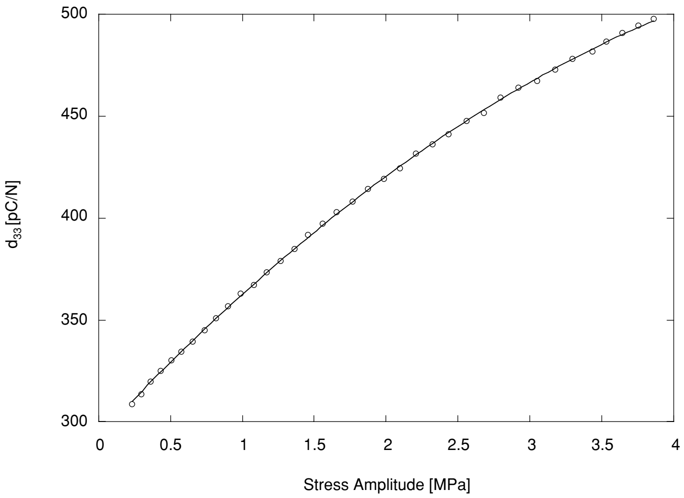

Figure 1.9: *Typical stress amplitude dependence of the longitudinal piezoelectric coefficient, d_{33} for lead zirconate titanate. The solid line represents a second order polynomial fit to the data points.*

In the transducers case, the piezoelectric nonlinearities lead to the shift of the resonance frequency at high strain [32-34] and to a strain dependence of the mechanical quality factor [35]. Such nonlinearities imply the development of complex equivalent circuits for an accurate description of the electrical characteristics of the resonant piezoelectric (see e.g. Ref. [36]) and limit the versatility of such transducers. A compromise between high properties and low nonlinearity is thus necessary.

In summary, even though it can be circumvented in some cases, piezoelectric nonlinearity is certainly an handicap for the application of high performance piezoelectrics. Therefore, in view of the possible reduction of those deleterious effects, the question arises whether the observed high properties are always related to a nonlinear behavior or not. The answer obviously lies in the physical understanding of such phenomena.

1.2.2 Microscopics of extrinsic contributions

The piezoelectric nonlinearities have been extensively studied since the discovery of PZT. No definite physical mechanisms have been yet acknowledged as the main explanation for this effect. However, in absence of final proof, it is nowadays widely accepted that the piezoelectric nonlinear behavior at weak to moderate fields mostly originates from extrinsic contributions. These contributions can be described as mechanisms that lead to a piezoelectric effect distinct from the intrinsic (lattice cell-related) response. Among them, the dominating one is domain wall motion [37, 38] but interphase boundary motion [39] and point defect displacement [40, 41] have also been proposed. In general, non-180° domain walls only can contribute to the piezoelectric effect as they couple polarization and elastic strain (for the dielectric properties, all ferroelectric walls may contribute). There are many experimental evidences for the influence of such DW on the piezoelectric response. For instance, grain size dependence of the piezoelectric coefficient was correlated to the domain wall density in PZT [42]. XRD studies upon electric field application have revealed in PZT a strong 90° DW switching [43]. Finally, measurements of PZT hydrostatic piezoelectric coefficient (independent of DW motion) show a constant value down to 20K while the longitudinal coefficient varied by a factor of 2 [44]. Whereas few evidences only exist for interphase boundary motion and point defects significant influence, all the previous reports tend to confirm a significant domain wall contribution to the piezoelectric response.

In more details, the extrinsic contributions can be separated in two types: reversible and irreversible. They are presented schematically on Figure 1.10. Under small field, the contributing DW (but also interphase boundary or point defects) can be considered as trapped in a potential well, as demonstrated for DW in Rochelle salt [45]. Hence, they will contribute to the response in a reversible way by oscillating in their energy potential [46, 47]. Such pinned motion has been observed directly for DW in lithium tantalate [48] and its consequences on the dielectric response have been evaluated for gadolinium molybdate [49]. The modeling of such piezoelectric reversible contributions from a damped vibrating 90° DW yielded an expression describing the observed losses in PZT [50, 51]. Moreover, extrinsic contributions to the dielectric and piezoelectric coefficients in RbH_2PO_4 crystals have been shown to agree with such a physical mechanism [52].

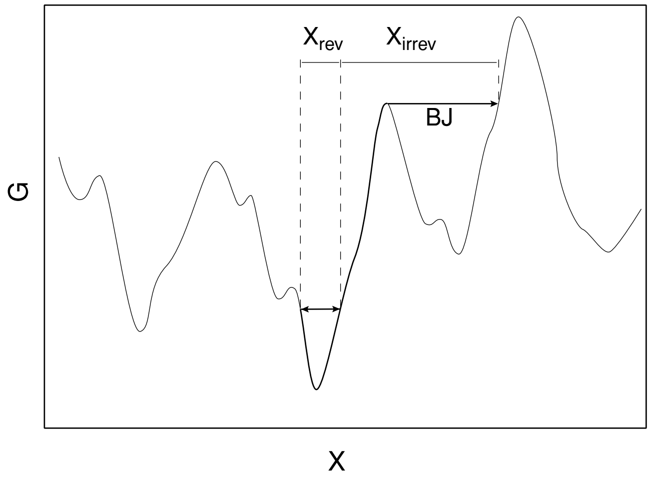

Figure 1.10: *Contributing defects path under field in a potential typical of weak pinning* [53]*.* X_{rev} *and* X_{irrev} *stand respectively for reversible and irreversible contributive paths. The BJ arrow corresponds to a Barkhausen jump (BJ)* [54]*.*

However, when the field becomes high enough to depin a DW or switch a defect dipole, then irreversible contributions are expected. As shown in Figure 1.10, such contributions will be hysteretic as the contributive defects reach a new metastable position after field application. Such contributions have been confirmed experimentally for PZT by correlating the onset of dielectric nonlinearity with the appearance of a response hysteresis [55]. Microscopically, randomly shaped hysteresis for single 90° DW positions under alternating field have been optically observed in barium titanate crystals [56]. An elaborate measurement set-up combining simultaneous strain and polarization measurements permitted to estimate such contributions to the order of several tens of percent [57]. Finally, Barkhausen jumps [54] can also be related to extrinsic contributions (the BJ arrow in Figure 1.10). Closer examination of acoustic measurements in soft PZT do indeed reveal an onset of acoustic emission related to the departure of the dielectric displacement from a linear behavior [58].

In conclusion, extrinsic contributions are widely confirmed for numerous ferroelectrics. The question about the nature of the main contributing defect remains open, but there are overwhelming evidences indicating that domain walls are the best candidates. Clearly, the extrinsic contributions to the piezoelectric response are quite varied, from the damped reversible motion to the hysteretic-related onset of nonlinearity. Moreover, they probably account for a significant part of the piezoelectric response in soft ferroelectrics. However, no general physical description is yet available for the modeling of such an important and varied phenomenon.

1.3 GOALS AND THESIS CONSTRUCTION

It has been shown that current high performance piezoelectrics have two common characteristics: they exhibit a morphotropic phase boundary and a good part of their piezoelectric response is probably due to extrinsic contributions. None of these two points is fully understood today. In this context, the goal of the present study is dual (as shown in Figure 1.11). First, the effect of the morphotropic phase boundary on the properties has to be further clarified. Second, the extrinsic contributions to the piezoelectric response need a general description accounting for the observed nonlinearities and hysteresis as well as for the associated increase in properties. In order to reach these objectives, the paths described in Figure 1.11 will be followed. The extrinsic contributions will be treated from both the piezoelectric coefficient field dependence and the hysteresis points of view. This will lead us to a general description of the extrinsic piezoelectric response using concepts of elementary contributing units (related to domain walls) and classical irreversible thermodynamics. Concerning the MPB, the study of a typical relaxor ferroelectric phase diagram will lead to an extension of the morphotropism concept to temperature-dependent transitions. Finally, these two separate issues will merge in the study of the crystallographic effects on the extrinsic contributions, presenting how the developed description tools can be applied to the understanding of the piezoelectric response in soft ferroelectrics and to the particular effects of the morphotropic phase boundary.

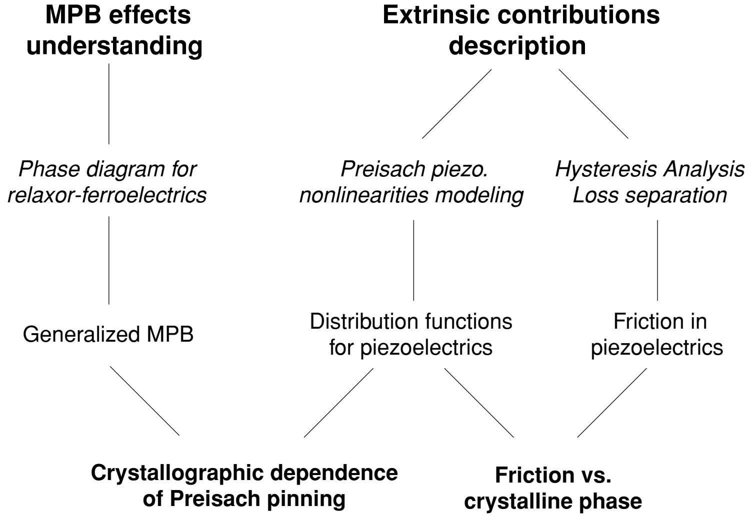

Figure 1.11: *Thesis structure. Lines state respectively the goals, the tools, the first level results and the final results of this study.*

The chapters of the present text correspond to the main steps outlined above as schematically presented in Figure 1.12. Although each chapter is intended to be readable almost by itself, the overall path starts at the materials synthesis where new methods for relaxor-ferroelectric synthesis are presented (Chapter II). Then, generalized MPB is introduced by studying the phase diagram of lead nickel niobate-lead zirconate titanate solid solutions (Chapter III). The piezoelectric coefficient nonlinearities are treated by the introduction of the Preisach model in Chapter IV and the piezoelectric hystereses are described using a mixed Preisach-viscous model in Chapter V. Finally, in Chapter VI the description tools developed in Chapters IV and V are applied to the study of the MPB evidenced in Chapter III, attaining the goals of the present thesis.

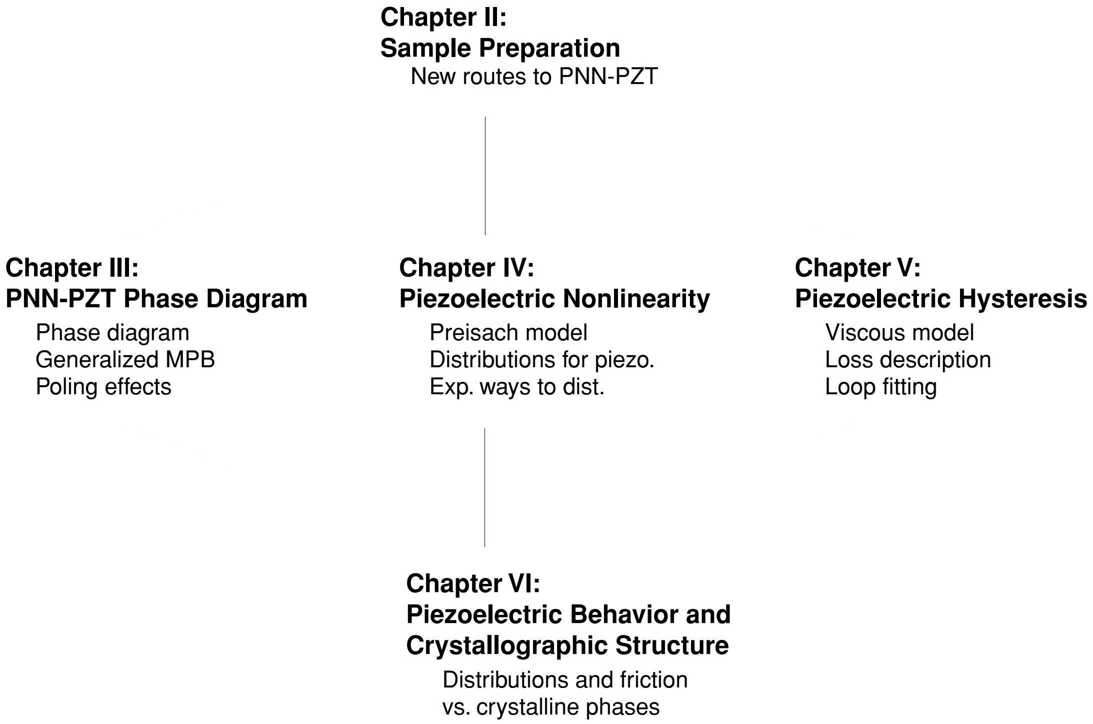

Figure 1.12: *Thesis chapter structure. The main achievements of each chapter are summarized below the titles.*

1.4 REFERENCES

1. B.M. Wul and I.M. Goldman, *Dielectric constant of barium titanate as a function of strength of an alternating field.* Cptes. Ren. Acad. Sci. URSS, (1945) **49** [3] p. 177-80.
2. S. Roberts, *Dielectric and piezoelectric properties of barium titanate.* Phys. Rev., (1947) **71** [12] p. 890-5.
3. B. Jaffe, R.S. Roth, and S. Marzullo, *Piezoelectric properties of lead zirconate-lead titanate solid-solution ceramics.* J. Appl. Pys., (1954) **25** p. 809-10.
4. G.A. Smolenskii and A.I. Agranovskaya, *Dielectric polarization and losses of some complex compounds.* Sov. Phys. Tech. Phys., (1958) **3** p. 1380.
5. J. Kuwata, K. Uchino, and S. Nomura, *Dielectric and piezoelectric properties of* $0.91Pb(Zn_{1/3}Nb_{2/3})O_3$*-*$0.09PbTiO_3$ *single crystals.* Jpn. J. Appl. Phys., (1982) **21** [9] p. 1298-302.
6. G. Shirane and A. Takeda, *Phase transitions in solid solutions of* $PbZrO_3$ *and* $PbTiO_3$ *(I) Small concentration of PbTiO3.* J. Phys. Soc. Jpn., (1952) **7** [1] p. 5-11.
7. G. Shirane, K. Suzuki, and A. Takeda, *Phase transitions in solid solutions of* $PbZrO_3$ *and* $PbTiO_3$ *(II) X-ray study.* J. Phys. Soc. Jpn., (1952) **7** [1] p. 12-8.
8. D.A. Berlincourt, C. Cmolik, and H. Jaffe, *Piezoelectric properties of polycrystallin lead titanate zirconate compositions.* Proc. IRE, (1960) **48** p. 220-9.
9. B. Jaffe, W.R. Cook, and H. Jaffe, *Piezoelectric Ceramics*. Non-Metallic Solids, ed. J.P. Roberts and P. Popper. Vol. 3. 1971, London: Academic Press.
10. V.M. Goldschmidt, T. Barth, G. Lunde, and W. Zachariasen, *Geochemische Verteilunggestze der Elemente VII Die Gesetze der Krystallochemie.* Srkrifter Utgitt av der Norske Videnskaps-Akademi i Oslo, I. Matem.-Naturvid. Klasse, (1926) **2**.
11. D.V. Taylor, *Dielectric and piezoelectric properties of sol-gel derived* $Pb(Zr,Ti)O_3$ *thin films*, in *Materials Dept.* 1999, Swiss Federal Institute of Technology Lausanne: Lausanne, Switzerland.
12. D.L. Corker, A.M. Glazer, R.W. Whatmore, A. Stallard, and F. Fauth, *A neutron diffraction investigation into the rhombohedral phases of the perovskite series* $PbZr_{1-x}Ti_xO_3$. J. Phys. Condens. Matter, (1998) **10** p. 6251-69.
13. M.J. Haun, E. Furman, T.R. Halemane, and L.E. Cross, *Thermodynamic theory of the lead zirconate-titanate solid solution system, Part IV: Tilting of the oxygen octahedra.* Ferroelectrics, (1989) **99** p. 27-44.

14. C.A. Randall, M.G. Matsko, W. Cao, and A.S. Bhalla, *A transmission electron microscopy investigation of the R3m -> R3c phase transition in* $Pb(Zr,Ti)O_3$ *ceramics.* Solid State Com., (1993) **85** [3] p. 193-5.
15. C.A. Randall, D.J. Barber, and R.W. Whatmore, *Ferroelectric domain configurations in a modified-PZT ceramic.* J. Mat. Sci., (1987) **22** p. 925-31.
16. B. Jaffe, R.S. Roth, and S. Marzullo, *Properties of piezoelectric ceramics in the solid-solution sereies lead titanate - lead zirconate - lead oxide : Tin oxide and lead titanate - lead hafnate.* J. Res. Natl. Bur. Stds., (1955) **55** [5] p. 239-254.
17. S.E. Park and T.R. Shrout, *Characteristics of relaxor-based piezoelectric single crystals for ultrasonic transducers.* IEEE T. Ultrason. Ferr., (1997) **44** [5] p. 1140-47.
18. Y. Yamashita and N. Ichinose, *Can relaxor piezoelectric materials outperform PZT? (review).* ISAF '96, Proc. of 10th IEEE Int. Symp. on Appl. Ferro., Ed. B.M. Kulwicki, A. Amin, A. Safari, East Brunswick, USA, (1996) p. 71-7.
19. M. Kondo, M. Hida, M. Tsukuda, K. Kurihara, and N. Kamehara, *Piezoelectric properties of PbNi1/3Nb2/3O3-PbTiO3-PbZrO3 ceramics.* Jpn. J. Appl. Phys., (1997) **36** [9B] p. 6043-5.
20. J. Kuwata, K. Uchino, and S. Nomura, *Phase transitions in the* $Pb(Zn_{1/3}Nb_{2/3})O_3$-$PbTiO_3$ *system.* Ferroelectrics, (1981) **37** p. 579-82.
21. X.H. Du, J. Zheng, U. Belegundu, and K. Uchino, *Crystal orientation dependence of piezoelectric properties of lead zirconate titanate bear the morphotropic phase boundary.* Appl. Phys. Lett., (1998) **72** [19] p. 2421-3.
22. S.E. Park and T.R. Shrout, *Ultrahigh strain and piezoelectric behavior in relaxor based ferroelectric single crystals.* J. Appl. Phys., (1997) **82** [4] p. 1804-11.
23. P. Ge and M. Jouaneh, *Generalized Preisach model for hysteresis nonlinearity of piezoceramic actuators.* Prec. Eng., (1997) **20** p. 99-111.
24. D. Hughes and J.T. Wen, *Preisach modeling of piezoceramic and shape memory alloy hysteresis.* Smart Mater. Str., (1997) **6** p. 287-300.
25. H. Janocha and K. Kuhnen, *real time compensation of hysteresis and creep in piezoelectric actuators.* Sensors Actuators A, (2000) **79** p. 83-9.
26. D.S. Païk, S.E. Park, S. Wada, S.F. Liu, and T.R. Shrout, *E-field phase transition in <001>-oriented rhombohedral* $0.92Pb(Zn_{1/3}Nb_{2/3})O_3$-$0.08PbTiO_3$ *crystals.* J. Appl. Phys., (1999) **85** [2] p. 1080-3.
27. M.K. Durbin, E.W. Jacobs, J.C. Hicks, and S.E. Park, *In-situ x-ray diffraction study of an electric field induced phase transition in the single crystal relaxor ferroelectric, 92%* $Pb(Zn_{1/3},Nb_{2/3})O_3$-8%$PbTiO_3$. Appl. Phys. Lett., (1999) **74** [19] p. 2848.

28. S.P. Joshi, *Non-linear constitutive relations for piezoceramic materials.* Smart Mater. Str., (1992) **1** p. 80-3.
29. D. Damjanovic, *Stress and frequency dependence of the direct piezoelectric effect in ferroelectric ceramics.* J. Appl. Phys., (1997) **82** [4] p. 1788-97.
30. V. Mueller and Q.M. Zhang, *Shear response of lead zirconate titanate piezoceramics.* J. Appl. Phys., (1998) **83** [7] p. 3 754-61.
31. V. Perrin, M. Troccaz, and P. Gonnard, *Nonlinear behaviour of the permittivity and of the piezoelectric strain constant under high electric field drive.* J. Electroceram., (2000) **4** [1] p. 189-94.
32. R.S. Woollett and C.L. LeBlanc, *Ferroelectric nonlinearities in transducer ceramics.* IEEE T. Son. Ultra., (1973) **Su-20** [1] p. 24-31.
33. H. Beige and G. Schmidt, *Electromechanical resonances for investigating linear and nonlinear properties of dielectrics.* Ferroelectrics, (1982) **41** p. 39-49.
34. A.F. Litvin, M.M. Pikalev, V.A. Doroshenko, and V.Z. Borodin, *Electromechanical nonlinearity of polycrystalline ferroelectrics under resonant excitation.* Ferroelectrics, (1984) **51** p. 159-71.
35. M. Umeda, K. Nakamura, and S. Uhea, *effects of vibration stress and temperature on the characteristics of piezoelectric ceramics under high vibration amplitude levels measured by electrical transient responses.* Jpn. J. Appl. Phys., (1999) **38** [9B] p. 5581-5.
36. P. Gonnard, *Investigation on dielectric, mechanical and piezoelectric non-linearities in piezoceramics through a new equivalent circuit.* ISAF 2000.
37. B. Lewis, *Energy loss processes in ferroelectric ceramics.* Proc. Phys. Soc., (1960) **73** [1] p. 17-24.
38. L.E. Cross, *Ferroelectrics ceramics: tailoring properties for specific applications.* "Ferroelectric Ceramics" ed. N. Setter, E. Colla , Birkhausen, (1993) p. 64-65.
39. S. Li, W. Cao, R.E. Newnham, and L.E. Cross, *Electromechanical nonlinearity of ferroelectric ceramics and related non-180° domain wall motions.* Ferroelectrics, (1993) **139** p. 25-49.
40. A.S. Nowick and B.S. Berry, *Anelastic Relaxation in Solids.* Academic Press, New-York, (1972) p. 427-434.
41. G. Arlt, *Piezoelectric relaxation.* Ferroelectrics, (1982) **40** p. 149-157.
42. C.A. Randall, N. Kim, J.P. Kucera, W. Cao, and T.R. Shrout, *Intrinsic and extrinsic size effects in fine-grained morphotropic-phase-boundary lead zirconate titanate.* J. Am. Ceram. Soc., (1998) **81** [3] p. 677-88.

43. H. Yamaguchi, *Behavior of electric-field-induced strain in PT-PZ-PMN ceramics.* J. Am. Ceram. Soc., (1999) **82** [6] p. 1459-62.
44. Q.M. Zhang, H. Wang, N. Kim, and L.E. Cross, *Direct evaluation of domain wall and intrinsic contributions to the dielectric and piezoelectric response and their temperature dependence on lead zirconate-titanate ceramics.* J. Appl. Phys., (1994) **75** [1] p. 454-9.
45. T. Mitsui and J. Furuchi, *Domain structure of Rochelle salt and* KH_2PO_4. Phys. Rev., (1953) **90** [2] p. 193-201.
46. B.D. Laikhtman, *Flexural vibrations of domain walls and dielectric dispersion of ferroelectrics.* Sov. Phys. Solid State, (1973) **15** [1] p. 62-68.
47. G. Arlt, *The role of domain walls on the dielectric, elastic and piezoelectric properties of ferroelectric ceramics.* Ferroelectrics, (1987) **76** p. 451-58.
48. T.J. Yang, V. Gopalan, P.J. Swart, and U. Mohideen, *Direct observation of pinning and bowing of a single ferroelectric domain wall.* Phys. Rev. Lett., (1999) **82** [20] p. 4106-9.
49. O.A. Tikhomirov, *Vibrations of domain walls in AC field and the low frequency permittivity of ferroelectrics.* Ferroelectrics, (1997) **190** p. 37-42.
50. G. Arlt and H. Dederichs, *Complex elastic, dielectric and piezoelectric constants by domain wall damping in ferroelectric ceramics.* Ferroelectrics, (1980) **29** p. 47-50.
51. G. Arlt, H. Dederichs, and R. Herbiet, *90°-domain wall relaxation in tetragonally distorted ferroelectric ceramics.* Ferroelectrics, (1987) **74** p. 37-53.
52. M. Stula, J. Fousek, H. Kabelka, M. Fally, and H. Warhanek, *Extrinsic contributions to the piezoelectric properties of* RbH_2PO_4 *crystals in the ferroelectric phase.* J. Kor. Phys. Soc., (1998) **32** p. S758-60.
53. T. Nattermann, Y. Shapir, and I. Vilfan, *Interface pinning and dynamics in random systems.* Phys. Rev. B, (1990) **42** [13] p. 8577-86.
54. M.E. Lines and A.M. Glass, *Principles and applications of ferroelectrics and related materials*. 1977, Oxford: Calrendon Press.
55. S. Li, W. Cao, and L.E. Cross, *The extrinsic nature of nonlinear behavior observed in lead zirconate titanate ferroelectric ceramic.* J. Appl. Phys., (1991) **69** [10] p. 7219-24.
56. J. Fousek and B. Brezina, *The movement of single 90° domain walls of* $BaTiO_3$ *in an alternating electric field.* Czech. J. Phys., (1960) **B 10** p. 511-28.
57. Y. Saito, *Measurements of complex piezoelectric* d_{33} *constant in ferroelectric ceramics under high electric field driving.* Jpn. J. Appl. Phys., (1995) **34** [9B] p. 5313-9.
58. D.C. Lupascu, J. Nuffer, and J. Rödel, *Acoustic emision from different PZT.* Ferroelectrics, (1999) **222** p. 249-55.

CHAPTER II
MATERIALS PREPARATION

Properties in real-world materials are known to heavily depend on their microstructure in general. By microstructure, we mean everything that distinguishes an actual material from the ideal crystal studied in basic physics: grains, grain boundaries, punctual, linear or planar defects, dipolar defects, impurities... All these parameters are strongly dependent on the way materials are prepared and can greatly vary with slight changes in the processing route. Moreover, for applications targeted materials where the obtention of highest figure of merit is critical, the issue of processing is also of primary importance. Hence, optimization of the preparation is one of the paths to follow. Such high performance materials should also exhibit reproducible characteristics and their production should be up-scalable to meet industrial standards. Again, to reach such goals, a good understanding and control of the manufacturing process is necessary.

It is the purpose of this chapter to describe the preparation of the compositions and samples studied in this work in order to gain a more thorough view of the observed properties. First, the synthesis procedures will be described and intermediate results (e.g. XRD analysis) will be presented. Then, the actual samples used for the piezoelectric measurements will be characterized from a crystallographic and microstructural point of view. A basic understanding of the mechanisms taking place during the processing will be sought as it permits to design more efficient routes and distinguish among issues in the material microstructure influence on the properties. In such a perspective, two new routes for the processing of advanced relaxor-ferroelectrics will be presented and validated. It will be shown that the synthesis of complex perovskites can be performed either faster or in a way yielding more homogeneous properties.

In our work, the main emphasis was put on the processing of PNN-PZT whereas the PZT was prepared by a standard mixed oxide route. Hence, we will treat more deeply the synthesis of PNN-PZT whereas PZT description will rather focus on the final characteristics of the studied samples. For completeness, there is also a brief review of samarium-doped PT (PTSm) sample preparation, but, as it is scarcely used and wasn't synthesized in the course of this study, the present characteristics were gathered from the supplier.

2.1 LEAD TITANATE (PTSm)

The lead titanate used in this study was doped with samarium and manganese according to $(Pb_{0.85}Sm_{0.10})(Ti_{0.98}Mn_{0.02})O_3$ with a PbO excess of 2.3 wt%, it was prepared by Damjanovic [1] by a mixed oxide method. The raw oxides were milled together in ethyl alcohol using zirconia balls during 24 h. The obtained slurry was then dried and sieved. The obtained powder was calcinated at 900°C for 2.5 h and then at 850°C for 6 h. XRD analysis showed a pure perovskite phase with some spurious peaks associated with remaining PbO. Then, the calcined powder was milled for 12 h, dried and sieved again. Approximately 10 wt% of the perovskite powder was pressed into disc, fired at 1230°C during 1 h, in a lead-compensating atmosphere provided by PZ powder. Discs were quenched from 1230°C into water at room temperature. Then, the quenched and calcined powders were mixed together in a 1:10 ratio. Finally, samples were uniaxially pressed and sintered at 1230°C during 3 h. The final density of the pellets was 97 % of the theoretical and the XRD spectra showed a pure perovskite phase. The samples were finally polished to optical quality and gold electrodes ($\approx$ 200 nm) were sputtered on the faces. Poling was performed at 150°C at 50 kV/cm for 5 min.

2.2 LEAD ZIRCONATE TITANATE (PZT)

Since the discovery of the very high properties of PZT solid solutions for MPB compositions, the processing of PZT ceramics has been refined and several routes were experimented. The objective of the present section is not to present innovative ways to synthesize PZT samples (e.g. very small grained) but rather to obtain good and reproducible samples which present uniform microstructural characteristics for various compositions allowing for comparison of properties independently of processing issues.

2.2.1 Mixed oxide route

The mixed oxide route is the most common route to synthesize PZT. It was applied since the first synthesis of PZT solid solutions containing a low amount of PT in PZ by Shirane *et al.* [2-4] and the first determination of the full PZT phase diagram [5]. Later, the discovery of very high electro-mechanical properties at MPB by Jaffe and his co-workers [6] was also made on samples prepared by a similar method.

Its principle is summarized on Figure 2.1 and consists in the mixing of the raw oxides weighted according to the desired composition. Then, firing at a moderate temperature (800°C to 1000°C) to prevent lead oxide evaporation permits the reaction forming the perovskite solid solution. The obtained powder compact is milled and finally pressed into pellets which are sintered at temperatures around 1200°C. In our work, we used the processing parameters developed by Demartin [7] in order to obtain pure and homogeneous PZT powders and sintered pellets.

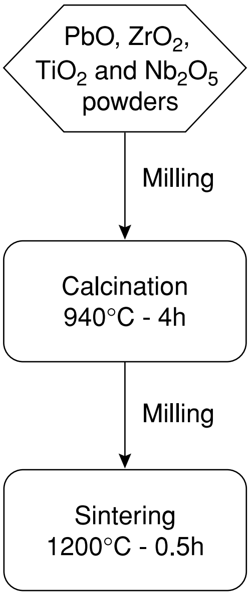

Figure 2.1: *Flow chart describing the mixed oxide route for synthesis of PZT. (Milling is performed using zirconia balls in isopropanol).*

As dopants and defects are well-known to control the properties of PZT (see e.g. Ref. [8]), compositions of the powders were chosen in order to prevent creation of too numerous defects in the ideal perovskite structure. In a pure PZT, there are two types of defects that cannot be avoided: lead vacancies due to evaporation and dopants due to starting powders impurities. Only a limited concentration of lead vacancies can be accommodated by the perovskite before transforming to pyrochlore-type phases. Moreover, it has been shown that PbO richer compositions tend to exhibit faster sintering [9] and better properties [10]. Here, to circumvent lead oxide evaporation during calcination and sintering, several techniques were used in parallel: a PbO excess of 2 wt% was added, all the thermal treatments were performed in sealed crucibles and a compensating atmosphere consisting in a bed of 90 wt% $PbZrO_3$ - 10 wt% PbO powder was used during the sintering stage. The effectiveness of such procedures cannot be exactly controlled in practice, but monitoring of the weight losses after sintering yields realistic figures for lead losses and hence for the necessary amount of initial compositional correction. Secondly, to prevent irreproducibility in properties coming from uncontrolled impurities, a doping level of 1 mol% Nb on the B-site was chosen. Thus, properties can be stabilized as any impurity coming either from raw materials or from processing procedure would have a much lower doping effect. Furthermore, it has been observed that doping PZT with Nb is inhibiting grain growth (see e.g. Ref. [11]) and thus stabilizes the grain size with respect to changes in compositions. Finally, as we aim at the study of nonlinear phenomena, it seems adequate to chose donor doping as it is supposed to enhance extrinsic contributions and thus nonlinearity. Thus, the following compositions were chosen in order to sweep through the MPB: $Pb(Zr_x,Ti_{1-x})_{0.99}Nb_{0.01}O_3$ + 2wt% PbO with x = 0.40, 0.45, 0.53, 0.60, and 0.65. In the following, the PZT compositions will be identified according to the code: 100x/100-100x.

For the processing, the procedure described in Figure 2.1 was used. After weighting, the raw oxide powders were mixed together and milled using zirconia balls in isopropanol. Then, the obtained slurry was dried and sieved before calcination. The temperature-time profile for the calcination was chosen at 940°C during 4 h with heating at 5°C/min in order to insure best reproducibility and phase purity of the obtained materials. The obtained fired body was hand-ground in a mortar to break the aggregates and milled using zirconia balls in isopropanol. Then, sintering was performed on pellets uniaxially pressed at 40 MPa in a sealed alumina crucible containing lead compensating powder isolated from the sample by sapphire. Again sintering conditions were selected as yielding best microstructural reproducibility at 1200°C for 1/2 h with heating at 2°C/min.

Monitoring of the crystalline purity was performed using XRD analysis. Figures 2.2 and 2.3 show the spectra obtained respectively after calcination and after sintering as a function of composition. The calcinated powders analyzed in Figure 2.2 show a distinct pseudo-cubic perovskite structure with the appropriate peak splittings expected from the non-centrosymmetric ferroelectric phases. No spurious peaks associated with pyrochlore phases are observed. However, given the high detection threshold for XRD, second phase absence cannot be strictly proven here. Above 53% PZ, the structure is rhombohedral with a distinct shoulder on the left of the (111) peak. Below 53% PZ a tetragonal structure is clearly obtained as (100) and (200) splittings appear. At 53% PZ, the structure is a mix of rhombohedral and tetragonal structures as generally observed [12] for MPB structures. Considering the relative peak intensities of the MPB composition, the rhombohedral structure seems predominant (see e.g. the (200) peak).

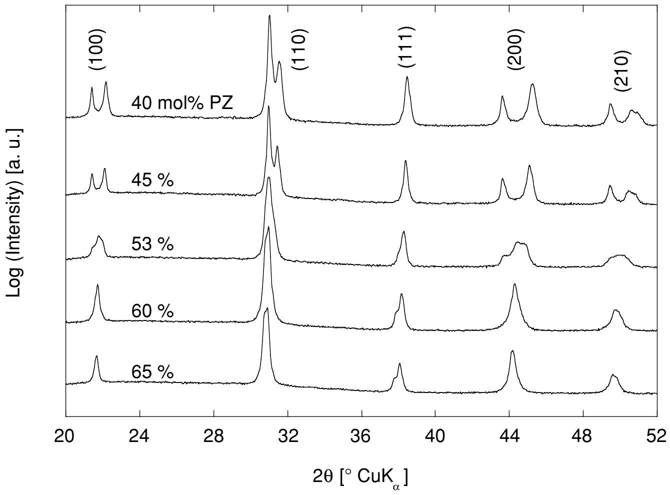

Figure 2.2: *XRD spectra of PZT calcinated powders as a function of composition. (Low angle hump is due to sample holder).*

Sintering effects on the PZT crystalline structure can be observed on Figure 2.3. Generally, peaks are getting sharper in agreement with a better crystallization or compositional homogenization due to higher temperatures [7]. $CuK_{\alpha2}$ shoulders can be seen e.g. on (200) reflections in tetragonal samples. Peak splittings are better defined, especially in the case of rhombohedral samples. The only significative change can be observed for the MPB 53/47 composition where, contrary to the calcined powder, the sintered pellet exhibits a predominantly tetragonal structure (as seen on the (200) peak). This phase change, already observed for commercial PZT powders [7], may be interpreted in terms of compositional homogenization kinetics. As PT is the most stable perovskite compound, a phase containing a higher than average Ti content is probably forming at the beginning of calcination, yielding an initial low volume fraction of Ti-rich tetragonal phase. Later, as PZT starts to crystallize, its average composition is shifted toward more rhombohedral compositions, leading to a high volume fraction of rhombohedral structure, as seen for 53/47 in Figure 2.2. Finally, during sintering, compositional homogenization occurs yielding a crystalline structure corresponding to the overall composition which is rather tetragonal as shown in Figure 2.3.

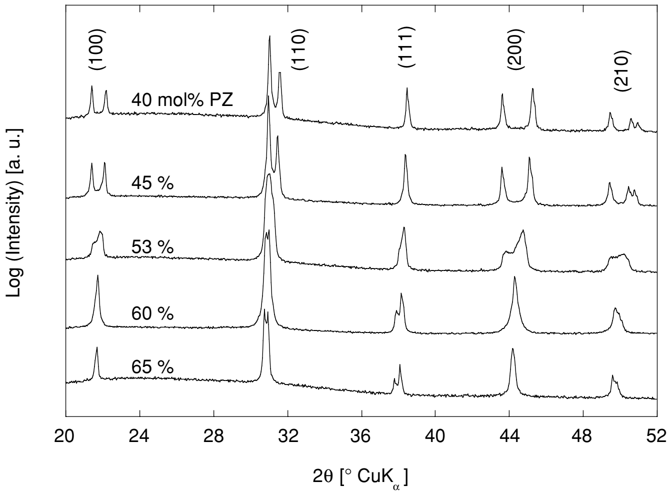

Figure 2.3: *XRD spectrum of PZT sintered samples as a function of composition. (Low angle hump is due to sample holder).*

A theoretical density can be calculated from lattice parameters extracted from Figure 2.3, assuming an ideal composition (i.e. no vacancies present in the structure). This permits to compute porosity in combination with an Archimedes-based determination of the apparent density of the sintered pellets. These results are presented in Table 2.3 in conjunction with the measured weight losses during sintering.

Table 2.1: *PZT compositions average characteristics after sintering.*

	65/35	60/40	53/47	45/55	40/60
Weight loss	1.0 %	0.7 %	0.6 %	0.3 %	0.6 %
ρ [g/cm^3]	7.82	7.76	7.81	7.71	7.77
Porosity	1.8 %	2.0 %	0.4 %	0.6 %	< 0.1 %

Lead evaporation stays below 1 wt%, which is reasonable considering the initial 2 wt% excess and the unevaluated losses during calcination. The observed weight loss variations with composition don't seem to be related to any reproducible event and may be due to small chips of pressed powder falling off the sample after green body weighting. The obtained relative densities are very satisfactory as the prepared samples show less than 2 % of porosity which is optimal for electro-mechanical properties. It can be noted that relative densities are higher for the tetragonal compositions, and that the value (< 0.1 %) obtained for 40/60 composition reflects the experimental imprecision.

To confirm phase purity and determine the average grain size of the obtained samples, SEM observations have been performed. The samples with the two extreme compositions were more particularly investigated. They were polished down to optical quality and etched using a solution containing HCl and HF. Their microstructures are presented at 4000× in Figures 2.4 and 2.5 for the 40/60 and 65/35 compositions respectively.

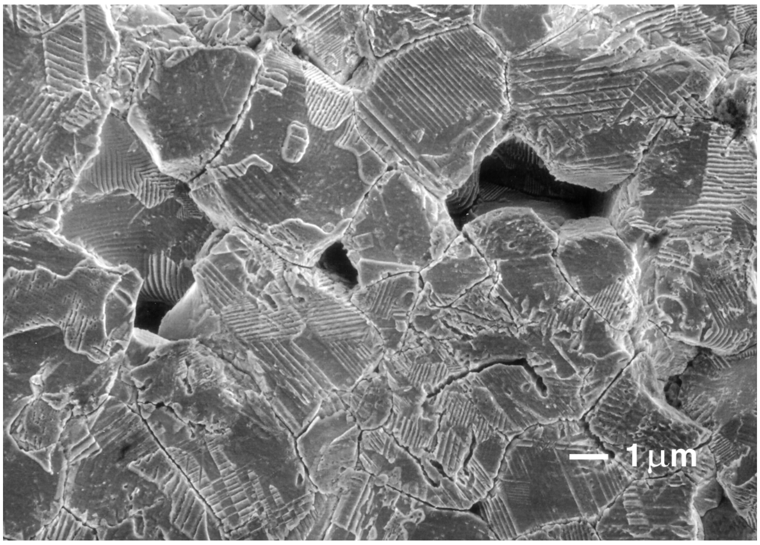

Figure 2.4: *SEM of 40/60 tetragonal PZT microstructure after etching.*

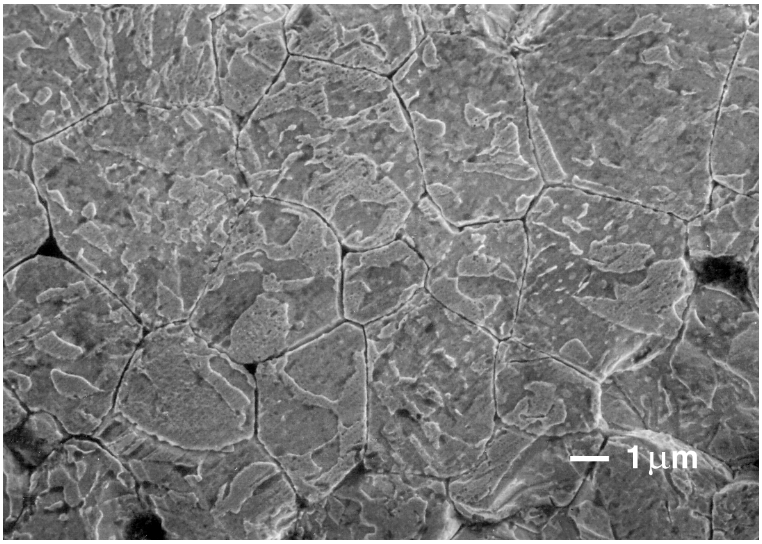

Figure 2.5: *SEM of 65/35 rhombohedral PZT microstructure after etching.*

For the tetragonal composition 40/60, the grain size goes from 2 to 5 µm and averages around 3 µm. The etching has revealed domain structures close to what is commonly observed in $BaTiO_3$ [13], such as herringbone domain patterns typical of tetragonal structures. No second phase can be observed, as suggested by XRD analysis. The microstructure of the rhombohedral composition 65/35 in Figure 2.5 shows a grain size similar to the tetragonal composition, grains are within 2 to 5 µm and the average size is around 3 µm. Some etching contrast can also be observed in the grains. However, it doesn't possess the classically observed shapes associated with ferroelectric domains. Still, they could be related to "watermarks" typical of 180° DW [13, 14] which only have to be parallel to the polarization direction. Finally, no second phase was observed in this sample.

The microstructural characteristics of the two extreme compositions are quite similar: they present no second phase and a homogeneous average grain size of about 3 µm. The observation of the other compositions revealed similar microstructures. Hence, it can be concluded that the samples prepared using the mixed oxides method present the sought microstructural characteristics and are suitable for further electro-mechanical characterization.

2.2.2 Samples basic electro-mechanical characterization

The PZT samples were prepared for the electro-mechanical characterization by polishing thin discs (aspect ratio ≈ 20) cut in the middle of the sintered pellets. Then, 200 nm Pt electrodes were sputtered and annealed at 900°C for 1 h to enhance conductivity and mechanical resistance. The samples were then poled in an oil bath at 120°C during 10 min using an electric field of 20 kV/cm. No field was applied to the sample while cooling. Then, the resonance and anti-resonance frequencies of the first and second harmonics of the planar mode and the first three resonance frequencies of the thickness mode were measured using an HP 4192A impedance analyzer. The corresponding electro-mechanical properties were obtained using a numerical procedure outlined in Ref. [1] and are presented in Table 2.2.

Dielectric characteristics in our PZT compositions present an usual trend: upon poling the dielectric permittivity decreases for rhombohedral samples and increases for the tetragonal ones. This is classically interpreted in terms of competition between dielectric permittivity anisotropy and 180° domains self-clamping removal [15, 16]. The first mechanism is predominant for rhombohedral compositions which exhibit low 180° domains clamping in the unpoled state. Whereas the latter is responsible for the low permittivity observed in unpoled tetragonal structures as their spontaneous deformation is much greater, thus leading to a sharp permittivity increase upon poling as most of the 180°domains are removed. However, note that this domain clamping mechanism is not valid anymore for very high PT contents where the intrinsic decrease in permittivity upon poling is greater than the clamping release effect.

Dielectric losses are in the expected range for such donor-doped compositions and do decrease upon poling due to the disappearance of DW.

Table 2.2: *PZT compositions average electro-mechanical characteristics.*

	65/35	60/40	53/47	45/55	40/60
$\varepsilon^{\text{as prepared}}$	531	534	1040	583	457
tg $\delta^{\text{as prepared}}$	3 ‰	3 ‰	2 ‰	2 ‰	3 ‰
$\varepsilon^{\text{poled}}$	454	486	1313	618	480
tg δ^{poled}	3 ‰	3 ‰	2 ‰	1 ‰	1 ‰
d_{31} [pC/N]	49	61	180	35	31
k_p	43 %	50 %	73 %	26 %	27 %
k_t	35 %	48 %	48 %	29 %	35 %

Concerning the piezoelectric properties, d_{31} values are indeed showing a sharp maximum at the MPB composition 53/47 as commonly observed [6, 17]. The planar coupling coefficient, k_p is following d_{31} trend but shows a broader maximum at MPB. This is due to the lower dielectric permittivity in rhombohedral phase which decreases the dielectrically stored energy [18]. This effect is even more accentuated in the case of k_t where the maximum shifts toward the rhombohedral side (as MPB and 60/40 compositions present the same value).

2.2.3 Conclusion

The prepared PZT samples present a pure perovskite phase (to the extent of XRD analysis and microstructural SEM observations). Their grain size is independent of composition and is situated around 2-3 µm. The electro-mechanical properties obtained by resonance method are in good agreement with previously published data, showing a typical maximum in the MPB region. Further investigations can thus be safely performed and analyzed in terms of crystalline phase (tetragonal or rhombohedral) and composition (amplitude of deviation from the prototype cubic symmetry) only.

2.3 LEAD NICKEL NIOBATE - LEAD ZIRCONATE TITANATE (PNN-PZT)

The complex perovskites were first foreseen and prepared by Smolenskii *et al.* [19, 20] in the late 1950's. They were based on the fact that the perovskite structure (ABO_3) can accommodate cations which sizes present large deviations from the ideal Goldschmidt (or tolerance) factor [21, 22]. However, as niobium is a very efficient pyrochlore former [23-25], the synthesis of Nb-containing relaxors is more difficult than of regular ferroelectric PZT [26]. Thus, since their first synthesis, new ways of preparation have been explored in order to neutralize the detrimental effects of Nb on the perovskite phase stability. As a consequence, the processing of good quality and reproducible relaxor-ferroelectric solid solutions is still a challenge.

In this section, we will focus on the synthesis of $Pb(Ni_{1/3}Nb_{2/3})O_3$-$PbTiO_3$ (PNN-PZT) compositions as they present one of the highest k_{33} (> 80 %) ever observed for ceramics as well as very good dielectric properties ($\varepsilon^{poled} > 6200$) for 50 mol% of PNN [27]. They were first synthesized by Buyanova *et al.* [28] for moderate PNN contents (up to 30 mol%) shortly after pure PNN first synthesis. Here, we will explore different routes leading to PNN-PZT solid solutions, aiming at the most efficient properties/processing methods. In particular, we will present two new routes for such compounds presenting either very good chemical homogeneity and second phase appearance resistance or very short processing with satisfying properties. The issue of relaxor content choice with respect to the desired properties will also be discussed and the advantages of using relaxor-PZT rather than relaxor-PT solid solutions will be presented.

2.3.1 Lead-based complex perovskite processing

Buyanova *et al.* [28] used a regular mixed-oxide route to obtain the first PNN-PZT solid solutions. However, this standard method is not yielding pyrochlore-free powders in a very reproducible way [29], as it depends on the raw oxides purity [30] and granulometry [29]. Studies on PMN synthesis have shown that Mg introduction in an early-formed $Pb_2Nb_2O_7$ pyrochlore is the critical step in the perovskite formation mechanism [31]. It was hence proposed to synthesize first a mixed compound of Mg and Nb: the columbite $MgNb_2O_6$ presenting the same Mg-Nb stoichiometry as in the final PMN [31] and preventing the formation of Mg-free pyrochlores by the atomic mixing of the two B-site cations. This method (along with an excess of MgO) was successfully applied to PMN yielding pure perovskite powders. It was then generalized to other compounds like pure PNN (e.g. Ref. [32, 33]). For PNN-PZT, this procedure is now used commonly [34-39], and is schematically represented in Figure 2.6. Relaxor B-site oxides (NiO and Nb_2O_5) are mixed and fired at high temperature (typically around 1000°C) for a long time (> 2 h) to form the columbite ($NiNb_2O_6$). Then, this precursor is mixed with Pb, Zr and Ti oxides, before calcining at moderate temperatures (800-900°C) to prevent lead losses. This method produces pyrochlore-free PNN-PZT with better properties than the ones obtained by a single calcination [39] which can be interpreted as an effect of the better compositional homogeneity. Some alternate routes based on the separate synthesis of PNN, PZ and PT [39] or starting with columbite, PbO and PT [40] and their subsequent co-firing yielded less interesting properties.

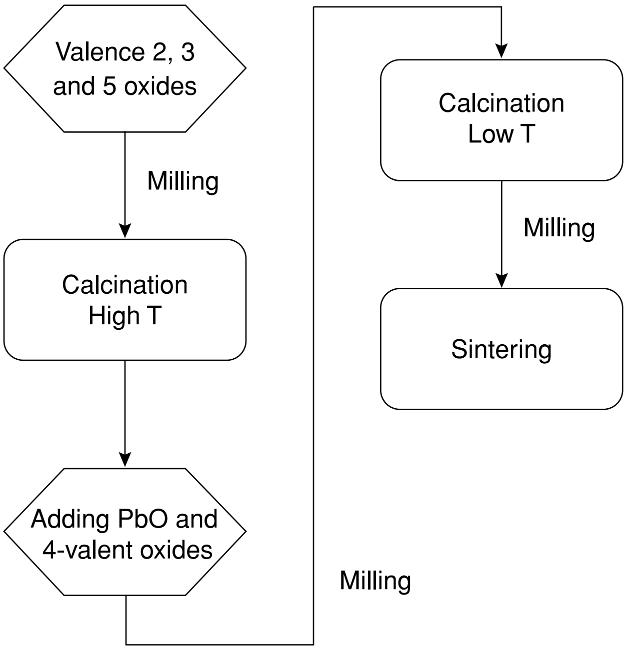

Figure 2.6: *General flow chart describing the various precursor routes for synthesis of relaxor-ferroelectric solid solutions.*

Among alternative ways to obtain PNN-ferroelectric powders, hydrothermal routes using nitrates, acetates and oxalates were attempted [41, 42] as well as alkoxide-based precursors [32], but the obtained properties were not significantly different from those obtained by classical methods. PNN-PT single crystals have also been produced by growth in PbO flux [43] in conditions similar to the pure PNN [44], unfortunately no PNN-PZT crystals have been reported yet.

Besides its high properties, PNN-PZT system also presents interesting low-temperature sintering abilities. Satisfactory sintering was reported at temperatures as low as 1050°C using various dopants (SiO_2 [45], CdO [46, 47]) or even 900°C with a large amount of frit [48, 49]. Such temperatures permit the use of co-sintered silver-palladium electrodes to produce cheaper multi-layer capacitors [50] or piezoelectric bimorphs [51]. However, the sintering temperature of such modified compositions seems to be proportional to the PNN content [40] and hence, only low PNN-content (≤ 20 mol%) compositions can be used for such applications.

2.3.2 B-site precursor route

In the processing of PNN-PZT, we will follow the same objectives as for PZT: to obtain powders free of second phase and sintered samples showing a uniform microstructure independent of composition. Moreover, as the number of cations is quite high (5) and as their distribution on the B-site is related to the relaxor behavior [52, 53] special attention has to be taken in order to optimize the B-site cationic homogeneity. The columbite route summarized in Figure 2.6 exhibits very good pyrochlore resistance characteristics. However, based on the PZT chemical homogeneity studies [7] and observations of the diffuseness of transition in PZN-PMN [54], the repartition of the cations on the B-site can be questioned. As complete homogeneity could not be achieved in PZT for low sintering temperatures, it seems doubtful that the case will be more favorable for PNN-PZT containing twice as many cations. Hence, the procedure schematized on Figure 2.7 was chosen to keep the advantages of Nb atomic mixing with Ni along with guaranteeing a better distribution of the B-site cations. Its principle can be exposed as follows: a precursor containing all the B-site oxides (i.e. NiO, Nb_2O_5, ZrO_2 and TiO_2) is prepared by calcination at high temperature (immediately below the lowest melting temperature of the binary oxide systems) in order to attain full reaction of the constitutive oxides and hence best initial chemical homogeneity. This B-site precursor is then mixed with PbO before final calcination at moderate temperature to prevent lead losses. Then, sintering is performed at a relatively high temperature to allow for variation of the PNN content while keeping the same processing procedure, as the necessary sintering temperature increases with the PNN content [40]. Finally, a long sintering time permits to homogenize the grain size in the material. Similar B-site precursor methods have been tested for both PZT [7] and PZN-PMN [54] but were involving less elements and more straight forward chemical structures.

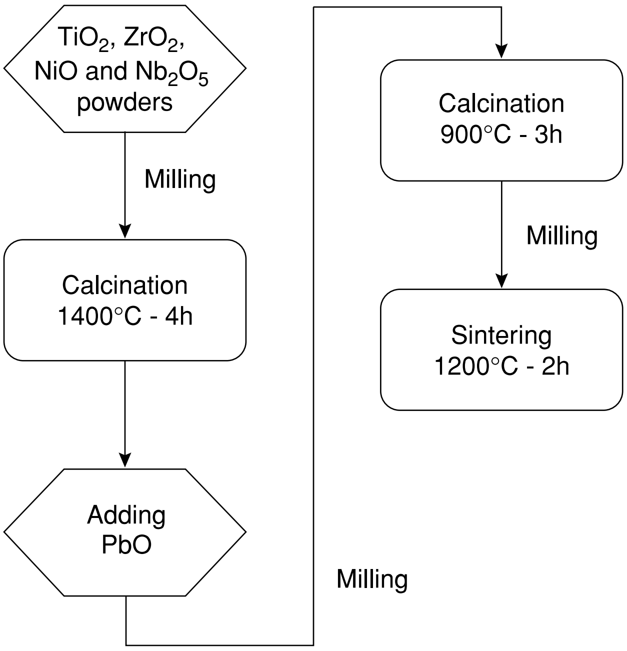

Figure 2.7: *Flow chart describing the B-site precursor route for synthesis of PNN-PZT. (Milling is performed using zirconia balls in isopropanol).*

Two types of compositions were chosen for this investigation: $0.50[Pb(Ni_{1/3}Nb_{2/3})O_3]$-$0.50[Pb(Zr,Ti)O_3]$ (50PNN-50PZT) and $0.40[Pb(Ni_{1/3}Nb_{2/3})O_3]$-$0.60[Pb(Zr,Ti)O_3]$ (40PNN-60PZT). The first corresponds to the highest properties reported for the PNN-PZT ternary system [27, 34] and the latter permits to study the effects of a variation of the relaxor content while keeping a reasonable amount of relaxor, i.e. not going into PNN-PZT compositions extremely sensitive to pyrochlore apparition (as the Nb content increases). The PZ/PT ratio was varied for both of the PNN contents in order to change the crystalline symmetry and thus reach the high properties region. Note that from the PNN-PZ-PT ternary diagram [55] a shift of the MPB position toward PT-rich region is expected with an increase of the PNN content (as 30 mol% PT corresponds to MPB without PZ, cf. Figure 1.4). Thus, the PZ/(PT+PZ) ratio corresponding to MPB will not be identical for two different PNN contents. Like in PZT, a constant PbO excess of 2 wt% was added to prevent lead losses during calcination and sintering. Concerning doping, as PNN acts as a buffer (i.e. a slight doping addition will not change significantly the number of cations having a valence $\neq 4$), neither donor nor acceptor doping were necessary.

The B-site precursors for 40PNN-60PZT were prepared by milling together the raw oxides using zirconia balls and isopropanol, sieving the dried slurry, and calcining them at 1400°C during 4 h in an alumina crucible. Their XRD spectra are presented in Figure 2.8. The effect of ZrO_2 content variation shows clearly the presence of two phases: a Ti-rich one (marked with circles) predominant in the 20 mol% ZrO_2 composition and a Zr-rich one (marked with diamonds) accommodating all the oxides in the 32 mol% ZrO_2.

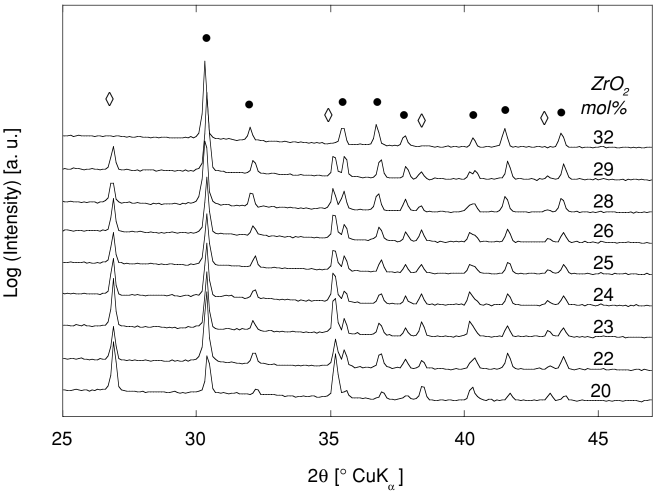

Figure 2.8: *XRD analysis of B-site precursors as a function of ZrO_2 content in 40PNN-60PZT compositions (◊ and • stand respectively for $Ti(Ni_{1/3}Nb_{2/3})O_4$ -type and $ZrTiO_4$ -type reflections).*

As the B-site precursors are a diphasic mixture, it was of interest to test whether the Ni and Nb oxides are effectively mixed according to correct stoichiometry in both phases to ascertain the beneficial effects of the attempted precursor route. Two main structure-types were the most likely: a columbite ($NiNb_2O_6$) hosting Zr and Ti elements as defects and a $ZrTiO_4$-type accommodating Ni and Nb in the $(Ni_{1/3}Nb_{2/3})$ substitutional form. Thus, $ZrTiO_4$ and $NiNb_2O_6$ were synthesized for comparison with the obtained precursors. As expected from JCPDS files, the columbite ($NiNb_2O_6$) did not correspond to any of the B-site precursors, whereas the $ZrTiO_4$ showed striking similarities with the Zr-rich observed phase as shown in Figure 2.9.

Putting aside the obvious distortions due to the non-stoichiometry in Zr/Ti and to the accommodation of Ni and Nb, the only difference between the two spectra in Figure 2.9 is the fact that in $ZrTiO_4$ (120) and (002) peaks are superimposed which is not the case for the precursor. Hence, the Zr-rich phase can certainly be identified with a Pnab space group similar to that of $ZrTiO_4$. The appearance of such a structure can be understood by considering ionic radii: in $ZrTiO_4$ the largest (Zr^{4+}) and the smallest (Ti^{4+}) cations are combined. Hence, Ni and Nb, both exhibiting intermediate ionic sizes, may easily sit on both Zr and Ti sites. The fact that a single phase can exist for 32 mol% of Zr seems to indicate that Ni^{2+} and Nb^{5+} tend to replace Ti rather than Zr. Concerning the Ti-rich phase, as columbite-like phases containing substitutional Ti are not very likely due to its small ionic size, a $TiBO_4$-type of compound seems more probable. And, indeed, the Ti-rich phase spectra is very similar to the rutile-like phase $Ti(Mg_{1/3}Nb_{2/3})O_4$ (JCPDS file # 40-366). Hence, a formulation close to

$Ti(Ni_{1/3}Nb_{2/3})O_4$ comes naturally (as Ni size is close to Mg size) with some probable inclusion of Zr preferably on the $(Ni_{1/3}Nb_{2/3})$ site due to its greater ionic size.

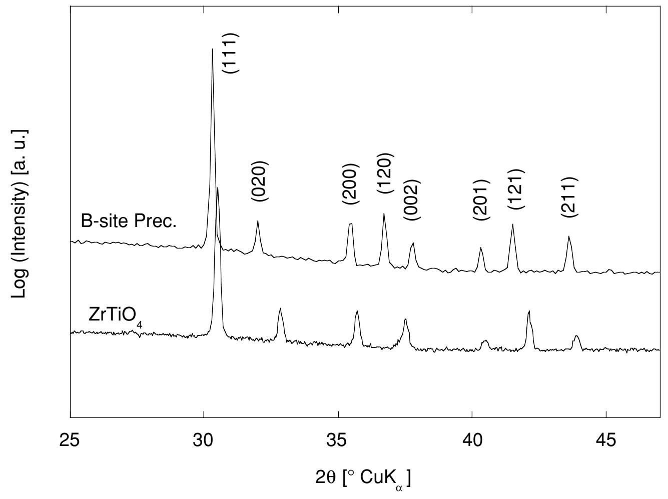

Figure 2.9: *XRD of $ZrTiO_4$ (Pnab) with the B-site precursor for the 40PNN-32PZ-28PT composition.*

In conclusion, as the assumed valence on each site of the two precursor phases is 4, there is a high probability that the synthesized precursors do contain Ni and Nb in the desired stoichiometry (1:2 ratio). The precursors can hence be effectively used for the synthesis of PNN-PZT perovskite with the same desirable effects of Ni-Nb atomic mixing as in columbite.

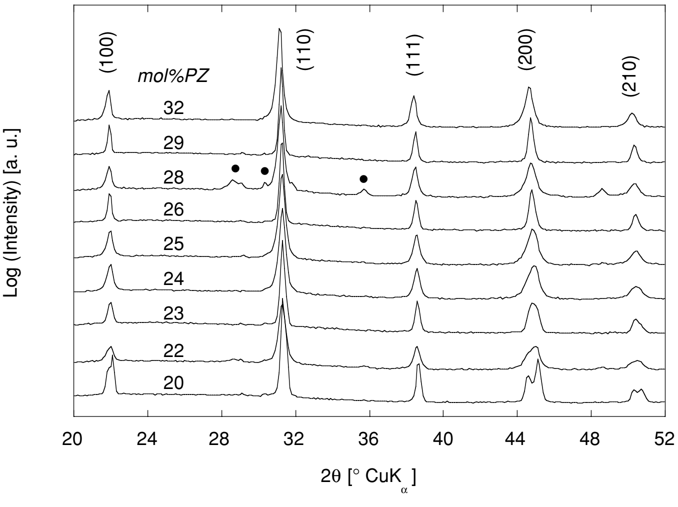

Figure 2.10: *XRD analysis of calcinated powders as a function of PZ content in 40PNN-60PZT compositions (sintering was performed at 1200°C - 2h). (• represents unreacted PbO).*

The obtained precursors were milled with PbO using zirconia balls and isopropanol. Then, the obtained slurry was dried, sieved and calcined in a covered alumina crucible for 3 h at 900°C. The XRD of the resulting powders is given in Figure 2.10 where a pure perovskite structure is obtained for all the compositions. The small supplementary peaks observed for 28 % PZ indicated by dots are due to unreacted PbO, maybe coming from the excess added to prevent losses. Figure 2.10 also indicates a tetragonal distortion of the cubic lattice for compositions below 25 %PZ. However, for PZ contents higher than 25 %, no definite rhombohedral structure (as expected from the reported ternary phase diagram [55]) can be identified. (111) peaks are getting only a bit wider than in the tetragonal phase, which may be due to a slight rhombohedral distortion not separated by our measurement set-up or to incomplete crystallization and homogenization of the powders.

Finally, the obtained powders were uniaxially pressed at 40 MPa and sintered at 1200°C during 2 h in a closed alumina crucible containing 90 wt% $PbZrO_3$ - 10 wt% PbO powder (similarly to PZT) to provide a lead compensating atmosphere during sintering. The final pellets were weighted to determine lead losses and their apparent density was measured using an Archimedes-based method. Lead evaporation during sintering is comprised between 0.3 and 1.8 wt% with an average of 1.3 wt% which is acceptable considering the initial 2 wt% lead excess and the probable losses during calcination. A portion of each sample was then cut and crushed to perform XRD analysis as presented in Figure 2.11. The obtained structures are all pure perovskite, without any second phase detectable by XRD. Alike raw powders, the structures of compositions below 25 %PZ exhibit a tetragonal symmetry, whereas no clear rhombohedral peak splittings can be identified for higher PZ contents. Even the (111) peaks do not look wider any more in the PZ-rich compositions.

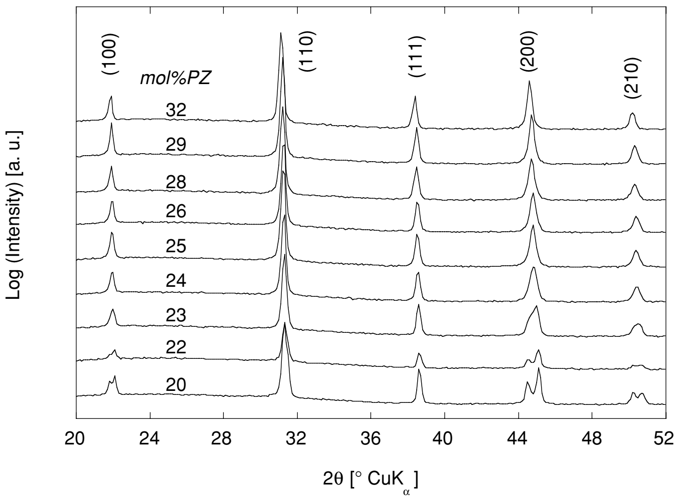

Figure 2.11: *XRD analysis of the final sintered samples as a function of PZ content in 40PNN-60PZT compositions.*

Absolute densities were calculated based on the lattice parameters extracted from XRD. Porosity of the samples was determined to range from 1.5 to 3.8 % with an average of 2.9 %. Close to those of PZT, these values are well adapted to electro-mechanical testing.

To determine grain sizes and to check for the presence of yet undetected second phase, the sintered samples were also observed using SEM after polishing to optical quality and etching using a solution of HCl and HF. As the results were quite similar for all the compositions, micrographs of the two extreme compositions (32 and 20 %PZ) only are presented on Figures 2.12 and 2.13 respectively.

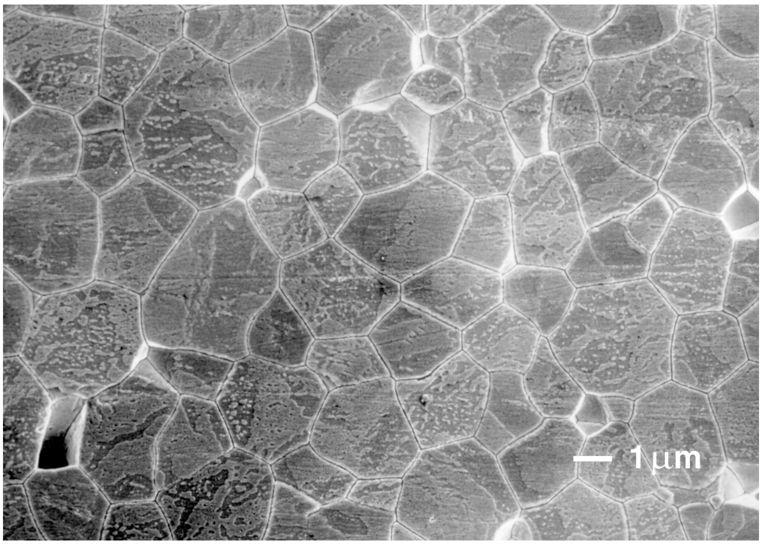

Figure 2.12: *SEM etched microstructure of a rhombohedral 40PNN-32PZ-28PT sintered sample.*

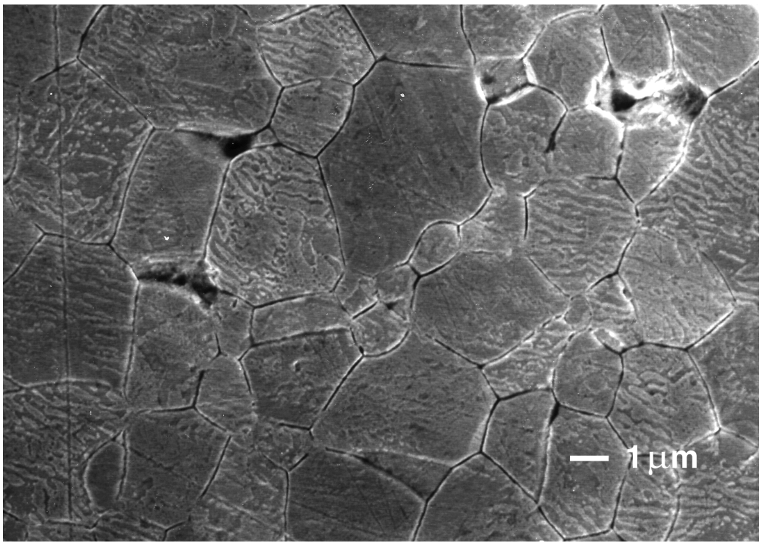

Figure 2.13: *SEM etched microstructure of a tetragonal 40PNN-20PZ-40PT sintered sample.*

The overall microstructures of both compositions are very similar: the grain size is situated around 3-4 µm and does not vary significantly with composition (although a slight grain size increasing tendency with PT content may be proposed). No second phase is observable and porosity is satisfying. The contrasts seen in the grains may be 180°domains as for 65/35 PZT in Figure 2.5, but they do look more regular than “watermarks” in barium titanate [13, 14]. Such stripes look indeed more periodic and thin especially in the tetragonal case and may be related to some relaxor effect on the ferroelectric domain structure [56]. Still, such a contrast may also have been created during etching.

In parallel with 40PNN-60PZT, compositions of 50PNN-50PZT have been prepared using the same B-site precursor procedure (as described in Figure 2.7). Their precursors also exhibited the two phases already observed on Figure 2.8 with the exception of the 50PNN-13PZ-37PT precursor which contained only $Ti(Ni_{1/3}Nb_{2/3})O_4$ rutile-like phase. This indicates that some Zr can indeed be accommodated in this phase. Compared to the 40PNN-60PZT case, this effect is probably favored by the higher content in large Ni and Nb cations contributing to the expansion of the precursor lattice cell volume. This hypothesis is confirmed by a systematic low angle shift of the 50PNN-50PZT precursor peaks compared to 40PNN-60PZT. Then, perovskite powders were prepared by calcination at 900°C - 3 h with extra PbO and pellets were sintered in the same conditions as before. The observed weight losses were ranging from 0.9 to 2.2 wt% with an average of 1.5 %. The XRD analysis of the sintered samples is presented in Figure 2.14 and shows that second phase-free samples of 50PNN-50PZT can be obtained by our B-site precursor route.

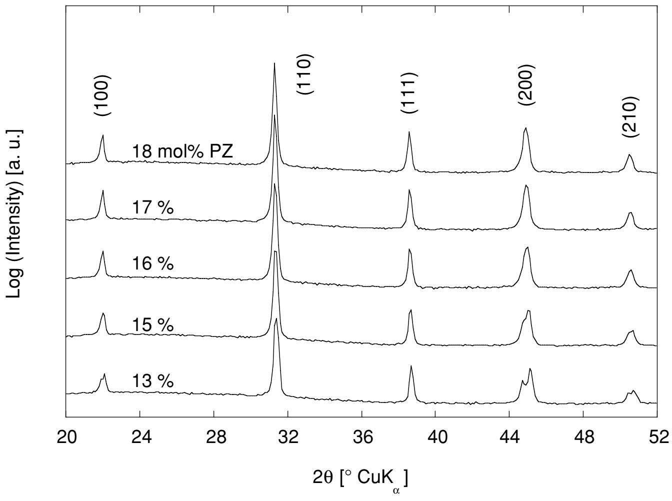

Figure 2.14: XRD analysis of the sintered samples as a function of PZ content in 50PNN-50PZT compositions (sintering was performed at 1200°C - 2h).

In Figure 2.14, alike 40PNN-60PZT, the structure is clearly tetragonal for compositions below 15 % PZ but is rather cubic for high PZ contents. The absolute densities could also be calculated from the XRD spectra and the relative porosities were determined to lay between 2.9 and 4 % averaging at 3.3 % which is a high but acceptable value in view of electro-mechanical testing.

SEM observations were also performed on these samples (after polishing and etching). The micrographs are presented in Figures 2.15 and 2.16 for the two end compositions (18 and 13 % PZ respectively).

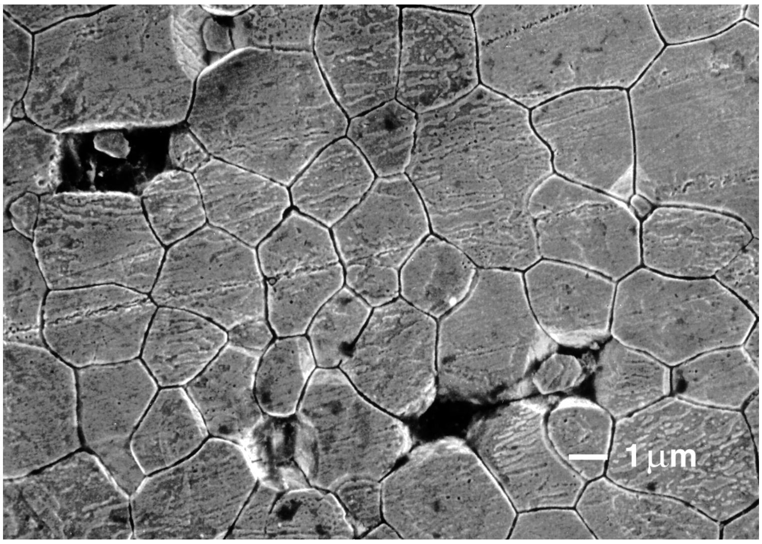

Figure 2.15: *SEM etched microstructure of a rhombohedral 50PNN-18PZ-32PT sintered sample.*

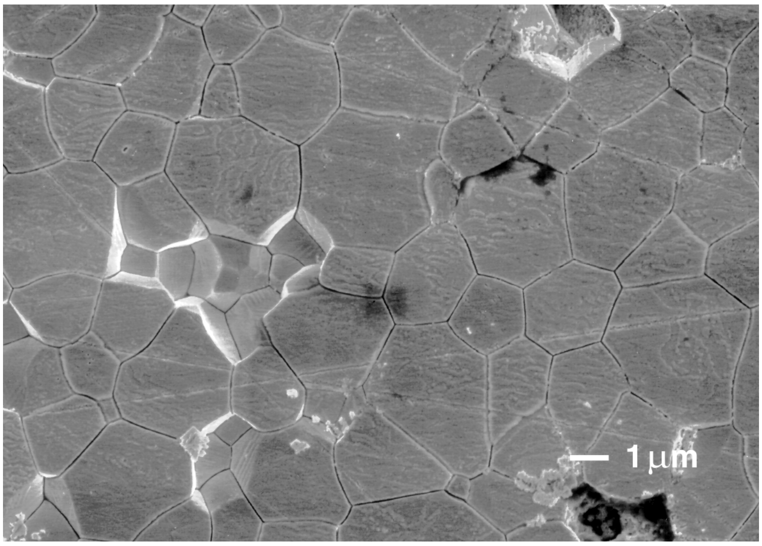

Figure 2.16: *SEM etched microstructure of a tetragonal 50PNN-13PZ-37PT sintered sample.*

Again, no second phase can be detected and the microstructures are alike with a grain size of approximately 2-3 µm. In this case, no grain size dependence with composition is observed. Some contrast is observed in the grains but it is less pronounced than for 40PNN-60PZT. This may be due to uncontrolled differences in etching conditions but may also be accounted for by the higher relaxor-content leading to less pronounced ferroelectric characteristics (e.g. lower spontaneous deformation). Contrary to 40PNN-60PZT, no significant changes in the grain stripe shapes as a function of crystalline symmetry can really be observed here.

2.3.3 Samples basic electro-mechanical characterization

Processing of pyrochlore-free PNN-PZT solid solutions has been successfully achieved by the proposed B-site precursor route. However, in order to validate such a processing method, electro-mechanical properties have to be determined. The sintered samples were hence cut and polished into discs presenting a diameter/thickness aspect ratio of approx. 20. Platinum electrodes (≈ 200 nm) were then sputtered and annealed at 900°C during 1h. Samples were poled at 20 kV/cm in an oil bath heated at 80°C. The cooling was performed without electrical field applied. Finally, the resonance frequencies of the radial and thickness modes were characterized using the same set-up as for PZT and data were treated in the same way as well.

The dielectric and piezoelectric results for the 40PNN-60PZT compositions are presented respectively in Figures 2.17 and 2.18. First, it is noteworthy that quasi-cubic compositions (i.e. PZ ≥ 24 mol%) are exhibiting a piezoelectric effect indicating that they are actually not cubic, they will be denoted as pseudo-cubic.

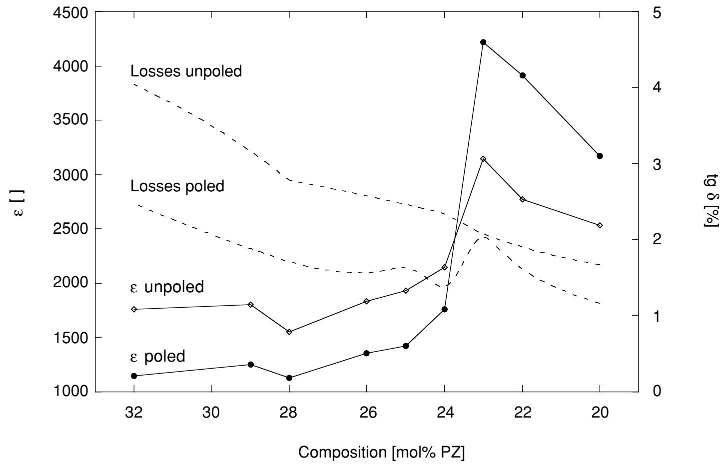

Figure 2.17: *Dielectric properties summary for the 40PNN-60PZT compositions as a function of PZ content.*

The variation of the dielectric permittivity with the PZ composition for 40PNN-60PZT is similar to what is observed for PZT: the permittivity increases with poling for the tetragonal symmetry and decreases once MPB is crossed. This phenomenon may probably be explained by the same mechanisms as for PZT (see section 2.2.2). This implies that an actual phase transition is observed and the compositions containing more than 23 %PZ are indeed constituted by a phase that behaves like the rhombohedral one in PZT. Hence, the transition region between the tetragonal structure and this high PZ-content pseudo-cubic region will be called MPB. Alike PZT, losses are decreasing with decreasing PZ content. The peak in losses for the poled 25PZ composition may be interpreted in terms of enhanced extrinsic contributions close to the MPB which are causing larger losses.

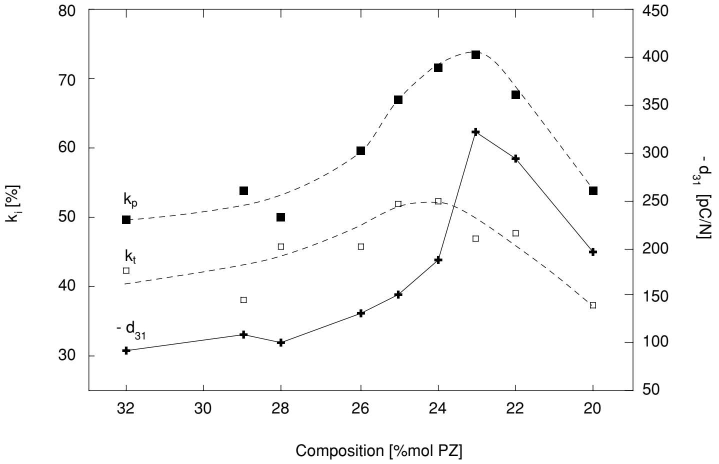

Figure 2.18: *Piezoelectric properties summary for the 40PNN-60PZT compositions as a function of PZ content.*

Piezoelectric properties of the 40PNN-60PZT compositions in Figure 2.18 are also behaving in a way very similar to PZT, with a maximum of d_{31} and k_p at the tetragonal composition closest to the morphotropic transition and a slight shift of k_t optimal value toward PZ-richer compositions. Again, the interpretation of such behaviors can be given in the same terms as for PZT (see above, section 2.2.2).

The 50PNN-50PZT samples were characterized in the same way as 40PNN-60PZT, their electro-mechanical properties are summarized in Table 2.3. Again, they exhibit the same qualitative compositional dependences as 40PNN-60PZT with a clear maximum of almost all the properties (excepted k_t) for 15 %PZ. Note that, exactly like in the lower PNN content compositions, the dielectric losses of the poled 15 %PZ sample are also significantly higher compared to the other compositions. k_t maximum is also shifted toward PZ-richer compositions with respect to the highest permittivity point. Quantitatively, the dielectric and pure piezoelectric (d_{31}) properties are significantly larger for such a composition than for 40PNN-60PZT. However, the coupling factors indicating the efficiency of the electro-mechanical conversion do not exhibit the same relative increase. This comes from the fact that dielectric permittivities are increasing by the same proportion as the piezoelectric coefficients are. Finally, it is noteworthy that the obtained dielectric and piezoelectric properties for the 50PNN-15PZ-35PT are significantly higher (+5 % in ε and +40 % in d_{31}) than those reported in the literature [27, 34] for the same composition processed by a standard columbite route.

Table 2.3: *50PNN-50PZT compositions average electro-mechanical characteristics (noted PZ/PT).*

	18/32	17/33	16/34	15/35	13/37
$\varepsilon^{\text{as prepared}}$	2821	3026	3555	4029	3512
$\text{tg}\,\delta^{\text{as prepared}}$	3.0 %	2.9 %	2.8 %	2.5 %	2.0 %
$\varepsilon^{\text{poled}}$	2284	2654	3200	6426	4770
$\text{tg}\,\delta^{\text{poled}}$	1.8 %	1.8 %	1.9 %	2.5 %	1.6 %
d_{31} [pC/N]	184	227	269	407	273
k_p	62 %	69 %	71 %	75 %	64 %
k_t	48 %	51 %	51 %	49 %	45 %

In conclusion, the PNN-PZT properties are behaving qualitatively like PZT with the notable exception that they are significantly higher. In that respect, those compositions are well within the requirements for new high performance piezoelectrics. In the compositional range studied, compositions with more PNN tend to exhibit larger electro-mechanical properties. However, this increase in properties is compensated by a decrease in Curie temperature, as PNN has a T_C of -120°C [19]. Hence, for practical applications, a trade-off has to be made in terms of thermal stability vs. material piezoelectric performance. This point also reveals one of the advantages to use PNN-PZT rather than PNN-PT solid solutions. As the highest properties are attained in the vicinity of the MPB, compositions in this region are the most desirable. However, in the case on PNN-PT, there is only one such composition exhibiting a definite T_C (around 40°C [43, 57]), whereas for PNN-PZT there is one MPB region per chosen PNN content. This allows for an optimization of the properties at constant T_C by a variation of the PZ/PT ratio with respect to the relaxor content. Finally, the B-site precursor method has been proven to yield improved electro-mechanical performances compared to the classical columbite route.

2.3.4 Reactive Ni oxide route

Although the results of the B-site precursor route are quite satisfying, a single calcination procedure would be more preferable from a practical point of view. However, it has been showed that raw oxides mixing and calcining is not a sufficiently efficient method [29]. To avoid the formation of stable Pb-Nb pyrochlores, the Ni has to be reactive from the very beginning of the synthesis. A previous work on PMN [58] has proposed a modification to the columbite route by using more reactive Mg hydroxy-carbonate rather than oxide in the columbite preparation. Moreover, the hydroxy-carbonates present the advantage of having an increased shelf-life compared to oxides which tend to hydrate or to carbonate. The same type of compounds (Ni acetate and Mg carbonate) were also used in mixed-oxide preparation of low sintering temperature PMN-PNN-PZT without explicit explanation. Based on these results, a new type of mixed-oxide route which uses more reactive Ni compound than NiO can be formulated. A Ni hydroxy-carbonate ($Ni_5(CO_3)_2(OH)_6 \cdot 4H_2O$) has been found to be readily available and was chosen for testing. Its decomposition temperature into Ni oxide is situated below 500°C [59] just below the range of PT formation in PNN-PZT [29].

Such a route will certainly not favor the chemical homogeneity with respect to the precursor-based processing. However, from a practical point of view, this method is definitely more work effective than the previous one. In the same perspective, it is favorable to look for the optimal calcination temperature as high temperature firing can be dissuasive. Hence, from this application oriented point of view, a composition exhibiting a T_C greater than 200°C (a classical industrial standard) and close to the high electro-mechanical properties region (MPB) was chosen for testing such a new method. After some preliminary synthesis, a composition of $0.34\ Pb(Ni_{1/3}Nb_{2/3})O_3$ - $0.27\ PbZrO_3$ - $0.39\ PbTiO_3$ (34PNN-27PZ-39PT) was selected. As for the previous routes, a lead oxide excess of 2 wt% was added to the initial composition. Finally, the procedure described in Figure 2.19 with varying calcination temperatures was followed.

Calcination temperatures were chosen from 700°C to 900°C, i.e. in the range of reported perovskite formation for PNN-PZT [29]. Following the technique used by Swartz *et al.* [31] in PMN synthesis, 2 mol% of Ni were also added for the two extreme calcination temperatures. The XRD spectra of the obtained powders after calcination during 3 h in a covered crucible are presented in Figure 2.20. It shows that a pyrochlore-free perovskite structure can be synthesized from 750°C, which is much better than previous studies on mixed oxide processing of PNN-PZT showing remanent pyrochlore up to 850°C [29].

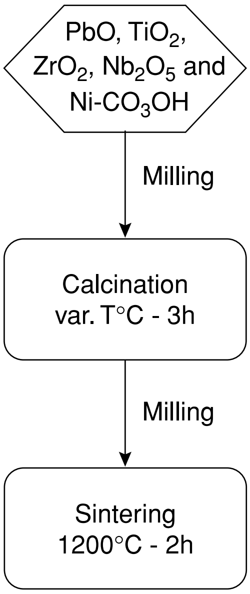

__Figure 2.19:__ Flow chart describing the reactive Ni oxide route for synthesis of PNN-PZT. (Milling is performed using zirconia balls in isopropanol).

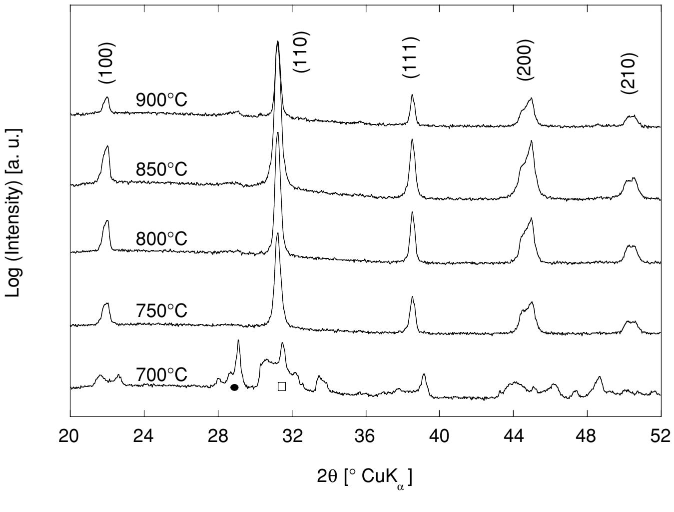

__Figure 2.20:__ XRD analysis of 34PNN-27PZ-39PT powders as a function of calcination temperature. Peaks indicated by a circle and a square correspond respectively to lead oxide and lead titanate peaks.

The powder calcinated at 700°C shows a mixture of PT-like perovskite (square in Figure 2.20), Pb-Nb pyrochlores, lead oxide (massicot, circle in Figure 2.20) and a small amount of NiO suggesting that it is already partially accommodated in the perovskite and pyrochlore phases. These intermediate phases react above 700°C to form a pure perovskite phase at 750°C. Some shoulders on the low-angle side of (110) peaks can be seen on the 850°C and 900°C calcinated powders. They are probably linked with the presence of Pb-Nb pyrochlore in a concentration just at the detection limit of the XRD analysis. Still, depending on its actual composition, this second phase may well decompose at higher temperatures yielding perovskite [23, 24].

Hence, the calcinated powders were all sintered after uniaxial pressing at 40 MPa in a covered crucible containing the usual lead compensating powder (90 wt% $PbZrO_3$-10 wt% PbO). The temperature profile was similar to the B-site precursor method and consisted in 2 h at 1200°C. After sintering, an average weight loss of 2.1 wt% was observed with a rough decreasing trend with increasing calcination temperature. XRD analysis was performed on the sintered pellets, as presented on Figure 2.21 where pure perovskite phase is exhibited by all the samples except the two extreme ones. All compositions also show distinct tetragonal distortion on the (200) peak, with a lower crystallization level of the samples sintered at 700°C and 900°C.

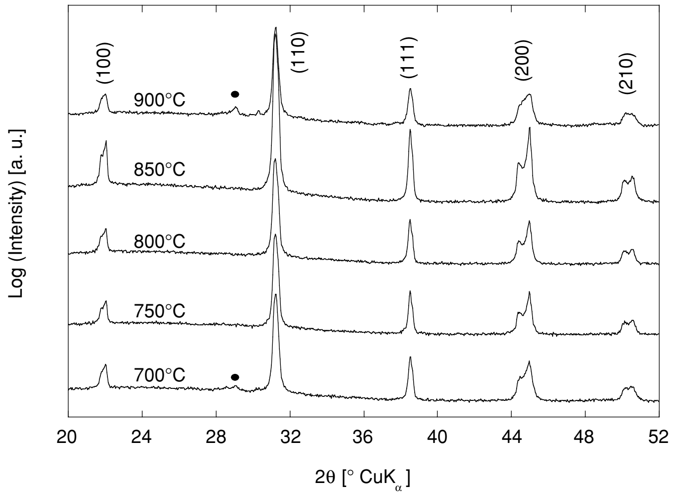

Figure 2.21: *XRD analysis of 34PNN-27PZ-39PT sintered samples as a function of calcination temperature (sintering was performed at 1200°C - 2h). Circles represent pyrochlore peaks.*

The reasons for the pyrochlore presence in 700°C and 900°C pellets are probably linked with the apparition of lead-deficient pyrochlore [24] which does not decompose into perovskite. This pyrochlore may be appearing in the 900°C fired sample due to too high lead losses during calcination, whereas in the case of 700°C sample remaining lead oxide in the powder may have preferentially evaporated before reacting during the heating to 1200°C. This may be confirmed by the fact that the highest weight loss at sintering (3 wt%) was observed for this sample. Absolute density was calculated from the XRD of the 850°C calcinated pellet to be 8.15 g/cm^3.

It yielded relative densities averaging at 97 % with the exception of the 900°C sample which was only 92 % dense. This may again be related to a higher lead loss during calcination as the effect of PbO as sintering aid is well-known [9, 48]. Concerning the supposed lead losses during the 900°C calcination, it may be argued that the same temperature of calcination was used for the B-site precursor route where no excessive lead losses were observed. However, the reaction sequence is not the same for the two procedures. In the case of the B-site precursor route, reaction of the lead oxide with the precursor phases certainly occurs earlier and more homogeneously than in the single calcination route. This leads to an enhanced stabilization of the compound toward lead losses. Considering the large amount of free lead oxide still present in the single calcined powder at 700°C, it is not unreasonable to assume that some would actually easily evaporate before reacting if it were heated to 900°C.

A pure perovskite phase is a prerequisite for good electro-mechanical properties, but crystallization issues (like compositional homogeneity) may also play a role in the final properties. Hence, samples for resonance testing were prepared by polishing discs with a diameter/thickness aspect ratio close to 20 and sputtering gold electrodes (≈ 200 nm). They were poled using the same procedure as for PZT: samples were heated in oil bath at 80°C and an electric field of 20 kV/cm was applied for 10 min before cooling without field. The samples were then characterized by the resonance method. The obtained electro-mechanical properties as a function of calcination temperature of powder are summarized in Table 2.4.

Table 2.4: *Electro-mechanical characteristics for 34PNN-27PZ-39PT as a function of calcination temperature.*

	700°C	750°C	800°C	850°C	900°C
$\varepsilon^{\text{as prepared}}$	2356	2485	2495	2596	2053
$\mathrm{tg}\,\delta^{\text{as prepared}}$	1.5 %	1.5 %	1.6 %	1.6 %	1.5 %
$\varepsilon^{\text{poled}}$	3135	3170	3380	3648	2668
$\mathrm{tg}\,\delta^{\text{poled}}$	1.1 %	1.5 %	1.4 %	1.4 %	1.4 %
d_{31} [pC/N]	254	242	277	302	198
k_p	66 %	64 %	70 %	73 %	51 %
k_t	48 %	44 %	47 %	46 %	50 %

Electro-mechanical properties show that good crystallization of the perovskite is necessary, as 850°C calcinated sample is exhibiting the best characteristics even though perovskite is formed 100°C lower. The poor properties observed for 900°C can be understood by both the presence of pyrochlore and the lower density (92 %) of the sample. The microstructures of the obtained samples were also investigated, they were similar to each other, with no significant grain size changes as a function of calcination temperature. A typical example of the obtained microstructure is given in Figure 2.22 which shows a grain size of approx. 2-6 µm. The grain size homogeneity is probably lower than in the B-site precursor route. Note that this may also be related to the chemical homogeneity. Indeed, if Nb is also inhibiting grain growth in PNN-PZT, the greater grain size differences observed in the single calcinated samples may be traced down to chemical inhomogeneities. As before, a contrast possibly arising from ferroelectric domains can be observed in the grains.

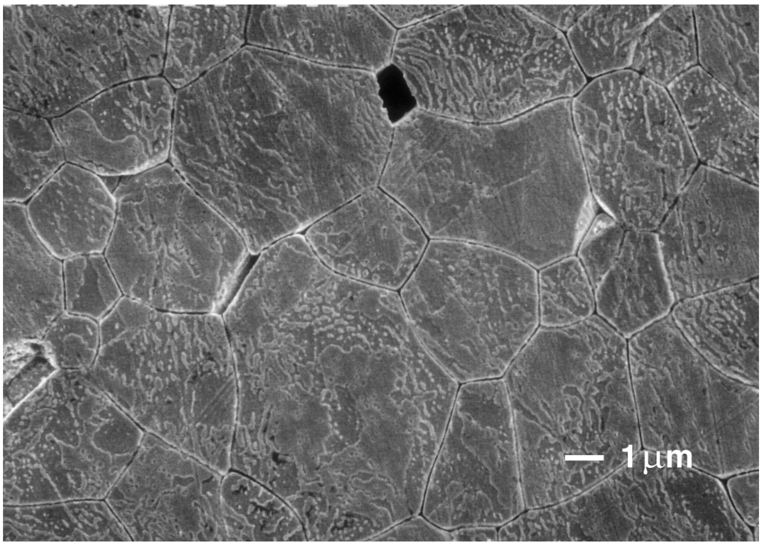

Figure 2.22: *Typical SEM etched microstructure of 34PNN-27PZ-29PT sintered sample (in this case calcinated at 850°C).*

To ascertain the fact that calcination at 850°C was indeed close to the optimal properties for the given composition, a sample of the same composition (34PNN-27PZ-39PT) was prepared by the “safer” B-site precursor route (c.f. Figure 2.7). It was characterized using the same procedure and its properties are compared to the ones obtained for the 850°C single calcination route in Table 2.5. Properties obtained through both routes are close enough to say that the single calcination route using Ni hydroxy-carbonate is as efficient for the synthesis of 34PNN-66PZT composition as the longer B-site precursor one.

***Table 2.5:** Comparison of electro-mechanical properties as a function of processing method for the 34PNN-27PZ-39PT composition.*

	$\varepsilon^{\text{poled}}$	tg δ^{poled}	d_{31} [pC/N]	k_p	k_t
850°C single cal.	3648	1.4 %	302	73 %	46 %
B-site precursor	3629	1.6 %	286	72 %	47 %

Considering Table 2.5, it can even be said that the single calcination route has to be preferred if optimization of the properties is the only objective. If grain size and chemical homogeneity are preferred, the B-site route yields comparable properties with more security regarding those two aspects.

2.3.5 Conclusion

The processing of PNN-PZT solid solutions has been investigated regarding the possibilities to obtain pyrochlore-free samples in a reproducible way. Such an objective was reached by introducing a novel route involving the synthesis of a B-site precursor consisting a mixture of two phases both containing Ni and Nb linked according to the PNN stoichiometry. This method permitted to successfully prepare samples containing 40 and 50 mol% PNN with variable PZ/PT ratio. The grain sizes were shown not to vary significantly with the PZ content for a given concentration of PNN. For both PNN contents a region similar to a MPB was identified. The properties were maximal in these regions and were increasing with PNN content. Secondly, another processing route involving only one calcination step was proposed and tested. It is based on the use of Ni hydroxy-carbonate instead of NiO for its increased reactivity. This processing method yielded pure perovskite for calcination temperatures as low as 750°C. However, it was necessary to fire the raw oxides mixture at 850°C to obtain properties comparable to the ones obtained by the B-site precursor route.

Regarding the study of the extrinsic contributions in PNN-PZT solid solutions, we chose to use samples obtained from the B-site precursor route because of the narrower grain size distribution (at least in the tested case of 34 mol%PNN) and because this route was presenting more guarantees of an optimal chemical homogeneity in the final samples.

2.4 REFERENCES

1. D. Damjanovic, *Highly Anisotropic Electromechanical Properties in Modified Lead Titanate Ceramics*, in *Department of Materials Science*. 1987, Pennsylvania State University.
2. G. Shirane and A. Takeda, *Phase transitions in solid solutions of* $PbZrO_3$ *and* $PbTiO_3$ *(I) Small concentration of* $PbTiO_3$. J. Phys. Soc. Jpn., (1952) **7** [1] p. 5-11.
3. G. Shirane, K. Suzuki, and A. Takeda, *Phase transitions in solid solutions of* $PbZrO_3$ *and* $PbTiO_3$ *(II) X-ray study.* J. Phys. Soc. Jpn., (1952) **7** [1] p. 12-18.
4. G. Shirane and K. Suzuki, *Crystal structure of* $Pb(Zr,Ti)O_3$. J. Phys. Soc. Jpn., (1952) **7** p. 333.
5. E. Sawaguchi, *Ferroelectricity versus antiferroelectricity in the solid solutions of* $PbZrO_3$ *and* $PbTiO_3$. J. Phys. Soc. Jpn., (1953) **8** [5] p. 615-29.
6. B. Jaffe, R.S. Roth, and S. Marzullo, *Piezoelectric properties of lead zirconate-lead titanate solid-solution ceramics.* J. Appl. Pys., (1954) **25** p. 809-10.
7. M. Demartin, *Influence de l'élaboration et de la microstructure sur le déplacement des parois de domaine et les propriétés électro-mécaniques de céramiques de* $Pb(Zr,Ti)O_3$ *et* $BaTiO_3$, in *Materials Dept.* 1996, Swiss Federal Institute of Technology Lausanne: Lausanne, Switzerland.
8. B. Jaffe, W.R. Cook, and H. Jaffe, *Piezoelectric Ceramics*. Non-Metallic Solids, ed. J.P. Roberts and P. Popper. Vol. 3. 1971, London: Academic Press.
9. A.I. Kingon and J.B. Clark, *Sintering of PZT ceramics: I Atmosphere control, II effect of PbO content on densification kinetics.* J. Am. Ceram. Soc., (1983) **66** [4] p. 253-60.
10. T. Ikeda and T. Okano, Watanabe, M., *A ternary system* $PbO\text{-}TiO_2\text{-}ZrO_2$. Jpn. J. Appl. Phys., (1962) **1** [4] p. 218-22.
11. R.B. Atkin and R.M. Fulrath, *Point defects and sintering of lead zirconate-titanate.* J. Am. Ceram. Soc., (1971) **54** [5] p. 265-70.
12. M.R. Soares, A.M.R. Senos, and P.Q. Mantas, *Phase coexistence in PZT ceramics.* J. Eur. Ceram. Soc., (1999) **19** p. 1865-71.
13. G. Arlt and P. Sasko, *Domain configuration and equilibrium size of domains in* $BaTiO_3$ *ceramics.* J. Appl. Phys., (1980) **51** [9] p. 4956-60.
14. R.C. DeVries and J.E. Burke, *Microstructure of barium titanate ceramics.* J. Am. Ceram. Soc., (1957) **40** [6] p. 200-6.
15. M.E. Drougard and D.R. Young, *Domain clamping effect in barium titanate single crystal.* Phys. Rev., (1954) **94** [6] p. 1561-4.

16. A.V. Turik, M.F. Kupriyanov, E.N. Sidorenko, and S.M. Zaitsev, *Behavior of piezoceramics of type $Pb(Zr,Ti)O_3$ near the region of morphotropic transition.* Sov. Phys. Tech. Phys., (1980) **25** [10] p. 1251-4.

17. B. Jaffe, R.S. Roth, and S. Marzullo, *Properties of piezoelectric ceramics in the solid-solution sereies lead titanate - lead zirconate - lead oxide : Tin oxide and lead titanate - lead hafnate.* J. Res. Natl. Bur. Stds., (1955) **55** [5] p. 239-54.

18. D.A. Berlincourt, D.R. Curran, and H. Jaffe, *Piezoelectric and Piezomagnetic Materials and their Function in Transducers*, in *Physical Acoustics - Principles and Methods*, W.P. Mason, Editor. 1964, Academic Press: New-York. p. 169-269.

19. G.A. Smolenskii and A.I. Agranovskaya, *Dielectric polarization and losses of some complex compounds.* Sov. Phys. Tech. Phys., (1958) **3** p. 1380-2.

20. G.A. Smolenskii and A.I. Agranovskaya, *Dielectric polarization of a number of complex compounds.* Sov. Phys. Solid State, (1960) **1** p. 1429-37.

21. V.M. Goldschmidt, T. Barth, G. Lunde, and W. Zachariasen, *Geochemische Verteilunggestze der Elemente VII Die Gesetze der Krystallochemie.* Srkrifter Utgitt av der Norske Videnskaps-Akademi i Oslo, I. Matem.-Naturvid. Klasse, (1926) **2**.

22. R.S. Roth, *Classification of perovskite and other ABO_3-type compounds.* J. Res. Natl. Bur. Stds., (1957) **58** [2] p. 75-88.

23. M. Lejeune and J.P. Boilot, *Formation mechanism and ceramic process of the ferroelectric perovskites: $Pb(Mg_{1/3}Nb_{2/3})O_3$ and $Pb(Fe_{1/2}Nb_{1/2})O_3$.* Ceram. Int., (1982) **8** [3] p. 99-103.

24. M. Dambekalne, I. Brante, and A. Sternberg, *The formation process of complex lead-containing niobates.* Ferroelectrics, (1989) **90** p. 1-14.

25. J. Chen and M.P. Harmer, *Microstructure and dielectric properties of lead magnesium niobate-pyrochlore diphasic mixtures.* J. Am. Ceram. Soc., (1990) **73** [1] p. 68-73.

26. T.R. Shrout and A. Halliyal, *Preparation of lead-based ferroelectric relaxors for capacitors.* Am. Ceram. Soc. Bull., (1987) **66** [4] p. 704-11.

27. M. Kondo, M. Hida, M. Tsukuda, K. Kurihara, and N. Kamehara, *Piezoelectric properties of $PbNi_{1/3}Nb_{2/3}O_3$-$PbTiO_3$-$PbZrO_3$ ceramics.* Jpn. J. Appl. Phys., (1997) **36** [9B] p. 6043-5.

28. E.A. Buyanova, P.L. Strelets, I.A. Serova, and V.A. Isupov, *Ferroelectric properties of $PbTiO_3$-$PbZrO_3$-$PbNi_{1/3}Nb_{2/3}O_3$ solid solutions.* Bull. Acad. Sci. USSR Phys. Ser., (1965) **29** p. 1877-80.

29. O. Babushkin, T. Lindbäck, J.C. Luc, and J.Y.M. Leblais, *Reaction sequence in the formation of perovskite* $Pb(Zr_{0.48}Ti_{0.52})O_3$-$Pb(Ni_{1/3}Nb_{2/3})O_3$ *solid solution: dynamic heat treatment.* J. Eur. Ceram. Soc., (1998) **18** p. 737-744.
30. J. Chen, A. Gorton, H.M. Chan, and M.P. Harmer, *Effect of powder purity and second phases on the dielectric properties of lead magnesium niobate ceramics.* J. Am. Ceram. Soc., (1986) **69** [12] p. C303-5.
31. S.L. Swartz and T.R. Shrout, *Fabrication of perovskite lead magnesium niobate.* Mat. Res. Bull., (1982) **17** p. 1245-50.
32. Y. Sasaki, A. Nagai, and T. Yoshimoto, *Mechanism of PNN based perovskite ceramics formation.* Proc. "Chemistry of electronic ceramic materials", Jackson WY, (1990) p. 99-104.
33. C.H. Lu and W.J. Hwang, *Phasic and microstructural developements of* $Pb(Ni_{1/3}Nb_{2/3})O_3$ *prepared by the columbite process.* Ceram. Int., (1996) **22** p. 373-9.
34. N. Ichinose and M. Kimura, *Preparation and properties of lead zirconate-titanate piezoelectric ceramics using ultrafine particles.* Jpn. J. Appl. Phys., (1991) **30** [9B] p. 2220-3.
35. A.V. Turik, V.G. Smotrakov, G.I. Khasabova, and E.S. Tsikhotskii, *PZTNN : Piezoceramic material with anoumalously high piezoelectric moduli.* Inorg. Mat., (1993) **29** p. 1148-50.
36. M.S. Yoon, H.M. Jang, and S. Kim, *Spontaneous micro-macro ferroeletric domain switching in* $PbZrO_3$*-doped* $Pb(Ni,Nb)O_3$-$PbTiO_3$ *system.* Jpn. J. Appl. Phys., (1995) **34** p. 1916-21.
37. X. Zhu and Z. Meng, *The influence of MPB on the dielectric and piezoelectric properties of the PNN-PZ-PT ternary system.* J. Mater. Sci., (1996) **31** p. 2171.
38. M. Kondo, M. Hida, M. Tsukuda, K. Kurihara, and N. Kamehara, *Piezoelectric properties of* $PbNi_{1/3}Nb_{2/3}O_3$-$PbTiO_3$-$PbZrO_3$ *ceramic near the MPB.* J. Ceram. Soc. Jpn., (1997) **195** [8] p. 719-21.
39. I.A. Cornejo, B. Jadidian, E.K. Akdogan, and A. Safari, *Dielectric and electromechanical properties of* $PbNi_{1/3}Nb_{2/3}O_3$-$PbTiO_3$-$PbZrO_3$ *system: a processing-property study.* ISAF '98, Proc. of 11th IEEE Int. Symp. on Appl. Ferro., Ed. E.L. Colla, D. Damjanovic, N. Setter, Montreux, Switzerland, (1998) **1** p. 337-40.
40. S. Takahashi, S. Miyao, S. Yoneda, and M. Kuwabara, *Preparation of dense and pure perovskite ceramics in* $Pb(Ni,Nb)O_3$-$PbTiO_3$ *system.* Jpn. J. Appl. Phys., (1993) **32** p. 4245-8.

41. C.H. Lu and W.J. Hwang, *Preparation of* $Pb(Zr,Ti)O_3$-$Pb(Ni_{1/3}Nb_{2/3})O_3$ *solid solution powder from hydrothermally-treated precursors.* Mater. Lett., (1996) **27** p. 229-32.

42. C.H. Lu and W.J. Hwang, *Phase evolution and dielectric characterization of lead nickel niobate - lead zirconate ceramics prepared from the hydrothermally derived precursors.* J. Mater. Res., (1999) **14** [4] p. 1364-70.

43. T. Sekiya, K. Kusumoto, H.J. Hwang, J.P. Reyes, J.P. Chaminade, and J. Ravez, *Flux growth and properties of* $Pb(Ni_{1/3}Nb_{2/3})O_3$-$PbTiO_3$ *single crystals.* J. Kor. Phys. Soc., (1998) **32** p. S1201-3.

44. I.E. Myl'nikova and V.A. Bokov, *Some dielectric properties of single crystals of* $Pb_3NiNb_2O_9$. Kristallographia, (1958) **4** [3] p. 408-409.

45. J.H. Moon, H.M. Jang, and B.D. You, *Densification behaviors and piezoelectric properties of* MnO_2, SiO_2 *doped PNN-PZT ceramics.* J. Mater. Res., (1993) **8** p. 3184.

46. J.H. Moon and H.M. Jang, *Effects of sintering atmosphere on densification behavior and piezo. prop. of PNN-PT-PZ ceramics.* J. Am. Ceram. Soc., (1993) **76** p. 549.

47. J.H. Cho, I.K. Park, and H.G. Kim, *Sintering behavior of cadium-doped* $Pb(Ni_{1/3}Nb_{2/3})O_3$-$PbZrO_3$-$PbTiO_3$ *ceramics.* J. Am. Ceram. Soc., (1997) **80** [6] p. 1523-34.

48. G. Zhilun, L. Longtu, G. Suhua, and Z. Xiaowen, *Low temperature sintering of lead based piezoelectric ceramic.* J. Am. Ceram. Soc., (1989) **72** p. 486-91.

49. S.Y. Chu and C.S. Hsieh, *Doping effects on the piezoelectric properties of low-temperature sintered PNN-PZT ceramics.* J. Mater. Sci. Lett., (2000) **19** p. 609-12.

50. M. Yonezawa, *New low-firing materials for multilayers capacitors.* Ferroelectrics, (1986) **68** p. 181-189.

51. X. Zhu, Q. Wang, and Z. Meng, *A functionnally gradient piezoelectric actuator prepared by powder metallurgical process in PNN-PZ-PT system.* J. Mater. Sci. Lett., (1995) **14** p. 516-8.

52. N. Setter and L.E. Cross, *The role of B-site cation disorder in diffuse phase transition behavior of perovskite ferroelectrics.* J. Appl. Phys., (1980) **51** [8] p. 4356-60.

53. M.P. Harmer, J. Chen, P. Peng, H.M. Chan, and D.M. Smyth, *Control of microchemical ordering in relaxor ferroelectrics and related compounds.* Ferroelectrics, (1989) **97** p. 263-74.

54. H.M. Jang, S.R. Cho, and K.M. Lee, *Mechanism of formation of perovskite phase and dielectric properties of* $Pb(Zn,Mg)Nb_{2/3}O_3$ *ceramics prepared by columbite precursor route.* J. Am. Ceram. Soc., (1995) **78** [2] p. 297-304.

55. H. Banno, T. Tsunooka, and I. Shimano, *Phase diagram and piezoelectric properties of* $Pb(Nb_{2/3}Ni_{1/3})O_3$ *-* $PbTiO_3$ *-* $PbZrO_3$ *and an application to ceramic wave filter.* Proc. 1st meeting ferroelec. mat'ls and app., ed. O. Omoto, A. Kunada, Keihin Printing Co, (1977) p. 339-344.

56. X. Zhu, J. Zhu, S. Zhou, Q. Li, Z. Meng, Z. Liu, and N. Ming, *Configurations of erroelectric domains in bismuth and zinc modified* $Pb(Ni_{1/3}Nb_{2/3})O_3$-$PbTiO_3$-$PbZrO_3$ *cxeramics.* J. Mater. Sci., (1999) **34** p. 1533-41.

57. K. Kusumoto and T. Sekiya, *Processing and properties of relaxor ferroelectric PNN-PT perovskite ceramics.* Ferroelectrics, (2000) **240** p. 327-334.

58. S.J. Butcher and M. Daglish, *The use of magnesium carbonate hydroxide pentahydrate in the production of perovskite lead magnesium niobate.* 3rd euroceramics proc. ed. P. Duran, J. F. Fernandez, (1993) **2** p. 121-6.

59. H. Henmi, M. Mori, T. Hirayama, N. Mizutani, and M. Kato, *Influence of the self-generated and controlled atmosphere on the thermal decomposition of basic nickel carbonate,* $NiCO_3 \cdot 2Ni(OH)_2 \cdot 4H_2O$. Termochimicha Acta, (1986) **104** p. 101-9.

CHAPTER III
PHASES IN PNN - PZT SOLID SOLUTIONS

The morphotropic region corresponding to high piezoelectric properties in PZT has a quite special crystalline structure. Therefore, to compare the morphotropic effects in relaxor ferroelectrics and PZT, a qualitative study of the phases present in ferroelectric-relaxor solid solutions is necessary. Since the landmark papers of Devonshire applying Landau-Ginzburg critical phenomena theory to barium titanate [1, 2], the apparition of tetragonal, orthorhombic, and rhombohedral crystalline symmetries in regular ferroelectrics is well understood. Yet, the discovery of the high properties in the PZT morphotropic region [3] unveiled questions about their microscopic physical causes, obviously related to crystalline structure, which are still unsolved today. Later, the first observation of the relaxor behavior in disordered perovskites [4] has challenged new attempts of properties modeling which have not yet yielded a complete physical description of such materials. Finally, as some relaxors are undergoing a spontaneous phase transition to the ferroelectric state [5], a general theory integrating relaxors and true ferroelectrics still remains to be worked out. As a consequence, and even though they are now widely applied, the structural understanding of relaxor-ferroelectric solid solutions and especially their morphotropic region is quite poor at the present time.

In this chapter, the phases appearing in the PNN-PZT solid solution will be explored as a function of temperature and composition. Previously reported results for PZT will be first presented to help interpretation of the observed phenomena. Dielectric and pyroelectric measurements will be performed to localize the phase transitions observed in the system. Then, XRD analysis at different temperatures will be used to identify the observed phase transformations. From these measurements, a phase diagram for the PNN-PZT solid solutions exhibiting a strongly curving MPB will be proposed. It will also be suggested that a such a phase diagram can be extended to the whole family of lead-based relaxor-ferroelectric solid solutions. Bearing in mind that local symmetry in ferroelectrics can be different from the global one [6], the issue of curving MPB in such systems will be discussed in more details. Eventually, the effects of the electrical and thermal history on the morphotropic transition will be examined. In particular, a study of poling effects on the properties of PNN-PZT system will finally be conducted.

3.1 PHASES IN CLASSICAL AND RELAXOR FERROELECTRIC SYSTEMS

Relaxor-PZ-PT solid solutions ternary phase diagrams [7] and, in particular, the PNN-PZ-PT one [8], present 4 different structures (see Figure 1.4): three ferroelectric ones (tetragonal, rhombohedral and pseudo-cubic), and one relaxor cubic (neglecting the antiferroelectric region close to pure PZ). Practically, the most interesting zone is around the boundary separating tetragonal and rhombohedral phases where the properties are highest. Hence, we will first review the main theoretical interpretations of observed phase coexistence close to the MPB region in PZT in order to relate them to PNN-PZT solid solutions features. Then, to clarify the effect of adding a relaxor into a ferroelectric, some relaxor-PT solid solutions phase diagrams will be reviewed. Finally, the case of spontaneous normal to relaxor ferroelectric transition will be treated as it was reported for the 60PNN-40PT composition [9, 10] and deserves a better understanding.

3.1.1 Phase coexistence in PZT

Observation of phase coexistence at MPB is common in PZT (c.f. Figure 2.3). Yet, the origins of such a coexistence are still debated: is it only a metastable state [11] or is there a region where tetragonal and rhombohedral phases are truly not forming a solid solution [12]?

Measuring lattice parameters across MPB by XRD, Ari Gur and Benguigui [12] observed that lattice parameters variations for both phases are very low in the coexistence region. Hence, they used a leverage law to model the variation of relative intensity for the tetragonal and rhombohedral (200) peaks postulating solubility gap values of $x_R = 0.49$ and $x_T = 0.64$ (x representing the Ti concentration in PZT). Their measurements were confirmed by Hanh *et al.* [13] and by Turik *et al.* [14] who also found composition independent lattice parameters in the coexistence region. Isupov, criticizing the solubility gap model, rather considered the MPB as a first order compositionaly hysteretic phase transformation where it is difficult to determine on which branch of the hysteresis one stays after cooling through T_C [11]. (This interpretation has been recently supported by Soares *et al.* [15] who found a tetragonal cell volume greater than the rhombohedral one in the MPB range.) Isupov later developed a thermodynamical theory [16] accounting for this metastable coexistence interval and describing mixing of phases by a normal distribution. Furthermore, considering the chemical homogeneity of the samples reported in the literature, Isupov [17] concluded that most of the commercially available PZT were compositionally heterogeneous (which was confirmed for fine-grained donor doped PZT in Ref. [18]). Phase coexistence in equilibrium is indeed possible, but only around the free energy equivalence point for both phases. If a mechanical stress or an electric field is applied to a PZT not far from this equivalent point, some stabilization of the concurrent phase may occur, and hence produce a thermodynamically equilibrated PZT exhibiting a true phase coexistence [19].

Later, Cao and Cross [20-22] developed a model of phase coexistence based on the assumption that in the MPB region, the Curie transition was of second order [23]. They postulated that thermal fluctuations at T_C were distributing the polarization vector in all the available polarization directions and that the variants formed at this point were frozen-in immediately below. The relative amount of each phase can then be determined by a probability polyhedron representing the overall distribution of polar vectors just after the transition and the width of the coexistence region is proportional to the variation of free energy difference between the two phases. This model indeed allows phase coexistence but always as a metastable state, except for one composition described by a tetragonal to rhombohedral volume fraction ratio of: $f_R/f_T = 1.45$ which corresponds to equivalent free energies for both phases. Lately, XRD measurements performed by Soares *et al.* [15] supported the latter model as a variation of the lattice parameters in the coexistence region was demonstrated. Furthermore, using extrapolation of dielectric permittivity dependence on lattice parameter for each phase, it was possible to account for the observed permittivities in the coexistence region. The fitted volume fraction for each phase were close to those predicted by Cao and Cross model. Investigating grain size dependence of coexistence region, Soares *et al.* [24] were also able to derive a relationship between grain size (G) and coexistence width (Δx): $\Delta x = G^{-3/2}$ indicating that domain rather than grain is the elementary volume to be considered in the model.

From these results, it can be concluded that phase coexistence in PZT is probably a metastable state for all except one composition and that due to non-equilibrium contributions (such as nucleation, stress or compositional inhomogeneities) the morphotropic phase transition (rhombohedral to tetragonal) can be seen as being first order-like with an hysteresis of transformation which compositional amplitude varies as a function of the processing parameters.

3.1.2 Relaxor-lead titanate solid solutions

To our knowledge, no temperature-dependent phase diagrams exist for ternary relaxor-PZ-PT compounds, even though they are of great practical interest [7]. The determination of phase diagrams for relaxor-ferroelectric systems focused on PMN-PT [25, 26] and PZN-PT [27] compositions close to the MPB. Studies were performed thoroughly on ceramics and single crystals. Structurally, the observed symmetry of the relaxor-rich phase was close to cubic. However, as ferroelectricity could be induced in such phases and as the field-induced ferroelectric state in PMN corresponds to rhombohedral distortion [28], they were associated with a rhombohedral structure. In these systems, MPB was reported to be curved at high temperatures, bending toward the relaxor-rich side. Hence, a transition from rhombohedral to tetragonal phase (a “morphotropic” transition) appears when heating rhombohedral samples close to the MPB. This transition is causing an anomaly on the dielectric permittivity or pyroelectric coefficient vs. temperature curves. Later, using high-resolution XRD analysis and dielectric measurements, Noblanc *et al.* [29] proposed a similar phase diagram for PMN-PT ceramics, containing an almost horizontal MPB. Below this boundary, a wide range of phase coexistence was observed with the composition corresponding to the highest properties lying in the center of the coexistence zone. A temperature independent relaxor state for compositions below 10 %PT as well as “depoling transitions” occurring below T_m for compositions greater than 10 %PT were also reported [29]. The interval between T_m and this depoling temperature is decreasing with increasing PT content and it disappears for composition greater than 40 %PT. Still, as the variation of the relaxor content in a solid solution is affecting the general ferroelectric behavior, these phase diagrams have to be considered carefully in the case of PNN-PZ-PT solid solutions containing a definite amount of relaxor.

Concerning PNN-PT solid solutions, Yoon *et al.* [9, 10] reported a first order spontaneous relaxor to ferroelectric transitions in ceramics of 60PNN-40PT containing a few percents of PZ. They also observed that PZ was favoring the relaxor state as the dielectric dispersion was increasing with the PZ content.

3.1.3 Normal to relaxor ferroelectric transition

The first observations of a spontaneous normal to relaxor ferroelectric phase transition were made on disordered $Pb(Sc_{1/2}Ta_{1/2})O_3$ (PST) [30] and $Pb(Sc_{1/2}Nb_{1/2})O_3$ (PSN) [5, 31]. Such a transition could be influenced by the degree of ordering of B-site cations (the more ordered, the higher the transition temperature) and by the presence of structural defects such as lead vacancies (the more defects, the more stable relaxor phase). Interpretation of such effects were given in terms of polarizing power difference (Δ) between the B-site cations which is given by:

$$\Delta = \frac{e\, Z_{B1}}{r_{B1}^2} - \frac{e\, Z_{B2}}{r_{B2}^2} \tag{3.1}$$

where *e*, Z and r stand for the electronic charge, the B-site cation valence and the ionic radius, respectively. For large Δ, a purely relaxor behavior is observed (e.g. $\Delta_{PMN} = 6.85\ C/m^2$) whereas for low Δ, a normal ferroelectric state appears (e.g. $\Delta_{PZT} = 2.24\ C/m^2$). For intermediate values of Δ, a mixed behavior is expected and a normal to relaxor ferroelectric transition is observed [5, 31].

Hence, in the case of PNN-PZT solid solutions ($\Delta_{PNN} = 6.30\ C/m^2$) with a significant amount of PZT, the overall Δ will decrease down to values close to those of PST and PSN ($\Delta \approx 5\ C/m^2$) and a normal to relaxor ferroelectric transition should be observed. Moreover, as Δ for PZT is at a maximum for a 50/50 composition and decreases toward zero for both pure PZ and PT, it can be said for a given relaxor content that the closer PZ/PT ratio is to 1, the greater the relaxor phase stability will be. In our case, as the tested compositions are rather PT-rich (see Chapter II), one can thus expect an increase of the relaxor zone with increasing PZ content.

3.2 DIELECTRIC CHARACTERIZATION

Identification of the existing phase transition in a ferroelectric system is most commonly performed by measuring dielectric permittivity dependence upon temperature. In this section, we will use such a method on both poled and depoled samples. Characterization on poled samples will be first presented as the typical transitions effects on permittivity are more accentuated.

3.2.1 Experimental

To perform the dielectric measurements as a function of temperature, an impedance meter (HP 4284A) and a heating/cooling chamber (Delta Designs 9023) were used. The sample temperature was measured with a Pt 100 probe (Omega Technologies) situated on the bottom electrode which resistance was acquired on a multi meter (HP 34401A). The heating/cooling rate was of 3°C/min and measurements at five frequencies (0.1, 1, 10, 100, and 1000 kHz) were taken every degree.

Poled samples were prepared in a similar way as for resonance measurements: a 20 kV/cm field was applied during 10 min in an oil bath at 80°C. The samples were cooled without field. All the measurements presented in this section were performed on 40PNN-60PZT samples prepared by the B-site precursor route.

3.2.2 Poled samples

The dielectric measurements on poled samples were obviously performed upon heating. Figure 3.1 depicts the variation of dielectric permittivity as a function of temperature for 4 poled compositions. Additional compositions were tested but are not shown in this figure to preserve clarity. The permittivity peak temperatures (T_m) decrease linearly with increasing molar fraction of PZ for a given measurement frequency. The dielectric dispersion (i.e. the temperature interval between peak values for two given frequencies) is also increasing with the PZ content. Furthermore, the peak permittivity value is reaching a maximum for the 26 %PZ composition.

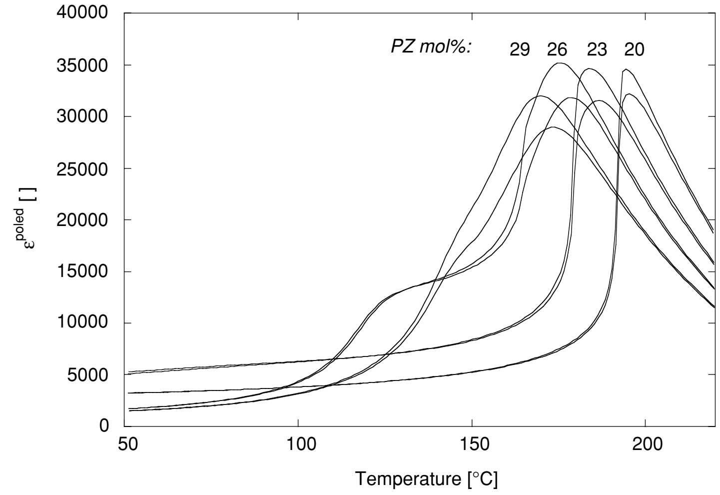

Figure 3.1: *Dielectric permittivity vs. temperature curves for various poled 40PNN-60PZT compositions. Measurements were performed at 100 Hz (upper curve) and 10 kHz (lower curve) upon heating.*

Beside the principal peak, two types of anomalies can be observed in Figure 3.1. The first one is present on all the curves and situated below T_m, it corresponds to a sudden change upon heating from a non-dispersive response to a frequency dependent dielectric behavior. The second anomaly can be observed clearly on the 26 % PZ curve around 120°C, it corresponds to a sharp step in permittivity without significant change in dispersive behavior. These two singularities are detailed on Figure 3.2.

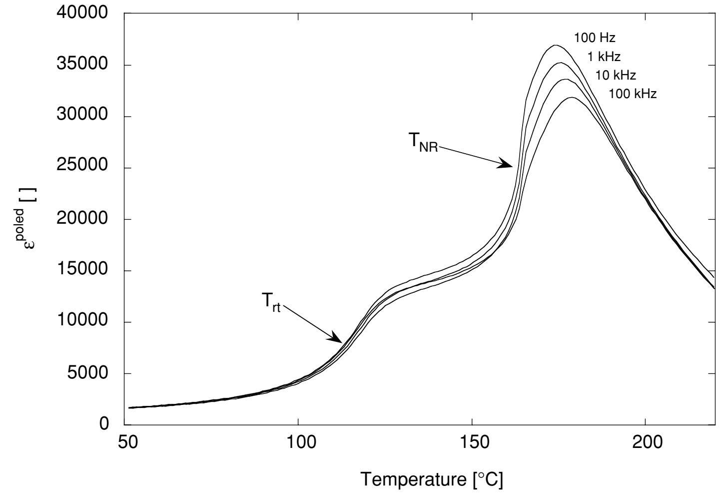

Figure 3.2: *Dielectric permittivity vs. temperature curve for the poled 40PNN-26PZ-34PT composition. Measurements were performed at 100 Hz, 1 kHz, 10 kHz, and 100 kHz upon heating.*

The first anomaly, T_{NR}, corresponds to the change in frequency dispersion. It is similar to that reported by Yoon *et al.* [10] for 60PNN-40PT containing a few precent PZ which they tentatively identified as “macro-micro domain switching [i.e. normal to relaxor ferroelectric transition] associated with a rhombohedral to tetragonal transition [i.e. a morphotropic transition]”. This association was based on high temperature XRD, as the reported (200) peaks showed a double to a single peak transition upon heating occurring near the anomaly temperature. Yet, a single (200) reflection alone is not sufficient to discriminate between a tetragonal and a cubic structure, the latter being more probably a single normal to relaxor ferroelectric transition fully compatible with Yoon *et al.* results. As mentioned in the previous section, similar transitions were already observed in other systems such as PST and PSN [5, 30, 31], as well as in (Pb,La)(Zr,Ti)O_3 (PLZT) [32, 33]. They are described as spontaneous normal to relaxor ferroelectric transitions. Thus, T_{NR} most probably corresponds to such a transition as expected from the calculations of section 3.1.3. The second anomaly shown in Figure 3.2, named T_{rt}, occurs only for compositions containing 23 to 26 mol% PZ and has no effect on the frequency dispersion. This anomaly exhibits a pattern similar to PMN-PT [25, 26] and PZN-PT [27] behaviors which are identified as a transition from rhombohedral to tetragonal ferroelectric phases due to the curvature of the MPB.

These two transitions are characterized by noticeable changes in the dielectric losses, as illustrated on Figure 3.3. Moreover, as they are both extending through a certain temperature range, the positions of the loss maxima can be conveniently used as reference temperatures for the transitions characterization. The peak corresponding to T_{rt} is a bit smeared compared to T_{NR} but presents a clear maximum. Note that T_{NR} maxima is showing a shoulder on its high temperature side alike PLZT [32]. Such peak shapes, being quite symmetrical, are roughly similar to those of a normal ferroelectric (as relaxors rather exhibit a step close to T_m [34]). The high temperature (> 190°C) loss increase is due to an increase in intrinsic conductivity and is probably not related to any transition.

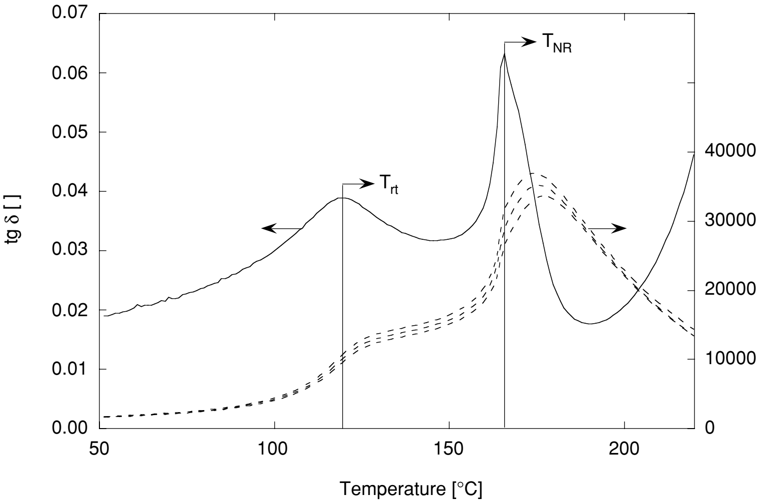

Figure 3.3: *Dielectric losses and permittivity vs. temperature curve for the poled 40PNN-26PZ-34PT composition. Loss measurements are performed at 1 kHz upon heating.*

Although the dielectric permittivity measurements suggest that T_{NR} is a normal to relaxor ferroelectric transition, its loss peak shape is different from the typical loss behavior in the model materials for such transitions (PST [30]) which exhibit a true relaxor-like decreasing step starting immediately below T_m (as in relaxor PMN [34]). The shoulder on the left of the T_{NR} loss peak may be interpreted as the signature of relaxor-like losses. However, the true relaxor nature of the high temperature phase of our compositions may still be questioned. Hence, following the works on relaxor-ferroelectric transition [5, 30, 31], a Vögel-Fulcher analysis of the dielectric dispersion of 26 %PZ composition was conducted. Vögel-Fulcher law was first introduced for 90PMN-10PT [35] and describes the frequency dependence of the peak temperature T_m as an Arrhenius-like law:

$$\omega = \omega_0 \exp\left(-\frac{E}{T_m - T_f}\right) \tag{3.2}$$

where ω_0, T_f , and E are constants. T_f is called the freezing temperature. In compounds undergoing a relaxor-ferroelectric transition temperature, T_f has been identified with this transition temperature [30]. As a temperature step of 1°C was not yielding sufficient accuracy, exact permittivity peak temperatures for the 26 %PZ composition were extracted from the data by fitting the top 20 measurement points with a third order polynomial and using the maximum value of this fitted function as the actual T_m for the considered frequency. Then, Equation (3.2) was fitted to the obtained values and yielded: $T_f = 162.6°C$, $\omega_0 = 2\pi \times 1.12 \times 10^{13}$ Hz and $E = 24.7°C$. The last two values are well in the expected range and T_f is 3°C below the temperature of the T_{NR} loss peak (165.6°C) which is quite satisfying as the normal to relaxor ferroelectric transition is obviously ending at the T_{NR} temperature. Agreement with Vögel-Fulcher law can also be checked by plotting the $(T_m\text{-}T_f)$ inverse as a function of the frequency logarithm which should yield a perfect line. This is the case here, as shown in Figure 3.4 where the regression coefficient of the fitted line is better than 0.9995.

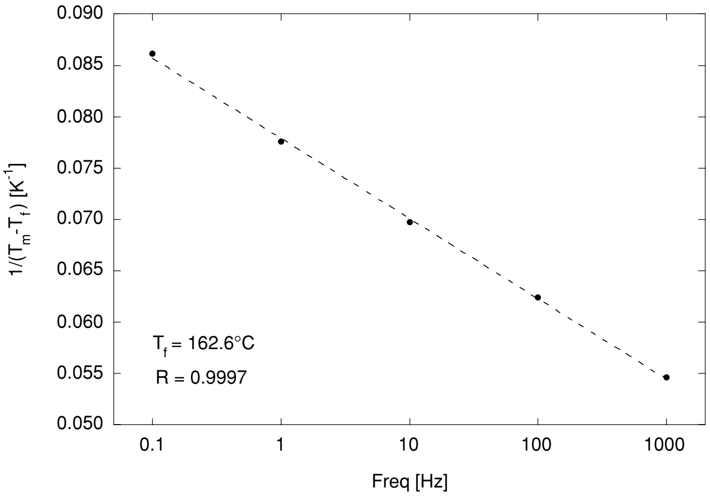

Figure 3.4: *Vögel-Fulcher plot for the 40PNN-26PZ-34PT composition. Circles represent inverse experimental (T_m - fitted T_f) and dotted line is a logarithmic fit to data points.*

Thus, it can be said that the T_{NR} anomaly most probably corresponds to a normal to relaxor ferroelectric transition. Still, as measurement were performed on poled samples and as it is well known that a ferroelectric state can be induced in relaxors (e.g. PMN [34]) by applying a sufficiently large electric field at low temperature, it can be argued that the observed transition is due to a metastable ferroelectric state induced during poling. Hence, measurements on unpoled samples are necessary to corroborate this conclusion.

3.2.3 Unpoled samples

Measuring permittivity upon heating, the influence of poling on the dielectric response is demonstrated on Figure 3.5 for the 26 %PZ sample. To ease perception of the low temperature anomaly (corresponding to T_{rt}), the 5-points derivatives of the 1 kHz permittivities are also plotted.

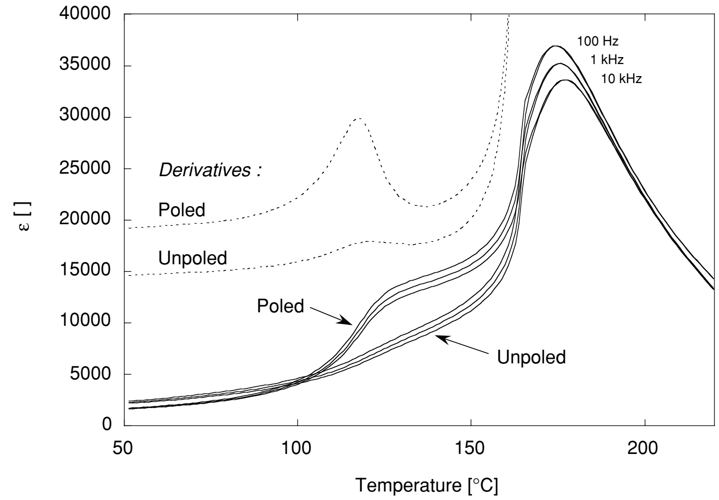

Figure 3.5: *Dielectric permittivity vs. temperature curve for the poled and unpoled 40PNN-26PZ-34PT composition. Measurements were performed at 100 Hz, 1 kHz, 10 kHz and 100 kHz upon heating. Dotted lines represent the five points derivatives of 1 kHz data.*

The anomalies in the unpoled sample (appearing more clearly on the derivative curve) occur at the same temperatures as in the poled sample, but are much less pronounced. Moreover, the frequency dispersion at room temperature is stronger for the unpoled sample which can be understood as an effect of the lower domain wall density in the poled state. Permittivity curves in the supposed relaxor region are superimposed, indicating, as expected from a relaxor state, that poling has no influence there. Furthermore, concerning T_{rt} interpretation as a rhombohedral to tetragonal transition, the fact that the initial permittivity of the poled sample is first lower and then, above T_{rt}, becomes much greater than the unpoled one, correlates with the well-known effects of poling on permittivity depending on the crystalline phase (see section 2.2.2).

Both normal to relaxor ferroelectric [30] and rhombohedral to tetragonal [11] transitions are supposed to be of first order type and should hence exhibit a thermal hysteresis. This has been tested by measuring permittivity upon heating and cooling at 2°C/min, the corresponding curves are reported on Figure 3.6. The marked transition temperatures were measured from the losses at 1 kHz which were not plotted to preserve clarity.

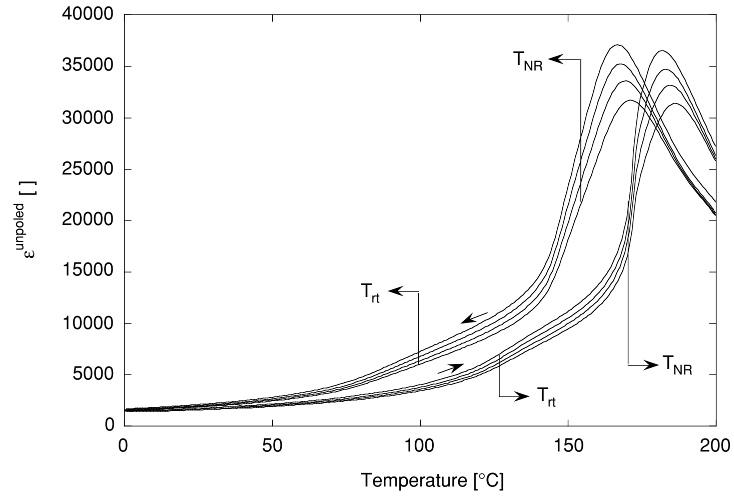

Figure 3.6: *Dielectric permittivity vs. temperature upon heating and cooling of the unpoled 40PNN-26PZ-34PT composition. Measurements were performed at 100 Hz, 1 kHz, 10 kHz and 100 kHz. Transition temperatures were measured on losses.*

A large thermal hysteresis suggesting first order phase transitions can be observed for both transitions. The temperature interval is different for the two transitions (19°C for T_{NR} and 27°C for T_{rt}) indicating that the two transitions are independent of each other. However, the thermal hysteresis observed for T_m is not characteristic of a pure relaxor behavior. For instance, in PMN [34] and in PST [30], no thermal hysteresis for the dispersed permittivity peak could be observed. This suggests that if there is indeed a relaxor behavior above T_{NR} for our compositions, it is superimposed on a first-order like anomaly causing the observed thermal hysteresis. This could be related to the previous comments on the shape of the T_{NR} losses peak (c.f. Figure 3.3) and would indicate that our relaxor-ferroelectric solid solutions are regular ferroelectrics once poled at low temperature but may actually be a mixture of normal ferroelectric and relaxor phases at high temperature (maybe related to compositional heterogeneities). The overall dielectric response would be dispersive because of the relaxor phase and exhibit a thermal hysteresis due to the ferroelectric one. This interpretation is supported by the dielectric dispersion being more pronounced in the cooling measurement that may indicate some remaining metastable relaxor phase below T_{NR} (although a higher domain wall density is expected as well). Furthermore, the peak permittivities are slightly lower for the measurement upon heating, suggesting again some missing relaxor-type contributions to the total dielectric response.

3.2.4 Conclusion

Studying the dielectric permittivity dependence upon temperature permitted identification of two anomalies. The first anomaly is appearing on all the tested compositions and is identified by the temperature T_{NR} which corresponds to a peak in the dielectric losses. It was associated with a normal to relaxor ferroelectric phase transition as the behavior above this temperature was that of a typical relaxor and showed a Vögel-Fulcher freezing temperature corresponding to T_{NR}. The second anomaly is only observed in the room temperature rhombohedral samples close to the MPB and is characterized by a smaller peak in losses at T_{rt}. An interpretation as a rhombohedral to tetragonal transition was proposed in analogy with other relaxor-PT solid solutions but no conclusive evidence of its nature could be obtained from dielectric measurements. Additional characterization, as conducted in the following sections (3.3 and 3.4), is thus needed to confirm this interpretation.

3.3 PYROELECTRIC CHARACTERIZATION

The characterization of ferroelectric transitions in the PNN-PZT systems using dielectric measurements cannot yield information about the basic property of ferroelectrics: the spontaneous polarization. Hence, to study the evolution of polarization with respect to the previously observed transitions (section 3.2), pyroelectric measurements were chosen as they allow to characterize the material using the same type of thermal profile used for the dielectric measurements. With such measurements, the nature of the normal to relaxor ferroelectric transition can be easily proven as polarization should go toward zero at this temperature and not at the permittivity peak temperature. Moreover, if the second transition observed in dielectric measurements is indeed of the rhombohedral to tetragonal nature, a change of polarization should be detected as the spontaneous polarization vector reorients from the <111> to the <001> directions.

3.3.1 Experimental

Pyroelectric measurements were conducted using the principle exposed by Byer and Roundy [36]. It based on the fact that spontaneous polarization is dependent on temperature,

$P_S = P_S(T)$. Hence, if a pyroelectric is heated at a constant rate, $dT/dt = k$, then the produced pyroelectric current density, I_{pyro}, can be written as:

$$I_{pyro} = \frac{dP_s}{dT}\frac{dT}{dt} = k\frac{dP_s}{dT} \tag{3.3}$$

and is thus proportional to $dP_S/dT = p$, the pyroelectric coefficient. If the measured material undergoes a ferroelectric to paraelectric transition in the measurement range, then the pyroelectric current goes to zero. Thus, the total polarization at a function of temperature can be calculated by integrating the pyroelectric current density up to this temperature, T_i:

$$P_s(T) = \frac{1}{k}\int_{T}^{T_i > T_C} I_{pyro}\,dT \tag{3.4}$$

However, Equation (3.4) is valid only if no other mechanisms are contributing to the measured current (e.g. noise charges). Hence, usually such pyroelectric measurements are performed by heating the poled sample above T_C and then cooling it to the initial temperature, measuring the current produced along the whole temperature profile. Then, the true pyroelectric response can be calculated by the substraction of the cooling values (coming from non-pyroelectric contributions) from the heating values.

Pyroelectric characterization was performed on B-site precursor route 40PNN-60PZT samples following the procedure outlined below. The system used for these measurements consisted of a climatic chamber (Delta designs 9023) and an electrometer (Keithley K486) to measure the current. The PID (Proportional, Integral and Differential) characteristics of the climatic chamber were optimized to guarantee the most constant heating/cooling rate (i.e. the integrative coefficient, I, of the PID controller was set close to zero). All measurements were performed at the same heating rate as for dielectric measurements: 3°C/min. Then, the spontaneous polarization, P_{pyro}, was calculated by numerical integration of the heating pyroelectric current without systematic substraction of the cooling values to preserve the effects associated with a possible non-pyroelectric rhombohedral to tetragonal transition. Still, noise current upon cooling the depoled samples was measured and values of equivalent spurious polarization at room temperature were calculated to be lower than 2 % of the total polarization.

As pyroelectric characterization necessitates poled samples, the poling procedure used here was similar to that used for the dielectric characterization: application of 20 kV/cm during 10 min at 80°C and cooling without field.

3.3.2 Pyroelectric transitions

Selected results for temperature dependence of the pyroelectric current for 40PNN-60PZT compositions are presented in Figure 3.7. All the curves exhibit a well defined peak which decreases with temperature as PZ content increases. The peak value reaches a maximum for the 23 %PZ composition. Besides the principal peak, a second one can be seen on the 26 and 29 %PZ curves. (Those two compositions are exhibiting a pseudo-cubic structure at room temperature, see Figure 2.11). This second peak is clearly defined for the 26 %PZ sample, but looks rather like a shoulder on the 29 %PZ composition. The background current (i.e. the value of the current between the peaks) is also increasing with PZ content. Note that this is not coming from increased noise as cooling noise current was found constant for all the tested compositions.

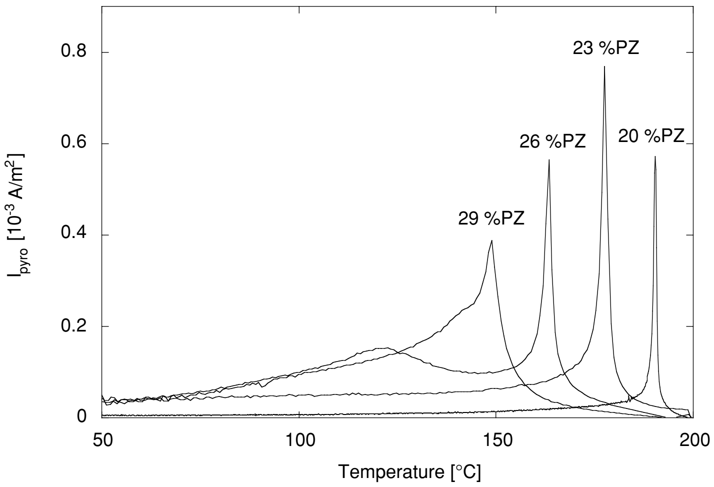

Figure 3.7: *Measured pyroelectric currents, I_{pyro} for various 40PNN-60PZT compositions.*

The polarization for the 26 %PZ composition was integrated from the pyroelectric current and is reported in Figure 3.8. As a result of peaks integration, the polarization dependence on temperature shows a clear inflexion in the region of the minor peak (T_1) and goes to zero above the principal peak (T_2). Nevertheless, the transition temperatures do appear much more clearly on the pyroelectric current response. Thus, it can be said that T_2 corresponds to the temperature of ferroelectric to paraelectric transition and T_1 is related to another type of event occurring in the ferroelectric state. The high level of background current observed below T_2 in Figure 3.8 is quite different from a pure ferroelectric response and may be related to the presence of an unstable ferroelectric phase in the poled samples. It yields a strong temperature dependence of the polarization in the ferroelectric state and, hence, a high value of the pyroelectric coefficient

($p \approx 400\ \mu C/m^2K$). This is the origin of the interesting properties of such materials for pyroelectric sensors in current response [37]. The shape of this pyroelectric current curve is very similar to what has been observed for rhombohedral PMN-PT ceramics [25] where T_1 and T_2 peaks were respectively interpreted as tetragonal to cubic and rhombohedral to tetragonal transitions.

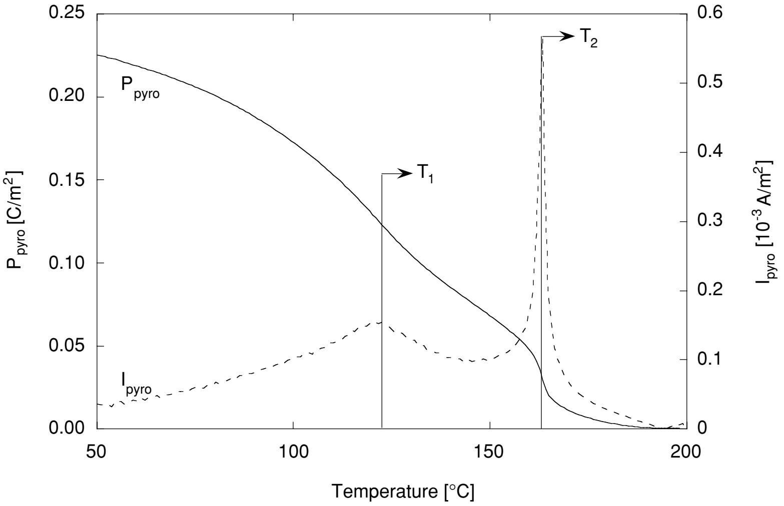

Figure 3.8: *Typical pyroelectric polarization,* P_{pyro} *and current density,* I_{pyro} *for the 40PNN-26PZ-34PT composition.*

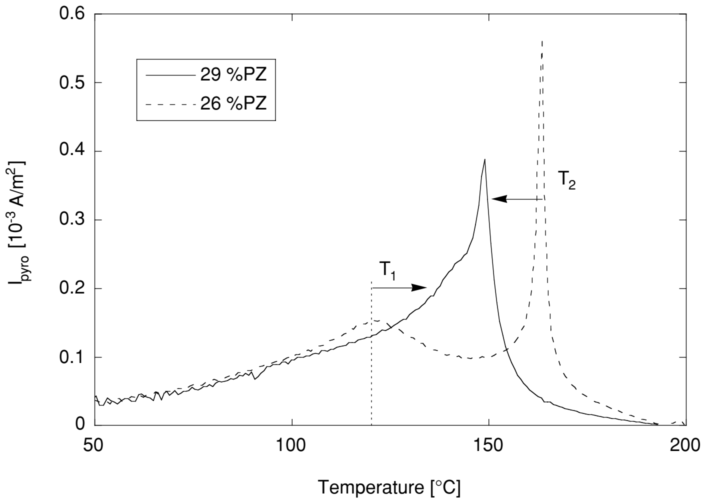

Figure 3.9: *Effect of composition change on the shape of the pyroelectric current,* I_{pyro} *as a function of PZ content for two 40PNN-60PZT compositions exhibiting a rhombohedral structure at room temperature.*

The effect of an increase in PZ content on the observed anomalies is presented in Figure 3.9. The shift of T_2 towards lower temperature corresponds well to what has already been observed for the dielectric measurements. Moreover, T_1 is clearly getting closer to T_2 as PZ content increases. Note that it eventually disappears in the main peak for the 32 %PZ composition, but is inducing an important peak asymmetry suggesting that it is still present.

To further identify the observed pyroelectric transitions, it is of interest to compare the pyroelectric current response with the dielectric permittivity dependence on temperature (as presented in Figure 3.10 and Figure 3.11).

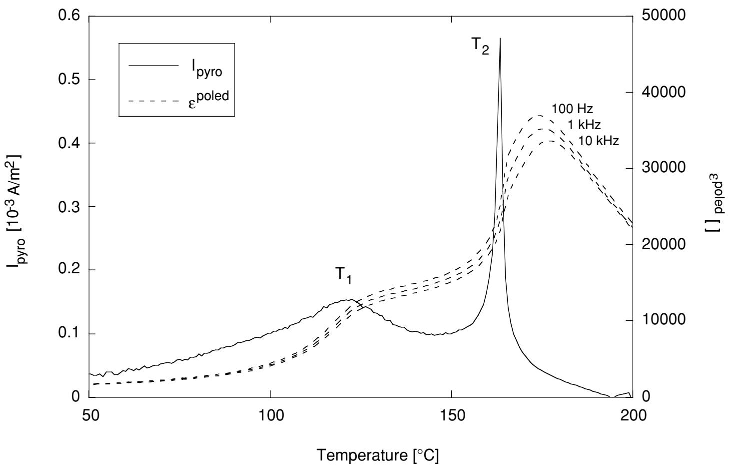

Figure 3.10: *Comparison of the obtained pyroelectric current, I_{pyro} with the dielectric permittivity, ε^{poled} measurement for the 40PNN-26PZ-34PT composition.*

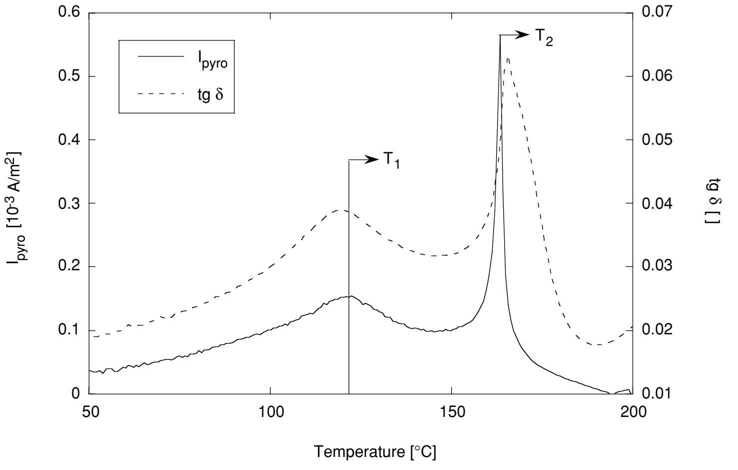

Figure 3.11: *Comparison of the obtained pyroelectric current, I_{pyro} with the dielectric losses, tg δ measurement for the 40PNN-26PZ-34PT composition.*

Comparison of $I_{pyro}(T)$ with the dielectric response, permits to identify T_1 and T_2 with T_{rt} and T_{NR}, respectively. However, some temperature shifts appear on Figure 3.11, where T_1 is situated at a slightly higher temperature than T_{rt} and T_2 is at a lower temperature than T_{NR}. Concerning the latter, this temperature effect can be understood as higher losses are expected in the region where the spontaneous polarization is already unstable and may only be stabilized by field application, whereas in the case of pyroelectric measurement (performed without electric field application) the current peak will be observed at the exact temperature where spontaneous polarization becomes unstable. This also confirms the interpretation of the normal to relaxor transition observed in dielectric measurements, as relaxor exhibits a pyroelectric response equivalent to a paraelectric state. Note also that the calculated Vögel-Fulcher freezing temperature (T_f = 162.6°C) is closer to the T_2 value of 163.4°C than to the dielectric loss T_{NR} (165.6°C).

3.3.3 Conclusion

Pyroelectric characterization permitted to observe two anomalies (appearing clearly on the current response) in the room temperature rhombohedral samples, whereas the tetragonal ones were exhibiting one transition only. The main (high temperature) peak corresponds to a ferroelectric to paraelectric transition and thus confirms the normal to relaxor ferroelectric transition proposed in the previous section. Concerning the second anomaly, it is clearly linked to the T_{rt} transition observed in dielectric measurements. Moreover, pyroelectric measurements permitted to put into evidence such an anomaly in rhombohedral samples containing a high level of PZ (> 26 %PZ) which was not the case for the dielectric response. Finally, no definite confirmation of the nature of T_{rt} transition as a rhombohedral to tetragonal transition could be made by such a characterization method.

3.4 XRD CHARACTERIZATION

In order to verify the nature of the T_{rt} transition, XRD analysis as a function of temperature was performed. Two different procedures were used. First, a sintered sample of the 40PNN-26PZ-34PT composition was crushed and analyzed at two defined temperatures (25°C and 145°C) both well in the range of expected rhombohedral and tetragonal phases. In particular, two peaks were more precisely studied: (200) and (222) as they permit to distinguish between the cubic, the tetragonal, and the rhombohedral structures. In a second type of experiment (conducted at Ecole Centrale de Paris by B. Dkhil), a sintered sample of 50PNN-16PZ-34PT composition (which exhibits the same basic transitions as 40PNN-26PZ-34PT) was cooled from 230°C through the T_{NR} transition while analyzing its (200), (220), and (222) peaks every 10°C with a high precision XRD diffractometer. Thus, using pseudo-Voigt functions and a Rietveld refinement method, lattice parameters and full width at half maximum (FWHM) could be extracted form the XRD spectra as a function of temperature.

3.4.1 Around the morphotropic transition

The (200) and (222) peak shapes as a function of temperature for the 40PNN-26PZ-34PT are presented in Figure 3.12. Note that the expected structures from both dielectric and pyroelectric measurements at 25°C and 145°C are rhombohedral and tetragonal, respectively.

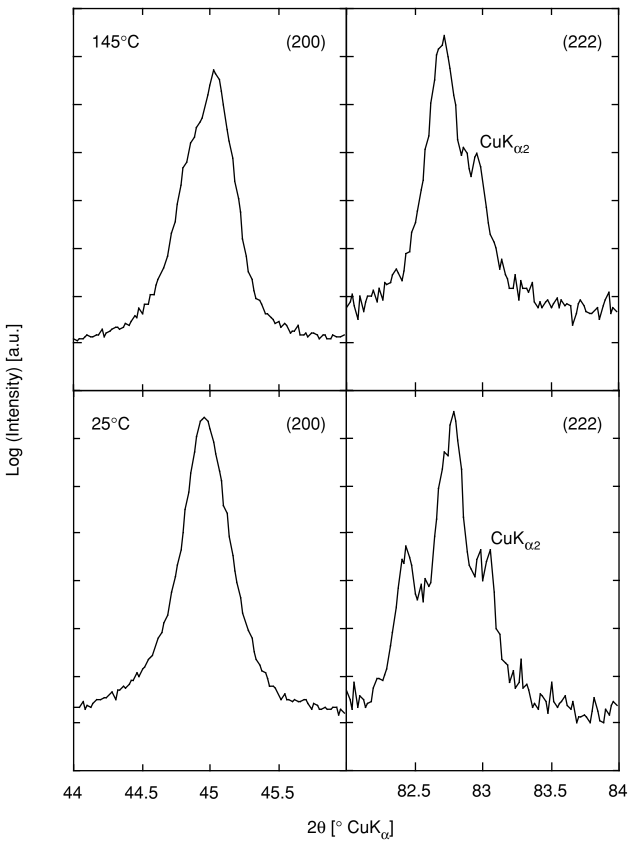

Figure 3.12: *Zoom of the (200) and (222) peaks as a function of temperature for 40PNN-26PZ-34PT composition.*

The transition from rhombohedral to tetragonal structure upon heating can be observed from the evolution of the (222) peak (excluding Cu $K_{\alpha 2}$) which goes from a double peak at room temperature to a single one at 140°C. But, to rigorously exclude a cubic structure at 145°C, the (200) peak should exhibit a tetragonal anomaly. A shoulder can indeed be observed on the left of the 145°C (200) peak. Thus, a structural phase transition from rhombohedral at room temperature to tetragonal at 145°C do indeed occur in the considered composition. The T_{rt} anomaly is thus most probably caused by this transition, confirming the interpretation proposed earlier for PMN-PT [25, 26] and PZN-PT [27]. Hence, the T_{rt}-associated transition may indeed be called morphotropic transition. Finally, in view of the recent developments of the MPB structural analysis in PZT [38], note that a monoclinic phase at 25°C with a a/b ratio close to 1 cannot be strictly ruled out by our measurements as the (200) width is quite considerable.

3.4.2 Around the dielectric peak

The temperature dependent measurements of the FWHM of (200), (220), and (222) peaks of the 50PNN-16PZ-34PT sample are presented in Figures 3.13 and 3.14. As XRD characterization was performed with constant temperatures, the transition temperatures reported on these figures were calculated by averaging heating and cooling values from dielectric measurements, which yielded T_{rt} = 45°C, T_{NR} = 112°C and T_m = 127°C at 1 kHz.

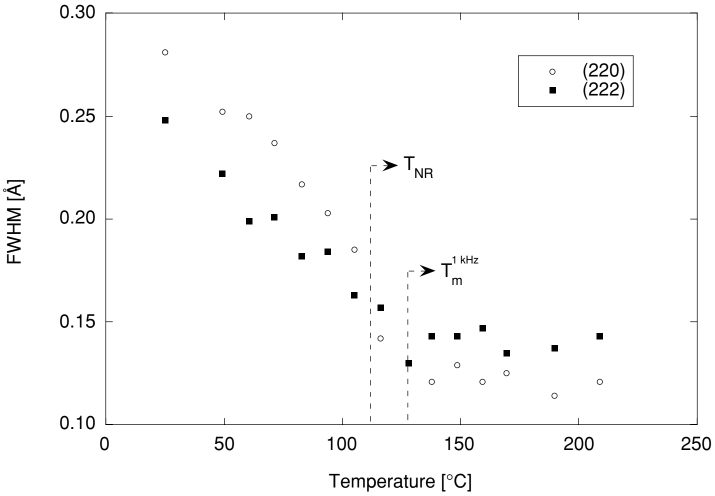

Figure 3.13: *FWHM of the (220) and (222) peaks for the 50PNN-16PZ-34PT composition as a function of temperature.*

The (222) FWHM shows a slow increase upon cooling from approx. 140°C which is above T_m and T_{NR}. It can probably be related to the presence of ordered nanodomains in the relaxor phase which strain their cubic matrix so that diffraction peaks are getting wider [39]. Concerning (220) FWHM, the increase looks sharper and is starting close to the T_{NR} temperature in a manner similar to PSN at relaxor to ferroelectric transition [40].

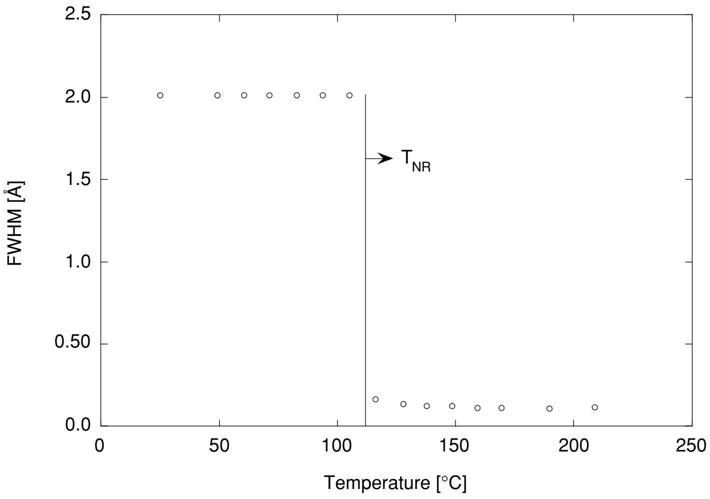

Figure 3.14: *FWHM of the (200) peak for the 50PNN-16PZ-34PT composition as a function of temperature.*

The sharp step observed on (200) FWHM as a function of temperature in Figure 3.14 corresponds exactly with the dielectric T_{NR}. It is caused by the tetragonal splitting occurring at this temperature, as the structure transforms from relaxor (cubic) to ferroelectric state. This explains the increase seen on the (220) FWHM as such a reflection is split for a tetragonal symmetry. (Note that the change in (222) FWHM noticed in Figure 3.13 cannot be explained by this structural transition). Again, this confirms the previous interpretation of a relaxor to normal ferroelectric transition occurring at T_{NR}.

3.5 PNN-PZT PHASE DIAGRAM AND CURVING MPB

Dielectric, pyroelectric and XRD characterization have permitted to identify two types of transitions occurring in the PNN-PZT system: the first one is present in all the investigated compositions and consists in a relaxor to normal ferroelectric phase transition (as expected from the polarizing power differences calculated in section 3.1.3). The second transition temperature, which can be detected in the best way by using pyroelectric current monitoring, has been identified with a tetragonal to rhombohedral structural phase transition using temperature dependent XRD. All the compositions being rhombohedral at room temperature exhibited to a certain extent the two transitions cited above upon heating. It was also possible to evidence a similar morphotropic transition by cooling tetragonal samples situated close to the MPB at room temperature. Hence, it is now possible to draw phase diagrams for the

PNN-PZT solid solutions by collecting the different transition temperatures as a function of PNN content and PZ/PT ratio, taking into account the direction of heat treatment during measurements (as thermal hysteresis is observed).

3.5.1 Final Phase diagrams for 40% and 50% PNN-PZT

Pyroelectric characterization was selected to determine transition temperatures (T_{rt} and T_{NR}) as it is probably the most sensitive method (e.g. it can distinguish between the two transitions for samples with a very high PZ content as in Figure 3.9). This directly implies that the obtained diagrams will be valid for the heating of poled samples only. Moreover, indication of the relaxor region extent was given through the permittivity peak temperature, T_m measured at 1 kHz upon heating (i.e. taking into account the observed thermal hysteresis). The regions were then labeled according to XRD and dielectric analysis. Thus, phase diagrams for the 40PNN-60PZT and 50PNN-50PZT compositions were obtained and are reported in Figures 3.15 and 3.16 respectively. One of them (40PNN-60PZT) has been already published elsewhere taking into account dielectric and XRD measurements only [41].

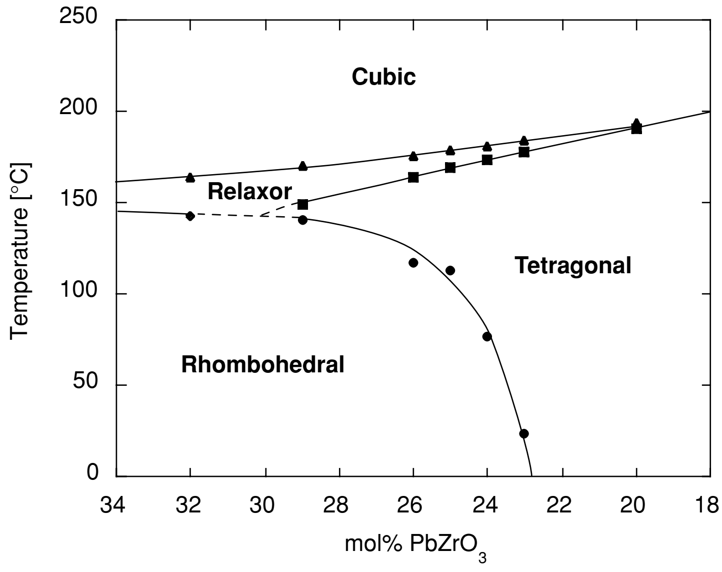

Figure 3.15: Suggested phase diagram for the 40PNN-60PZT in the region of the MPB. The points are derived from dielectric and pyroelectric measurements and phases regions were identified with XRD.

The triple point region between tetragonal, rhombohedral and relaxor phases situated between the 29 %PZ and 32 %PZ compositions in Figure 3.15 is only indicative. As discussed in section 3.3.2, it rather seems that the rhombohedral to tetragonal transition is merging with the normal to relaxor ferroelectric transition. Hence, it is difficult to say whether the two transitions T_{rt} and T_{NR} merge or not into a single rhombohedral to relaxor transition. Recent dielectric characterization of PNN-PZ solid solutions [42] have shown that 40PNN-60PZ composition exhibits a relaxor behavior with reduced frequency dispersion of the peak temperature with a T_m at 128°C for 1 kHz. This value is coherent with a linear extrapolation of the T_m line (i.e. relaxor-cubic limit) in Figure 3.15. The reported relaxor behavior for 40PNN-60PZ suggests that the ferroelectric state is weakening with increasing PZ content. Thus, in the high PZ content region, the T_{NR} transition is probably smeared out over a wider temperature range, causing a disappearance of the T_{rt} transition.

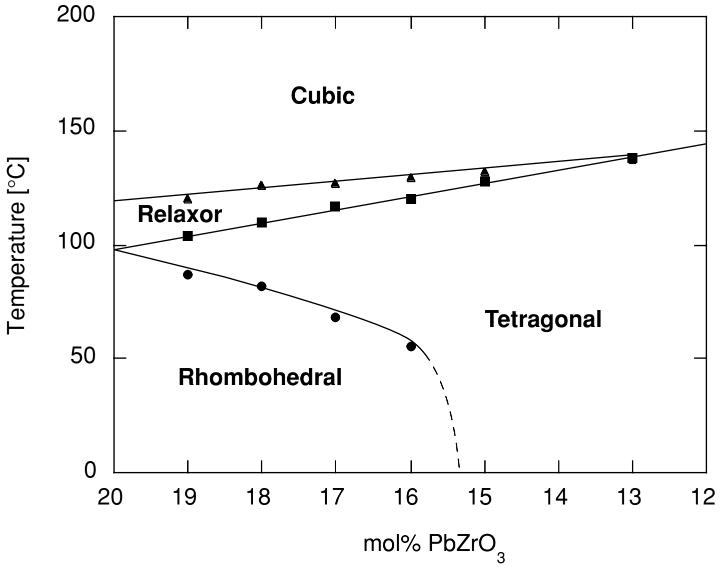

Figure 3.16: Suggested phase diagram for the 50PNN-50PZT in the region of the MPB. The points are derived from dielectric and pyroelectric measurements and phases regions were identified with XRD.

The two phase diagrams exhibit a quite similar pattern. Their MPB (i.e. the line separating rhombohedral and tetragonal phases) is curved toward PZ-rich region and is getting almost flat in the triple point region in agreement with observations on PMN-PT [29] and PZN-PT [27] (even though other mechanisms are certainly involved when the relaxor content is changed). The MPB curvature is more pronounced in the 50PNN-50PZT phase diagram (Figure 3.16). This may be related to the higher relaxor content as the relaxor-free MPB for PZT is almost vertical. The analogy with relaxor-PT systems and the general shape of the ternary phase diagram for lead-based relaxor-PZ-PT solid solutions [7] strongly suggest that the overall shape of the presented phase diagrams is similar to that in other relaxor-PZ-PT solid solutions.

Furthermore, the relaxor temperature interval is increasing with increasing PZ content (with the notable exception of 40PNN-32PZ-28PT which shows a narrower relaxor zone than

40PNN-29PZ-31PT). This would confirm the very rough model for spontaneous relaxor to normal ferroelectric phase transition prediction proposed in section 3.1.3, as the expected widest relaxor region was predicted for 40PNN-30PZ-30PT. Figure 3.16 does not permit to infirm such an interpretation as all the tested PZ/PT ratios are lower than 1.

The relative flatness of the rhombohedral-relaxor boundary compared to the tetragonal-relaxor one indicates that the crystallographic structure influences the spontaneous normal to relaxor ferroelectric transition. A major difference between tetragonal and rhombohedral phases is the amplitude of internal strain which may influence the relaxor state stability as it implies an overall cubic symmetry. As the structure is almost pseudo-cubic on the rhombohedral side of the diagram, the strain energy varies very little in this composition range. This could account for the approximately stable T_{NR} on the rhombohedral side. For the tetragonal side, as the strain effects are increasing on going further away from the MPB toward tetragonal region, a steeper slope for the T_{NR} dependence on PZ/PT ratio is expected. This leads to a quick disappearance of the relaxor state for high PT contents (e.g. in 40PNN-20PZ-40PT and in 50PNN-13PZ-37PT) as predicted by *ab initio* energy calculations showing that tetragonal strain stabilizes the ferroelectric state [43].

3.5.2 Exploring the curving MPB in PNN-PZT

For a long time, MPB has been associated with a phase boundary defined as perpendicular to the compositional axis. Actually, when Goldschmidt introduced the term “morphotropic” transition [44], it was to express the possibility of a structural transition which thermodynamical set of variables contained composition. This was grounded on his works on tolerance factors [45] which showed that a structural transition can occur in “rock salts” when the average size of an ion situated on a given site is varying. It is obviously the case for PZT, where the substitution of Zr for Ti in the tetragonal structure leads to a tetragonal to rhombohedral transition. However, this does not imply that the composition at which the transition takes place is independent of temperature. For instance in PZT, the morphotropic phase boundary is not ideally vertical and can be crossed by heating a rhombohedral sample or by cooling a tetragonal one [38]. In our case, MPB is quite curved indicating that mechanisms stronger than in PZT take place in PNN-PZT and lead to a strongly favored tetragonal phase at high temperatures (or a lower stability for the rhombohedral phase at high temperature). Such mechanisms may be related to the numerous space charges induced by the PNN off-valence B-site cations. At low temperature, the generated random fields may shield more effectively the ferroelectric long-range interactions, destabilizing the tetragonal ferroelectric state [43]. Another interpretation may be based on the similarity of the observed MPB curving and the phase transitions in barium titanate[46]. It has been proposed [47] that such phase transitions could be caused by the condensation of random <111> distortions along 3 (tetragonal), 2 (orthorhombic) and 1 (rhombohedral) directions. If, in our case, the MPB lies in the region where the structural strain is not large enough to fully stabilize the tetragonal phase [43], similar distortions ordering may hence be observed in our system. In general, considering the MPB bending on the PNN-PZ-PT ternary diagram [8] and our temperature bending toward the Zr-rich side, it may imply that the effect of PNN is structurally similar to PZ (i.e. inducing a rhombohedral tendency) but has a stronger temperature dependence than for pure PZT.

In any case, a curved MPB implies the existence of some tetragonal to rhombohedral transition occurring by a change of temperature only. As there is no group to sub-group relationship between those two structures, such a transition is most probably indirect and first order in nature [11]. Hence, tetragonal and rhombohedral phases are very likely to coexist in a given temperature range, as hinted by the transition broadness (up to some tens of °C) observed in both dielectric and pyroelectric measurements (see e.g. Figures 3.3 and 3.8). However, such a broadness can also be accounted by large compositional inhomogeneities (similar to Känzig regions in BT [48]) or by some intrinsic diffuseness of the morphotropic transition [49].

Recently, studies on the PZT phase diagram have revealed that a monoclinic phase appears when cooling a tetragonal composition close to the MPB [38, 50]. This result was related to the condensation of lead displacements along a quasi-orthorhombic direction [50]. Concerning relaxor-ferroelectric solid solutions, a similar symmetry has been evidenced on the rhombohedral side of the MPB in PZN-PT single crystals [51] and was interpreted in terms of metastable adaptive martensite theory. Note also that a coexistence of rhombohedral and tetragonal phases in a single grain, as suggested by TEM studies for PNN-PZT [52], would imply an overall macroscopic monoclinic symmetry. Nevertheless, these results suggest that the curving of the MPB is somehow related to the existence of a “bridging phase” between the tetragonal and rhombohedral phases. This phase, monoclinic or orthorhombic, would permit the morphotropic transition. Moreover, as this intermediate phase is mainly interpreted in terms of lead cation displacements, easy transition mechanisms and influence of an applied electric field can be pictured by the change or condensation of lead displacements along given directions. Furthermore, as such regions may be quite “soft” with respect to the applied field, they could explain the very high dielectric properties observed in this region. The piezoelectric properties would also benefit from the existence of wide monoclinic rhombohedral-tetragonal interfaces as they would be less subjected to pinning [53] and, hence, contribute to the piezoelectric response in a mostly reversible manner.

In conclusion, the MPB curvature observed on the proposed PNN-PZT phase diagrams can probably be generalized to the main solid solutions exhibiting such a boundary (including PZT) as it is very similar to other relaxor-PT phase diagrams. In our case, the curving character seems to increase with relaxor content. Moreover, the existence of a curvature may be related to the presence of an intermediate phase between the tetragonal and rhombohedral ones which symmetry would provide a structural bridge for the morphotropic transition. Such a curved MPB also tends to confirm the compositional hysteresis model proposed by Isupov [11], as phase coexistence is a quite probable consequence of a first order temperature-dependent morphotropic transition [49]. Moreover, the mechanism of polarization freezing at T_C proposed by Cao and Cross [20] to explain the phase coexistence in PZT cannot be applied here as no paraelectric to ferroelectric transition can be linked to the observed morphotropic transition.

3.6 POLING STUDIES

The differences in dielectric behavior upon cooling or heating (cf. the higher dielectric dispersion upon cooling in Figure 3.6) and the effect of the poling state on the transition sharpness (cf. Figure 3.5) suggest an influence of the electro-thermal history on the properties of the PNN-PZT solid solutions.

As those issues are closely related to the poling process, a study of the influence of electric field and thermal treatments on the morphotropic transition was conducted. Hence, the effects of the poling temperature (i.e. in the tetragonal or rhombohedral zones) on the T_{rt} transition were investigated. Moreover, in order to characterize the stability of the transition, the variation of transition temperature with thermal cycling across the MPB was measured. Finally, the influence of poling method was studied by poling various samples using either the regular procedure (electric field is applied only at a given temperature) or by cooling through relaxor to normal ferroelectric phase transition down to room temperature with electric field applied on the sample.

3.6.1 Phase stabilization due to electric field

In order to check for any influence of the poling temperature on T_{rt}, a 40PNN-24PZ-36PT sample exhibiting a rhombohedral structure at room temperature was poled by applying an electric field of 20 kV/cm during 10 min in an oil bath at two different temperatures: 25°C and 100°C. According to the phase diagram (Figure 3.15), each temperature is corresponding to a different crystalline structure. Then, the sample was cooled without field and its pyroelectric response was measured as described in section 3.3.1. It has to be noted that when such "step poling" is performed at 100°C, the sample undergoes a first "unrecorded" morphotropic transition upon cooling in the oil bath. This may alter the structure induced by poling in the tetragonal zone.

The results for the pyroelectric current as a function of temperature in the morphotropic region for the two poling temperatures are presented in Figure 3.17.

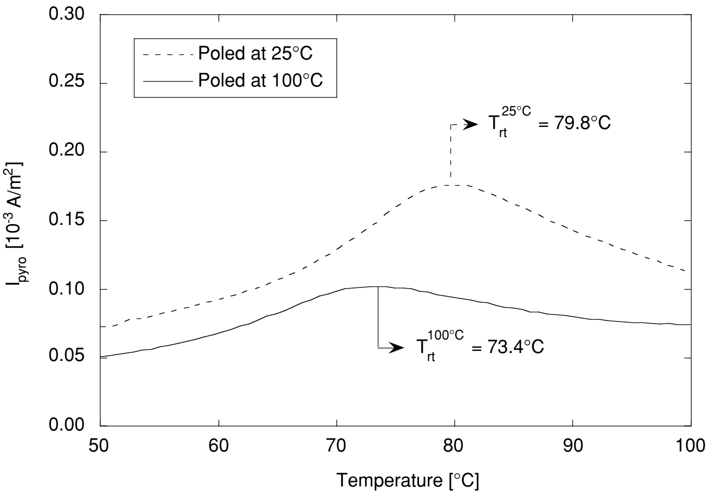

Figure 3.17: *Pyroelectric current response, I_{pyro} in the morphotropic transition region as a function of poling temperature for the 40PNN-24PZ-36PT composition.*

The rhombohedral to tetragonal transition temperature is indeed dependent on the poling temperature. It is shifted to higher temperatures when the sample is poled in the rhombohedral (low-temperature) region and *vice versa* for the 100°C poled. This fact advocates for a phase stabilization effect of the electric field. Several non-exclusive mechanisms may be proposed for this stabilization. First, some metastable tetragonal phase might be remaining below T_{rt} (in agreement with Noblanc observations on PMN-PT [29] and Isupov's considerations on phase coexistence in PZT [11]). And, if an electric field is applied, it will favor the phase corresponding to the poling temperature. Thus, the 25°C poled sample may be deprived of tetragonal nucleus and exhibit a higher transition temperature than the 100°C poled sample. Second, the poling may induce a defect pattern stabilizing the phase corresponding to the poling temperature. Third, as the sample poled at 100°C has already undergone a morphotropic transition before the measurement displayed in Figure 3.17, an intermediate phase (as discussed in section 3.5.2) may have appeared and is easing the morphotropic transition upon subsequent heating.

Furthermore, the polarization change associated with T_{rt} on Figure 3.17 is larger when the sample was poled at room temperature as illustrated on Figure 3.18.

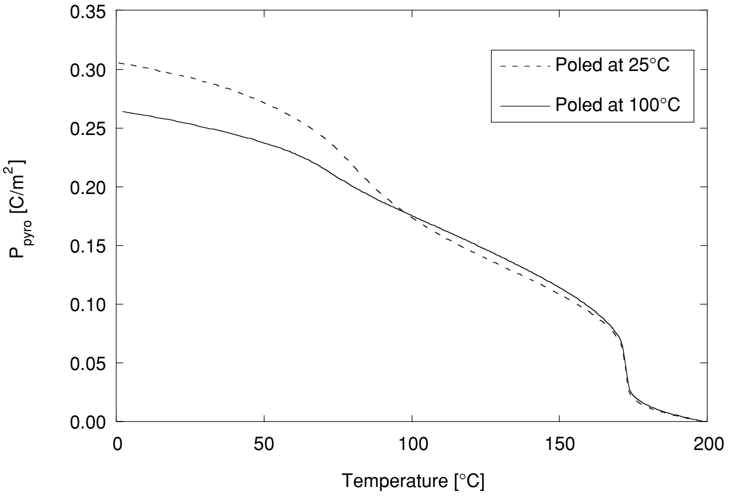

Figure 3.18: *Pyroelectric polarization,* P_{pyro} *as a function of temperature for different poling temperatures of the 40PNN-24PZ-36PT composition.*

To explain the polarization differences for the two poling temperatures, it can be again argued that going through the morphotropic transition for the 100°C poled sample may have released charges trapped during poling. They may be in part responsible of the larger T_{rt} anomaly in the 25°C poled sample. However, if poling does trap a significant amount of charges, a charge peak should also appear close to the poling temperature (25°C). As such a peak cannot be distinguished on Figure 3.18, it can be said that trapped charges effects are probably negligible. Depoling at T_{rt} for the 100°C poled sample may also account for the polarization difference. At the morphotropic transformation, the <001> spontaneous polarization can switch to four energetically equivalent <111> directions where, in the general case, only one corresponds to the most polarized state. This could also occur with the apparition of the previously mentioned intermediate phase. Hence, each time the morphotropic transition is crossed, depoling is expected. Moreover, considering the sudden increase of the dielectric dispersion after T_{rt} on Figure 3.2, the high temperature state certainly contains a much more dispersive phase, which may be accounted by an increase in domain wall density due to depoling.

Above T_{rt} in Figure 3.18, the polarization for 25°C poling is lower than the one for 100°C poling. Therefore, the rhombohedral to tetragonal transition is not exactly equivalent for the two poling temperatures as superimposition of their polarization curves for $T > T_{rt}$ would have been expected. Seemingly, “more” polarization is located in the poling-stabilized tetragonal structure than in the tetragonal phase obtained by the rhombohedral transformation. This implies that some kind of template (second phases, defects) for the phase induced by poling at

100°C were still present at room temperature and guided the growth of the tetragonal phase from the rhombohedral one in the poling direction. At this point, the hypothesis of a stabilizing defect pattern can really be questioned as it would have to overcome two radical morphotropic transformations. An intermediate phase is also not very likely to template the growth of the tetragonal phase in the correct direction as it is certainly already misoriented with respect to its parent phase. Hence, remaining tetragonal phase seems to be the more reasonable mechanism for this high temperature polarization stabilization. Finally, it is noteworthy that the relative offset of the two polarization curves stays constant around 5 % from 120°C up 160°C. This indicates that, even though the poling levels are different, the two measurements correspond to similar phases as the intrinsic polarization dependence on temperature is identical.

To deepen the investigation on the morphotropic transition effects on the 100°C step poling, a sample was poled directly in the pyroelectric measurement set-up at 100°C and its pyroelectric response measured immediately afterwards, without any cooling to room temperature. The obtained polarization response is compared to the previous ones in Figure 3.19.

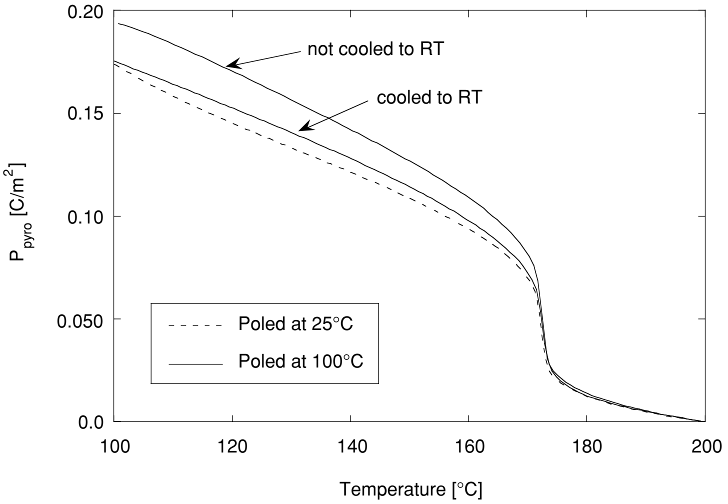

Figure 3.19: *Pyroelectric polarization, P_{pyro} as a function of poling temperature and thermal history for the 40PNN-24PZ-36PT composition.*

As expected, the sample poled at 100°C without cooling to room temperature exhibits the highest polarization. Its relative offset from the two other measurements is decreasing upon heating. This confirms that the phase composition is truly altered by application of an electric field, i.e. inducing a global structure which is different from the one obtained by mere heat treatment. Moreover, the result of the electric field alteration is unstable upon morphotropic transition crossing. In our view and as proposed by Isupov for PZT [19], only a second phase (rhombohedral or intermediate) stabilized by the electric field can account for such a polarization behavior. By providing additional polarization directions, it would account for the higher polarization observed in 100°C poling without cooling. Moreover, as soon as the electric field is removed, it will become metastable and hence disappear much faster upon heating or morphotropic transition crossing. Still, this interpretation implies that a second phase may also be induced in the rhombohedral one. Indeed, this is observed in rhombohedral PZN-PT single crystals [54] when a field is applied along the [001] direction. However, it is not compatible with the observed increase in T_{rt} for 25°C poling. Cao and Cross [20] have shown that, given a random orientation of polarization and equivalent free energies, the probability of having a direction closer to a rhombohedral direction is 1.45 times greater than to a tetragonal one. Therefore, when an electric field is applied along an arbitrary direction, the rhombohedral phase is favored with respect to the tetragonal one. Thus, rhombohedral phase is expected to be stabilized in tetragonal phase at a greater distance from the equilibrium temperature than tetragonal phase in rhombohedral one. This, along with the fact that 25°C may be further from the thermodynamical equilibrium temperature than 100°C, may account for the fact that no tetragonal phase is induced by the poling field at room temperature. Note that the rhombohedral single crystals poled in the [001] direction may very well exhibit field induced tetragonal phase as it is the most favored phase considering the special orientation of the electric field.

To test the proposed poling influence on phase repartition, pyroelectric measurements were performed while cycling across the morphotropic transition (0°C - 100°C). Starting at the poling temperature, T_{rt} was determined from the associated pyroelectric current peak upon heating and cooling several times through the morphotropic transition. The results are presented in Table 2.1 for heating and Table 2.2 for cooling.

Table 2.1: *Rhombohedral to tetragonal transition temperatures, T_{rt} at heating as a function of cycling number for the 40PNN-24PZ-36PT composition.*

Cycle #	T_{rt} [°C] poled at 25°C	T_{rt} [°C] poled at 100°C
1	$79.8^{\dagger}$	$73.4^{\dagger}$
2	74.1	72.3
3	73.3	71.6

† as measured in Figure 3.17.

Table 2.2: Tetragonal to rhombohedral transition temperatures, T_{rt} at cooling as a function of cycling number for the 40PNN-24PZ-36PT composition.

Cycle #	T_{rt} [°C] poled at 25°C	T_{rt} [°C] poled at 100°C
1	–	53.8
2	51.9	51.6
3	51.5	51.4

Table 2.1 and Table 2.2 show clearly that crossing T_{rt} once after poling is sufficient to stabilize the transition temperature and make it independent of poling temperature. This is compatible with a large hysteresis of transformation [11] where a poling-induced state [19] is removed by the first morphotropic transition. This induced state is a pure rhombohedral phase for poling at 25°C and a favored rhombohedral phase for poling at 100°C. Afterwards, the samples probably exhibit phase coexistence for the whole temperature range and hence phase transitions just affect the volume fraction of each phase, requiring identical undercooling.

Summarizing, the study of the morphotropic transition temperatures as a function of the poling temperature revealed an influence of electric field on the ferroelectric-relaxor solid solution structure. This influence is schematized on Figure 3.20, assuming hysteretic rhombohedral and tetragonal phase coexistence [11] (represented by a thick line) and taking into account the field preferential stabilization of the rhombohedral phase (represented by a dashed line).

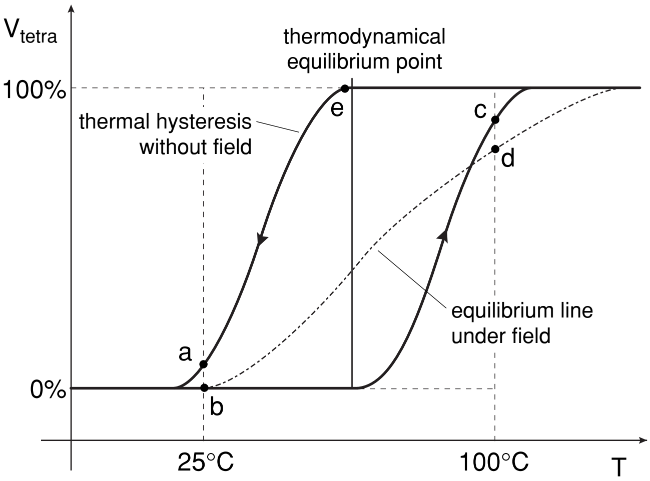

Figure 3.20: Schematized effects of temperature and electric field on tetragonal phase volume fraction (V_{tetra}) in the MPB region.

Starting with a sample at 25°C in state (a), when poling is performed at 25°C, the sample switches to a rhombohedral single state (b). Thus, the rhombohedral phase is stabilized toward heating as no tetragonal nucleus are present in state (b) and follows the (b) to (c) path. Then, starting cooling at (c), some remaining rhombohedral phase acts as nucleation point and causes a relative decrease in T_{rt} upon cooling. In the case of 100°C poling, the sample is initially in state (c) and switches to state (d) upon field application. As state (d) contains more rhombohedral phase than state (c) (due to polarization orientation stabilization [19, 20]), the transition to rhombohedral upon subsequent cooling is occurring at a lower undercooling than upon natural cooling (i.e. passing through the (e) state). After a heating phase transition without field applied, T_{rt} upon cooling is decreasing again as less rhombohedral phase is present at 100°C (c). Thus, it can be concluded that poling indeed induces a metastable structure which contains favored rhombohedral phase. A single crossing of the morphotropic transition is sufficient to erase the poling induced effects and permit to regain a state almost independent of the poling temperature. This observations invalidate the Cao and Cross model for phase coexistence [20] in relaxor-ferroelectric solid solutions as rhombohedral and tetragonal phases presence is not linked to the ferroelectric transition (T_{NR}). However, these results are still consistent with the idea of only one equilibrium temperature for phase coexistence corresponding to a high rhombohedral phase content [20] associated with a large hysteresis of transformation [11].

3.6.2 Poling method influences on morphotropic phase transition

Knowing the influence of the poling temperature on the morphotropic transition, it is also interesting to explore the effects of another type of poling procedure: the field cooling. This method consists in heating a ferroelectric material above its Curie temperature, applying an electric field and cooling the sample through the paraelectric to ferroelectric transition with the field applied. Thus, the appearing polarization will align with the applied field. As our materials are sensitive to the electric field (see Figure 3.20), such a treatment may actually induce a quite different state than the regular poling method.

To test the effects of the poling method on relaxor-ferroelectric solid solutions, two different compositions of 50PNN-50PZT exhibiting different symmetries at room temperatures were chosen: 50PNN-13PZ-37PT (tetragonal) and 50PNN-16PZ-34PT (rhombohedral). These two samples were first poled in the regular way using a field of 20 kV/cm at a temperature corresponding to their room temperature phase (80°C and 30°C, respectively for the tetragonal and rhombohedral samples). Their permittivity dependence on temperature was then measured upon heating until depoling. Later, the same samples were both heated at 150°C (above their respective T_{NR}) and the same field as before (20 kV/cm) was applied on the sample while cooling them to room temperature. Again, their permittivity dependence on temperature was measured in the same conditions as for the regular poling method. The permittivity curves as a function of temperature for both compositions are presented in Figures 3.21 and 3.22 for the tetragonal and the rhombohedral compositions, respectively.

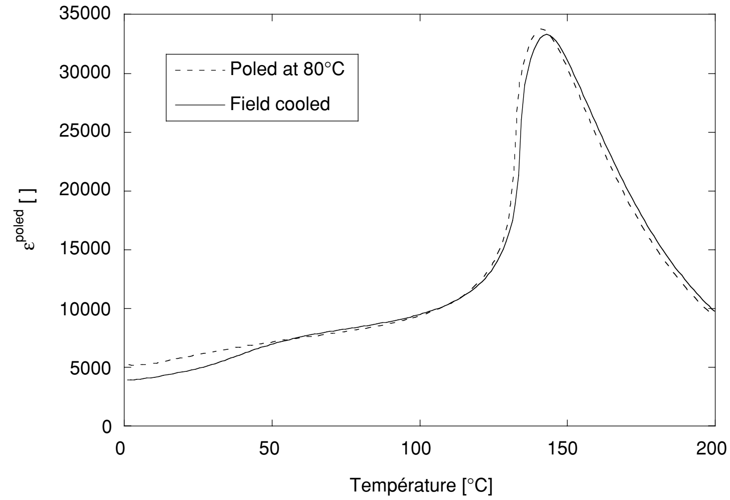

Figure 3.21: *Effect of poling method on the dielectric permittivity,* ε^{poled} *dependence on temperature for the 50PNN-13PZ-37PT composition (tetragonal symmetry at room temperature). Measurements performed upon heating at 1 kHz.*

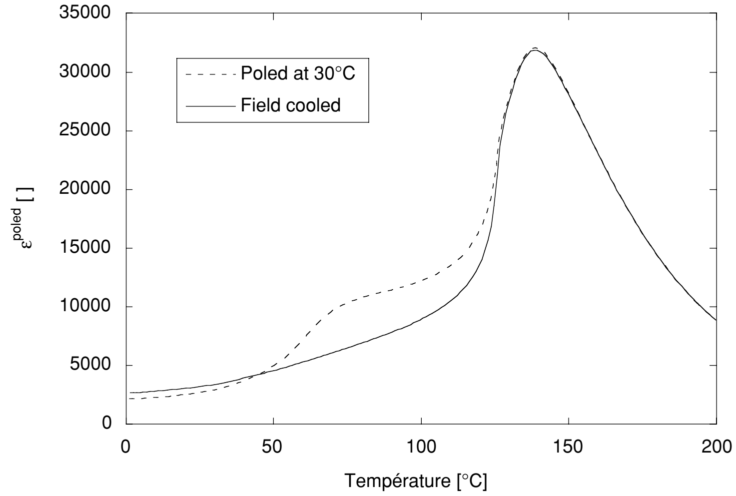

Figure 3.22: *Effect of poling method on the dielectric permittivity,* ε^{poled} *dependence on temperature for the 50PNN-16PZ-34PT composition (rhombohedral symmetry at room temperature). Measurements performed upon heating at 1 kHz.*

The tetragonal sample poled in a regular way at 80°C shows no anomaly in its permittivity curve whereas the field cooled measurement reveals a typical T_{rt} anomaly just below 50°C. In the case of rhombohedral sample, the anomaly is only appearing for the regularly poled sample and not when field cooling was applied. These results can be interpreted in the framework developed in the previous section (see Figure 3.20): when regular poling is performed far enough from the morphotropic transition, a stabilization of the corresponding phase is occurring. This is observed for the regular poling of both samples as they exhibit respectively pure tetragonal and rhombohedral phases at room temperature. In the case of field cooling, the applied field tends to stabilize a mixture of phases for a wider range of temperature. Hence, a morphotropic transition-related anomaly is observed close to room temperature on the tetragonal sample when field cooling is applied. In the rhombohedral case, the state reached by field cooling is different than by regular poling as initial permittivities are different. The higher permittivity at room temperature for field cooled sample suggests that tetragonal phase is still present, probably stabilized by cooling through T_{NR}. This point certainly necessitates further study.

3.7 SUMMARY

The study of the phases in the PNN-PZT solid solution system using permittivity, pyroelectric and XRD methods permitted to identify two types of phase transformations in this system. The first one consists in a spontaneous transition from relaxor to normal ferroelectric state. The second one can be better observed on samples rich in PZ and consists in a transition from the tetragonal to the rhombohedral symmetry upon cooling which corresponds to the transformation observed at MPB in PZT. Monitoring those transition temperatures as a function of PZ/PT ratio and relaxor content permitted to build two phase diagrams for the 40PNN-60PZT and the 50PNN-50PZT systems. These diagrams revealed a strongly temperature-dependent MPB separating the rhombohedral and the tetragonal states. This was interpreted in terms of temperature-dependent effects of the relaxor content on the ferroelectric tetragonal phase stability. The presence of a supplementary bridging phase between the tetragonal and rhombohedral states and its probable implications in the high properties observed close to MPB were also discussed.

Finally, the influence of the poling parameters (method and temperature) on the morphotropic transition temperature were investigated, revealing a strong field influence on the structure and temperature behavior of the considered PNN-PZT solid solutions. Such poling effects were interpreted in terms of a wide hysteresis for the morphotropic transformation and a rhombohedral phase preferential stabilization by electric field. These results permit to conclude that the morphotropic phase boundary observed in the PNN-PZT system is qualitatively equivalent to PZT with a more general temperature dependence.

3.8 REFERENCES

1. A.F. Devonshire, *Theory of Barium Titanate - Part I.* Philos. Mag., (1949) **40** p. 1040-63.
2. A.F. Devonshire, *Theory of Barium Titanate - Part II.* Philos. Mag., (1951) **42** p. 1065-79.
3. B. Jaffe, R.S. Roth, and S. Marzullo, *Piezoelectric properties of lead zirconate-lead titanate solid-solution ceramics.* J. Appl. Pys., (1954) **25** p. 809-10.
4. G.A. Smolenskii and A.I. Agranovskaya, *Dielectric polarization and losses of some complex compounds.* Sov. Phys. Tech. Phys., (1958) **3** p. 1380-2.
5. F. Chu, I.M. Reaney, and N. Setter, *Investigation of relaxors that transform spontaneously into ferroelectrics.* Ferroelectrics, (1994) **151** p. 343-8.
6. S. Wada, T. Suzuki, M. Osada, and N. Kakihana, T., *Change of macroscopic and microscopic symmetry of barium titanate single crystal around Curie temperature.* Jpn. J. Appl. Phys., (1998) **37** [9B] p. 5385-93.
7. Y. Yamashita, *Large electromechanical coupling factors in perovskite binary material system.* Jpn. J. Appl. Phys., (1994) **33** p. 5328-5331.
8. H. Banno, T. Tsunooka, and I. Shimano, *Phase diagram and piezoelectric properties of* $Pb(Nb_{2/3}Ni_{1/3})O_3$ - $PbTiO_3$ - $PbZrO_3$ *and an application to ceramic wave filter.* Proc. 1st meeting ferroelec. mat'ls and app., ed. O. Omoto, A. Kunada, Keihin Printing Co, (1977) p. 339-44.
9. M.S. Yoon, H.M. Jang, and S. Kim, *Spontaneous micro-macro ferroeletric domain switching in* $PbZrO_3$*-doped* $Pb(Ni,Nb)O_3$-$PbTiO_3$ *system.* Jpn. J. Appl. Phys., (1995) **34** p. 1916-21.
10. M.S. Yoon and H.M. Jang, *Relaxor-normal ferroelectric transition in tetragonal-rich field of* $Pb(Ni_{1/3}Nb_{2/3})O_3$-$PbTiO_3$-$PbZrO_3$ *system.* J. Appl. Phys., (1995) **77** [8] p. 3991.
11. V.A. Isupov, *Comments on the paper "X-ray study of the PZT solid solution near the morphtropic phase transition".* Solid State Com., (1975) **17** p. 1331-3.
12. P. AriGur and L. Benguigui, *X-ray study of the PZT solid solution near the morphtropic phase transition.* Solid State Com., (1974) **15** p. 1077-79.
13. L. Hanh, K. Uchino, and S. Nomura, *On the phenomenon of morphotropic tetragonal-rhombohedral phase boundary in the ferroelectric ceramics.* Jpn. J. Appl. Phys., (1978) **17** [4] p. 637-41.

14. A.V. Turik, M.F. Kupriyanov, E.N. Sidorenko, and S.M. Zaitsev, *Behavior of piezoceramics of type* $Pb(Zr,Ti)O_3$ *near the region of morphotropic transition.* Sov. Phys. Tech. Phys., (1980) **25** [10] p. 1251-4.
15. M.R. Soares, A.M.R. Senos, and P.Q. Mantas, *Phase coexistence region and dielectric properties of PZT ceramics.* J. Eur. Ceram. Soc., (2000) **20** [3] p. 321-4.
16. V.A. Isupov, *Thermodynamic analysis of phase transitions in perovskite ferroelectrics.* Sov. Phys. Solid State, (1977) **19** [5] p. 783-6.
17. V.A. Isupov, *Reasons for discrepancies relating to the range of coexistence of phases in lead zirconate-titanate solid solutions.* Sov. Phys. Solid State, (1980) **22** [1] p. 98-101.
18. M. Demartin, *Influence de l'élaboration et de la microstructure sur le déplacement des parois de domaine et les propriétés électro-mécaniques de céramiques de* $Pb(Zr,Ti)O_3$ *et* $BaTiO_3$, in *Materials Dept.* 1996, Swiss Federal Institute of Technology Lausanne: Lausanne, Switzerland.
19. V.A. Isupov, *Some aspects of the physics of piezoelectric ceramics.* Ferroelectrics, (1983) **46** p. 217-25.
20. W. Cao and L.E. Cross, *Theoretical model for the morphotropic phase boundary in lead zirconate-lead titanate solid solutions.* Phys. Rev. B, (1993) **47** [9] p. 4825-30.
21. H. Cao and A.G. Evans, *Nonlinear deformation of ferroelectric ceramics.* J. Am. Ceram. Soc., (1993) **76** [4] p. 890-6.
22. W. Cao and L.E. Cross, *Distribution functions of coexisting phases in a complete solid solution system.* J. Appl. Phys., (1993) **73** [7] p. 3250-5.
23. M.J. Haun, E. Furman , H.A. McKinstry, and L.E. Cross, *Thermodynamic theory of the lead zirconate-titanate solid solution system, Part II: Tricritical behavior.* Ferroelectrics, (1989) **99** p. 27-44.
24. M.R. Soares, A.M.R. Senos, and P.Q. Mantas, *Phase coexistence in PZT ceramics.* J. Eur. Ceram. Soc., (1999) **19** p. 1865-71.
25. S.W. Choi, T.R. Shrout, S.J. Jang, and A.S. Bhalla, *Morphotropic phase boundary in* $Pb(Mg_{1/3}Nb_{2/3})O_3$-$PbTiO_3$ *system.* Mat. Lett., (1989) **8** [6-7] p. 253-5.
26. T.R. Shrout, Z.P. Chang, N. Kim, and S. Markgraf, *Dielectric behavior of single crystals near the* $(1-x)Pb(Mg_{1/3}Nb_{2/3})O_3$-$xPbTiO_3$ *morphotropic phase boundary.* Ferroelectrics Lett., (1990) **12** p. 63.
27. J. Kuwata, K. Uchino, and S. Nomura, *Phase transitions in the* $Pb(Zn_{1/3}Nb_{2/3})O_3$-$PbTiO_3$ *system.* Ferroelectrics, (1981) **37** p. 579-82.
28. H. Arndt, F. Sauerbier, G. Schmidt, and L.A. Shebanov, *Field-induced phase transition in* $Pb(Mg_{1/3}Nb_{2/3})O_3$ *single crystals.* Ferroelectrics, (1988) **79** p. 145-8.

29. O. Noblanc, P. Gaucher, and G. Calvarin, *Structural and dielectric studies of* $Pb(Mg_{1/3}Nb_{2/3})O_3$*-*$PbTiO_3$ *ferroelectric solid solutions around the morphotropic boundary.* J. Appl. Phys., (1996) **79** [8] p. 4291-7.

30. F. Chu, N. Setter, and A.K. Tagantsev, *The spontaneous relaxor-ferroelectric transition of* $Pb(Sc_{0,5}Ta_{0,5})O_3$. J. Appl. Phys., (1993) **74** [8] p. 5129.

31. F. Chu, I.M. Reaney, and N. Setter, *Spontaneous (zero-field) relaxor-to-ferroelectric phase transition in disordered* $Pb(Sc_{1/2}Nb_{1/2})O_3$. J. Appl. Phys., (1995) **77** [4] p. 1671.

32. X. Dai, A. DiGiovanni, and D. Viehland, *Dielectric properties of tetragonal lanthanum modified lead zirconate titanate ceramics.* J. Appl. Phys., (1993) **74** [5] p. 3399.

33. X. Dai, Z. Xu, and D. Viehland, *The spontaneous relaxor to normal ferroelectric transformation in La-modified lead zirconate titanate.* Philos. Mag. B, (1994) **70** [1] p. 33-48.

34. E.V. Colla, N.K. Yushin, and D. Viehland, *Dielectric properties of* $(PMN)_{(1-x)}$ $(PT)_x$ *single crystals for various electrical and thermal histories.* J. Appl. Phys., (1998) **83** [6] p. 3298-304.

35. D. Viehland, S.J. Jang, L.E. Cross, and M. Wuttig, *Freezing of the polarization fluctuations in lead magnesium niobate relaxors.* J. Appl. Phys., (1990) **68** [6] p. 2916.

36. R.L. Byer and C.B. Roundy, *Pyroelectric coefficient direct measurement technique and application to a nsec response time detector.* Ferroelectrics, (1972) **3** p. 333-8.

37. D. Luff, R. Lane, BrownK.R., and H.J. Marshallsay, *Ferroelectric ceramics with high pyroelectric properties.* Brit. Ceram., (1974) **73** p. 251-64.

38. B. Noheda, D.E. Cox, G. Shirane, J.A. Gonzalo, L.E. Cross, and S.E. Park, *A monoclinic ferroelectric phase in the* $Pb(Zr_{1-x}Ti_x)O_3$ *solid solution.* Appl. Phys. Lett., (1999) **74** [14] p. 2059-61.

39. N. de Mathan, E. Husson, G. Calvarin, J.R. Gavarri, A.W. Hewat, and A. Morell, *A structural model for the relaxor* $PbMg_{1/3}Nb_{2/3}O_3$ *at 5K.* J. Phys.-Condens. Matter, (1991) **3** p. 8159-71.

40. C. Malibert, B. Dkhil, J.M. Kiat, D. Durand, J.F. Bérar, and A. Spasojevic de Biré, *Order and disorder in the relaxor ferroelectric perovskite* $PbSc_{1/2}Nb_{1/2}O_3$ *(PSN): Comparison with simple perovskites* $BaTiO_3$ *and* $PbTiO_3$. J. Phys.: Condens. Matter, (1997) **9** p. 7485-500.

41. G. Robert, M. Demartin, and D. Damjanovic, *Phase diagram for the* $0.4Pb(Ni_{1/3}Nb_{1/3})O_3$*-*$0.6Pb(Zr,Ti)O_3$ *solid solution in the vicinity of a morphotropic boundary.* J. Am. Ceram. Soc., (1998) **81** [3] p. 749-53.

42. C.H. Lu and W.J. Hwang, *Phase evolution and dielectric characterization of lead nickel niobate - lead zirconate ceramics prepared from the hydrothermally derived precursors.* J. Mater. Res., (1999) **14** [4] p. 1364-70.

43. R.E. Cohen, *Origin of ferroelectricity in perovskite oxides.* Nature, (1992) **358** p. 136-8.

44. V.M. Goldschmidt, T. Barth, G. Lunde, and W. Zachariasen, *Geochemische Verteilunggestze der Elemente VII Die Gesetze der Krystallochemie.* Srkrifter Utgitt av der Norske Videnskaps-Akademi i Oslo, I. Matem.-Naturvid. Klasse, (1926) **2**.

45. V.M. Goldschmidt, *Geochemische Verteilunggestze der Elemente VIII Untersuchungen über Bau und Eigenscahften von Krystallen.* Srkrifter Utgitt av der Norske Videnskaps-Akademi i Oslo, I. Matem.-Naturvid. Klasse, (1926) **8** p. 7-142.

46. M.E. Lines and A.M. Glass, *Principles and applications of ferroelectrics and related materials*. 1977, Oxford: Calrendon Press.

47. R. Comès, M. Lambert, and A. Guinier, *Structure disorder of* $BaTiO_3$ *type ferroelectrics.* J. Phys. Soc. Jpn., (1970) **28** p. 195-8.

48. W. Känzig, *Röntgenuntersuchung über die Seignetteelektrizität von Bariumtitanat.* Helv. Phys. Acta, (1951) **24** [I] p. 175-216.

49. C.S. Tu, F.C. Chao, C.H. Yeh, C.L. Tsai, and V.H. Schmidt, *Hypersonic and dielectric anomalies of* $(Pb(Zn_{1/3}Nb_{2/3})O_3)_{0.905}(PbTiO_3)_{0.095}$ *single crystal.* Phys. Rev. B, (1999) **60** [9] p. 6348-51.

50. B. Noheda, J.A. Gonzalo, L.E. Cross, R. Guo, S.E. Park, D.E. Cox, and G. Shirane, *Tetragonal to monoclinic phase transition in a ferroelectric perovskite: The structure of* $PbZr_{0.52}Ti_{0.48}O_3$. Phys. Rev. B, (2000) **61** [13] p. 8687-95.

51. D. Viehland, *Symmetry-adaptative ferroelectric mesostates in oriented* $Pb(B^{I}_{1/3}B^{II}_{2/3})O_3$-$PbTiO_3$ *crystals.* J. Appl. Phys., (2000) **88** [8] p. 4794-806.

52. X. Zhu, J. Zhu, S. Zhou, Q. Li, Z. Meng, Z. Liu, and N. Ming, *SAED and TEM investifgations of domain structure in bismuth and zinc modified* $Pb(Ni_{1/3}Nb_{2/3})O_3$-$PbTiO_3$-$PbZrO_3$ *ceramics at morphotropic phase boundary.* Ferroelectrics, (1998) **215** p. 265-76.

53. T. Nattermann, Y. Shapir, and I. Vilfan, *Interface pinning and dynamics in random systems.* Phys. Rev. B, (1990) **42** [13] p. 8577-86.

54. D.S. Païk, S.E. Park, S. Wada, S.F. Liu, and T.R. Shrout, *E-field phase transition in <001>-oriented rhombohedral* $0.92Pb(Zn_{1/3}Nb_{2/3})O_3$-$0.08PbTiO_3$ *crystals.* J. Appl. Phys., (1999) **85** [2] p. 1080-3.

CHAPTER IV
PIEZOELECTRIC COEFFICIENT NONLINEARITY

Piezoelectric nonlinearity is a key-issue toward better response control of high performance actuators, sensors and transducers [1]. At first, piezoelectrics were seen as purely linear elements. However, as soon as materials exhibiting enhanced properties (in particular soft ferroelectrics) were introduced, the piezoelectric coefficient could not be considered as constant anymore. It was varying with frequency and applied field in various ways depending on parameters such as doping, field amplitudes and material composition. In the beginning, such effects were neglected, but nowadays, as control requirements increase and as high performance compositions are getting more and more nonlinear, it is necessary to take these effects into account. Descriptions can be empirical introducing frequency and field dependences when observed. However, such an approach multiplies the number of parameters and has very limited benefits in materials improvement. Therefore, more basic and systematic studies of this phenomenon should be conducted in order to determine what are the actual variables leading to nonlinear behaviors. Such an approach is believed to be beneficial to both the physical understanding of the piezoelectric nonlinearity and the application of nonlinear piezoelectrics in areas such as high sensitivity pressure sensors and micropositionners.

In this chapter, we will address the description of the piezoelectric coefficient nonlinearities by extending the Preisach modeling of ferromagnetics to the field of piezoelectricity. This approach relates the apparition of a rate-independent hysteresis in the piezoelectric response with the field dependence of the piezoelectric coefficient by using the concept of bistable units distributed in the system. We will focus in this chapter on the piezoelectric coefficient nonlinearities rather than on the loops description as the Preisach description does not handle naturally relaxation phenomena. The issue of loop modeling will be extensively treated in the next chapter. In such a perspective, the basic concepts of the Preisach approach and its microscopical physical interpretation will be first presented. Then, possibilities of describing piezoelectric nonlinearities through various contributing units distribution functions will be explored. Finally, comparison with experimental data and direct determination of the distribution functions will be treated. As the proposed description for piezoelectric nonlinearity is assumed to be applicable to a wide range of ferroelectrics, experimental data validating the Preisach approach will originate from various piezoelectric compositions.

4.1 HYSTERESIS AND PREISACH MODELING

Efforts toward the description of piezoelectric nonlinearities can be separated in two kinds of approaches: extrinsic mechanisms and thermodynamic descriptions. The former is focused on microscopic response description by taking into account extra contributions (e.g. domain walls motion). The latter usually consists in introducing some field dependence in the thermodynamical definition of the piezoelectric coefficient, often justified by anharmonic potential wells. The extrinsic approach is probably more general as it can handle mathematical expressions for the response which are non-analytical (e.g. special hysteretic mechanisms) whereas intrinsic descriptions will always yield analytical response expressions. Moreover, as extrinsic mechanisms do not interfere with the intrinsic response, they are hence compatible with any intrinsic approach.

4.1.1 Piezoelectric nonlinearity: between empirical and physical descriptions

Several approaches based on thermodynamic description of the piezoelectric coefficient field dependence have been proposed starting either from the free energy equation or from the constitutive piezoelectric equations and using polynomial expansions in terms of field, $\mathcal{F}$ [2-4], as in:

$$d = d_0 + a_1 \mathcal{F} + a_2 \mathcal{F}^2 + a_3 \mathcal{F}^3 + \ldots \tag{4.1}$$

where d and d_0 are respectively the nonlinear and the intrinsic piezoelectric coefficients, $\mathcal{F}$ is the amplitude of the applied field (mechanical or electric) and a_i are parameters. Perrin *et al.* [5] introduced empirically bias and amplitude dependences without extended thermodynamical considerations, obtaining the following expression:

$$d = d_0 (1 + a_{ac} \mathcal{F}_{ac} + a_{dc} \mathcal{F}_{dc}) \tag{4.2}$$

where $\mathcal{F}_{ac}$ and $\mathcal{F}_{dc}$ are the applied field amplitude and bias respectively. A field power-law [6, 7], inspired by a hypothetical critical phenomena description of domain wall depinning, was also put forward:

$$d = d_0 + a\,\mathcal{F}^{\phi} \tag{4.3}$$

with ϕ, a supposedly universal exponent situated around 1.2. All these approaches do not model actual microscopic mechanisms but rather postulate some hidden internal variables that will lead to the observed nonlinearities

Modeling of extrinsic microscopic features was used in ferroelectrics by Arlt and Dederichs [8] who modeled the damped vibration of a 90° domain wall in a quadratic potential well. Later, Li, Cao and Cross [9] extended this model to a phenomenological potential profile yielding a polynomial dependence of the piezoelectric response and linking piezoelectric nonlinearity with response hysteresis. Several microscopic models were also directly derived from ferromagnetics. A description of the dielectric coefficient nonlinearity [10] based on domain wall oscillation in a statistically described potential profile has been extrapolated from magnetics [11] to acceptor doped $BaTiO_3$ ceramics. Furthermore, dielectric and piezoelectric switching have been described using a 5-parameter model [12, 13] inspired from the Jiles-Atherton model [14] for ferromagnetic loops. Piezoelectric response hysteresis at subswitching fields has also been explored with tools originating from ferromagnetics. Damjanovic *et al.* [15-17] proposed a modeling of the piezoelectric charge response based on the Rayleigh magnetization description [18, 19] of non-linear ferromagnetics. It yields a linear field dependence of the piezoelectric coefficient which is in agreement with a wide part of the available experimental data:

$$d = d_0 + \alpha\,\mathcal{F} \tag{4.4}$$

where α, the nonlinear parameter, is often called the Rayleigh constant. Later, looking for a minimal piezoelectric loop description, Kugel *et al.* [20] extended the Rayleigh formulas by introducing field dependence for its main parameters.

$$d = d_0(\mathcal{F}) + \alpha(\mathcal{F})\,\mathcal{F} \tag{4.5}$$

Actually, a more rigorous extension of the Rayleigh model for ferromagnetics was proposed by Preisach [21] who considered a statistical approach to the magnetization nonlinearity. In any case, these Rayleigh-based piezoelectric models are the only ones to yield a satisfactory description of the typical piezoelectric response hysteresis along with acceptable experimental agreement for the piezoelectric coefficient field dependence. Thus, considering the phenomenological analogies observed between ferromagnetic and ferroelectric systems [16] and the valuable work already performed in the statistical description of dielectric response [10 22], the Preisach formalism is a promising candidate for the description of nonlinear and hysteretic response of piezoelectrics. Hence, we will first present in more details the current physical theories behind the Rayleigh description of hysteresis. Second, an appropriate implementation of these theories for the characterization of experimental piezoelectric nonlinearity will be developed.

4.1.2 The Preisach approach: collections of bistable units

The Preisach hysteresis description [21, 23, 24] was first developed as an extension of the empirical Rayleigh formulas [18]. Its application to piezoelectricity may significantly extend possibilities for description of the piezoelectric behavior in ferroelectrics while establishing the previously derived Rayleigh relations for piezoelectrics as a special case. This approach considers hysteretic systems as containing a collection of simple bistable units (e.g. domain walls in a pinning field) where each unit is characterized by two parameters: a bias (or internal) field ($\mathcal{F}_i$) and a coercive field ($\mathcal{F}_c$). Each state of the unit is assumed to contribute to the total response $\mathcal{R}$ by the same amount ± $\mathcal{R}_0$ (see Figure 4.1).

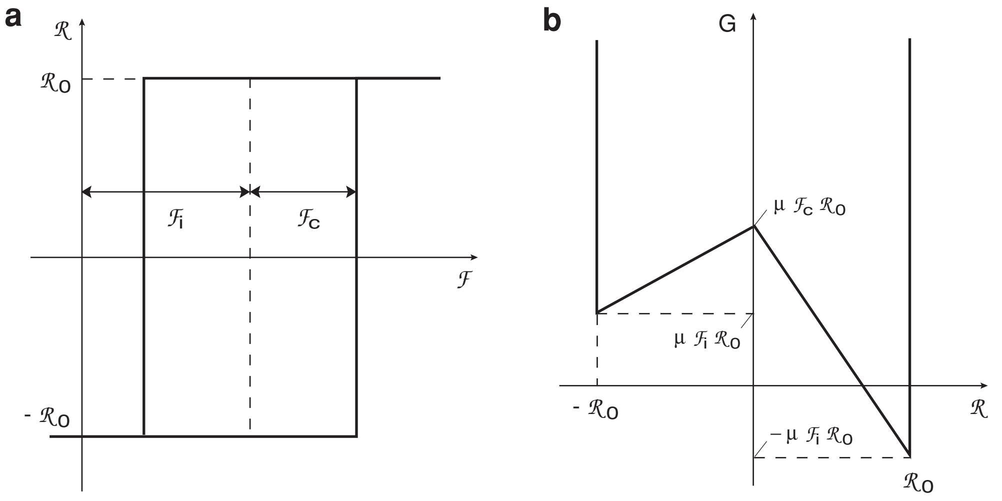

Figure 4.1: *Elementary bistable unit (from Ref. [24]) represented as square hysteresis (**a**) and as energy profile (**b**) (μ is a generalized susceptibility). Néel in his microscopic analysis of Rayleigh formulas considered domain walls trapped in energy profiles such as the (**b**) representation [19].*

The bias field can take any value from -∞ to +∞ while the coercive field is defined as positive. The half-plane of possible values for $\mathcal{F}_i$ and $\mathcal{F}_c$ is called the Preisach plane. In a given system, the bistable units exhibit a statistical distribution of these parameters which can be characterized by a distribution function f($\mathcal{F}_i$, $\mathcal{F}_c$) defining the number of bistable units between

$[\mathcal{F}_i; \mathcal{F}_i+d\mathcal{F}_i]$ and $[\mathcal{F}_c; \mathcal{F}_c+d\mathcal{F}_c]$ as $f(\mathcal{F}_i,\mathcal{F}_c)\,d\mathcal{F}_i d\mathcal{F}_c$. It obeys the following normalization condition:

$$\int_0^{\infty}\int_{-\infty}^{\infty} f(\mathcal{F}_i, \mathcal{F}_c)d\mathcal{F}_i d\mathcal{F}_c = 1 \tag{4.6}$$

Of course the Preisach description holds only for a definite class of hysteretic processes. It has been proven that the agreement of a given experimental hysteretic system with this formalism is verified if and only if it exhibits two basic properties [25] (apart from frequency independence, treated in time domain in Ref. [26]):

> *wiping-out property:* for a given field profile, the final state of the system depends only on the series of local extrema that are greater than any subsequent extremum, i.e. intermediate extrema between greater ones do not alter the final state of the system. This property can be recast into a form which is of higher practical interest: when a field alternating between two definite values is applied to the system, the generated loop will be closed for any arbitrary profile of the field having these two values as extrema. This property is called return point memory.
>
> *congruency property:* stationary hysteresis loops between two defined fields extrema are geometrically superimposable independently of the history of the system.

These properties are sometimes difficult to demonstrate and the scalar description might not be adapted to the expected response. However, Preisach-type descriptions were applied in numerous fields as varied as ferromagnetics [23], superconductors [27], spin glasses [28] and dielectrics [22, 29].

The Preisach formalism is implemented as follows: let us consider the Preisach plane for zero external field. It can be divided into three regions (cf. Figure 4.2):

> **a** – Region where $\mathcal{F}_i > \mathcal{F}_c$, hence a negative zero-field-state ($-\mathcal{R}_0$).
>
> **b** – Region where $\mathcal{F}_c > |\mathcal{F}_i|$, hence an indefinite zero-field-state depending on history.
>
> **c** – Region where $\mathcal{F}_i < -\mathcal{F}_c$, hence a positive zero-field-state ($\mathcal{R}_0$).

Once an external field, $\mathcal{F}$, is applied, its acts in the same way as a homogeneous biasing field. The b-region cone, $\mathcal{F}_i = \mathcal{F} \pm \mathcal{F}_c$, is thus moved upward or downward accordingly and units crossing the region-limits are, if necessary, switched to the stable state.

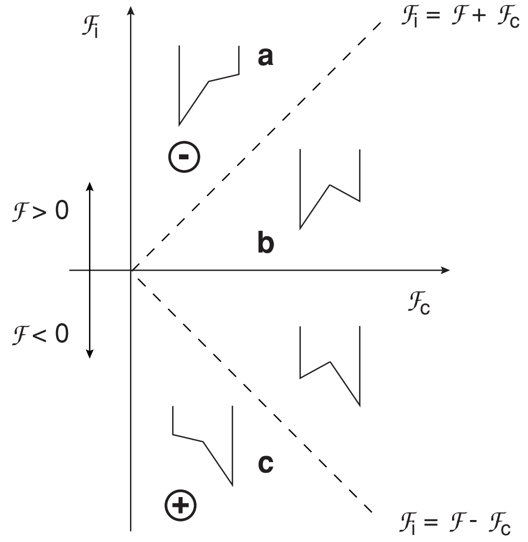

Figure 4.2: *State of the bistable units as a function of their position on the Preisach plane at zero applied field (from Ref. [24]).*

So, for increasing fields the cone is shifted up and all the bistable units where $\mathcal{F}_i + \mathcal{F}_c < \mathcal{F}$ are switched to a positive state and for decreasing fields the cone is shifted down and all the units where $\mathcal{F}_i - \mathcal{F}_c > \mathcal{F}$ are switched to a negative state contributing by $\pm 2\mathcal{R}_0$ to the total response. Clearly, this extrinsic contributions will depend on the number of switched units characterized by the distribution function, $f(\mathcal{F}_i, \mathcal{F}_c)$. The Rayleigh case corresponds to a uniform distribution function and associated extrinsic contributions only depend on the swept area of the Preisach plane.

The nonlinear part of the total response is calculated in the following way. For an alternating field (amplitude: $\mathcal{F}_0$ and offset: $\mathcal{F}_=$), the total nonlinear contributions are proportional to the integral of the distribution function over the large triangle defined by the vertices $(0; \mathcal{F}_= + \mathcal{F}_0)$, $(0; \mathcal{F}_= - \mathcal{F}_0)$ and $(\mathcal{F}_0; \mathcal{F}_=)$. The hysteresis equation can be obtained from the field-dependent integrals of the distribution function over the growing gray regions (as shown in Figure 4.3) taking into account the sign of the applied field derivative $\mathcal{F}$ (i.e. considering increasing or decreasing $\mathcal{F}$). In the case of a uniform distribution (Rayleigh case) nonlinear response contributions are proportional to the area of the large triangle $A = \mathcal{F}_0^2$ and a linear dependence for the piezoelectric coefficient ($d_{33} = \mathcal{R} / \mathcal{F}$) with respect to the amplitude of the applied field is thus obtained.

For arbitrary fields the nonlinear response can be obtained only when the state of the units situated in the metastable cone (b-region of Figure 4.2) is known. This is not the case when the initial state is obtained directly from a temperature-dependent phase transition. However, if the sample has been prepared by applying some known field profile $\mathcal{A}(t)$ after the appearance of the bistable units, the state line $b(\mathcal{F}_c)$ representing the field history of the sample can be defined up to maximum value of the applied field (see Figure 4.4). So, a fully determined state is obtained by applying an infinite (practically, large) field to the sample to permit the subsequent calculation of the contributing switched units. This preparation is often referred to as education.

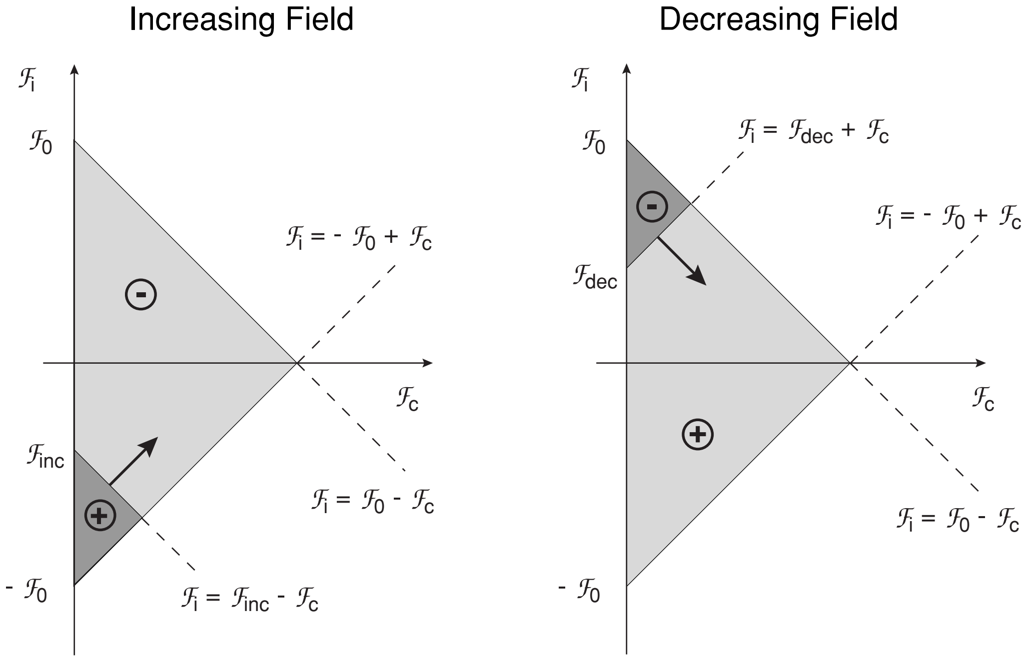

Figure 4.3: *Schematic view of the switched bistable units for an alternating external field without bias* ($\mathcal{F}_= = 0$). $\mathcal{F}_{inc}$ *and* $\mathcal{F}_{dec}$ *stand for respectively increasing and decreasing applied field ,* $\mathcal{F}$.

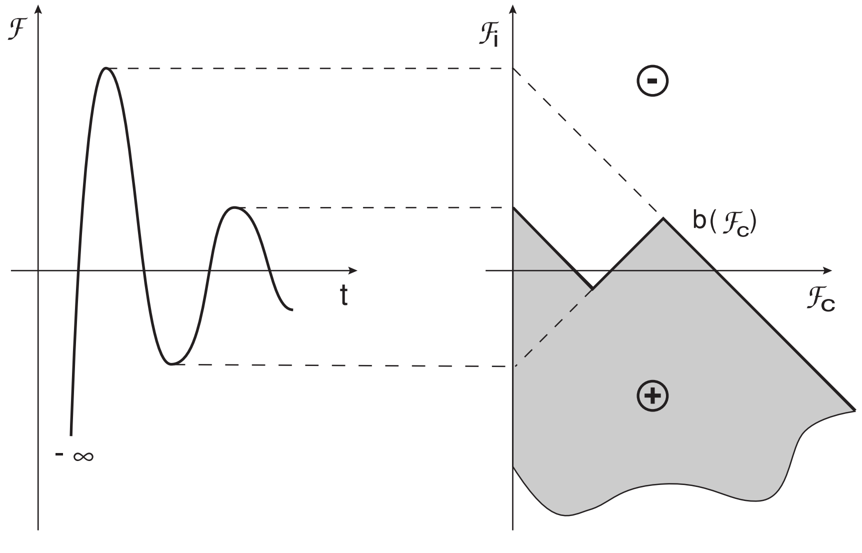

Figure 4.4: *Definition of the state line* $b(\mathcal{F}_c)$ *as a function of the field history since the application of a negative infinite field and subsequent series of local field extrema (from Ref. [24]).*

4.1.3 Microscopical interpretations: stochastic processes

Until recently, Preisach descriptions were regarded as purely formal, i.e. as long as the wiping-out and the congruency properties were experimentally verified, the description was considered as valid without any insight into the microscopical processes leading to the hysteretic behavior. The only hint of physical mechanism contained in Preisach approach was the presence somewhere in the system of the equivalent of a statistically distributed collection of bi-stable elements.

In the same spirit as statistical physics yielding a microscopical image of the classical thermodynamic theory, there has been efforts to determine physical mechanisms behind the Preisach behavior. The first contribution to such microscopic interpretations is due to Néel [19] who derived Rayleigh formulas by considering Bloch walls trapped in double wells (similar to those shown in Figure 4.1.b) with internal segments slopes ($\mu(\mathcal{F}_c - \mathcal{F}_i)$ and $\mu(\mathcal{F}_c + \mathcal{F}_i)$) uniformly distributed. Still, he had to neglect the contributions of domain walls trapped in energy profiles containing more than two metastable states. Recent works in ferromagnetics [30-32] have shown that if one considers pinning energy profiles, G_p, described by some defined stochastic processes (e.g. having zero single step average, $\langle dG_p \rangle = 0$, such as a Wiener-Lévy process) superimposed on a uniform parabolic potential (cf. Figure 4.5) then the average response of a pinned object presents the Preisach-required properties. This means that a single element trapped in a Wiener-Lévy (WL) random profile will, in average, contribute to the total response in agreement with the Preisach formalism [32]. Hence, there exists a distribution function over the Preisach plane that can describe the macroscopical (microscopical average) behavior of such a system [33].

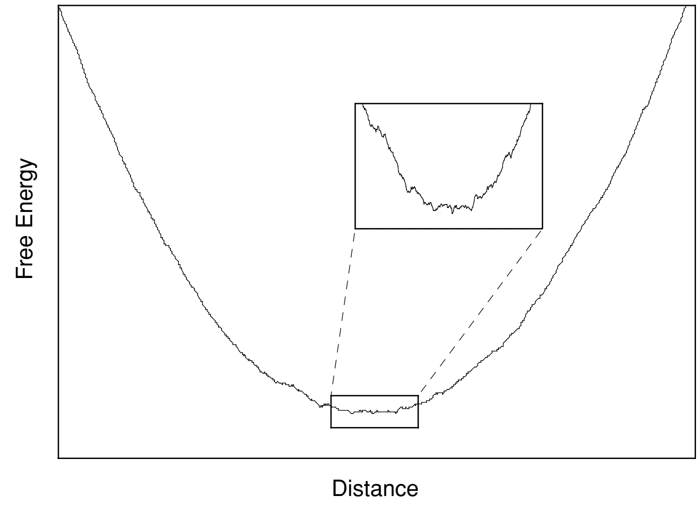

Figure 4.5: *Free energy profile combining a quadratic behavior with a random walk roughness.*

This result indeed bridges the description proposed in the Preisach formalism with physical microscopical features, like Barkhausen jumps [34] of domain walls in a random pinning field. Moreover, it extends the idea of distributed bistable elements to the well-known level-crossing-problem for a random walk process [32]. It also permits to extend Preisach's and Néel's restrictive concept of bistable units to the general idea of a domain wall moving in a well defined potential profile. However, the implementation of a single WL stochastic process in the Preisach formalism is problematic. To actually generate hysteresis from a stochastic pinning field, it has to be differentiable (to obtain a restoring force from the free-energy profile) and stationary (i.e. invariant with respect to translation, the equivalent of spatial homogeneity). As this is not the case for a simple WL process, Magni *et al.* [35] have extended it to a "three-layer" model consisting of a differentiable low scale profile, a WL medium scale, and an Ornstein-Uhlenbeck (OU) process large scale profile. The OU process is a generalized WL process exhibiting stationarity when the random parameter exceeds a certain parameter value. Hence, differentiability is insured by the flat low-scale behavior and OU process provides large-scale stationarity. With this type of complex energy profile compatible with the Preisach formalism, it was possible to successfully describe both Preisach and dynamic (e.g. response rate, $\partial\mathcal{R}/\partial t$, dependent) loops for ferromagnetic systems.

Finally, note that in the piezoelectric case, as stress and charge displacement are not conjugate work variables, the description of the actual pinning field is a complex question, we will nevertheless assume in the following similarity with ferromagnetics and consider that a single pinning energy profile is sufficient for piezoelectrics.

4.2 DISTRIBUTION FUNCTIONS AND PIEZOELECTRIC NONLINEARITY

The Preisach model theory presented in the previous section was based on the basic concept of bistable contributing units distributed in terms of bias and coercive fields. In the following, some expressions for this distribution function will be theoretically explored. First, a generalized MacLaurin series respecting the symmetry requirements will be derived and the associated extrinsic contributions to the piezoelectric coefficient will be calculated. Then, more specific shapes for the distribution function will be proposed in order to match the experimentally observed piezoelectric nonlinearities in high performance PNN-PZT and PZT.

4.2.1 Generalized distribution function

Turik [22, 29, 36] used the Preisach formalism analyzing dielectric nonlinear behavior of $BaTiO_3$. He treated $\mathcal{F}_i$ as an effective field applied on a given domain, created by surrounding domains and free charges in the ferroelectric, and $\mathcal{F}_c$ as the field at which polarization of the isolated domain switches, without considering long range electrostatic influence. With applied external electric field considered as homogeneous inside the ceramic, it is then possible to introduce a function of the statistical distribution of domains according to their coercive and internal fields f($\mathcal{F}_i$,$\mathcal{F}_c$). At weak fields (i.e. at small $\mathcal{F}_c$ and $\mathcal{F}_i$), f($\mathcal{F}_i$,$\mathcal{F}_c$) may be expanded in a MacLaurin series which is symmetrical with respect to $\mathcal{F}_i$ [22]:

$$f(\mathcal{F}_i, \mathcal{F}_c) = f_0 + g\mathcal{F}_c + h\mathcal{F}_c^2 + k\mathcal{F}_i^2 + \ldots \tag{4.7}$$

At high fields, Equation (4.7) may be considered as an approximation. In the case of ferroelectrics, the distribution function f($\mathcal{F}_i$,$\mathcal{F}_c$) may change with time at large fields (as depoling occurs, for example). Thus, one can usually determine f($\mathcal{F}_i$,$\mathcal{F}_c$) not in the initial state but at a settled state, which depends on the amplitude of the applied field. At weak fields, typically in the Rayleigh range (i.e. where f($\mathcal{F}_i$,$\mathcal{F}_c$) = f_0), such problems do not arise and f($\mathcal{F}_i$,$\mathcal{F}_c$) permits description of both initial and final states of the ceramic. Assuming that the distribution function described in Equation (4.7) is valid for the piezoelectric effect, it is possible to obtain expressions for the descending and ascending branches of the electromechanical hysteresis (with $\mathcal{R}_0$ taken either as spontaneous strain or polarization and $\mathcal{F}$ respectively as electric or mechanical field depending on the piezoelectric effect considered).

Considering domain wall contributions in the case of a bias field ($\mathcal{F}_=$) and an alternating field (with amplitude $\mathcal{F}_0$) simultaneously applied on a ferroelectric ceramic along the direction of remnant polarization, the region of the Preisach plane within which reorientation of 90° domains causes irreversible contributions to the piezoelectric coefficient has a triangular shape as shown in Figure 4.6, this region is called the “working range”. An increase in $\mathcal{F}_0$ leads to an area increase of the “working range”, which causes monotonous increase in contributions of domain switching to the piezoelectric coefficient.

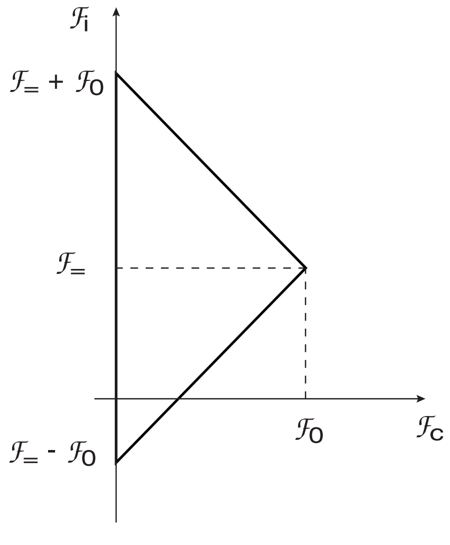

Figure 4.6: *Portion of the Preisach plane reoriented by a field of amplitude* $\mathcal{F}_0$ *and offset* $\mathcal{F}_=$.

To reduce the problem to the scalar form of the Preisach formalism, we assume that 2/3 of the total number of domains can switch in the direction of the applied field (the equivalent of 90° domain wall movement). Then, according to Figure 4.6, the following expressions for the increasing ($\mathcal{R}^+$) and decreasing ($\mathcal{R}^-$) branches of the electro-mechanical hysteresis can be derived (see above and Ref. [22, 37]) using the totally switched down state as reference:

$$\mathcal{R}^-(\mathcal{F}) = \mathcal{R}_m - \frac{4\mathcal{R}_0}{3}\int_0^{\frac{1}{2}(\mathcal{F}_= + \mathcal{F}_0 - \mathcal{F})}\int_{\mathcal{F} + \mathcal{F}_c}^{\mathcal{F}_= + \mathcal{F}_0 - \mathcal{F}_c} f(\mathcal{F}_i, \mathcal{F}_c)d\mathcal{F}_i d\mathcal{F}_c \qquad (4.8)$$

$$\mathcal{R}^+(\mathcal{F}) = \frac{4\mathcal{R}_0}{3}\int_0^{\frac{1}{2}(-\mathcal{F}_= + \mathcal{F}_0 + \mathcal{F})}\int_{\mathcal{F}_= - \mathcal{F}_0 + \mathcal{F}_c}^{\mathcal{F} - \mathcal{F}_c} f(\mathcal{F}_i, \mathcal{F}_c)d\mathcal{F}_i d\mathcal{F}_c \qquad (4.9)$$

$$\text{with } \mathcal{R}_m = \frac{4\mathcal{R}_0}{3}\int_0^{\mathcal{F}_0}\int_{\mathcal{F}_= - \mathcal{F}_0 + \mathcal{F}_c}^{\mathcal{F}_= + \mathcal{F}_0 - \mathcal{F}_c} f(\mathcal{F}_i, \mathcal{F}_c)d\mathcal{F}_i d\mathcal{F}_c \qquad (4.10)$$

$\mathcal{R}_m$ corresponds to the total nonlinear contributions depending on the amplitude of the alternating pressure $\mathcal{F}_0$ applied simultaneously with the constant bias stress $\mathcal{F}_=$ .With the help of Equations (4.8)-(4.10), it is possible to determine the equation of the final hysteresis corresponding to the distribution function $f(\mathcal{F}_i, \mathcal{F}_c)$. Such a loop has been calculated for a uniform distribution, $f(\mathcal{F}_i, \mathcal{F}_c) = f_0$ (Rayleigh case) and is presented in Figure 4.7.

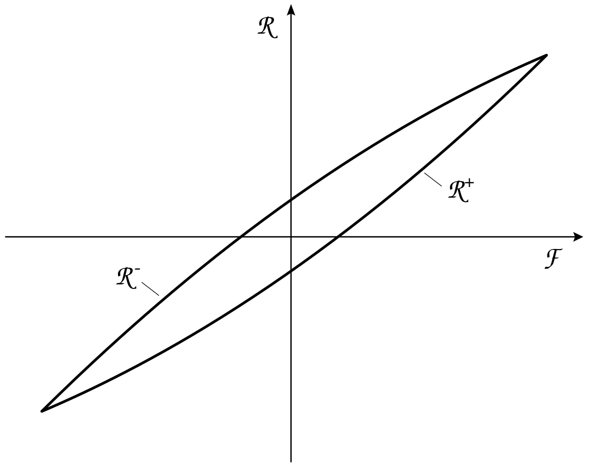

Figure 4.7: *Calculated loop from Equations (4.8)-(4.10) using a uniform distribution function,* $f(\mathcal{F}_i, \mathcal{F}_c) = f_0$ *(Rayleigh case).*

For the expanded distribution function $f(\mathcal{F}_i, \mathcal{F}_c)$ of Equation (4.7), $\mathcal{R}_m$ is given by:

$$\mathcal{R}_m = \frac{4\,\mathcal{R}_0}{3}\,\mathcal{F}_0^2\left(f_0 + \frac{g}{3}\,\mathcal{F}_0 + \frac{1}{6}(h+k)\,\mathcal{F}_0^2 + k\,\mathcal{F}_=^2 + \ldots\right) \tag{4.11}$$

which finally corresponds to the following contribution to the piezoelectric coefficient:

$$\begin{aligned}\Delta d_{33}\,(\mathcal{F}_0, \mathcal{F}_=) &= \frac{\mathcal{R}_m}{2\,\mathcal{F}_0} \\ &= \frac{2\mathcal{R}_0}{3}\,\mathcal{F}_0\left(f_0 + \frac{g}{3}\,\mathcal{F}_0 + \frac{1}{6}(h+k)\,\mathcal{F}_0^2 + k\,\mathcal{F}_=^2 + \ldots\right)\end{aligned} \tag{4.12}$$

This last expression permits to describe the behavior of the piezoelectric coefficient nonlinearity in the case of a general analytical distribution function. It will be compared to experimental results in section 4.3.3. As polynomials can be integrated in all cases, any piezoelectric behavior can be described by such a function provided it contains enough terms. For instance, assuming that the distribution of bistable units follows a Gaussian law which cannot be explicitly integrated over the Preisach plane, then the appropriate expression for the distribution function will be a compromise between the number of parameters needed and the mathematical simplicity of the final piezoelectric nonlinear expressions. In this perspective, more specific functions will be proposed in the next section in order to account for more "intuitive" distribution topographies and actual piezoelectric nonlinearities.

4.2.2 Specific distribution functions

The observed piezoelectric nonlinearities can usually be described through a two or three parameter function (see e.g. Refs. [5, 7, 16]). Hence, if the Preisach description holds for such systems, the associated distribution function may not have more than 2 or 3 parameters to be fully determined by the experimental results. In order to reduce the number of parameters in Equation (4.12), Equation (4.7) can be simplified to the following quadratic form describing an ellipsoid:

$$f(\mathcal{F}_i, \mathcal{F}_c) = f_0 + h\,\mathcal{F}_c^2 + k\,\mathcal{F}_i^2 \tag{4.13}$$

with f_0 positive and h, k negative. The corresponding distribution is illustrated in Figure 4.8.

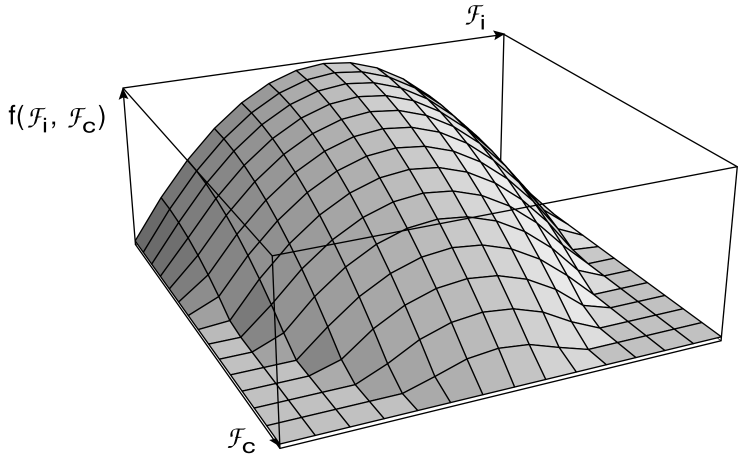

Figure 4.8: *Ellipsoidal distribution function based on Equation (4.13). The maximum of this distribution is situated at the Preisach plane origin.*

From Equation (4.12), its piezoelectric coefficient nonlinearity is given by (when considering an alternative field of amplitude $\mathcal{F}_0$):

$$\Delta d_{33} \propto f_0 \mathcal{F}_0 + \frac{1}{6}(h+k) \mathcal{F}_0^3 \tag{4.14}$$

Unfortunately, such a linear-cubic dependence is not observed in actual measurements (see Figure 1.9). Actually, second order dependences are the common case in high performance piezoelectrics (cf. Ref. [38] and section 4.3), as expressed by:

$$d_{33} = d_0 + \alpha \mathcal{F}_0 + \beta \mathcal{F}_0^2 \tag{4.15}$$

where d_0 represents the reversible and intrinsic contributions; α and β are the Rayleigh and quadratic nonlinear coefficients. Equation (4.12) reveals that such a quadratic dependence can be obtained from Equation (4.7) by considering a linear dependence in coercive field ($g \neq 0$) alone. However, such a distribution cannot be normalized as its value at $\mathcal{F}_i = \infty$ is different from zero. If one is looking for a global distribution function, it has to contain an $\mathcal{F}_i$ term. From Equation (4.12), it is clear that a cubic dependence will appear as soon as any analytical even powered internal field term is added to the distribution function. Therefore, an expression containing non-analytical terms should be introduced to account for the experiments. A linear dependence on $\mathcal{F}_i$ for the distribution function may be proposed in order to eliminate the cubic term in Equation (4.14). It yields a conical distribution (as displayed in Figure 4.9) expressed by:

$$f(\mathcal{F}_i, \mathcal{F}_c) = f_0 - \sqrt{h\mathcal{F}_c^2 + k\mathcal{F}_i^2}\ , \tag{4.16}$$

with f_0, h and k positive. Note that such a distribution is not the result of a MacLaurin expansion of the global distribution function, but nevertheless satisfies the requested $\mathcal{F}_i$ symmetry.

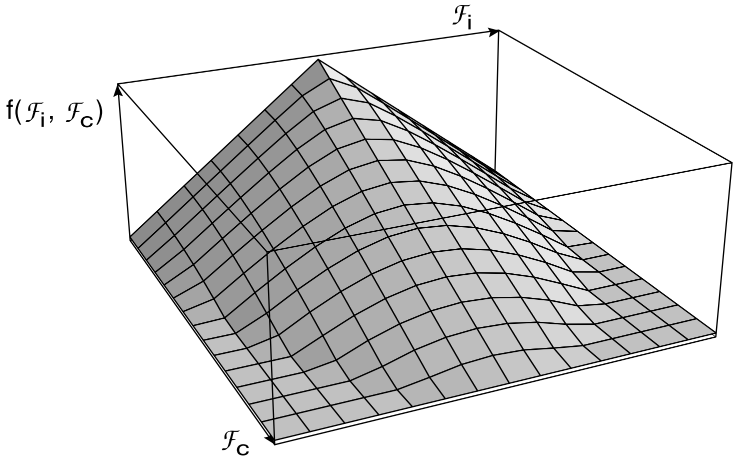

Figure 4.9: *Conical distribution function based on Equation (4.16). The maximum of this distribution is situated at the Preisach plane origin.*

Integrating for an alternative field of amplitude $\mathcal{F}_0$, the extrinsic contributions to the piezoelectric coefficient are then given by:

$$\Delta d_{33} \propto u(\ln \mathcal{F}_0, f_0, h, k)\, \mathcal{F}_0 + v(\ln \mathcal{F}_0, f_0, h, k)\, \mathcal{F}_0^2 \tag{4.17}$$

where u and v are intricate functions of f_0, h, k and ln $\mathcal{F}_0$. The field dependence of the obtained piezoelectric nonlinearity is almost of the second order type as no cubic field term appears. However, the logarithm of the applied field intervenes in both u and v functions which is not confirmed by the experimental data. A simplified version of the conical distribution presenting a roof-like topography (as shown in Figure 4.10) may hence be put forward. Such a distribution is represented by the following non-analytical expression:

$$f(\mathcal{F}_i, \mathcal{F}_c) = f_0 + g\,\mathcal{F}_c + k\,\mathrm{Abs}(\mathcal{F}_i) \qquad (4.18)$$

where f_0 is positive and g, k are negative. Such a distribution present a sharp edge at $\mathcal{F}_i = 0$ which is certainly not physical. Its domain of application is thus limited to the cases where the working range is sufficiently wide to neglect these border effects.

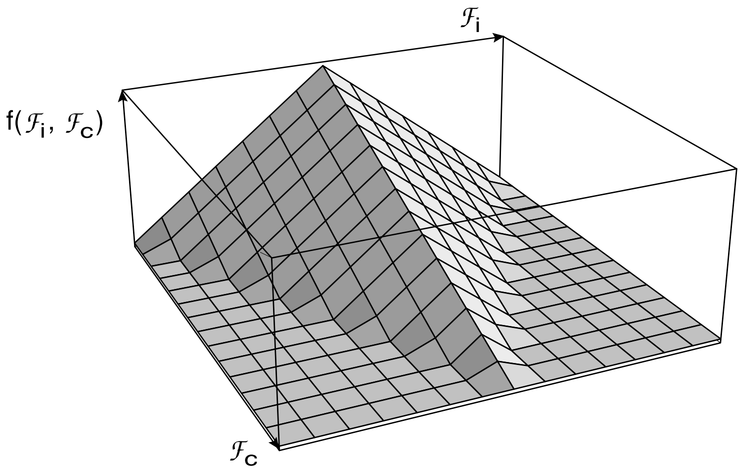

Figure 4.10: *Roof-like distribution function based on Equation (4.18). The maximum of this distribution is situated at the Preisach plane origin. Intersections of the distribution function with $\mathcal{F}_i$ and $\mathcal{F}_c$ axis correspond to $\pm f_0/k$ and $-f_0/g$ respectively.*

After integration for an alternating field, this roof-like distribution yields the following field dependence for the extrinsic contributions:

$$\Delta d_{33} \propto f_0\,\mathcal{F}_0 + \frac{1}{3}(g + k)\,\mathcal{F}_0^2 \qquad (4.19)$$

In this case, the extrinsic contributions are in agreement with the observed field dependence of the piezoelectric coefficient (see Equation (4.15)). Hence, the global profile of the distribution function for piezoelectrics behaving in such a quadratic behavior is pyramid-like. Moreover, it demonstrates that a purely analytical approach, like in section 4.2.1, may exhibit some shortcomings for a simple description of the piezoelectric non-linearity.

Thus, it has been shown above that the Preisach distribution functions can be explored “inductively”, i.e. by proposing sound topographies for the bistable units distribution and comparing the associated contributions to the piezoelectric coefficient with the general experimental data. Using this method, a non-analytical roof-like distribution exhibiting linear dependence on internal and bias fields was determined to best describe the usual quadratic piezoelectric nonlinearity observed in high performance piezoelectrics.

4.3 VALIDATION OF THE PREISACH APPROACH FOR PIEZOELECTRICS

In the preceding section, theoretical examples of piezoelectric nonlinearities calculations were presented. The purpose of this section is to validate the application of the Preisach approach to actual direct piezoelectric measurements. Hence, the generalized field, $\mathcal{F}$ will be replaced the stress, σ, and the generalized response, $\mathcal{R}$, by the charge displacement, D. First, arguments validating the two necessary Preisach properties (wiping-out and congruency) will be presented. Second, the generalized expression of Equation (4.12) for piezoelectric coefficient nonlinearity will be shown to be qualitatively applicable to most of the observed piezoelectric coefficient behaviors. Finally, the issue of the experimental determination of the distribution function will be treated in detail and the applicability of the proposed roof-like distribution will be examined in the light of bias field dependence of the piezoelectric coefficient.

4.3.1 Experimental

The direct piezoelectric measurements presented below were performed as follows. The tested sample, a piezoelectric actuator and a quartz force sensor were placed in mechanical series in a press allowing to apply a compressive bias stress on the whole. Then, using a signal generator (HP 3245A or Fluke PM5136) and an amplifier (PI P-268), a biased sinusoidal signal was applied on the piezoelectric actuator. The actuator being clamped by the bias stress, a resulting sinusoidal force is thus applied on the piezoelectric sample. The responses of both the force sensor and the sample are collected using two charge amplifiers (Kistler 5011) and acquired by a computer through a digital oscilloscope (Tektronix TDS 410). The amplitude of the applied stress can be varied by changing the amplitude of the signal applied on the actuator and the actual bias stress applied on the sample is given by the sum of the compressing stress applied initially to the mechanical chain and the stress corresponding to the bias of the actuator applied signal. Thus, if amplitude and bias of the actuator exciting signal are controlled separately, variations of bias and amplitude can be obtained independently.

The measurements were performed at low frequency (1 Hz) well below the press mechanical resonance (≈ 1 kHz). As the compressive stress causes depoling, the sample is submitted to high bias and amplitude stress for one hour before each measurement, in order to stabilize the poling level and the internal domain structure. Note also that the actuator itself is nonlinear which prevents any true harmonic study of sample response because of harmonic coupling effects. However, when the sample charge signal is considered as a function of the force measured by the quartz force sensor, the actuator nonlinearities cancel out.

Of course, direct measurements are performed in compression only, hence the working range is different from a purely alternative field (e.g. Figure 4.3) as illustrated in Figure 4.11.

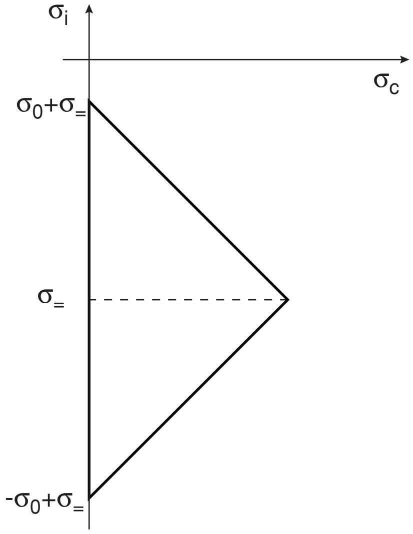

Figure 4.11: *Schematic view of the switched units for the direct piezoelectric characterization technique presented in this section.* σ_i *and* σ_c *represent the internal and coercive stresses of the units respectively.* σ_0 *and* $\sigma_=$ *are the characteristics of the stress applied on the sample* ($\sigma = \sigma_0 \sin(\omega t) + \sigma_=$).

Thus, only a half of the Preisach plane is actually probed in this type of measurements. However, symmetry implies a symmetrical distribution with respect to internal field and hence the knowledge of one half of the plane is sufficient.

Moreover, in the piezoelectric case, any poling level change of polycrystalline sample causes a strong variation of the averaged intrinsic response. For instance, the initial depoling of the piezoelectric samples may induce up to 20% decrease in the total piezoelectric coefficient (especially in the very soft PNN-PZT compositions). Hence, the Preisach model cannot be verified for piezoelectricity if there is a marked change either in the poling level or in the domain wall density during experiment. This limits the domain of validity of such an approach to the low field amplitudes.

4.3.2 Wiping-out and congruency

It has been demonstrated that if wiping-out (or return point memory) and congruency are exhibited by an hysteretic system, then there exists a distribution function characterizing the considered system in the Preisach formalism [25]. Hence, a natural starting point for the experimental investigation of the piezoelectric hysteresis using the Preisach approach is the verification of these two properties in some practical cases. Of course, the experimental verification of these properties will never be rigorous in the sense that no experimental data is general enough for a strict validation. It can be noted that some arguments for the experimental confirmation of these two properties in ferroelectrics have already been presented for dielectric loops of $SrBi_2Ta_2O_9$ [39]. There, return point memory was presented as a "physical" property of the subswitching dielectric loops and congruency was proven for poled and unpoled dielectric loops. Moreover, a study on piezoelectric actuators control based on the Preisach approach showed that wiping-out was verified [40]. However, congruency was not observed in the considered actuator [41], maybe because dynamic effects were neglected. In fact, the piezoelectric loops are not frequency independent and, hence, the verification of the congruency has to be performed for a given signal type and frequency (in our case a sinusoidal stress at 1 Hz).

Wiping-out property states that a sequence of intermediate field maxima is erased by the application of a larger field. This property can be verified by the equivalence of piezoelectric coefficients measured for increasing and decreasing stress amplitudes. In the decreasing case, there are no intermediate maxima as the previous fields were all higher than the considered one. For increasing amplitudes, there are intermediate maxima corresponding to the previous measurement amplitudes which have to be wiped out by the following. Hence, if the piezoelectric coefficients, d_{33} are equivalent for the two directions of measurement, the wiping-out property is demonstrated. This effect is shown in Figure 4.12 for a 50PNN-13PZ-37PT sample poled at 80°C during 15 min with a field of 20 kV/cm and measured twice upon both increasing and decreasing stress amplitudes, σ_0.

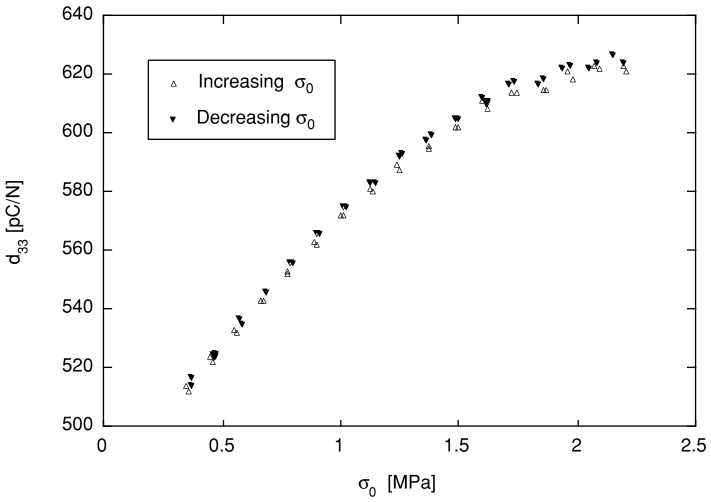

Figure 4.12: *Piezoelectric coefficient, d_{33} dependence on stress amplitude, σ_0 for measurements made with increasing and decreasing field amplitude on a 50PNN-13PZ-37PT sample.*

Piezoelectric coefficients for both directions of measurement are well aligned along the same curve. However, it cannot be said that they are exactly superimposing as measurements performed upon increasing σ_0 are standing slightly below the ones obtained for decreasing σ_0 (experimental drift can be ruled out as measurements were interleaved). Still, the relative differences are lower than 0.5 %, allowing the wiping-out property to be assumed in practice.

The congruency property stating that the shapes of loops measured between the same field extrema are identical independently of the field history is more difficult to demonstrate than wiping-out as the state of the piezoelectric switching units cannot be changed as drastically as in ferromagnetics because of depoling and domain wall density changes issues. Considering again how measurements are performed at low fields, it can be noted that each stress amplitude change intervenes at a random time, as the computer sends a change of amplitude command to the signal generator at an undetermined time relatively to the phase of the generated signal. Hence, for decreasing stress amplitude measurements, the state-line of the sample is different if the loops are measured between the same stress extrema for two distinct measurements as illustrated in Figure 4.13.

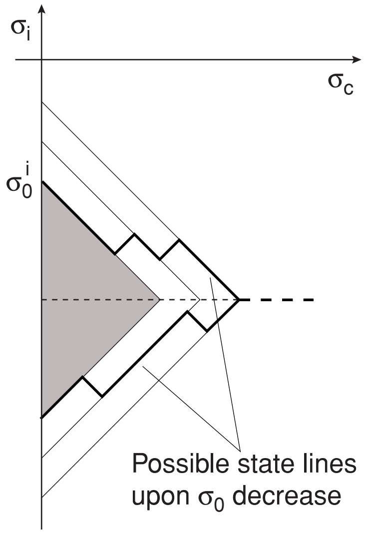

Figure 4.13: *Different state lines for a decreasing stress amplitude measurement. The grey triangle corresponds to the tested stress amplitude.*

Furthermore, when loops are extracted from decreasing and increasing stress amplitude measurements, their state lines are certainly different as the one corresponding to the increasing stress amplitude measurement depends only on the education procedure (see Figure 4.4). Hence, if loops of different decreasing and increasing stress amplitude measurements can be superimposed, the congruency property is satisfactorily verified. The case illustrated in Figure 4.14 for the same composition as before (50PNN-13PZ-37PT) consists in three different loops corresponding to the same stress extrema (i.e. 4.47 and

1.77 MPa in compression) but obtained in different conditions. Two loops were obtained in two distinct decreasing σ_0 measurements and the third one comes from an increasing σ_0 characterization. Congruency of the three distinct piezoelectric loops is obvious, thus this second property is demonstrated within the experimental uncertainty.

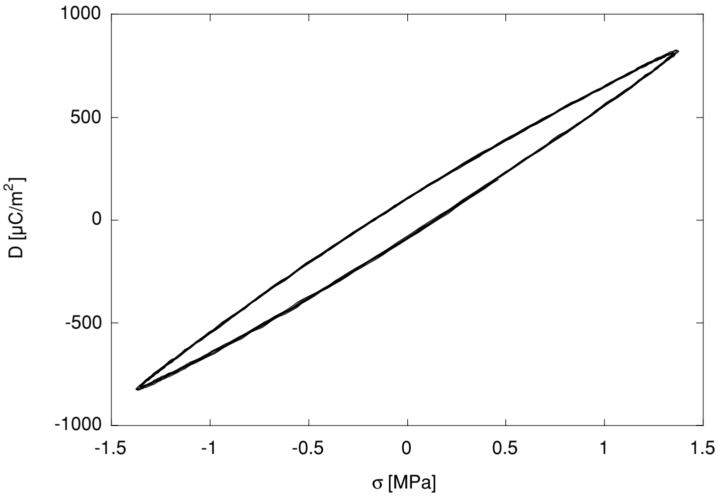

Figure 4.14: *Piezoelectric loops obtained from two distinct decreasing amplitude measurements and one increasing amplitude measurement on a 50PNN-13PZ-37PT sample. The loops correspond to 1.35 MPa stress amplitude superimposed on a 3.12 MPa compressive stress bias (the stress label presents the value of the oscillating stress only, the actual stress value corresponds to* σ *- 3.12 MPa).*

In conclusion, the two necessary properties for the Preisach approach are satisfied for a typical PNN-PZT composition in the usual range of applied stresses. As this constitutes only a limited experimental verification, it cannot be concluded definitely that Preisach modeling applies to piezoelectric subswitching properties in general. Nevertheless, we will assume so in the following discussion.

4.3.3 Description of experimental d_{33} nonlinearities

In this section, various typical experimental examples of direct piezoelectric nonlinearities will be examined and explained in terms of the formalism developed in the section 4.2.1 for the generalized distribution function, using specifically Equations (4.7) and (4.12). To show the clearest examples of typical piezoelectric nonlinearities, some results for lead-free materials are presented and references to similar behaviors in lead-containing materials are given in text. Note that for direct piezoelectric measurements the sample is always in compression and hence the applied bias stress $\sigma_=$ is always greater than the applied amplitude σ_0, the swept area is thus situated in one quadrant only of the Preisach plane (as shown in Figure 4.6).

Piezoelectric coefficient field amplitude dependence, $d_{33}(\sigma_0)$ manifests itself qualitatively differently for piezoelectrics with different ease of domain wall motion. Various types of dependences are illustrated in Figure 4.15.

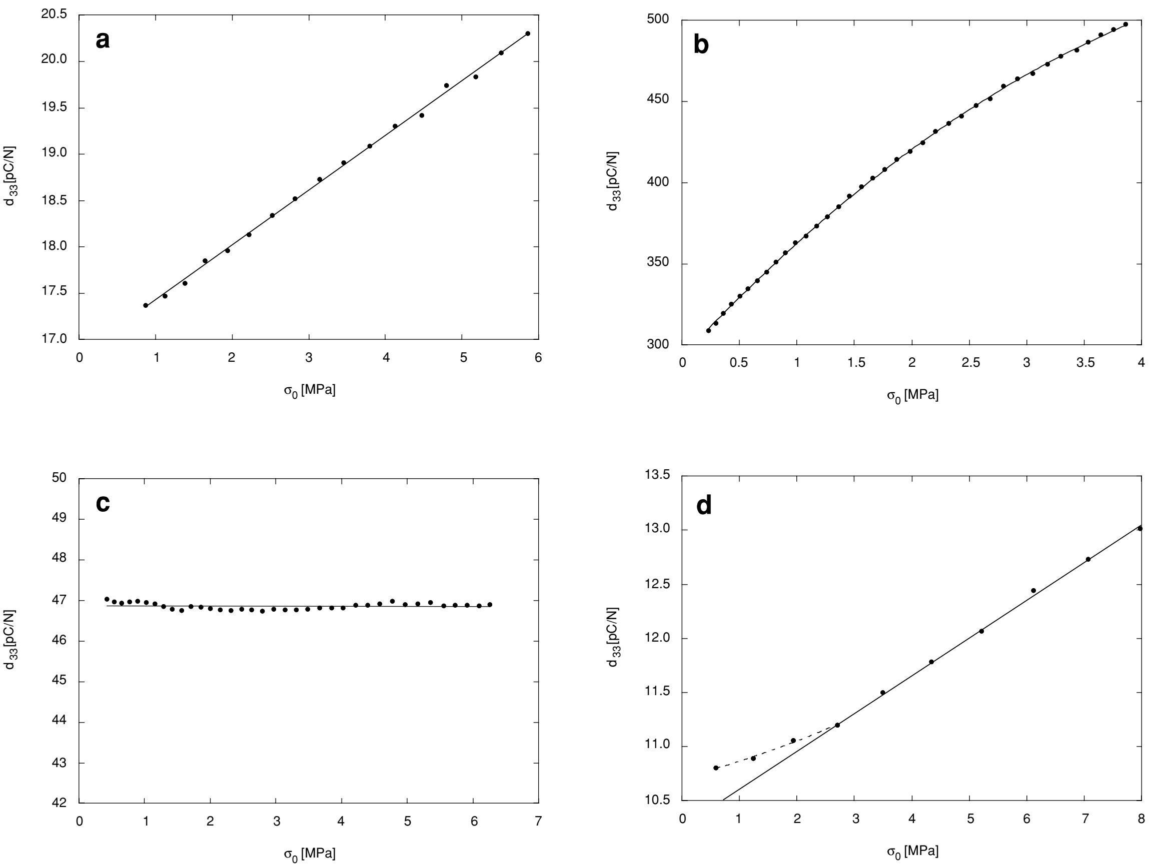

Figure 4.15: *Various types of piezoelectric coefficient,* d_{33} *dependence on amplitude of applied stress,* σ_0*, (**a**) Nb-doped* $Bi_4Ti_3O_{12}$*, (**b**)* $Pb(Zr_{0.53},Ti_{0.47})O_3$*, (**c**) Sm doped* $PbTiO_3$ *and (**d**)* $0.95Bi_4Ti_3O_{12}$*-*$0.05Bi_3TiO_9$*. Fitted curves on experimental data points are displayed as solid lines, the dotted line in (**d**) is drawn to guide the eye along the data points.*

In the first approximation, the distribution of domains with respect to σ_c and σ_i may be considered as uniform i.e. in the "working range", $f(\sigma_i, \sigma_c) \cong f_0$. Hence, no noticeable deviation of $d_{33}(\sigma_0)$ from the linear dependence would be observed. This is yields the Rayleigh law valid in the case of small stress amplitudes in PZT [16] or for materials containing very homogeneously distributed defects, as shown for $Bi_4Ti_3O_{12}$ in Figure 4.15.a.

For high performance materials, the defects are usually not uniformly distributed. In general σ_c and σ_i are small, i.e. the switching units are concentrated near the origin of the

Preisach coordinate system. As σ_0 increases, regions with different distribution densities are involved in the reorientation process. The associated distribution function is then given by:

$$f(\sigma_i, \sigma_c) = f_0 + g\sigma_c + \ldots < f_0 \quad (g < 0) \tag{4.20}$$

leading to a decrease in the rate of increase of d_{33} with σ_0, $\partial d_{33}/\partial \sigma_0$. Piezoelectric coefficient dependence thus becomes nonlinear, deviating more and more from the Rayleigh law, as illustrated in Figure 4.15.b for lead zirconate titanate at the MPB. Note that if the distribution function is precisely given by Equation (4.20) a quadratic dependence of the piezoelectric coefficient is expected from Equation (4.12), and indeed the fitted second order polynomial in Figure 4.15.b shows a strong agreement (regression coefficient > 0.9999) with the experimental data. However, as seen in section 4.2.2 for roof-like distribution, Equation (4.20) can only be a local description of the total distribution function as it cannot be normalized.

This deviation from the linear dependence of $d_{33}(\sigma_0)$ can even yield a quasi-saturation of the nonlinear contribution (see Figure 4.16) as the working range reaches Preisach plane regions where the number of units goes to zero. This saturation can be reached in both very soft materials where most of the domains are situated close to the origin of the Preisach plane and in hard materials where very few domains may be mobile with the exception of some units close to the origin (case illustrated in Figure 4.16 for a tetragonal PZT).

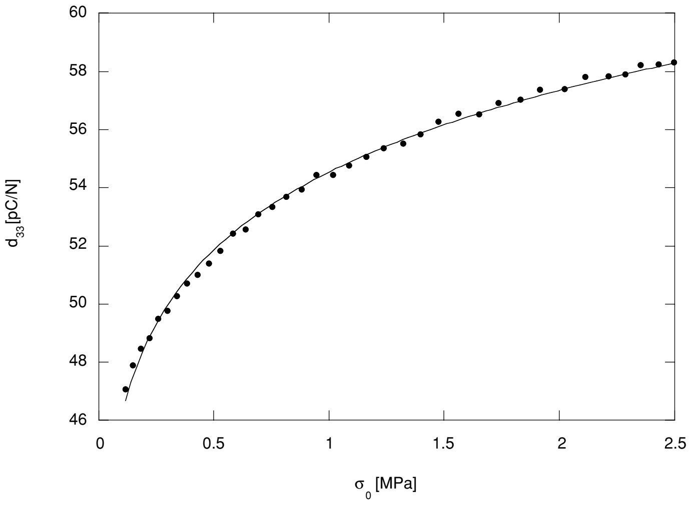

Figure 4.16: *Piezoelectric coefficient d_{33} dependence on amplitude of applied stress, σ_0, for a 40/60 PZT with a bias stress of 2.45 MPa.*

Some very hard ceramics may also be characterized with an almost complete absence of mobile domains in the region of small σ_c and σ_i. This leads to the absence or to very weak

$d_{33}(\sigma_0)$ dependence as shown in Figure 4.15.c for samarium doped lead titanate.

Threshold field i.e. the independence of d_{33} on σ_0 at small σ_0 can also be interpreted in the Preisach formalism as a depletion of moving domain walls close to a $(0; \sigma_=)$ point of the Preisach plane leading to no extrinsic contributions at low σ_0. The threshold field can then be seen as the stress corresponding to mobile domain walls having σ_c or σ_i close to the value of the applied field. In this case the distribution function may look like:

$$f(\sigma_i, \sigma_c) \cong g\sigma_c + \ldots \quad (g > 0) \tag{4.21}$$

and the obtained $d_{33}(\sigma_0)$ dependence would be close to what is displayed in Figure 4.15.d for $0.95Bi_4Ti_3O_{12}$-$0.05Bi_3TiO_9$. In PZT ceramics, where the region of d_{33} independent of σ_0 is not observed, the region containing no mobile domain walls may be too "small" to be reached experimentally or not exist at all. However, threshold fields are observed in PZT transverse piezoelectric coefficients [6]. Clearly, a threshold field accompanied by a subsequent quadratic behavior of the piezoelectric coefficient would require more terms in the expansion of Equation (4.7).

The developed Preisach formalism can also be applied to the investigation of piezoelectric coefficient dependence on bias stress $d_{33}(\sigma_=)$, as the triangular working range in Figure 4.6 displaces to the region of larger internal stresses σ_i as $\sigma_=$ increases. A typical bias stress dependence of the piezoelectric nonlinear behavior in tetragonal PZT is shown in Figure 4.17.

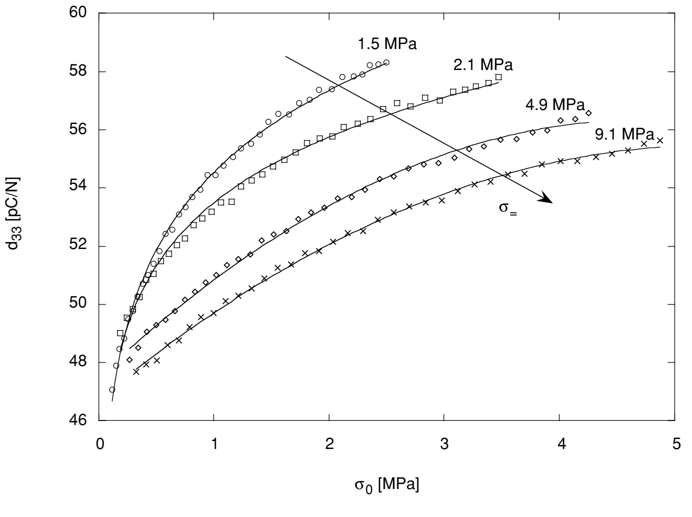

Figure 4.17: *Bias stress, $\sigma_=$ dependence of the non-linear behavior of the piezoelectric coefficient, d_{33}, for a 40/60 PZT. Note that there is no depoling of the sample as $\sigma_=$ is changed, as measurements were performed with decreasing $\sigma_=$.*

For a qualitative interpretation of results presented in Figure 4.17 for $d_{33}(\sigma_=)$ dependence, it is sufficient to assume that in Equations (4.12) coefficient $k < 0$, i.e. that the Preisach units density decreases as $\sigma_=$ increases. This means that an increase in $\sigma_=$ displaces the working range in regions of the Preisach plane where there are less switchable units per swept area. In such a case, stress amplitude dependence $d_{33}(\sigma_0)$ is preserved, and relative decrease of d_{33} with $\sigma_=$ is proportional to σ_0. The results exhibited in Figure 4.17 show indeed this decrease of nonlinear contributions with increasing bias stress. However, the comparison of the theoretical analysis results (in Equations (4.7) and (4.12)) with experimental data (Figure 4.17) shows that, for a quantitative description of the experiments (especially the saturating behavior at low bias stress) an increase in the number of terms in the expansion $f(\sigma_i, \sigma_c)$ is necessary . This point will be treated in more details in the next section.

In summary, the results of a generalized form of the distribution function were qualitatively compared to actual piezoelectric nonlinearity data and shown to be compatible with a wide range of experimental behaviors such as high performance lead zirconate titanate, hysteretic bismuth titanate and fully linear lead titanate. The versatility of the Preisach-based nonlinear piezoelectric description is thus qualitatively demonstrated.

4.3.4 Experimental determination of distribution functions

In the previous section, it was shown that a formal generalized distribution function is sufficient to describe qualitatively the usual piezoelectric coefficient nonlinearities. However, a direct experimental determination of the distribution functions would be of great practical interest. As the Preisach distribution is a two-variable function, it necessitates a two dimensional mapping of the Preisach plane to be characterized completely. Efficient algorithms based on the Preisach approach for the displacement control of a piezoelectric actuator [40, 41] were already reported. They are based on the Everett functions [42] describing the integral values of the distribution function over some defined domains of the Preisach plane which can be experimentally obtained from minor loops (i.e. situated inside the operating range of the considered actuator). However, such Everett functions do not lead to actual distribution shapes which may yield interesting hints toward the actual defect structure of the considered material. Hence, a new easy-to-implement method of determination of the distribution function will be presented in the following. This will demonstrate some of the limitations of the roof-like distribution proposed in section 4.2.2. Hence, an extension to this basic distribution function will be then proposed in order to match the experimental results.

The distribution function can be probed along the internal stress axis by a variation of the applied field bias, $\sigma^{\mathrm{i}}_=$, with very low amplitudes, as shown in Figure 4.18. Thus, if the distribution can be approximated by a constant in the small triangular regions, linear stress amplitude dependences for the piezoelectric coefficient will be obtained which slopes will be proportional to the number of bistable units in this region. Hence, varying the bias stress, one can determine the shape of the distribution function along the σ_i axis.

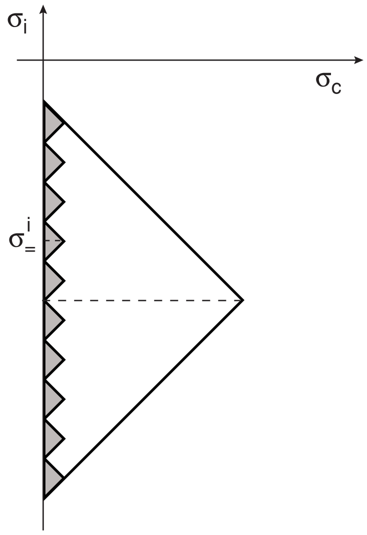

Figure 4.18: *Principle of distribution function characterization along the internal field axis.*

Such measurements were performed on a rhombohedral 60/40 PZT composition poled at 80°C as the nonlinearities are greater for this symmetry. The stress amplitudes, σ_0, were varied up to 0.2 MPa and stress bias, $\sigma_=$, in the range of 2 to 5 MPa. Then, the obtained piezoelectric coefficients as a function of stress amplitude were fitted with the well-known Rayleigh law (Equation (4.4)), corresponding to a uniform Preisach distribution:

$$d_{33} = d_0 + \alpha \sigma_0 \tag{4.22}$$

where d_0 represents the intrinsic and reversible contributions and α is the nonlinear parameter, described by the product of the bistable unit response (2/3 D_0) and the number of units in the swept region (f_0) in Equation (4.12). Selected resulting piezoelectric coefficient dependences on stress amplitude with varying bias stress are presented in Figure 4.19. As expected, the piezoelectric coefficients are linearly dependent on the applied stress amplitude, σ_0, in the limited testing range confirming that the bistable units density can indeed be considered as constant in the 0.2 MPa range. Moreover, they are exhibiting a practically constant d_0 independently of the stress bias. This is in agreement with the Preisach approach as intrinsic and reversible response should be independent of the applied stress. To homogenize the fitting results, all the d_0 obtained for the different stress biases were averaged and the d_{33} vs. σ_0 curves were fitted again keeping d_0 constant at this averaged value. The resulting nonlinear parameters, α, are plotted as a function of bias stress, $\sigma_=$ in Figure 4.20. As, they are proportional to the value of the distribution function along the internal stress axis, their dependence on bias stress corresponds to the trace of the distribution function in the $\sigma_c = 0$ plane.

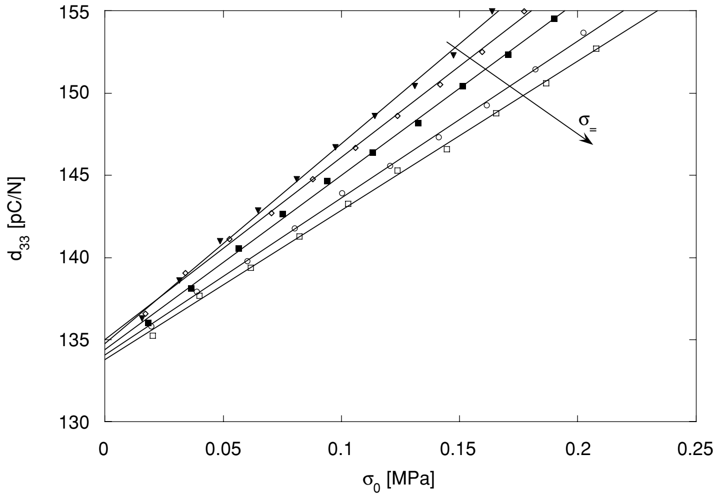

Figure 4.19: *Bias stress, $\sigma_=$, dependence of the piezoelectric coefficient, d_{33}, nonlinearity for a 60/40 PZT at low stress amplitudes, σ_0. The arrow indicates growing values of bias stress in absolute value.*

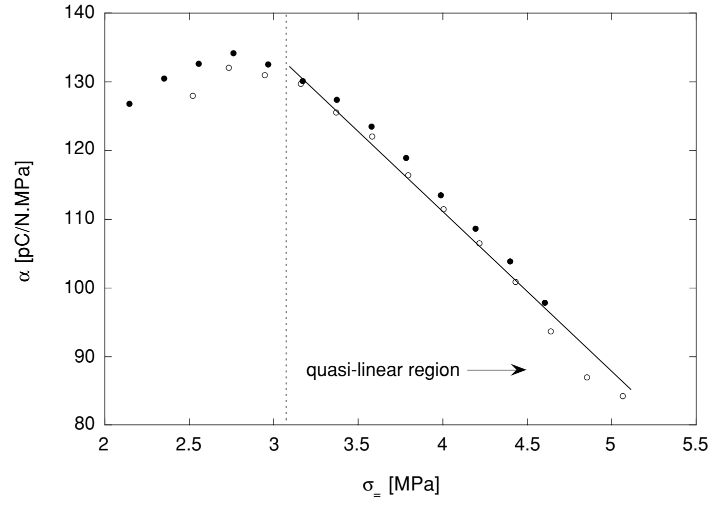

Figure 4.20: *Absolute bias stress, $\sigma_=$, dependence of the nonlinear parameter, α, for 60/40 PZT. Open and closed circles represent two different measurements. In the Preisach formalism, the displayed α are proportional to the trace of the distribution function in the $\sigma_c = 0$ plane.*

The high $\sigma_=$ region (above 3 MPa) of the α vs. $\sigma_=$ dependence is exhibiting a quite linear behavior. Characterization of α for bias stresses below 2 MPa was not possible because of experimental limitations. As this corresponds to the region predominantly swept for measurements at constant stress bias and high stress amplitude, it is not surprising that the roof-like distribution proposed in section 4.2.2 (cf. Figure 4.10) exhibiting a linear dependence on σ_i corresponds well to the measurements. Moreover, the saturating behavior as observed on Figure 4.16 for a different composition, can be explained by the departure from linear dependence observed at low bias stress. As the working range increases and reaches the region where the number of contributing units decreases relatively to the linear dependence, the extrinsic contributions will be relatively lower and the piezoelectric coefficient will tend to saturate at high stress amplitudes and depart from the quadratic stress amplitude dependence.

The previous experiment could be made under the assumption that the actual Preisach distribution is not varying significantly away from the internal stress axis. Now that roof-like distribution function is practically confirmed for the high internal stress values (> 3 MPa), it is of interest to check whether its supposed coercive stress dependence is correct. As direct probing of the coercive stress axis is not possible, a way to test the roof-like distribution can be found in the extrinsic contributions expression when the distribution function (Equation (4.18)) is integrated for the case considered in the direct piezoelectric measurements (as shown in Figure 4.11), yielding:

$$\Delta d_{33} \propto (f_0 + k\,\sigma_=)\sigma_0 + \frac{1}{3}\,g\,\sigma_0^2 \tag{4.23}$$

In Equation (4.23), the quadratic nonlinear coefficient ($\beta = 1/3$ g) is independent of the bias stress, $\sigma_=$. This strong implication of the roof-like distribution function can be checked by performing measurements similar to the ones presented immediately above. Still using a variation of the bias stress but increasing the range of stress amplitudes permits to measure the nonlinear coefficients, α and β, as a function of the bias stress (in the same spirit as in Figure 4.17 but with a lower bias stress step). Such typical d_{33} stress amplitude dependence are presented as a function of bias stress in Figure 4.21.

The obtained curves are exhibiting a quadratic behavior typical of high stress amplitude measurements. The bias stress effect is similar to what has already been observed in Figure 4.17 for 40/60 PZT, i.e. the higher the bias stress the lower the extrinsic contributions. The intrinsic and reversible contributions are again independent of $\sigma_=$ (as in Figure 4.19) with a d_0 of ca 138 pC/N. As previously, the obtained d_{33} stress dependences were fitted with a second order field polynomial corresponding to the roof-like distribution function adapted to the direct piezoelectric case (see Equation (4.15)):

$$d_{33} = d_0 + \alpha\,\sigma_0 + \beta\,\sigma_0^2 \tag{4.24}$$

The obtained nonlinear parameters (α and β) are plotted in Figure 4.22 and Figure 4.23 as a function the bias field. The first order nonlinear parameters, α, should be exactly equivalent to the values presented in Figure 4.20. Actually, they are higher indicating that the previous linear fits were probably already containing some quadratic contributions which caused the underestimation of the actual α (as β is negative). Hence, even if the data is more noisy, the α coefficients presented in Figure 4.22 are probably more quantitatively reliable than in Figure 4.20.

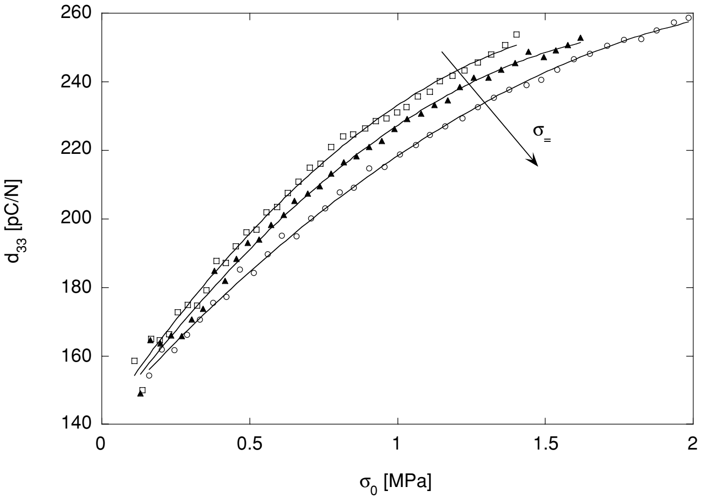

Figure 4.21: *Bias stress, $\sigma_=$, dependence of the piezoelectric coefficient, d_{33}, nonlinearity for a 60/40 PZT at high stress amplitudes, σ_0. The solid lines were obtained by fitting the experimental points with Equation (4.24). The arrow indicates growing values of bias stress in absolute value.*

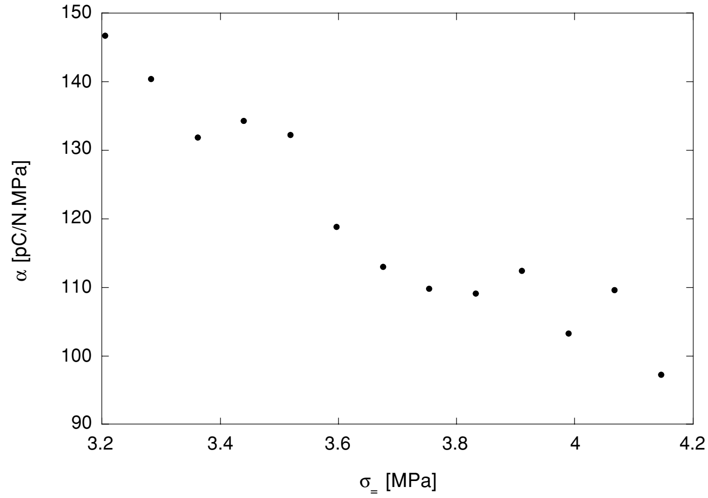

Figure 4.22: *Bias stress dependence of the nonlinear parameter, α, for PZT 60/40.*

As before, the α dependence on bias stress is close to linear as expected in this range if the distribution function is roof-like. Concerning the nonlinear parameter β, Figure 4.23 shows that it is clearly not independent of bias stress contrary to what would be expected from Equation (4.23). This means that the roof-like distribution function is not adequate for the description of the actual bistable units distribution away from the internal stress axis.

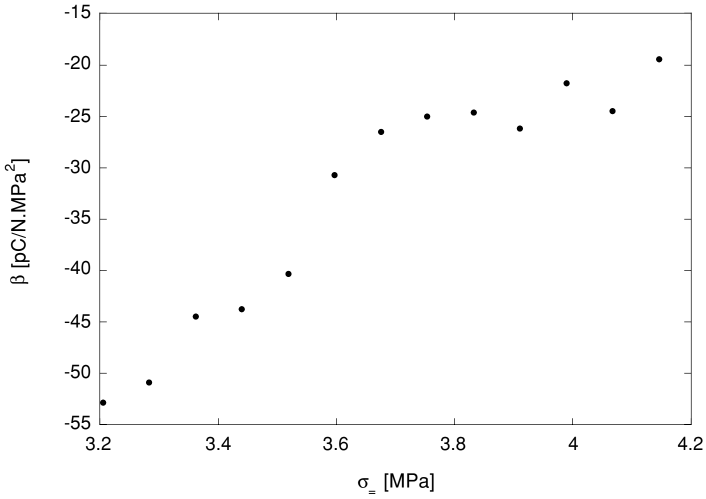

Figure 4.23: *Bias stress dependence of the quadratic nonlinear parameter, β, for PZT 60/40.*

The bias stress dependence of the quadratic nonlinear parameter, β, on Figure 4.23 is close to a linear one with a minimum at zero bias. Hence, the formula of the proposed roof-like distribution function has to be corrected in order to reflect this bias stress dependence. A natural extension would be based on the MacLaurin expansion as presented in section 4.2.1. A closer look at Equations (4.7) and (4.12) indicates that only internal stress distribution terms yield a change in the bias stress behavior. As symmetry of the internal stress has to be respected, even powered terms of the internal stress only are allowed. Thus, Equation (4.7) can be naturally extended with a σ_i^4 term. As integration is a distributive operation, the contribution of a σ_i^4 term to the piezoelectric field dependence can be directly obtained by Equation (4.10), yielding:

$$\Delta d_{33}\,(\sigma_i^4) \propto \frac{1}{15}\,\sigma_0^5 + \sigma_0^3\,\sigma_=^2 + \sigma_0\,\sigma_=^4 \tag{4.25}$$

which is not compatible with the experimental data, as it implies a fifth-order dependence on the stress amplitude. Thus, no “natural” analytical extension to the roof-like distribution can be considered. Therefore, non-analytical extensions including a crossed non-analytical term, such as the following, have to be considered:

$$f(\sigma_i, \sigma_c) = f_0 + g\,\sigma_c + k\,\mathrm{Abs}(\sigma_i) + j\,\sigma_c \mathrm{Abs}(\sigma_i) \tag{4.26}$$

Its associated piezoelectric stress dependence is then given by:

$$\Delta d_{33} \propto (f_0 + k\,\sigma_=)\,\sigma_0 + \frac{1}{3}(g + j\,\sigma_=)\,\sigma_0^2 \tag{4.27}$$

The experimentally observed bias stress dependences of the nonlinear parameters are present in Equation (4.27). The crossed extension term ($j\,\sigma_c\,\mathrm{Abs}(\sigma_i)$) expresses accurately the β coefficient dependence on bias stress without impinging on the other stress dependences. The sign of the j coefficient being clearly positive from Figure 4.23, the distribution function can be plotted considering negative g and k, as shown in Figure 4.24. This schematic view shows that the corrected roof-like distribution is exhibiting an intermediate topography between the original shape (cf. Figure 4.10) and the conical distribution (cf. Figure 4.9). Moreover, it is physically more likely as there was no reason for assuming linear traces in the $f(\sigma_i, \sigma_c) = 0$ plane.

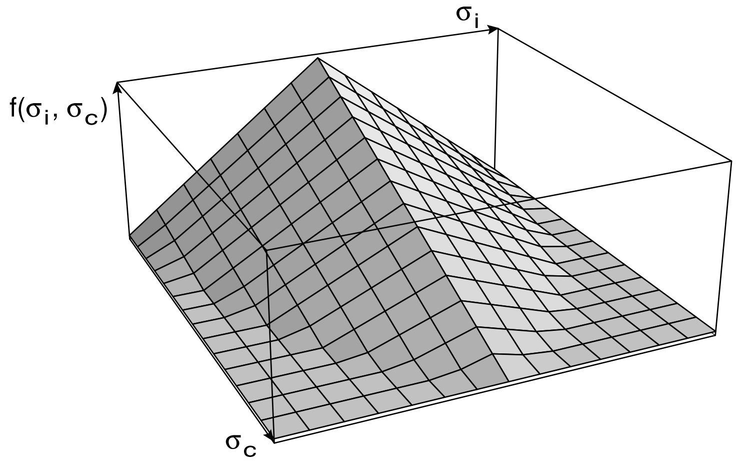

Figure 4.24: *Schematic view of the corrected roof-like distribution with the extra σ_i-σ_c coupled term. The maximum of this distribution is situated at the Preisach plane origin. Note that the introduced coupled term causes a curving of both roof planes. Intersections of the distributions function with σ_i and σ_c correspond to $\pm f_0/k$ and $-f_0/g$ respectively.*

Such a distribution function can be fully characterized by the method used above. The α bias stress dependence will yield the f_0 and k parameters and the β bias stress dependence will lead to the g and j parameters. All the obtained parameters will actually be the product of the proportionality factor in Equation (4.27) with the actual coefficients of the distribution function. Such values will be denoted as “equivalent parameters”. They fully characterize the nonlinear piezoelectric behavior in the considered region of stress amplitudes. The values of these equivalent parameters for the considered composition are presented in Table 4.1:

Table 4.1: *Equivalent distribution parameters values for PZT 60/40.*

f_0 [pC/N MPa]	k [pC/N MPa^2]	g [pC/N MPa^2]	j [pC/N MPa^3]
297	-48.1	-496	108

It is finally interesting to evaluate the nonlinear piezoelectric behavior in the hypothetical case of a symmetrical applied stress (i.e. $\sigma_= = 0$). The integration of Equation (4.26) yields:

$$\Delta d_{33} \propto f_0 \sigma_0 + \frac{1}{3}(g + k)\sigma_0^2 + \frac{1}{12} j \sigma_0^3 \tag{4.28}$$

which implies a positive third order stress amplitude contribution. Hence, it can be predicted that symmetric characterization of the considered material may yield some positive cubic dependence on the applied field amplitude which is in agreement with some published data on converse piezoelectric coefficient nonlinearity (e.g. Ref. [9] for d_{33} and [7] for d_{15}).

In conclusion, a corrected roof-like distribution with a non-analytical crossed term describes effectively the piezoelectric nonlinearities of rhombohedral PZT. All the parameters of this distribution can be determined experimentally and were evaluated for the considered sample. From the applied point of view, this expression for a distribution function constitutes the minimal set of parameters ever proposed for the piezoelectric coefficient nonlinearity description. Moreover, considering the formal analogies between the piezoelectric behaviors of different PZT and PNN-PZT, the proposed model of distribution can be extended to such compositions.

4.4 SUMMARY

In this chapter, the Preisach approach to nonlinear and hysteretic systems was presented and successfully applied to piezoelectricity. First, a generalized expression for the distribution function was used to derive the associated piezoelectric nonlinearities. It was then qualitatively demonstrated that such a distribution can efficiently describe the most widely observed piezoelectric coefficient field dependencies. Then, some specific distribution functions were explored, in order to model the commonly observed second order field dependence of the piezoelectric coefficient, yielding a non-analytical roof-like distribution valid for high values of bias stress (> 3MPa). Finally, using direct measurements with varying bias and amplitude stresses, this distribution was further refined and its parameter were experimentally obtained for a rhombohedral PZT. This corrected distribution function is able to describe the piezoelectric coefficient nonlinearity with four parameters only, the lowest number yet.

4.5 REFERENCES

1. R.S. Woollett and C.L. LeBlanc, *Ferroelectric nonlinearities in transducer ceramics.* IEEE T. Son. Ultra., (1973) **Su-20** [1] p. 24-31.
2. H. Beige and G. Schmidt, *Electromechanical resonances for investigating linear and nonlinear properties of dielectrics.* Ferroelectrics, (1982) **41** p. 39-49.
3. M.D. Bryant, *A characterization of the linear and non-linear dynamic performance of a practical piezoelectric actuator. Part 2: Theory.* Sens. Act., (1986) **9** p. 105-14.
4. S.P. Joshi, *Non-linear constitutive relations for piezoceramic materials.* Smart Mater. Str., (1992) **1** p. 80-3.
5. V. Perrin, M. Troccaz, and P. Gonnard, *Nonlinear behaviour of the permittivity and of the piezoelectric strain constant under high electric field drive.* J. Electroceram., (2000) **4** [1] p. 189-94.
6. V. Mueller and Q.M. Zhang, *Nonlinearity and scaling behavior in donor doped lead zirconate titanate piezoceramic.* Appl. Phys. Lett., (1998) **72** [21] p. 2692-4.
7. V. Mueller and Q.M. Zhang, *Shear response of lead zirconate titanate piezoceramics.* J. Appl. Phys., (1998) **83** [7] p. 3 754-61.
8. G. Arlt and H. Dederichs, *Complex elastic, dielectric and piezoelectric constants by domain wall damping in ferroelectric ceramics.* Ferroelectrics, (1980) **29** p. 47-50.
9. S. Li, W. Cao, and L.E. Cross, *The extrinsic nature of nonlinear behavior observed in lead zirconate titanate ferroelectric ceramic.* J. Appl. Phys., (1991) **69** [10] p. 7219-24.
10. O. Boser, *Statistical theory of hysteresis in ferroelectric materials.* J. Appl. Phys., (1987) **62** [4] p. 1344-8.
11. H. Kronmüller, *Statistical theory of Rayleigh law.* Z. Angew. Physik, (1970) **30** [1] p. 9-13.
12. R.C. Smith and C.L. Hom, *A domain wall theory for ferroelectric hysteresis.* J. Intel. Mat. Sys. Str., (1999) **10** [3] p. 195.
13. R.C. Smith and Z. Ounaies, *A domain wall model for hysteresis in piezoelectric materials*. (unpublished).
14. D.C. Jiles and D.L. Atherton, *Theory of ferromagnetic hysteresis.* J. Appl. Phys., (1984) **55** [6] p. 2115-20.
15. D. Damjanovic, D.V. Taylor, A.L. Kholkin, M. Demartin, K.G. Brooks, and N. Setter, *Domain wall contributions to the piezoelectric properties of ferroelectric ceramics and thin films, and their signifiance in sensor and actuator applications.* Proc. of "Advances in materials for smart systems" Boston, (1996).

16. D. Damjanovic, *Stress and frequency dependence of the direct piezoelectric effect in ferroelectric ceramics.* J. Appl. Phys., (1997) **82** [4] p. 1788-97.

17. M. Demartin and D. Damjanovic, *Dependence of the direct piezoelectric effect in coarse and fine grain BT ceramics on dynamic and static pressure.* Appl. Phys. Lett., (1996) **68** p. 3046.

18. L. Rayleigh, *Notes on electricity and magnetism : III. On the behaviour of iron and steel under the operation of feeble magnetic forces.* Philos. Mag. S. 5, (1887) **23** [142] p. 225-45.

19. L. Néel, *Théorie des lois d'aimantation de Lord Rayleigh. I - les déplacements d'une paroi isolée.* Cah. Phys., (1942) **12** p. 1-20.

20. V.D. Kugel and L.E. Cross, *Behavior of soft piezoelectric ceramics under high sinusoidal electric fields.* J. Appl. Phys., (1998) **84** [5] p. 2815-30.

21. F. Preisach, *Ueber die magnetische Nachwirkung.* Z. Physik, (1935) **94** p. 277-302.

22. A.V. Turik, *Theory of polarization and hysteresis of ferroelectrics.* Sov. Phys. Solid State, (1963) **5** [4] p. 885-6.

23. I.D. Mayergoyz, *Hysteresis model from the mathematical and control theory point of view.* J. Appl. Phys., (1985) **57** [1] p. 3803-5.

24. G. Bertotti, *Hysteresis in Magnetism*. Electromagnetism, ed. I. Mayergoyz. 1998, San Diego: Academic press.

25. I.D. Mayergoyz, *Mathematical models of hysteresis.* Phys. Rev. Lett., (1986) **56** [15] p. 1518-21.

26. G. Bertotti, *Application of the Preisach model of hysteresis.* Mater. Sci. Forum, (1999) **302-3** p. 43-52.

27. I.D. Mayergoyz and T.A. Keim, *Superconducting hysteresis and Preisach model.* J. Appl. Phys., (1990) **67** [9] p. 5466-8.

28. R. Rammel and J. Souletie, *Two levels systems in spin glasses - Phenomenological description of the non-ergodic properties below T_C.* "Magnetism of metals and alloys", ed. M. Cryot, North-Holland, (1980) p. 408-86.

29. A.V. Turik, *Experimental investigation of the statistical distribution of domains in a ferroelectric ceramic.* Sov. Phys. Solid State, (1964) **5** [10] p. 2141-3.

30. G. Bertotti, V. Basso, and G. Durin, *Random free energy model for the description of hysteresis.* J. Appl. Phys., (1996) **79** [8] p. 5764-66.

31. G. Bertotti, *Energetic and thermodynamic aspects of hysteresis.* Phys. Rev. Lett., (1996) **76** [10] p. 1739-42.

32. G. Bertotti, I.D. Mayergoyz, V. Basso, and A. Magni, *Functional integration approach to hyteresis.* Phys. Rev. E, (1999) **60** [2] p. 1428-40.
33. G. Bertotti, V. Basso, and A. Magni, *Stochastic dynamics in quenched-in disorder and hysteresis.* J. Appl. Phys., (1999) **85** [8] p. 4355-7.
34. M.E. Lines and A.M. Glass, *Principles and applications of ferroelectrics and related materials*. 1977, Oxford: Calrendon Press.
35. A. Magni, C. Beatrice, G. Durin, and G. Bertotti, *Stochastic model for magnetic hysteresis.* J. Appl. Phys., (1999) **86** [6] p. 3253-61.
36. A.V. Turik, *A statistical method for the investigation of repolarization processes in ferrolectric ceramics.* Sov. Phys. Solid State, (1964) **5** [9] p. 1751-3.
37. N.S. Akulov and P.P. Galenko, *On the theory of rectangular loop hysteresis of ferromagnetics.* Dokl. Akad. Nauk BSSR (in Russian), (1962) **6** [9] p. 551-5.
38. G. Robert, D. Damjanovic, and N. Setter, *Separation of nonlinear and friction-like contributions to the piezoelectric hysteresis.* ISAF 2000.
39. B. Jiang, J.C. Lee, P. Zurcher, and R.E. Jones, *Modeling ferroelectric capacitor switching using a parallel-elements model.* Int. Ferroelectrics, (1997) **16** p. 199-208.
40. P. Ge and M. Jouaneh, *Modeling hysteresis in piezoceramic actuator.* Prec. Eng., (1995) **17** p. 211-21.
41. P. Ge and M. Jouaneh, *Generalized Preisach model for hysteresis nonlinearity of piezoceramic actuators.* Prec. Eng., (1997) **20** p. 99-111.
42. R.M. delVechio, *An efficient method for modeling complex hysteresis processes in ferromagnetic materials.* IEEE T. Mag., (1980) **16** [5] p. 809-11.

CHAPTER V
PIEZOELECTRIC RESPONSE HYSTERESIS

In the Preisach approach, hysteresis and coefficient nonlinearities are intimately related (cf. Chapter IV), hence its successful application to the piezoelectric nonlinearity makes it also promising for hysteresis description. In practice, this issue is essential to control actuator displacement [1, 2] where soft piezoelectrics are widely used. Classically, the piezoelectric losses have been considered using dissipative thermodynamics, leading to ellipsis-type of hysteresis (i.e. with response containing an imaginary part) [3]. Such an approach permits to interpret the losses frequency dependence in great detail. However, the actual shape of the observed piezoelectric hysteresis are often quite different from an ellipsis (as in PZT exhibiting "end-pinched" loops rather well described by the Rayleigh formulas [4]). Moreover, such thermodynamical approach does not explain the observed field dependence of losses (linked to the field dependence of the piezoelectric coefficient). It is the purpose of this chapter to yield a unified and coherent description of the piezoelectric hysteresis, using concepts from both irreversible thermodynamics and Preisach modeling of piezoelectric nonlinearity. By this approach, more insight into the physical mechanisms leading to losses in piezoelectrics will be gained. Besides, the displacement control of piezoelectric actuators will certainly benefit from loop descriptions involving a minimal set of parameters.

Focusing on the piezoelectric hysteresis description, a rigorous derivation of the apparent piezoelectric viscosity and a general losses model combining the basic Rayleigh-type of hysteresis with the viscous contributions will first be presented. This model will be tested on experimental results for linear and nonlinear piezoelectrics by fitting the loops with the proposed expression. Then, the loop expression will be further refined by using a more elaborated Preisach distribution function and a new method for obtaining distribution function parameters from the experimental loops will be described. Finally, the versatility of the Preisach loop modeling will be demonstrated by deriving a pinched loop, often encountered in ferroelectrics [5-7], from a physically sound distribution function.

5.1 PIEZOELECTRIC LOSS DESCRIPTION

In the implementation of piezoelectric ceramics, losses have always been considered as an important parameter, first as they may induce overheating in high frequency operation and second as they are responsible for hysteretic response of actuators. These losses were initially approached phenomenologically, i.e. by introducing response rate dependences for the various coefficients. Holland [3] formally described complex expressions for the dielectric, elastic and piezoelectric coefficients in a global electro-mechanical loss framework. Then, introduction of non-linear thermodynamics in the piezoelectric loss analysis [8, 9] permitted to demonstrate that complex piezoelectric coefficients could be obtained assuming coexisting dielectric and elastic dipoles only [10]. Still, such phenomenological approaches yielded little information on the mechanisms leading to losses in the piezoelectric effect. Concomitantly, domain walls (DW) have been very early identified as a potential candidate to explain the lossy behavior of ferroelectrics [11]. Optical observation of isolated 90° DW motion in barium titanate single crystals led to an equation of motion for DW containing inertia, viscous and pinning terms [12]. Concerning dielectric losses, several works [13-15] modeled domain wall motion obtaining a viscous response. Piezoelectric losses were related to DW motion by Arlt and Dederichs [16] who obtained a viscous expression for the piezoelectric response related to 90° DW vibration. Using comparable oscillating DW model, Stula *et al.* [17] were also able to describe effectively the ratios between the dielectric, mechanical, and piezoelectric complex parts of RbH_2PO_4 response. Lately, as all the above-cited contributions were unable to describe the observed field dependence of the piezoelectric losses, a different approach was attempted. Considering the extrinsic contributions to the piezoelectric response, an adaptation of the Rayleigh model [18, 19] for ferromagnetics was proposed [4, 20]. This model describes effectively the field-response hysteresis observed at sub-switching fields. New losses description can hence be proposed where energy dissipation is related to the piezoelectric coefficient field dependence. In ferromagnetics, it has been numerically demonstrated [21] that this elaborated type of “field dependent losses” can be coupled to the more classical viscous losses to effectively generate realistic field-magnetization hysteresis.

Let us first consider the viscous description of the piezoelectric losses. The total response, D for the direct piezoelectric effect can be expressed generally as the sum of the reversible piezoelectric part with the mechanical and piezoelectric viscous contributions [22]:

$$D = d_0\sigma + d_0\eta\,\dot{u} + d_0\psi\dot{D} \tag{5.1}$$

where d_0 is the intrinsic and reversible piezoelectric coefficient, u is the strain and η and ψ are respectively the mechanical and piezoelectric viscosities. In practice, piezoelectric losses are usually considered through the classical differential equation for a viscous hysteresis loop:

$$D = d_0\sigma + d_0\gamma\dot{D} = d^*\sigma \tag{5.2}$$

where γ is the apparent piezoelectric viscosity and d^* the apparent piezoelectric coefficient. Unfortunately, no direct equivalence to γ can be found in Equation (5.1). To unveil the physical meaning of such a parameter, a more rigorous derivation has thus to be conducted.

In the direct case, the piezoelectric dielectric displacement D is proportional to the effective stress, σ_e (given by the sum of the applied value σ and an anelastic, defect-related part σ'):

$$D = d_0\sigma_e = d_0(\sigma + \sigma') \tag{5.3}$$

The proportionality constant, d_0, reflects the intrinsic and the reversible contributions to piezoelectricity. Considering the rate of entropy density increase for a piezoelectric material at temperature, T, as a function of anelastic stress, σ', rate of deformation, $\dot{u}$, electric field, E, and rate of dielectric displacement, $\dot{D}$ (according to Ref. [22]):

$$\dot{S} = \frac{1}{T}(\sigma'\dot{u} + E\dot{D}) \tag{5.4}$$

and identifying $-\sigma'/T$, $-E/T$, $\dot{u}$ and $\dot{D}$ with respectively generalized velocities and forces, it can be written that:

$$\begin{aligned} \sigma' &= \eta\,\dot{u} + \psi\,\dot{D} \\ E &= \psi\,\dot{u} + \zeta\,\dot{D} \end{aligned} \tag{5.5}$$

where η, ζ and ψ can be identified with respectively the mechanical, dielectric and piezoelectric viscosities and are obeying the Onsager relations (see e.g. Ref. [3] for more details). In the direct piezoelectric case, the electric field can be assumed to be zero, hence introduction of Equation (5.5) second line into the first line yields:

$$\sigma' = \left(\psi - \frac{\zeta}{\psi}\eta\right)\dot{D} = \gamma\dot{D} \tag{5.6}$$

where the apparent piezoelectric viscosity, γ appears by identification of Equation (5.3) with Equation (5.2). With this expression of the γ parameter, Equation (5.2) can be solved leading to a relaxation equation for the piezoelectric coefficient:

$$d^* = d_\infty + \frac{\Delta d}{1 + i\,\omega\,\gamma\,d_0} \qquad (\text{with } d_0 = d_\infty + \Delta d\ ) \tag{5.7}$$

In the quasi-static approximation (i.e. $\omega\,\gamma\,d_0 << 1$), Equation (5.7) is similar to the view of piezoelectric losses formalized by Holland [3] where the piezoelectric coefficient is taken as complex and frequency independent such as :

$$d^* = d_0 - i\,d'' \qquad (\text{with } d'' = \omega\,\gamma\,d_0\,\Delta d) \tag{5.8}$$

This general view of a complex piezoelectric coefficient can be used away from the quasi-static regime provided that d_0 and d'' are considered frequency dependent. Hence, for an alternating applied stress ($\sigma = \sigma_0 \sin(\omega t)$), in the absence of external electric field, the dielectric displacement is given by:

$$D = d_0\,\sigma_0 \sin(\omega t)\ - d''(\omega)\,\sigma_0 \cos(\omega t) = d_0\,\sigma_0 \sin(\omega t - \delta(\omega)) \tag{5.9}$$

where the phase angle, δ is defined by the viscous loss tangent:

$$\mathrm{tg}\,\delta = \frac{\mathrm{Im}\,(D)}{\mathrm{Re}\,(D)} = \frac{d''(\omega)}{d_0} \tag{5.10}$$

which amplitude is frequency dependent (linearly in the quasi-static case). Such type of losses can be identified by its classical ellipsoidal stress-charge density hysteresis. However, Equation (5.10) cannot take into account any variation of the losses with the applied stress amplitude σ_0 whereas it is commonly observed (e.g. in PZT [4]). Another type of losses being field dependent has thus to be invoked.

Let's consider the Rayleigh description of losses where the dielectric displacement is given by [4, 18]:

$$D = (d_0 + \alpha\,\sigma_0)\,\sigma - \mathrm{Sign}(\dot{\sigma})\,\frac{\alpha}{2}\,(\sigma_0^2 - \sigma^2) \tag{5.11}$$

with α, the Rayleigh parameter (equivalent to the first order nonlinear parameter in Equation (4.4)). The piezoelectric response as given in Equation (5.11) is characterized by a typical end-pinched stress-charge displacement hysteresis and is thus clearly different from the viscous behavior. As seen in the previous chapter, this model describes effectively field-dependent contributions to the piezoelectric response as it implies the following linear field-dependence of the piezoelectric coefficient:

$$d = \frac{dD}{d\sigma} = d_0 + \alpha\,\sigma_0 \tag{5.12}$$

In the Rayleigh framework, the piezoelectric losses (i.e. the area of the stress-charge density hysteresis) are indeed increasing with the applied stress amplitude σ_0 [20]. Frequency dependence might also be taken into account by some observed relaxational behavior of the parameters [20]. Nevertheless, such a description is not sufficient to fully describe the losses, as shown by Damjanovic for PZT [20] who observed a constant offset from the measured losses with respect to the Rayleigh-calculated ones. As this offset between Rayleigh and actual losses is independent of the applied field, it seems natural to superimpose the two models presented above (similarly to Shil'nikov *et al.* [23]). Such a procedure leads to encouraging results for the numerical simulation of ferromagnetic loops [21]. If field separation condition holds (i.e. contributions from both loss processes to the dielectric displacement are strictly additive at each stress level [21]) the total response can then be written as a combination of viscous (Equation (5.2)) and field-dependent (Equation (5.11)) loss contributions with the intrinsic and reversible response $d_0\,\sigma$:

$$D = (d_0 + \alpha\,\sigma_0)\,\sigma - \mathrm{Sign}(\dot{\sigma})\,\frac{\alpha}{2}\,(\sigma_0^2 - \sigma^2) - \gamma d_0 \dot{D} \tag{5.13}$$

The mixed model obtained in Equation (5.13) represents a "composite" hysteresis made of the addition of viscous and field-dependent loops. The losses associated with this equation can thus be separated in Rayleigh-like losses given by the normalized integration of the Rayleigh loop as [20]:

$$\mathrm{tg}\,\delta_R = \mathrm{tg}\left(\frac{4\,\alpha\,\sigma_0}{3\,\pi\,d_{33}}\right) \tag{5.14}$$

and by viscous losses characterized by (following Equation (5.10)):

$$\mathrm{tg}\,\delta_V = \omega\gamma(\omega)\Delta d \tag{5.15}$$

for a given frequency. Hence, the sum of these losses does exhibit the necessary field (σ_0) and frequency (ω) dependences and should permit to describe precisely the losses in piezoelectrics. Note that such a description is valid for a given frequency range only as d_0 and α may be dependent on frequency. Its adequacy with experimental data will be examined in the next section by attempting to fit purely viscous and more elaborate hysteresis with Equation (5.13).

5.2 HYSTERESIS FITTING AND LOSS SEPARATION

Here below, experimental hysteresis characterization results are presented for PTSm, PZT, and PNN-PZT. PTSm is taken here as model material for pure viscous losses. It is used to test for the ability of both the mixed model and the fitting procedure to accurately describe a pure viscous behavior before treating PZT and PNN-PZT as representatives of the mixed behavior. A perfect agreement of the proposed model, Equation (5.13), with the experimental data for PZT and PNN is not expected as the Rayleigh hysteresis equation does not correspond to the actual distribution function shape for those materials. However, parameters are allowed to vary as a function of the stress amplitude which provides a supplementary degree of freedom to describe the actual hysteresis. Moreover, when the number of fitting parameters is large (as in the actual Preisach distribution function determined in section 4.3.4), the dispersion in the adjusted values is increased. It will be shown that such a procedure works satisfactorily for the tested materials and allows to effectively separate field-dependent from frequency-dependent losses. Finally, these losses will be interpreted for the different materials in terms of domain wall motion and piezoelectric viscous mechanisms.

5.2.1 Experimental

To investigate the possibility to model the response hysteresis with a mixed model as described in Equation (5.13), direct piezoelectric measurements were performed under sinusoidal stress on PTSm, PZT 45/55 and 50PNN-19PZ-31PT. The obtained stress and charge density signals were fitted with two sine functions neglecting the harmonics of the field dependent losses [18]. The piezoelectric coefficient, d_{33}, was then calculated as the ratio of the charge density and stress amplitudes. The overall loss tangent (different from the viscous loss tangent, as it contains all loss mechanisms) was obtained from the phase shift between stress and charge density fitted functions. Finally, the stress-charge density hysteresis were fitted using either Equation (5.11) or Equation (5.13) using a Levenberg-Marquardt non-linear least squares optimization procedure [24]. To limit noise introduction in the fitting procedure, the derivative of the response was calculated by applying the following conversion to the charge quasi-sinusoidal response:

$$\frac{dD}{dt} \approx \frac{d}{dt} D_0 \sin(\omega t) = \omega D_0 \cos(\omega t) = \omega D_0 \sin\left(\frac{\pi}{2} - \omega t\right) \qquad (5.16)$$

rather than numerically derivate it. The fitted parameters can then be compared to the ones obtained directly from the piezoelectric coefficient stress dependence (according to Equation (5.12)).

In the case of PTSm, both direct and converse piezoelectric measurements were performed. To measure the piezoelectric strain, a modified Mach-Zender double beam interferometer [25] adapted for low frequency measurements was used. This set-up was preferred to single beam as many mechanical resonances could be eliminated by such a method. A typical frequency dependence of the piezoelectric coefficient for a bulk quartz sample is presented in Figure 5.1.

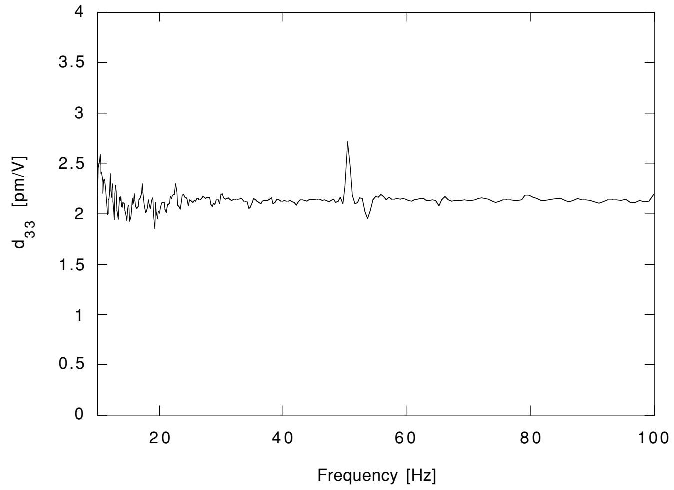

Figure 5.1: *Frequency dependence of the piezoelectric coefficient,* d_{33} *of a quartz sample.*

Excepting 50 Hz, the frequency independence of the quartz piezoelectric response demonstrates that measurements can be performed from 30 Hz up to 100 Hz. Moreover, sufficient precision is attained as the expected piezoelectric response for our lead-based materials at least one order of magnitude higher than quartz.

5.2.2 Linear piezoelectric: PTSm

A typical stress-charge density hysteresis for modified lead titanate is presented in Figure 5.2.a and the corresponding piezoelectric coefficient (d_{33}) stress dependence is plotted in Figure 5.2.b.

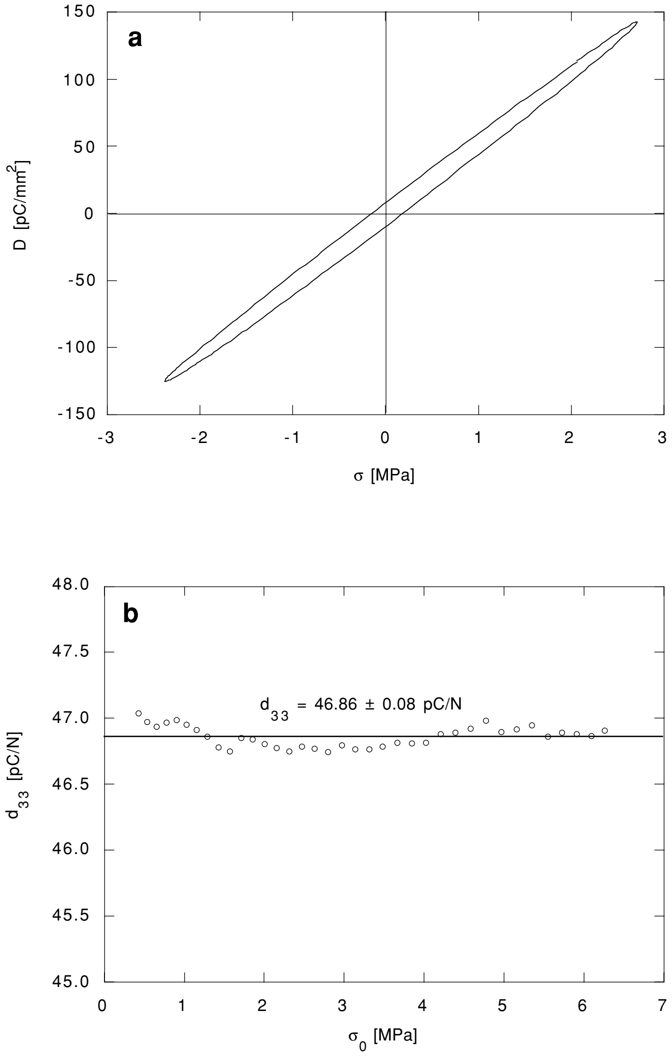

Figure 5.2: *Typical charge density, , vs. stress, σ hysteresis (**a**) and piezoelectric coefficient, d_{33} vs. stress amplitude, σ_0 (**b**) dependences obtained for PTSm at 35 Hz.*

Figure 5.2 shows clearly that even though PTSm exhibits a stress-charge density hysteresis, no stress amplitude dependence of d_{33} is observed. Hence, we are probably in presence of a fully viscous case with no field-dependent losses (i.e. Rayleigh coefficient, $\alpha = 0$ and $d_{33} = d_0$ in Equation (5.12)). Note that a similar overall behavior would be obtained in the case of a Maxwell-Wagner process [26] (the mathematical expressions would actually be equivalent), however we will assume in the following that viscosity is predominant. After fitting the hysteresis with Equations (5.11) and (5.13), the stress dependences of loop parameters were obtained. The fit with the pure Rayleigh model (i.e. Equation (5.11)) was performed in order to test whether the fitting procedure will yield, as expected, aberrant results with an unadapted model. The resulting stress dependences of loop parameters are presented in Figure 5.3.

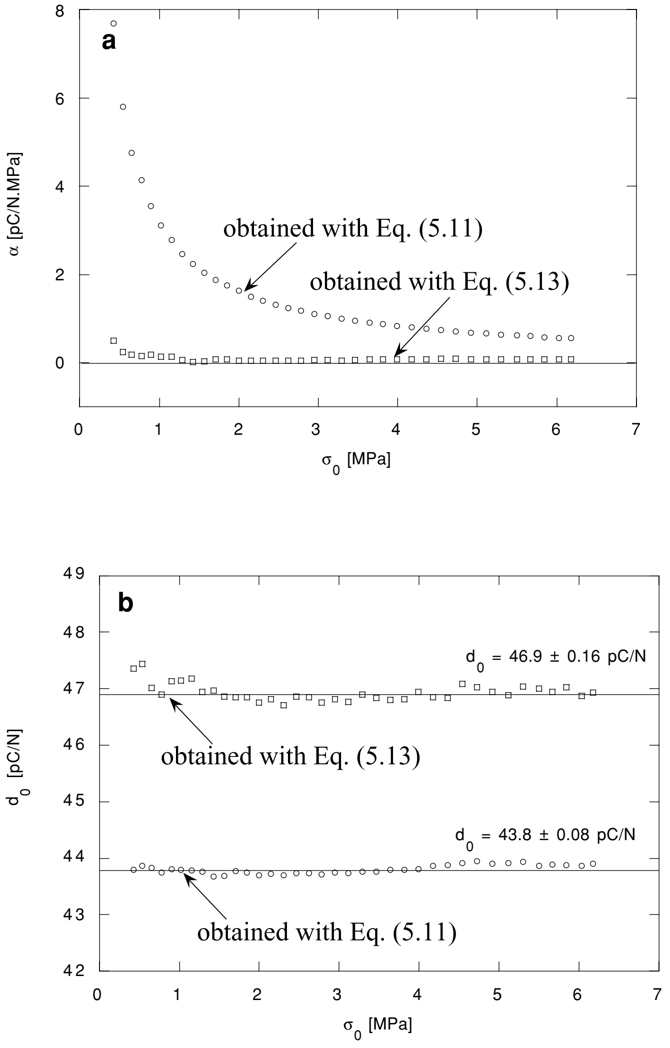

Figure 5.3: *Dependence of fitted loop parameters on stress amplitude,* σ_0 *for PTSm (Rayleigh parameter,* α *in* ***a*** *and intrinsic and reversible coefficient* d_0 *in* ***b*** *for a purely field-dependent model (Equation (5.11)) and a mixed model (Equation (5.13)).*

Figure 5.3.a shows a clear $1/\sigma_0$ dependence for α when a purely field-dependent model (Rayleigh law of Equation (5.11)) is used for fitting. As expected, this behavior is in contradiction with the physical meaning of α because upon insertion in Equation (5.12), it would yield no final stress dependence of d_{33}. Therefore, a $\alpha \propto 1/\sigma_0$ stress dependence is a hint for the existence of viscous loss contributions wrongly accounted for by a field-dependent

loss description. The results for α using the mixed model (Equation (5.13) adjustment in Figure 5.3.a) for the fit are in much better agreement with the observations. In this case, α is close to zero and independent of the stress amplitude, which corresponds well to the observed d_{33} independence on σ_0 (Figure 5.2.b). Moreover, when considering the results for d_0 in Figure 5.3.b, it is clear that the d_0 obtained for the mixed model fitting (i.e. Equation (5.13)) are much closer to the actual value of d_{33} in Figure 5.2.b. To ascertain the pure viscous model for PTSm, the values of the viscous loss tangent tg δ_V obtained by the fitting of the PTSm loop with Equation (5.13) should be equivalent to the overall loss tangent calculated by the phase shift between applied stress and charge response. Both type of losses are presented in Figure 5.4. As expected, the viscous loss tangent tg δ_V is not dependent on the applied stress as it only depends on the energy dissipation per cycle relative to the intrinsic and reversible response. Moreover, the fitted value is in a good agreement with the directly measured value. Unfortunately, processes relaxing in the experimental frequency range (around 1 Hz) prevent the calculation of a pertinent quasi-static piezoelectric viscosity, γ, for PTSm.

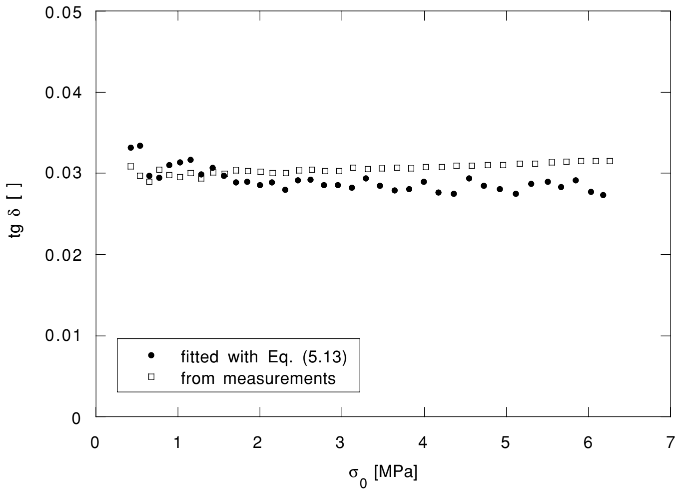

Figure 5.4: *Stress amplitude, σ_0 dependence of the viscous loss tangent obtained when fitting PTSm hysteresis with Equation (5.13) (circles) and obtained directly from measurements (squares).*

To further check for any artifact due to the measurement set-up, converse measurements as a function of frequency (in a range limited by mechanical resonances of the set-up) were performed. The obtained hysteresis were then fitted with the same equations (Equations (5.11) and (5.13)) as for the direct measurements (replacing D by the deformation, and σ by the electric field). The values obtained for d_0 (after averaging over electric field range of measurements) are reported for both cases and compared with the average value obtained directly from the electric field dependence of the converse piezoelectric coefficient d_{33}. These results are reported as a function of measurement frequency in Figure 5.5.

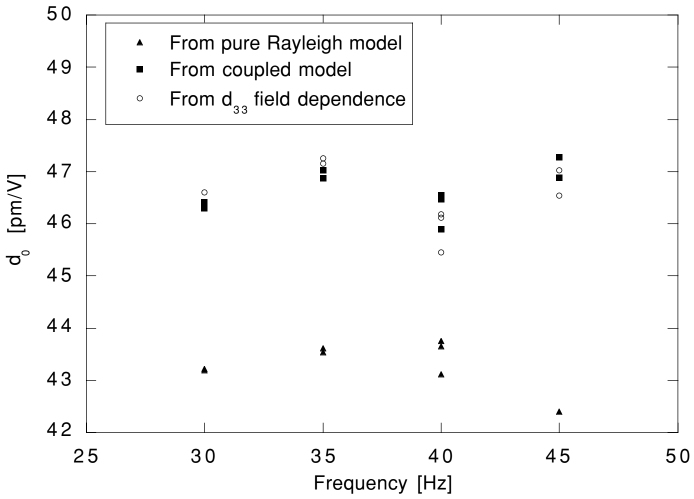

Figure 5.5: *Frequency dependence of the measured (circles), fitted with Equation (5.11) (triangles) and fitted with Equation (5.13) (squares) converse piezoelectric coefficients for PTSm.*

The converse measurements from Figure 5.5 show clearly that the mixed model describes in the best manner the d_{33} measured directly form the electric field dependence. Moreover, the mean viscous loss tangent obtained in this case (3.1 ± 0.04 %) is very close to the one observed for direct measurements (2.9 ± 0.02 % in Figure 5.4) which confirms in an other way the adequacy of the viscous model for PTSm. In conclusion, PTSm can be best described by a purely viscous losses model as presented in Equation (5.2). Moreover, fitting PTSm loops with Equation (5.13) has also yielded correct purely viscous losses, which demonstrates that our procedure is truly able to separate between the two mechanisms (viscous and field-dependent) in the proposed model.

5.2.3 Nonlinear Piezoelectrics: PZT & PNN-PZT

Considering the results obtained in the previous chapter for the piezoelectric coefficient nonlinearities, PZT and PNN-PZT compositions are expected to exhibit not only viscous losses (as in PTSm) but also field dependent losses (as they are following a Preisach-type behavior). A typical stress-charge density hysteresis is presented in Figure 5.7 for PZT only, as the PNN-PZT loop is very similar.

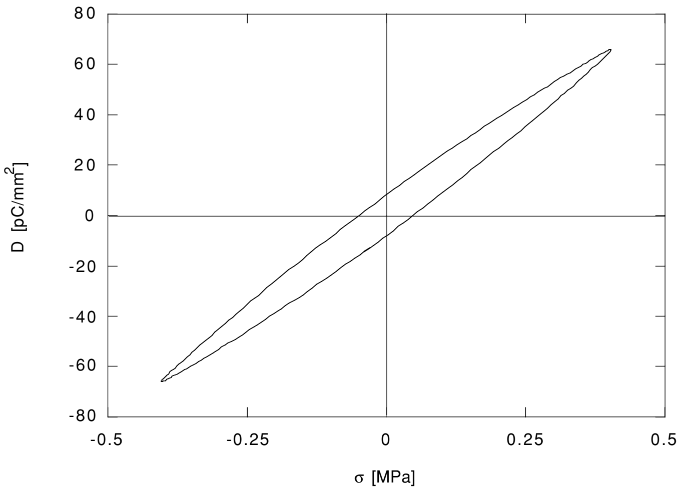

Figure 5.6: *Typical charge density, D vs. stress, σ hysteresis obtained for PZT at 35 Hz.*

The obtained hysteresis in Figure 5.7 is similar to the one obtained for PTSm in Figure 5.2.a, excepted some differences in the tip shape which is sharper in the PZT case. This is due to supplementary nonlinear terms in PZT. The piezoelectric coefficient dependences on stress amplitudes, σ_0 are presented in Figures 5.7 and 5.8 for PZT and PNN-PZT respectively.

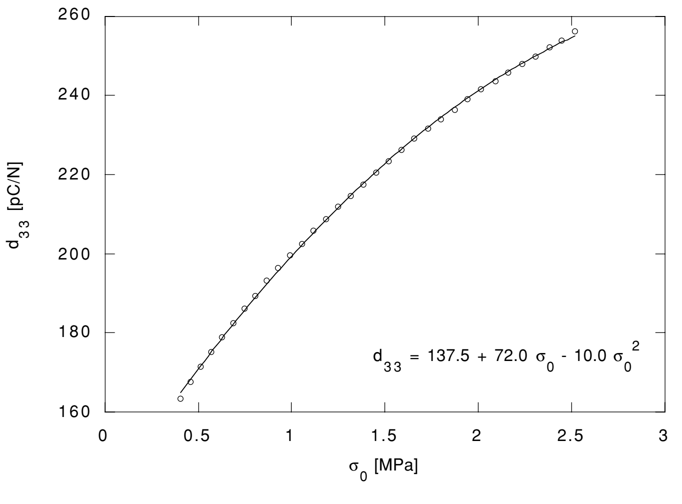

Figure 5.7: *Piezoelectric coefficient, d_{33} vs. stress amplitude obtained for PZT at 35 Hz. The solid line represents a second order polynomial fit to Equation (5.17) which result is displayed in the graph.*

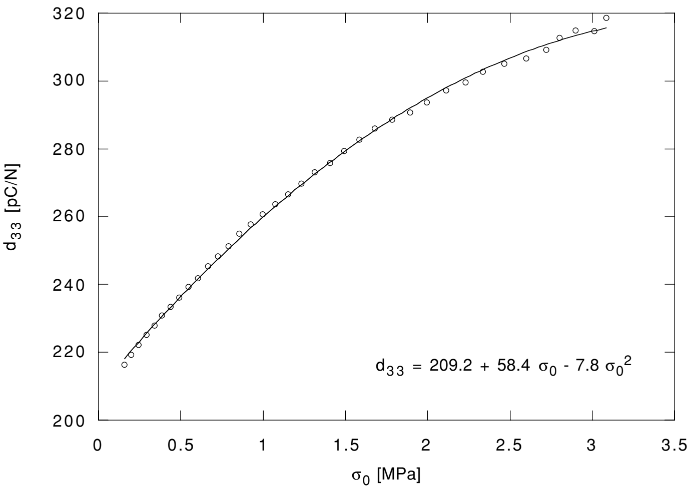

Figure 5.8: *Piezoelectric coefficient, d_{33} vs. stress amplitude, σ_0 obtained for PNN-PZT at 1 Hz. The solid line represents a second order polynomial fit to Equation (5.17) which result is displayed in the graph.*

The d_{33} dependence on stress amplitude in Figures 5.7 and 5.8 are completely different from PTSm (Figure 5.2.b) as a strong quadratic dependence is observed. It has been shown in the previous chapter how such a behavior can be rigorously described by the Preisach model. However, in a rough approximation, the quadratic dependence can be seen as a field dependence of the Rayleigh parameter, α:

$$d_{33} = d_0 + (\alpha + \beta\sigma_0)\,\sigma_0 = d_0 + \alpha\,\sigma_0 + \beta\,\sigma_0^2 \tag{5.17}$$

Thus, the experimental hysteresis obtained for PZT and PNN-PZT were fitted with Equations (5.11) and (5.13) (with the d_0 held constant at the zero field values of 137.5 and 209.2 pC/N as fitted in Figures 5.7 and 5.8 to ease fit convergence). The obtained stress dependences of the Rayleigh parameter, α, are presented in Figures 5.9 and 5.10, for PZT and PNN-PZT, respectively.

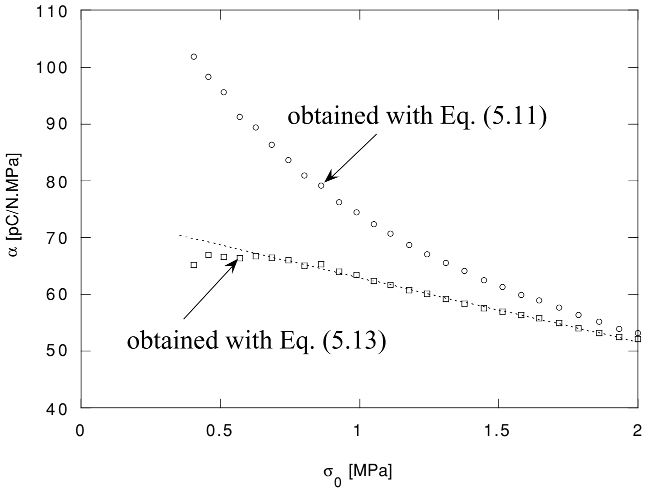

Figure 5.9: *Dependence of the Rayleigh parameter,* α *on stress amplitude,* σ_0 *for a purely field-dependent model (circles) and a mixed model (squares) in the case of PZT. The dotted line represents a linear fit to the* α *obtained by Equation (5.13).*

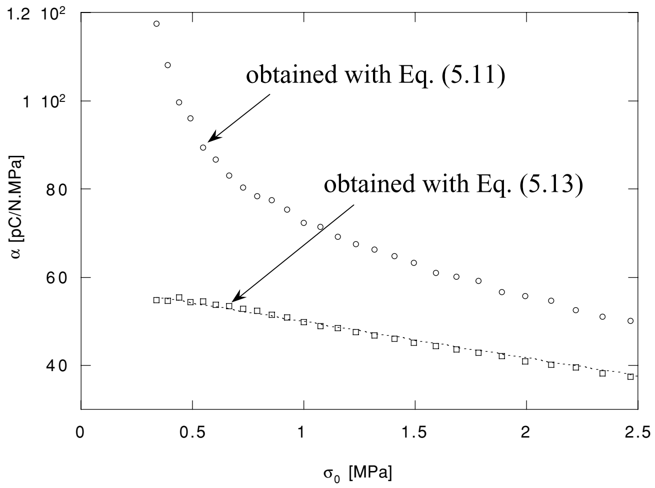

Figure 5.10: *Dependence of the Rayleigh parameter,* α *on stress amplitude,* σ_0 *for a purely field-dependent model (circles) and a mixed model (squares) in the case of PNN-PZT. The dotted line represents a linear fit to the* α *obtained by Equation (5.13).*

When the purely field-dependent model of Equation (5.11) is used, the α vs. σ_0 dependences of both PZT and PNN-PZT show approximately a $1/\sigma_0$ dependence superimposed on a linear behavior ($\alpha \propto A + B\sigma_0 + C/\sigma_0$). As for PTSm, this probably indicates the presence of viscous losses unaccounted for by the purely field dependent model.

The case is much clearer for the α obtained after fitting with the mixed model of Equation (5.13). There, an approximately linear dependence of α on σ_0 is observed ($\alpha \propto A + B\sigma_0$) for both materials. Fitting these linear dependences yields a slope value, B, and an extrapolated value at zero stress, A. In our linearized model of quadratic dependence of d_{33} on σ_0, these last values (A and B) should correspond respectively to the parameters α and β in Equation (5.17). These parameters are compared for PZT and PNN-PZT in Table 5.1.

Table 5.1: *Comparison of stress dependency parameters of the nonlinear coefficient for PZT and PNN-PZT.*

	PZT	PNN-PZT
A [pC/N.MPa]	72.2	58.3
α [pC/N.MPa]	72.0	58.4
B [pC/N.MPa^2]	-9.8	-8.3
β [pC/N.MPa^2]	-10.0	-7.8

The A and B values are indeed very close to what is measured on the $d_{33}(\sigma_0)$ curves by completely different means. It confirms that our linearized model of Equation (5.17) is a good approximation of the actual loop behavior. Moreover, the converging values of Table 5.1 clearly demonstrate the link between the piezoelectric hysteresis and the coefficient nonlinearity, in agreement with the Preisach model. However, for the mixed model to truly hold for description of hysteresis and associated losses in piezoelectrics, the viscous loss tangent obtained from fitting with Equation (5.13) presented in Figures 5.11 and 5.12 has to remain constant with σ_0.

In our rough model, the fitted viscous loss tangent, tg δ_V for PZT and PNN-PZT are approx. constant with stress amplitude, σ_0. The deviations observed from the mean value are probably due to the partial inadequacy of the Rayleigh loop expression (Equation (5.11)) which is, for instance, unable to yield a quadratic field dependence of d_{33}. Moreover, note that the presented viscous loss tangent variation are obtained for a fit of half of the loop only. The reason for choosing half loop values comes from the fact that direct piezoelectric measurements are performed under asymmetrical stress conditions (see Figure 4.11). The bias stress induces loop asymmetry leading to strong departure from Rayleigh type for one half of the loop which influence the fit of the full loop. Moreover, the fitting procedure may introduce some artifacts in the viscous characterization at high stress as Rayleigh-type contributions become predominant. Still, as tg δ_V fitted values for full and half loops are converging for low stress hysteresis (i.e. where the overall loops show less deviation from Equation (5.13)), the results shown in Figures 5.11 and 5.12 certainly account for the actual viscous losses behavior in this asymmetrical case.

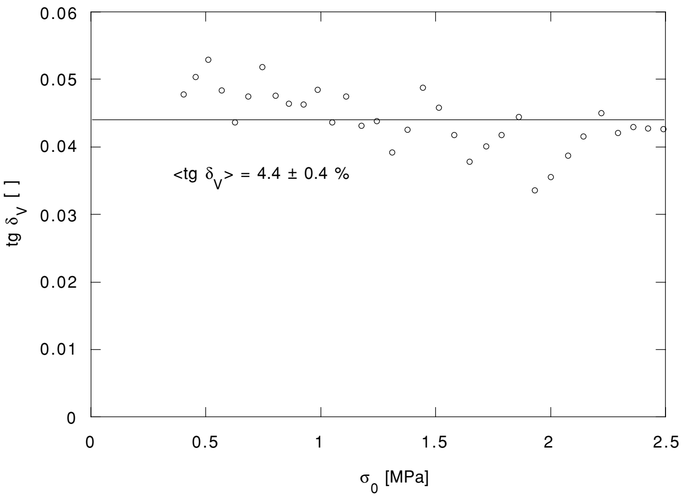

Figure 5.11: *Stress amplitude, σ_0 dependence of the viscous loss tangent, tg δ_V obtained when fitting half of PZT hysteresis with Equation (5.13).*

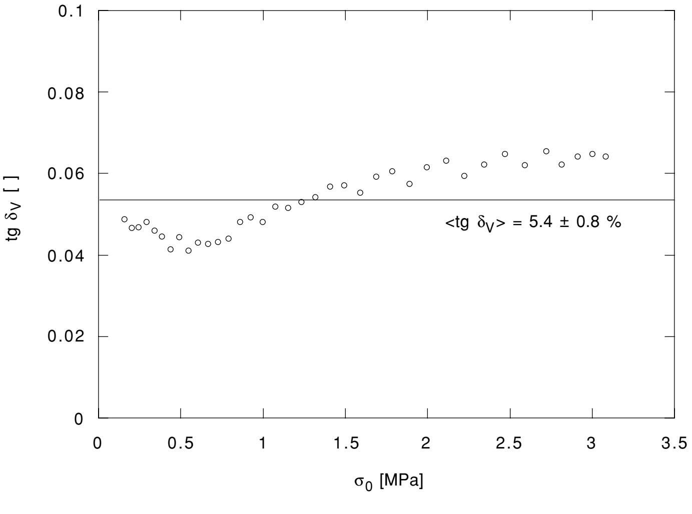

Figure 5.12: *Stress amplitude, σ_0 dependence of the viscous loss tangent, tg δ_V obtained when fitting half of PNN-PZT hysteresis with Equation (5.13).*

The quite constant behavior of half loop tg δ_V along with the $1/\sigma_0$ α dependence obtained when fitting with a pure Rayleigh behavior (Figure 5.9) strongly advocate for the adequacy of the mixed model for high performance piezoelectrics such as PZT and PNN-PZT. Finally, PZT and PNN-PZT complex frequency relaxation, similar to that of PTSm, prevent the calculation of an apparent piezoelectric viscosity. Nevertheless, losses in ferroelectrics can in general be more precisely described by a mixed model containing both viscous and field-dependent losses as in Equation (5.13) rather than by any model separately. Of course, as in the case of PTSm, a viscous description may sometimes be sufficient.

To further confirm the adequacy of the proposed mixed model, loss calculations using the loop area method were performed. The hysteresis areas represent the total of the losses of a given system during one cycle. Based on the relations used by Damjanovic [20], it is possible to calculate the loop area generated by a pure Rayleigh mechanism and hence predict the losses as if Rayleigh mechanisms only were responsible for the observed losses (similarly to Equation (5.14)). Here, to take into account the stress dependence of α for the loop area calculation, some approximations were necessary which unfortunately limit the validity of the calculated area to low stress levels. In this range, the losses caused by the extended Rayleigh mechanism are approximated by:

$$\mathrm{tg}\,\delta_R = \mathrm{tg}\left(\frac{4\,\alpha\,\sigma_0 + 6\beta\,\sigma_0^2}{3\,\pi\,d_{33}}\right) \tag{5.18}$$

where α and β are the nonlinear parameters obtained from fitting the piezoelectric coefficient dependence on stress amplitude by Equation (5.17). The obtained loss values by the different methods (directly measured, calculated from loop area integration and obtained from d_{33} vs. σ_0 dependence) are compared in Figures 5.13 and 5.14 for PZT and PNN-PZT respectively. The difference between the calculated losses from a strictly field-dependent model (Equation (5.18) expression) are always lower than the actually measured losses by a constant value, tg δ_Δ, for both PZT and PNN-PZT (see Figures 5.13 and 5.14). In our mixed losses model, this constant offset should correspond to the viscous losses, the corresponding values are compared in Table 5.2.

Table 5.2: *Comparison of viscous losses obtained by hysteresis fitting (tg δ_V) and by area substraction of Rayleigh-like contributions (tg δ_Δ).*

	PZT	PNN-PZT
tg δ_V [%]	4.4 ± 0.4	5.4 ± 0.8
tg δ_Δ [%]	3.7 ± 0.5	4.6 ± 0.5

Error is given by one standard deviation.

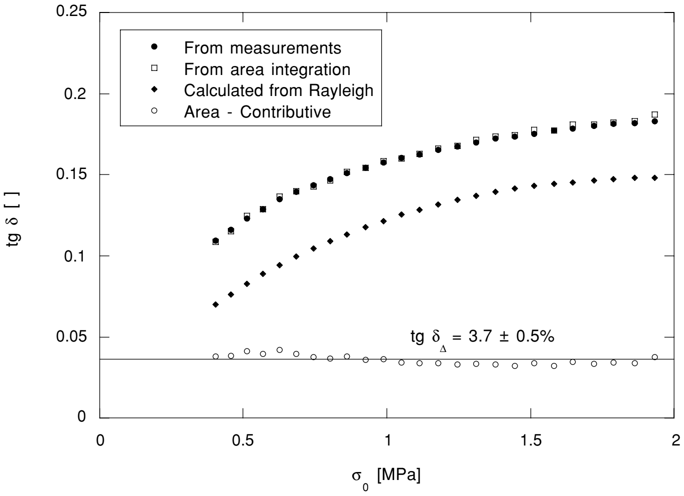

Figure 5.13: Stress amplitude, σ_0, dependence of losses, tg δ, obtained from measurements (full circles), area integration (triangles) and Rayleigh loop area calculation (diamonds) for PZT. The difference between actual and calculated losses, tg δ_Δ, is represented by open circles.

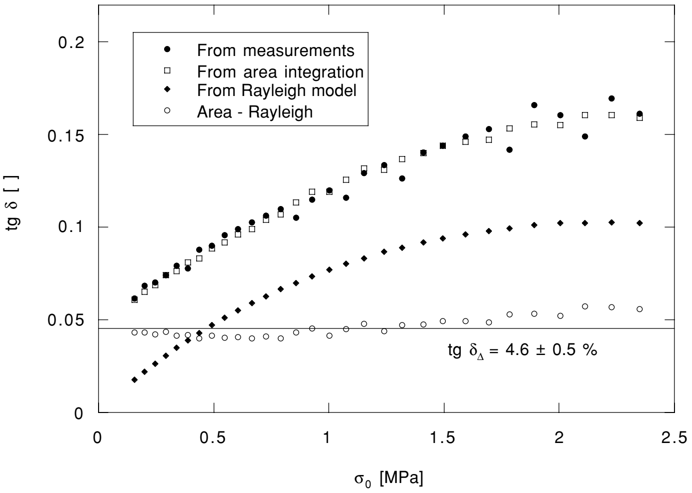

Figure 5.14: Stress amplitude, σ_0, dependence of losses, tg δ, obtained from measurements (full circles), area integration (open squares) and Rayleigh loop area calculation (diamonds) for PNN-PZT. The difference between actual and calculated losses, tg δ_Δ, is represented by open circles.

The loss tangents values presented in Table 5.2 are overlapping, even though they were obtained by completely different means. Hence, PZT and PNN-PZT seem to be best described by a model coupling both viscous and field-dependent losses. Moreover, these mechanisms can be effectively separated by the fitting procedure outlined above.

5.2.4 Loss mechanisms in piezoelectrics

The mixed model presented here has been shown to describe the loss features of piezoelectrics such as PTSm, PZT and PNN-PZT, but the question of the physical mechanisms behind these two separate loss types remains open. Concerning viscous losses, two different mechanisms were proposed by Postnikov *et al.* [27, 28] for the description of mechanical losses (internal friction) in PZT. Although mechanical anelasticity is not an actual viscous piezoelectric process, the mechanisms proposed here suggest that mechanical viscosity may have an effect on the apparent piezoelectric friction (as in Equation (5.6)). Experimentally, Postnikov observed two relaxation peaks for internal friction as function of temperature which were identified with two different mechanisms involving charged DW:

> **a** – Vibration damping of 90° DW [27]: at rest, mobile charged defects diffuse toward DW. Upon stress application DW are instantaneously displaced, and the restoring force is in part determined by the electrostatic interaction between DW and the previously pinned defects. After a certain period, the defects diffuse toward DW new position and reduce the total restoring force.
>
> **b** – Charge varying 90° DW [28]: upon application of shear stress on 90° domains, the solution to the Poisson's equation yields an apparition of charges on the corresponding DW. Thus, created charges attract the mobile charged defects according to their sign. Hence, when the applied shear stress is varied, losses arises due to the alternate drift of charged defects.

Postnikov *et al.* [29] later identified the **a** and **b** mechanisms with, respectively, the low and high temperature internal friction relaxation peaks observed in PZT. Concerning the charged 90° DW implied by these mechanisms, it has been observed by Arlt and Sasko [30] for $BaTiO_3$ that charged domain configurations do appear and, lately, Yin and Cao [31] demonstrated the existence of charged domain walls in 0.955 PZN-0.045 PT single crystals. Hence, the concentration of mobile charged defects in the material could be one of the controlling factor of viscous losses for a given DW density. However, to discuss the obtained piezoelectric viscosity for PZT and PNN-PZT in terms of Postnikov's proposed mechanisms quantitatively, the case of 90° DW motion and their interaction with elastic defects would have to be taken into account (like in Ref. [9]).

Concerning the mechanisms leading to field-dependent losses, it has been said in the Preisach approach introduction in section 4.1.3 that they could be linked to the displacement of

DW in a stochastic pinning field [32] superimposed on a "smooth" potential to account for restoring forces. Hence, for a pinning roughness being of the order of the applied field but much greater than thermal activation, only field-dependent losses should be observed. However, if the lower energy scale of the roughness is on the order of thermal activation energy, as illustrated in Figure 5.15, then both field-dependent and viscous losses should be observed.

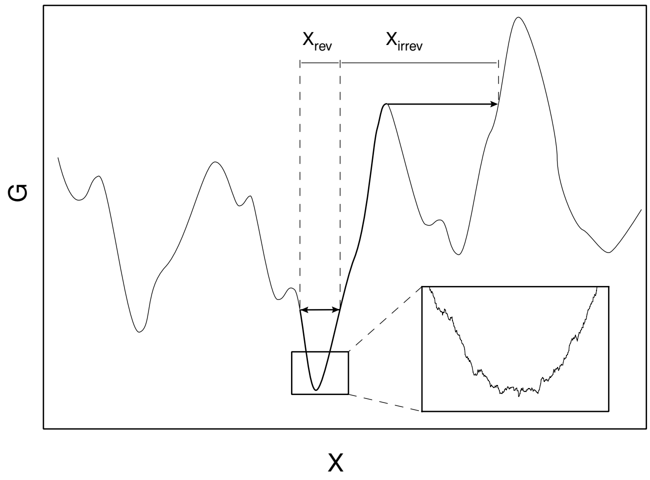

Figure 5.15: *Schematic representation of the proposed pinning energy profile, G to account for field dependent losses (large scale roughness) and viscous losses (inset, low scale roughness). X represents the position of the DW.*

After application of the field, a DW would rapidly move to a new metastable position (at $x = x_{rev} + x_{irrev}$) contributing irreversibly to the piezoelectric response and then relax on the smaller roughness because of thermal activation (as described by Arlt [9]) leading to an overall behavior close to the proposed mixed model. This mechanism could also explain the observed frequency dependence of nonlinear parameters (α and d_0) observed for PZT [20]. Hence, in the case of PTSm, one may assume that 90° DW are trapped in potential wells (inset of Figure 5.15) due to the high spontaneous deformation and the large number of defects induced by the Sm^{3+} doping. Hence, PTSm exhibit viscous losses only as charged defect are interacting with DW. In the case of soft ferroelectrics, the roughness height distribution might go from levels lower than thermal activation energy up to values of the order of the macroscopic coercive fields and, thus the observed response exhibits a mixed loss behavior.

5.2.5 Conclusion

A mixed model for the losses integrating both viscous and field-dependent (Rayleigh type) mechanisms has been proposed for the description of subswitching piezoelectric hysteresis in ferroelectrics. This model describes accurately the observed hysteresis in linear (PTSm) and nonlinear (PZT, PNN-PZT) ferroelectrics. Moreover, it is fully compatible with the experimental observations of piezoelectric coefficient applied field dependence. Most experimental artifacts were excluded as shown by the characterization of PTSm with such a model using both direct and converse piezoelectric effects yielding very similar results. In particular, this model shows that, contrary to what is usually assumed in the literature, for the most general description of piezoelectric losses, it is inadequate to consider losses as viscous only, field-dependent losses have also to be considered. In this perspective, first value of the apparent piezoelectric viscosity could be obtained for PZT under the quasi-static approximation. Finally, interpretations of the observed viscous losses were given in terms of mobile charged defects interacting with moving charged DW and of DW pinning energy roughness ranges.

5.3 ADVANCED PREISACH DESCRIPTION OF HYSTERESIS

In the previous section, the most basic type of hysteresis that can be obtained through the Preisach approach (with a constant distribution) was used to model the hysteresis of piezoelectrics. As shown in Chapter IV, the Preisach distribution corresponding to the actual nonlinearities in soft ferroelectrics is actually more complicated than a constant value. It is the purpose of this section to exploit the possibilities of hysteresis modelling using more elaborate expressions of the distribution function. This presents an interest from both basic and applied point of views. Practically, a more precise description of the hysteresis may help to control more effectively the displacement of an actuator. Scientifically, the extraction of the distribution parameters from a series of measured hysteresis loops is interesting in order to get informations on the distribution shape.

Thus, in this section, the formula describing the hysteresis associated with the corrected roof-like distribution (cf. section 4.3.4) will be calculated. After fitting experimental hysteresis loops with this expression, the resulting distribution parameters will be compared to the ones obtained in the previous chapter by a different method (see section 4.3.4). Finally, to explore the versatility of Preisach loop description, pinched (or constricted) loops modeling will be treated by proposing a physically sound distribution function and deriving the resulting analytical expression for the associated pinched loop.

5.3.1 Fitting hysteresis for distribution parameters

It was shown in the previous section that nonlinear parameters could be extracted from the loops using an appropriate expression derived from the Rayleigh loop equation. As actual distribution functions in PZT and PNN-PZT are quite different from the Rayleigh one, the general formula of the associated loop is more complex. If fitting the experimental hysteresis with such an expression is possible, it should yield the corresponding distribution function parameters. Thus, the equation of the loop corresponding to the corrected roof distribution function (see section 4.3.4) was calculated. As a reminder, the distribution function is given by (Equation (4.26)):

$$f(\sigma_i, \sigma_c) = f_0 + g\,\sigma_c + k\,\mathrm{Abs}(\sigma_i) + j\,\sigma_c \mathrm{Abs}(\sigma_i) \tag{5.19}$$

Again, as the exact total response of one bistable unit is not known ($\mathcal{R}_0$ in Equation (4.11)), the parameters used here are in fact the equivalent parameters (see section 4.3.4). When the distribution of Equation (5.19) is integrated along Equations (4.8) and (4.9), the following expression for the loop is obtained:

$$\begin{aligned} D = {} & -\frac{k\,\sigma_0^3}{4} - \frac{j\,\sigma_0^4}{24} + \left(d_0 + f_0\,\sigma_0 + k\,\sigma_=\,\sigma_0 + \frac{g\,\sigma_0^2}{4} - \frac{j\,\sigma_=\sigma_0^2}{4}\right)\sigma \\ & + \frac{k\,\sigma_0}{4}\,\sigma^2 + \left(\frac{g}{12} + \frac{j\,\sigma_=}{12}\right)\sigma^3 - \frac{j}{24}\sigma^4 \\ & + \mathrm{Sign}\left(\frac{d\sigma}{dt}\right)\left[\frac{f_0\,\sigma_0^2}{2} + \frac{k\,\sigma_=\,\sigma_0^2}{2} + \frac{g\,\sigma_0^3}{4} + \frac{j\,\sigma_=\,\sigma_0^3}{4} + \left(\frac{k\,\sigma_0^2}{4} + \frac{j\,\sigma_0^3}{12}\right)\sigma \right. \\ & \left. + \left(-\frac{f_0}{2} - \frac{k\sigma_=}{2} - \frac{g\sigma_0}{4} - \frac{j\sigma_=\sigma_0}{4}\right)\sigma^2 + \left(-\frac{k}{4} - \frac{j\,\sigma_0}{12}\right)\sigma^3\right] \end{aligned} \tag{5.20}$$

The experimental hysteresis obtained for the PZT 60/40 sample at 3.5 MPa bias stress used in section 4.3.4 were then fitted to this loop expression extended by a viscous term. As the number of parameters is quite large, it was necessary to keep the k and the d_0 parameters constant (at -48.1 PC/N.MPa^2 and 139 pC/N, respectively) to improve the fit convergence. A typical hysteresis with its fitted function is presented in Figure 5.16.

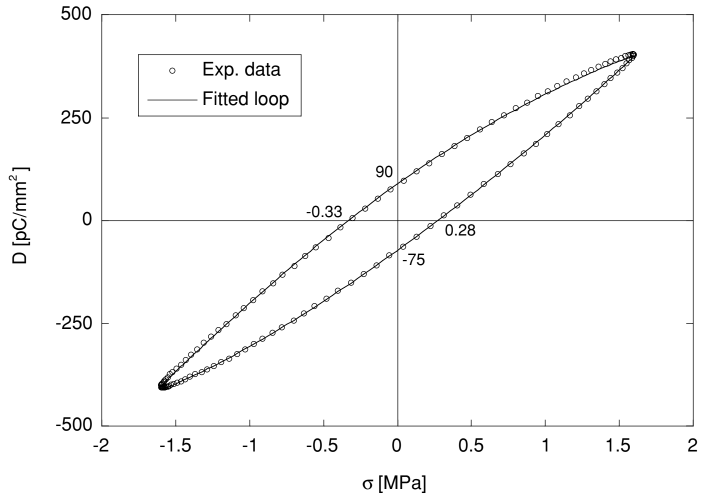

Figure 5.16: *Example of PZT 60/40 loop fitted with Equation (5.20) and a viscous term with indication of axes intersecting values.*

The agreement of the fit with the experimental loop is very good. Note that the loop asymmetrical shape (observable on the axes-cutting values) is very well described by the model. However, agreement with loops is not sufficient to demonstrate the description pertinence of Equation (5.20) as piezoelectric coefficient nonlinearity should also be modeled by the obtained parameters. Thus, the piezoelectric coefficient field dependence was recalculated from the fitting parameters and the expression derived from the corrected roof-like distribution (equivalent to Equation (4.21)):

$$d_{33} = d_0 + (f_0 + k\,\sigma_=)\,\sigma_0 + \frac{1}{3}\,(g + j\,\sigma_=)\,\sigma_0^2 \tag{5.21}$$

Then, the obtained nonlinear piezoelectric coefficients were compared with the experimental values, as shown in Figure 5.17 where the values obtained by completely different means (either direct measurement or by hysteresis-based reconstruction) are exactly superimposing.

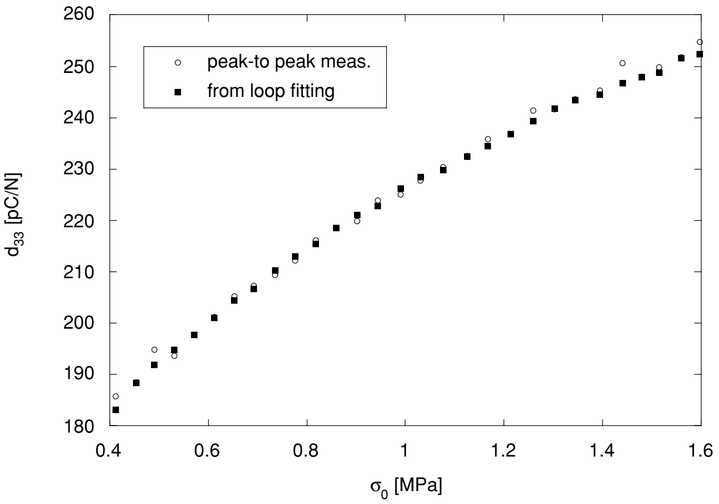

Figure 5.17: *Generated piezoelectric coefficient,* d_{33} *vs. stress amplitude,* σ_0 *(through Equation (5.21)) compared to values measured classically.*

Although the agreement between the different piezoelectric coefficients is very good, the values of the distribution function parameters have also to remain constant with varying stress amplitude. This is demonstrated in Figure 5.18 for the f_0 parameter (equivalent to α in Rayleigh law).

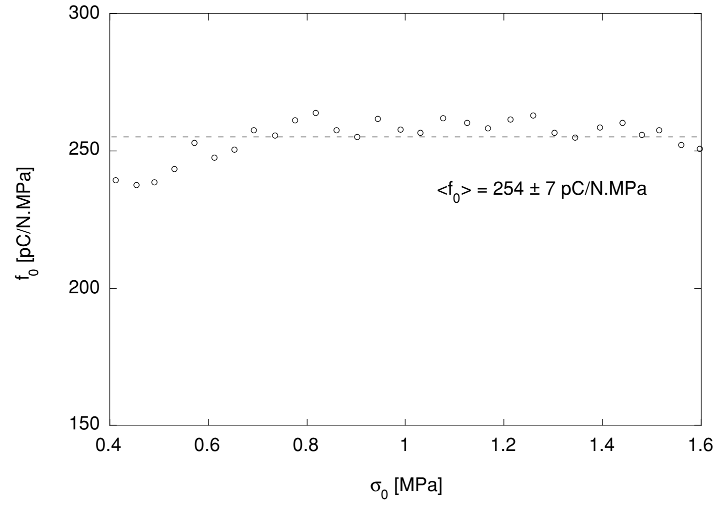

Figure 5.18: *Stress amplitude,* σ_0 *dependence of the fitted* f_0 *parameter.*

The g and j parameters values are varying a bit more with stress amplitude, especially at low σ_0 because of the decreasing nonlinear character of the loops. However, for high enough amplitudes (i.e. $\sigma_0 > 0.8$ MPa), their values were dispersed but acceptably constant as shown by the errors reported in Table 5.3. This table compares the values obtained by loop fitting and by direct experimental determination. Given the complexity of both experiments and fitting procedure, the fact that the obtained equivalent parameters are within the same order of magnitude (and even closer) is a further confirmation of the applicability of the Preisach approach to the description of the hysteresis as well as for the piezoelectric coefficient nonlinearity.

Table 5.3: *Comparison of the equivalent distribution parameters obtained by loop fitting and by varying bias stress measurements (reported from section 4.3.4).*

	f_0 [pC/N MPa]	k [pC/N MPa^2]	g [pC/N MPa^2]	j [pC/N MPa^3]
Loop fitting	254 ± 7	-48.1[†]	-592 ± 104	156 ± 29
Varying $\sigma_=$	297	-48.1	-496	108

[†] k parameter was held constant during the fit. Errors are given by one standard deviation.

Finally, strong nonlinearity of PZT and PNN-PZT loops caused problems when fitting full loops for the viscous loss tangent, tg δ_V using a Rayleigh law-based equation (see section 5.2.3). With the new expression given in Equation (5.20) combined with a viscous term, the fitting of the experimental hysteresis is more accurate and yields viscous loss tangents for the whole loop, as presented in Figure 5.19.

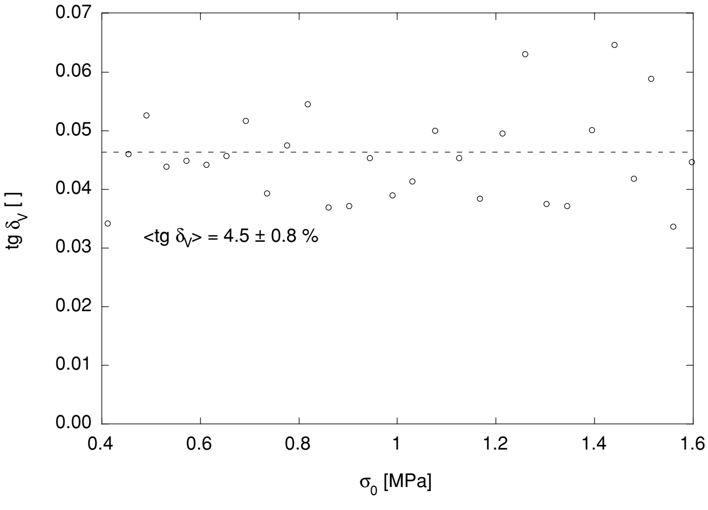

Figure 5.19: *Stress amplitude, σ_0 dependence of the viscous loss tangent, tg δ_V.*

Note that in this case, the viscous losses have been measured on the full hysteresis and are independent on stress amplitude. This fact demonstrates, once again, the adequacy of the proposed loop description combining the corrected roof-distribution function with viscous losses.

5.3.2 Pinched loops description

After demonstrating how the Preisach approach combined with dynamic effects can account for nonlinear piezoelectric hysteresis, it is of interest to show how more exotic experimental loops can be described in such an approach. Pinched (or constricted) ferroelectric loops are often encountered in ferroelectrics [5-7]. Their interpretation is based on the classical paper of Carl and Härdtl [5] who related pinched loops in Mn or Fe doped lead zirconate titanate, Pb(Zr,Ti)O_3, with the presence of charged defects by analyzing ferroelectric loop evolution with respect to the number of field cycles. They proposed two different qualitative mechanisms to explain the apparition of such loops: domain wall pinning due to diffusion of charged defects and volume effects leading to alignment of dipolar defects with the surrounding polarization. In both cases, domain walls displacement is affected by the presence of the considered defects which in turn determine the hysteresis shape. In the following, the Preisach approach will be used to determine whether information on the defects properties can be obtained through an analytical description of the pinched loops and, in an inverse problem, whether it is possible to derive an expression for the loop from the knowledge of the defect structure.

Polarization hysteresis in ferroelectrics originates in displacement of domain walls, defects and their interactions [33]. In the case of ferroelectric pinched loops, dipolar defects proposed by Carl and Härdtl [5] can very well stand for the bistable units considered in the Preisach approach. Even though microscopical mechanisms related to domain wall displacement and dipolar defects interactions are still unclear, the domain wall motion can be assumed, in our case, to be controlled by the dipolar defects behavior. Due to the presence of space charges in the material, defect dipoles will be subjected to distributed internal electric fields. Moreover, spontaneous strain associated to the paraelectric-ferroelectric phase transition will lead to distributed mechanical boundary conditions. As dipolar defects in ferroelectrics, especially those associated with oxygen vacancies, are also elastic dipoles [10, 34], their switching characteristics will depend on the strain field. Consequently, the combined effects of inhomogeneous mechanical and electrical internal fields will result in distributed coercive fields for the dipolar defects [34]. Thus, we will start from the defect distribution point of view. First, some general shape for the defect structure within the material will be proposed. Then, a suitable and integrable mathematical form as close as possible to the proposed distribution will be put forward. From integration over the working range, the loop will eventually be calculated. Note that the procedure followed here is reverse with respect to the classical Preisach method which is usually looking first for loop or coefficient properties (as above) and then to distribution functions to describe accurately the observed hysteresis.

The defect dipoles contained in the ferroelectric material are considered as bistable units. Their switching behavior can be described by a coercive field, $\mathcal{F}_c$, and an internal field, $\mathcal{F}_i$, either positive or negative depending on the orientation of the considered dipole with respect to the surrounding polarization orientation. This switching behavior will in the end determine the loop properties through their dominating influence on domain wall motion behavior. In a well aged material, according to Carl and Härdtl [5], majority of dipolar defects within grains are oriented along the polarization direction of individual domains. But as domain walls move upon field application, they may switch to another direction. To match such a defect structure, a distribution with a double maximum is appropriate and can be described by, for example, a 4th order polynomial symmetric in terms of bias field ($\mathcal{F}_i$) combined with a cut-off at high coercive field level ($\mathcal{F}^*$) (see Figure 5.20):

$$f(\mathcal{F}_i, \mathcal{F}_c) = \begin{cases} -c\mathcal{F}_i^4 + k\mathcal{F}_i^2 & \text{if } \mathcal{F}_c < \mathcal{F}^* \text{ and } -c\mathcal{F}_i^4 + k\mathcal{F}_i^2 > 0 \\ 0 & \text{if } \mathcal{F}_c > \mathcal{F}^* \text{ or } -c\mathcal{F}_i^4 + k\mathcal{F}_i^2 < 0 \end{cases} \tag{5.22}$$

Of course, such a function has to be normalized:

$$\int_0^\infty \int_{-\infty}^\infty f(\mathcal{F}_i, \mathcal{F}_c)\,d\mathcal{F}_i\,d\mathcal{F}_c = 1 \tag{5.23}$$

The plot of $f(\mathcal{F}_i, \mathcal{F}_c)$ in Figure 5.20 shows that it consists of a symmetrical distribution peaking at opposite bias fields representing the interaction between the dipole and the surrounding polarization. The whole distribution extends up to a given value of the coercive field $\mathcal{F}^*$ without decrease as mechanical effects on dipoles coercive fields are assumed to be homogeneously distributed and limited in amplitude. The proposed distribution is only one possible mathematical expression for a double maximum topography and was chosen to permit explicit integration of the distribution function for loop computation. A physically more realistic distribution and a sounder dependence on $\mathcal{F}_c$ may be obtained by two superimposed Gaussian functions. While this would probably lead to even more realistic results, it will require numerical integration and hence cannot easily yield an analytical result.

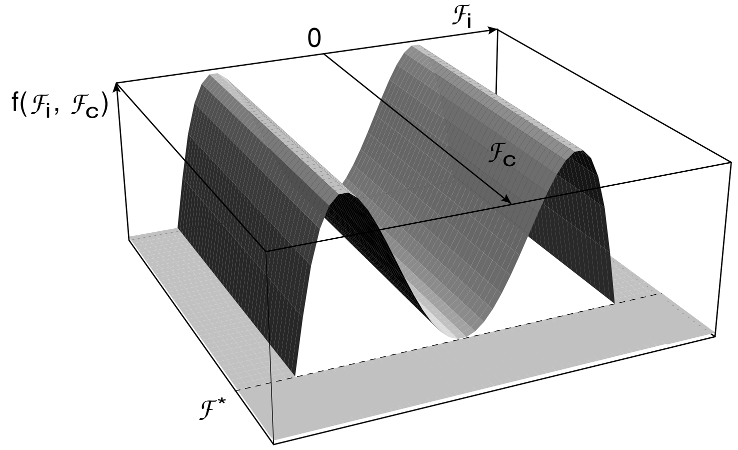

Figure 5.20: *Plot of the proposed polynomial distribution function for a system containing dipolar defects oriented in different directions.*

Upon integration of Equation (5.22) following Equation (4.8) and Equation (4.9), an analytical expression for the loop was obtained using an alternating field given by $\mathcal{F} = \mathcal{F}_0 \sin(\omega t)$:

$$
\begin{aligned}
P = {} & \left(d_0 + \frac{\mathcal{F}_0^3 k}{12} - \frac{\mathcal{F}_0^5}{80}\right)\mathcal{F} + \left(\frac{\mathcal{F}_0 k}{12} - \frac{\mathcal{F}_0^3}{24}\right)\mathcal{F}^3 - \frac{\mathcal{F}_0}{80}\mathcal{F}^5 + \\
& \mathrm{Sign}\left(\frac{d\mathcal{F}}{dt}\right)\left[-\frac{\mathcal{F}_0^4 k}{48} + \frac{\mathcal{F}_0^6}{480} + \left(-\frac{\mathcal{F}_0^2 k}{8} + \frac{\mathcal{F}_0^4}{32}\right)\mathcal{F}^2 + \left(\frac{7k}{48} + \frac{\mathcal{F}_0^2}{32}\right)\mathcal{F}^4 - \frac{31\mathcal{F}^6}{480}\right]
\end{aligned}
\tag{5.24}
$$

The corresponding loop is presented in Figure 5.21 where d_0, the linear response coefficient is taken as 5, c as 1, k as 25 and the amplitude of the applied field $\mathcal{F}_0$ as 5.

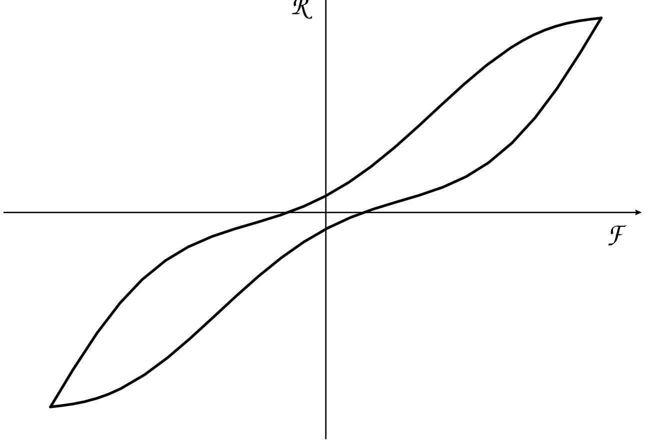

Figure 5.21: *Plot of the loop obtained using Equation (5.24) with $d_0 = 5$, $c = 1$, $k = 25$ and $\mathcal{F}_0 = 5$.*

As parameters were chosen arbitrarily, no normalization was applied. The loop in Figure 5.21 is hence representative of the general shape generated by a distribution such as Equation (5.22). Notwithstanding its apparent awkwardness, Equation (5.24) constitutes the first physically-based analytical expression ever obtained from dipolar defect arrangement in aged ferroelectric materials.

The shape of the obtained hysteresis is clearly close to that in experimentally observed loops [5-7] and constitutes, to our knowledge, the first quantitative (through the distribution function expression and its parameters) and physical description of a pinched loop. As the parameters used for the loop generation are very general, such an approach could be used to quantify the defect structure in any material exhibiting a symmetrically pinched loop.

Finally, even though the Preisach approach is valid for steady-state distribution functions only, if one assumes that distribution is stable during one field cycle, the evolution of the defect distribution with field cycles can be monitored by fitting several consecutive loops. In this particular case, the transition from a pinched loop to a single but heavily shifted loop [5, 6] would correspond to a decrease of one peak of the distribution function while the other is growing as dipoles are orienting in one direction only. In the end, a single peak distribution would be obtained which is actually the characteristic distribution corresponding to a shifted (biased) loop. This evolution is quite similar to what was actually observed in the study of switching current peaks by Carl and Härdtl [5] as a function of the number of cycles indicating that defect distribution functions could certainly be worked out in this way.

In summary, it was shown that pinched loops can be obtained from the Preisach approach. Starting from classical considerations about dipolar defects interaction with their environment, a realistic distribution function was proposed and integrated. It yielded an analytical expression for a pinched loop and permitted to correlate the supposed presence of switchable defect dipoles with the appearance of pinched loops. Considering the possibility to obtain distribution parameters from analytical expressions of the hysteresis loops, the Preisach approach seems quite appropriate to describe various kind of hysteresis and to relate them with actual defect structures.

5.4 SUMMARY

The adequacy of the Preisach description for piezoelectric hysteresis was explored. First, a thermodynamically sound expression for the apparent piezoelectric viscosity was derived. It was then combined with the Rayleigh loop expression to account for both field and frequency dependences of the losses. Such a model of hysteresis was demonstrated to be applicable to PTSm by fitting its viscous-only loops. Then, the possibility of describing the losses in piezoelectrics by two distinct mechanisms (viscous and Rayleigh-like) was proved to be appropriate in the cases of PZT and PNN-PZT. For those materials, it was possible to derive the actual piezoelectric coefficient dependences on the stress amplitude and the viscous losses from the fitting parameters of the loops. Then, the possibility of loop description through more elaborated Preisach distributions was demonstrated by PZT hysteresis fitting with the corresponding loop expression. It yielded distribution function parameters in agreement with the ones obtained with a different method in the previous chapter for the same composition. Finally, the versatility of the Preisach modeling was demonstrated through the derivation of a physically-based distribution function leading to the widely observed pinched-loops.

5.5 REFERENCES

1. P. Ge and M. Jouaneh, *Generalized Preisach model for hysteresis nonlinearity of piezoceramic actuators.* Prec. Eng., (1997) **20** p. 99-111.
2. D. Hughes and J.T. Wen, *Preisach modeling of piezoceramic and shape memory alloy hysteresis.* Smart Mater. Str., (1997) **6** p. 287-300.
3. R. Holland, *Representation of dielectric, elastic and piezoelectric losses by complex coefficients.* IEEE T. Son. Ultra., (1967) **U-14** [1] p. 18-20.
4. D. Damjanovic and M. Demartin, *The Rayleigh law in piezoeletric ceramics.* J. Phys. D: Appl. Phys., (1996) **29** p. 1.
5. K. Carl and K.H. Härdtl, *Electric after-effects in* $Pb(Ti,Zr)O_3$ *ceramics.* Ferroelectrics, (1978) **17** p. 473-486.
6. M. Kohli, P. Muralt, and N. Setter, *Removal of 90° domain pinning in (100)* $Pb(Zr_{0.15}Ti_{0.85})O_3$ *thin films by pulsed operation.* Appl. Phys. Lett., (1998) **72** [24] p. 3217-19.
7. E.G. Lee, D.J. Wouters, G. Willems, and H.E. Maes, *Effects of top electrode annealing on the PZT thin films.* Int. Ferroelectrics, (1997) **16** p. 165-74.
8. J.G. Smits, *Influence of moving domain walls and jumping lattice defects on complex material coefficients of piezoelectrics.* IEEE T. Son. Ultra., (1976) **23** [3] p. 168-74.
9. G. Arlt, *Piezoelectric relaxation.* Ferroelectrics, (1982) **40** p. 149-157.
10. A.S. Nowick and W.R. Heller, *Dielectric and anelastic relaxation of crystals containing point defects.* Adv. Phys., (1965) **14** p. 104-66.
11. B. Lewis, *Energy loss processes in ferroelectric ceramics.* Proc. Phys. Soc., (1960) **73** [1] p. 17-24.
12. J. Fousek and B. Brezina, *Relaxation of 90° domain walls of* $BaTiO_3$ *and their equation of motion.* J. Phys. Soc. Jpn., (1964) **19** [6] p. 830-38.
13. V.M. Rudyak, *On the role of dielectric viscosity in polarization switching processes in ferroelectric crystals.* Bull. Acad. Sci. USSR Phys. Ser., (1969) **33** p. 292-6.
14. B.D. Laikhtman, *Flexural vibrations of domain walls and dielectric dispersion of ferroelectrics.* Sov. Phys. Solid State, (1973) **15** [1] p. 62-8.
15. J.O. Gentner, P. Gerthsen, N.A. Schmidt, and R.E. Send, *Dielectric losses in ferroelectric ceramics produced by domain-wall motion.* J. Appl. Phys., (1978) **49** [8] p. 4485-9.
16. G. Arlt and H. Dederichs, *Complex elastic, dielectric and piezoelectric constants by domain wall damping in ferroelectric ceramics.* Ferroelectrics, (1980) **29** p. 47-50.

17. M. Stula, J. Fousek, H. Kabelka, M. Fally, and H. Warhanek, *Extrinsic contributions to the piezoelectric properties of RbH_2PO_4 crystals in the ferroelectric phase.* J. Kor. Phys. Soc., (1998) **32** p. S758-60.

18. L. Rayleigh, *Notes on electricity and magnetism : III. On the behaviour of iron and steel under the operation of feeble magnetic forces.* Philos. Mag. S. 5, (1887) **23** [142] p. 225-245.

19. L. Néel, *Théorie des lois d'aimantation de Lord Rayleigh. I - les déplacements d'une paroi isolée.* Cah. Phys., (1942) **12** p. 1-20.

20. D. Damjanovic, *Stress and frequency dependence of the direct piezoelectric effect in ferroelectric ceramics.* J. Appl. Phys., (1997) **82** [4] p. 1788-97.

21. A. Magni, C. Beatrice, G. Durin, and G. Bertotti, *Stochastic model for magnetic hysteresis.* J. Appl. Phys., (1999) **86** [6] p. 3253-61.

22. V.L. Gurevich, *Transport in Phonon Systems*. Modern Problems in Condensed Matter Sciences, ed. V.M. Agranovich and A.A. Maradudin. Vol. 18. 1986, Amsterdam: North-Holland.

23. A.V. Shil'nikov, V.N. Nesterov, and A.I. Burkhanov, *Mechanisms of motion of domain and interphase boundaries and their computer simulation.* Ferroelectrics, (1996) **175** p. 145-151.

24. W.H. Press, B.P. Flannery, S.A. Teukolsky, and W.T. Vetterling, *Numerical Recipes in C*. 1998: Cambridge University Press.

25. A.L. Kholkin, C. Wüthrich, D.V. Taylor, and N. Setter, *Interferometric measuremenst of electric field-induced displacements in piezoelectric thin films.* Rev. Sci. Instrum., (1996) **67** [5] p. 1935-41.

26. A.R. von Hippel, *Dielectrics and Waves*. 1954, Cambridge, MA: MIT Press.

27. V.S. Postnikov, V.S. Pavlov, S.A. Gridnev, B.M. Darinskii, and I.A. Glozman, *Internal friction in $Pb_{0.95}Sr_{0.05}(Zr_{0.53}Ti_{0.47})O_3$ + 3% PbO ferroelectric ceramic.* Bull. Acad. Sci. USSR Phys. Ser., (1967) **31** p. 1888-92.

28. V.S. Postnikov, V.S. Pavlov, S.A. Gridnev, and S.K. Turkov, *Interaction between 90° domain walls and point defects of the crystal lattice in ferroelectric ceramics.* Sov. Phys. Solid State, (1968) **10** [6] p. 1267-70.

29. V.S. Postnikov, V.S. Pavlov, and S.K. Turkov, *Internal friction in ferroelectrics due to interaction of domain boundaries and point defects.* J. Phys. Chem. Sol., (1970) **31** p. 1785-91.

30. G. Arlt and P. Sasko, *Domain configuration and equilibrium size of domains in $BaTiO_3$ ceramics.* J. Appl. Phys., (1980) **51** [9] p. 4956-60.

31. J. Yin and W. Cao, *Domain configurations in domain engineered* $0.955Pb(Zn_{1/3}Nb_{2/3})O_3 - 0.045PbTiO_3$ *single crystals.* J. Appl. Phys., (2000) **87** [10] p. 7438-41.

32. G. Bertotti, V. Basso, and G. Durin, *Random free energy model for the description of hysteresis.* J. Appl. Phys., (1996) **79** [8] p. 5764-6.

33. M.E. Lines and A.M. Glass, *Principles and applications of ferroelectrics and related materials*. 1977, Oxford: Calrendon Press.

34. G. Arlt and H. Neumann, *Internal bias in ferroelectric ceramics: origin and time dependence.* Ferroelectrics, (1988) **87** p. 109-20.

CHAPTER VI
PIEZOELECTRIC BEHAVIOR AND CRYSTALLINE STRUCTURE

As pointed out in the introduction, the existence of a morphotropic phase boundary is one of the main characteristics of high performance piezoelectrics. In its vicinity, the dielectric and piezoelectric properties are reaching a maximum. However, the mechanisms associated with this properties increase are still debated. This uncertainty prevents the undertaking of rigorous efforts towards optimization. The successful application of the Preisach description to the piezoelectric response of high performance piezoelectrics suggests that it can lead to a better understanding of such mechanisms. In particular, a Preisach analysis may permit to determine which ratio of extrinsic and intrinsic effects leads to the observed properties peak. Moreover, a temperature dependent MPB was evidenced for PNN-PZT in Chapter III. As it had been demonstrated to be qualitatively equivalent to PZT, such a morphotropic phase boundary allow to explore properties “vertically”, i.e. as a function of temperature rather than “horizontally”, i.e. as a function of composition.

Hence, the goal of this chapter is to provide new experimental evidences about the origins of the high properties at MPB using the piezoelectric modeling developed above. First, the existing scenarios for such an increase in PZT will be briefly reviewed. Then, PZT distribution functions and losses will be characterized as a function of composition. Finally, taking advantage of the temperature dependent MPB, PNN-PZT properties will be measured as a function of temperature for a sample undergoing a morphotropic transition around 50°C. Both studies will permit to monitor the extrinsic contributions across the MPB and discuss the crystallographic influence on the piezoelectric response. As the methods used here are still exploratory, the general approach will be qualitative, attempting to indicate trends in the various piezoelectric contributions rather than giving definite evaluations of the nonlinear mechanisms dependence on crystallography.

6.1 PIEZOELECTRIC PROPERTIES AT MPB IN FERROELECTRICS

Increase in dielectric and piezoelectric properties at the MPB is the reason for wide use of PZT in applications [1, 2], even though there is still debate about the origins of such a peak in properties. Moreover, some confusion occurs because MPB location is not equivalent with the composition where the dielectric or the piezoelectric responses peak. Although the high properties in this region are probably related to the phase transition, their maxima cannot be considered as the definite criteria for the determination of the exact crystallographic position of the morphotropic transition.

Most of the authors have approached the explanation of the high properties at MPB from the thermodynamical point of view. Concerning dielectric properties, phenomenological calculations of permittivities parallel to the polarization direction yielded diverging values on both sides of the MPB [3-5]. Piezoelectric coefficients which are proportional to the permittivity hence also attain a maximum [5]. Such an increase has been recently verified experimentally by Soares *et al.* [6], where lattice parameter dependence of the dielectric permittivities for both phases indicated a monotonic increase of the permittivities while getting closer to the hypothetical position of the MPB. Concerning piezoelectric properties, Heywang [7] and Isupov [8] also explained the increase in properties close to MPB due to the better polarizability of randomly oriented grains when there is more polar directions available upon field application. Using LGD formalism and assuming a second order Curie transition for compositions close to the MPB while neglecting mechanical contributions to the free energy, Benguigui [9] derived that close to T_C coercive fields at MPB have an infinitely low value. Hence, the 3 polar structures appearing in the perovskite system (tetragonal, orthorhombic, and rhombohedral) can be obtained and susceptibility is practically going to infinity in this region as any field applied will lead to a polarization tilt along the most favorable direction among the three crystallographic systems.

Extrinsic contributions have also been studied [8, 10, 11] as in the MPB region usual DW contributions are augmented with interphase boundary motion [8, 12]. Such interphase domain walls (IDW) correspond to the interface between tetragonal and rhombohedral phases coexisting in one grain. Across such boundaries, the misorientations of the polarization vector are 54.74° or 125.26° (i.e. $\mathrm{acos}(\pm 1/\sqrt{3})$). Hence, these IDW can be associated to non-180° DW which may contribute to the total electro-mechanical response. Moreover, assuming equivalent values of the spontaneous polarization in both phases, IDW are charged [8]. They will thus interact with electrical defects more than regular neutral DW and contribute significantly to the piezoelectric viscosity. However, the mechanism of motion of these IDW remains open as there are no direct crystallographic transition accounting for the tetragonal/rhombohedral morphotropic phase boundary [13]. Hence, a local hysteresis of motion is to be expected due to the necessity of having an indirect transition from tetragonal to rhombohedral and vice-versa. Nevertheless, if the monoclinic bridging phase for PZT proposed by Noheda *et al.* [14] does exist, then such a transition might be eased. In any case, the extrinsic contributions may be linked to the motion of some contributing defects (e.g. DW or IDW) in a pinning energy potential. Hence, the total of extrinsic contributions will be dependent either on the contributing defects number or on the average contribution per defect which is inversely proportional to the roughness of the pinning energy profile.

6.2 COMPOSITIONAL DEPENDENCE OF PIEZOELECTRICITY IN PZT

As the best documented piezoelectric, PZT is the material of choice for the study of the effects of the crystalline phases on the piezoelectricity at constant temperature. Although the extrinsic contributions with respect to composition were already approached (see e.g. Refs. [15-17]), no rigorous study taking into account the various nonlinear effects evidenced in Chapters IV and V was ever conducted. In this section, the reversible, irreversible and viscous contributions will be separated and analyzed for various PZT compositions using the approach developed in the previous chapters.

6.2.1 Experimental

PZT samples with compositions ranging from 40 to 65 mol% PZ were characterized using direct piezoelectric measurements. They were first poled at 80°C during 15 min and cooled without field. Then, they were placed in the piezoelectric press described in section 4.3.1 and were all stabilized under the same conditions ($\sigma_{=} = 4.5$ MPa and $\sigma_0 = 3$ MPa) during 2 hours. Afterwards, piezoelectric response was measured as a function of stress amplitude (up to 3 MPa) for bias stresses varying between 2.5 to 3.5 MPa at two different frequencies (1 and 35 Hz). At all moments, the temperature was kept constant at 25 ± 0.1°C.

The overall piezoelectric coefficients were obtained by fitting both the applied stress and charge response with sinusoidal functions and calculating the amplitudes ratio. To obtain the distribution functions parameters a special fitting procedure based on the corrected roof-like distribution (see section 5.3.1) was developed. Rather than adjusting the loop equation to one hysteresis at a time, this procedure fits all the measurements performed for one bias stress with the same set of parameters. Equation (5.20) plus a viscous term (which derivative was calculated through Equation (5.16)) is used in order to determine the corrected roof distribution parameters, f_0, g, k, j and the viscous loss tangent tg δ_V for each bias stress. During this procedure, the intrinsic and reversible response coefficient, d_0, is kept constant at the value obtained by fitting the overall piezoelectric coefficient dependence on stress amplitude with a second order polynomial. Finally, confidence band of the adjusted parameters was calculated under the assumption that the proposed loop expression was adequate using the Student law and setting the confidence width at 95 %. An example of such a fit is displayed in Figure 6.1 where the piezoelectric dielectric displacement signals corresponding to different stress amplitudes are juxtaposed.

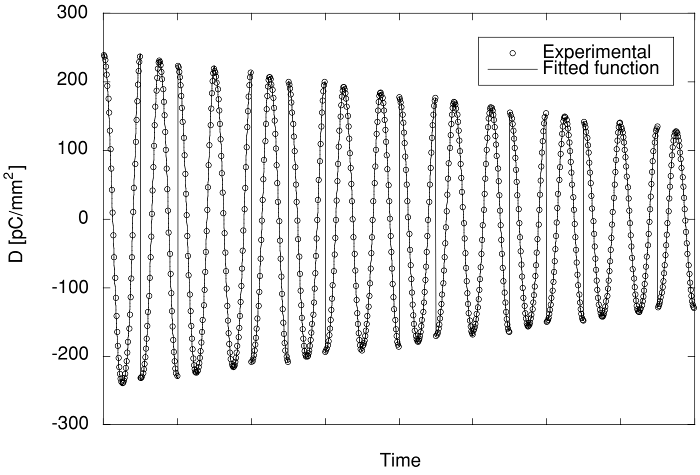

Figure 6.1: *Dielectric displacement data, D (circles) and their fit by Equation (5.20) plus a viscous term for a 45/55 PZT sample at* $\sigma_=$ *= 3 MPa for different* σ_0 *values.*

6.2.2 Distributions characteristics across MPB

The intrinsic and reversible contributions, d_0, obtained at 1 and 35 Hz from the overall piezoelectric coefficient dependence on the applied stress amplitude are presented in Figure 6.2. The d_0 values obtained at 35 Hz are slightly lower than those measured at 1 Hz. This has already been observed for PZT [18] and may be related to relaxing reversible contributions. In any case, a clear peak of intrinsic and reversible contributions to the piezoelectric response is present at the MPB. As such a measurement alone does not permit to separate the intrinsic contributions from the reversible extrinsic ones, it is not yet possible to conclude on the origins of such a peak. It might be linked to either increased intrinsic effects (i.e. phenomenological [5] and related to better polarization alignment at poling [7, 8]) or to enhanced reversible extrinsic contributions (e.g. appearance of supplementary contributing defects, like IDW [8]).

Starting with the d_0 values reported in Figure 6.2, the corrected roof distribution parameters were obtained by the procedure described above in section 6.2.1. They are presented in Table 6.1 as a function of the PZT composition along with their 95 % confidence band.

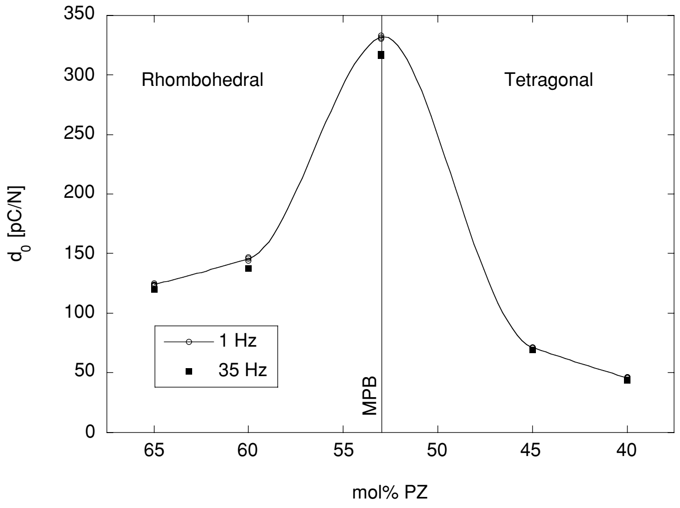

Figure 6.2: *Compositional dependence of the intrinsic and reversible piezoelectric contributions, d_0 (measured at 1 and 35 Hz).*

Table 6.1: *Compositional dependence of the equivalent corrected roof distribution parameters (average of 1 Hz and 35 Hz values).*

	65/35	60/40	53/47	45/55	40/60
f_0 [pC/N MPa]	53.8 ± 0.5	90 ± 1	114 ± 2	11.6 ± 0.2	7.0 ± 0.1
g [pC/N MPa^2]	-16.4 ± 0.9	-27 ± 3	-36 ± 3	-5.7 ± 0.4	-3.0 ± 0.1
k [pC/N MPa^2]	-3.7 ± 0.2	-6.7 ± 0.5	-12.5 ± 0.5	-1.16 ± 0.06	-0.57 ± 0.02
j [pC/N MPa^3]	1.5 ± 0.3	2.3 ± 1.1	6.7 ± 0.9	1.0 ± 0.1	0.36 ± 0.04

Indicated errors correspond to the 95% confidence band assuming that the proposed distribution function describes effectively the experimental loops.

Globally, all the distribution function parameters reach a maximum at the MPB composition, indicating that either the contributing defects number greatly increases or that each given defect contributes more. The 95 % confidence band is quite low for all the values except for the j parameter where it is significant. Note that an increase in the contributing defects number could very well account for the observed increase in both d_0 and distribution parameters. However, an increase of intrinsic contributions along with extended irreversible extrinsic contributions would also be compatible with results of Figure 6.2 and Table 6.1.

To examine the irreversible contributions variation in more details, the compositional dependence of f_0 is plotted on Figure 6.3. Rewriting Equation (4.27) for the extrinsic contributions to the piezoelectric coefficient in the case of a corrected roof-like distribution function as:

$$\Delta d_{33} \propto f_0\left[\left(1+\frac{k}{f_0}\sigma_=\right)\sigma_0 + \frac{1}{3f_0}\,(g + j\,\sigma_=)\,\sigma_0^2\right] \tag{6.1}$$

It can be seen that f_0 is representing the first order approximation of the absolute amplitude of irreversible extrinsic contributions.

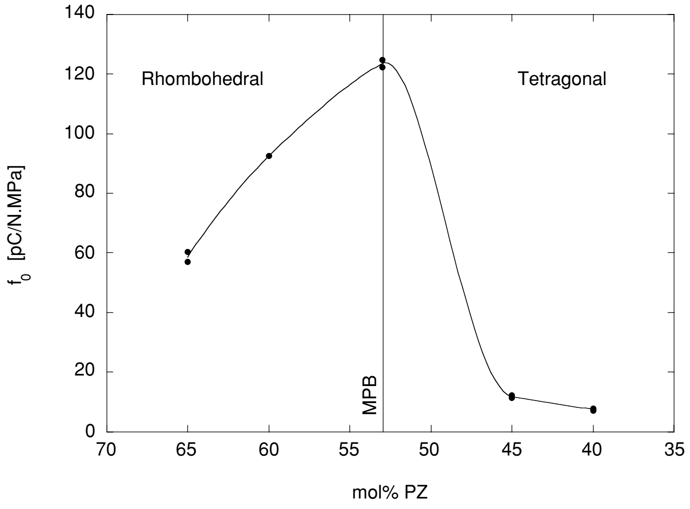

Figure 6.3: *Compositional dependence of the f_0 parameter, representing the absolute amplitude of the irreversible extrinsic contributions for PZT at 1 Hz.*

As noted on Table 6.1, f_0 peaks at MPB, it also shows much larger values for the rhombohedral compositions than for tetragonal ones. Similar high extrinsic contributions in the rhombohedral phase have been already observed [15, 16] and linked to the lower spontaneous deformation possibly diminishing the pinning sensitivity of the contributing defects. Indeed, the overall behavior of f_0 correlates well with the reported evolution of the spontaneous deformation across MPB in PZT [6], showing a slower increase on the rhombohedral side (0.43 % to 0.55 % from 52 %PZ to 64 %PZ) than on the tetragonal side (1.5 % for 54 %PZ to

3.1 % for 43 %PZ). Hence, the observed increase of irreversible contributions seems rather due to extended extrinsic contributions caused for example by a lower spontaneous strain than to an increase in the contributing defects number.

Further evaluating the distribution function parameters, the extent of the distribution function over the Preisach plane can be estimated by considering the intersecting values of the distribution function with the main axes of the Preisach plane (i.e. the stresses at which the distribution vanishes along internal and coercive stresses axes, see e.g. Figure 4.24 caption). Using Equation (4.26), these stress values can be computed as $-f_0/g$ for internal stress axis and $-f_0/k$ for coercive axis. They are presented in Figure 6.4.

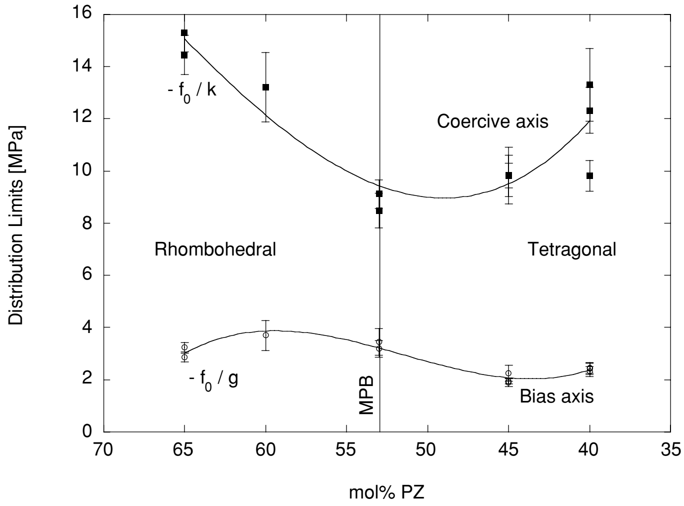

Figure 6.4: *Preisach distribution limits along coercive stress axis: $-f_0/k$, and internal stress axis: $-f_0/g$, as a function of PZT composition (1 Hz measurements).*

On both sides of the MPB, the distribution function is significantly more extended along the coercive stress axis (i.e. k values are lower than g values, see Figure 4.24). Taking into account the experimental errors, no significant compositional variation of the internal stress distribution limit is noticeable. A decrease of the distribution limit along coercive stress axis, $-f_0/k$, can possibly be observed around MPB which may confirm the hypothesis of more contributions per unit caused by a lower pinning in this region.

Concerning the distribution curvature, the j parameter represents the absolute amplitude of the coupled term involving internal and coercive stresses as it can be observed by comparing Figure 4.10 (the roof-like distribution) with Figure 4.24 displaying the same distribution corrected by the coupled term. Its relative evolution with composition can be monitored in Figure 6.5 by the equivalent ratio j/f_0 as f_0 is representative of the overall amplitude of the irreversible extrinsic contributions (see Equation (6.1)).

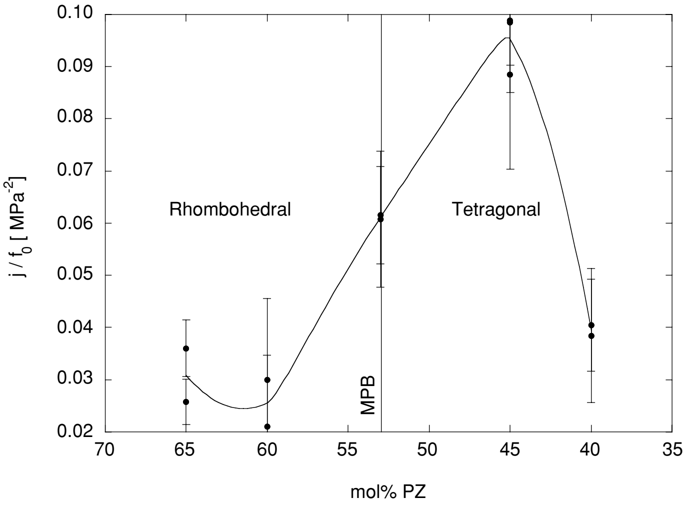

Figure 6.5: *Compositional dependence of the j/*f_0 *ratio, representing the curvature of the distribution function for PZT at 1 Hz.*

The curvature parameter, j/f_0 is exhibiting a maximum on the tetragonal side of MPB, meaning that the distribution function extends significantly to regions far away from both axis in the tetragonal MPB region. This probably indicates that electrical and mechanical random fields are more pronounced on the tetragonal side of the MPB and may be linked to the greater spontaneous strain in this region [6]. The drop of the equivalent curvature parameter for the 40/60 composition cannot be explained by the previous interpretation and may be correlated to domains self-clamping effects. In any case, this question needs further study.

Besides the distribution parameters, the viscous loss tangents were also extracted from the loops. They are presented as a function of the composition in Figure 6.6 for 1 and 35 Hz. Note that these values cannot be compared directly to the ones presented in Figure 5.19, as the stabilizing initial stress used in section 5.3.1 was higher, increasing the contributing defects concentration and hence the total losses. Of course, loss tangents must be compared for a given frequency as they are related to thermally activated mechanisms (see section 5.2.4).

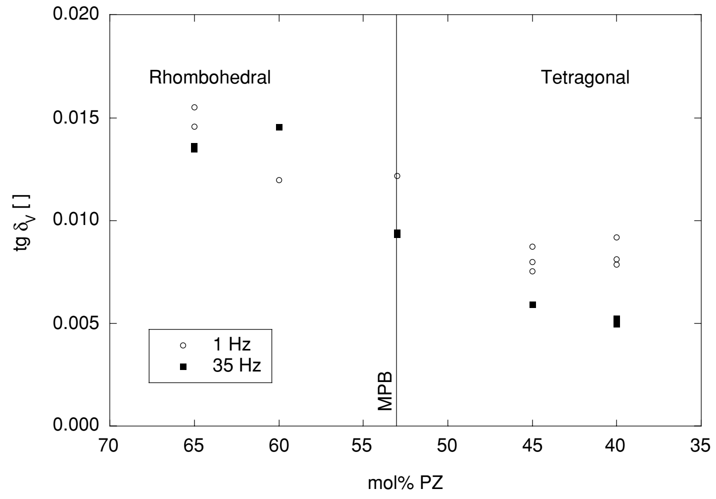

Figure 6.6: *Viscous loss tangent, tg δ_V as a function of PZT composition for measurements at 1 and 35 Hz.*

Viscous losses are varying very little with frequency, with a slight tendency for the 35 Hz losses being lower than 1 Hz ones. In the quasi-static case (see section 5.1), the losses at 35 Hz should be 35 times higher than 1 Hz. However, following recent works on time-dependence in the Preisach formalism [19], such a decrease of the observed viscous losses with increasing frequency can be explained if the distribution is non-zero close to the origin of the Preisach plane (i.e. where the pinning energy roughness is close to the thermal activation). Those shallow-trapped units may actually relax around the measurement frequencies and cause the observed viscous loss decrease with increasing frequency.

Compositionaly, the viscous losses are higher in the rhombohedral region. This might be explained by the lower rhombohedral spontaneous strain allowing for a greater number of non-180° DW during stabilization and hence increased viscous losses. Furthermore, the viscous losses do not exhibit any significant peak in the MPB region and rather show a regular increase with increasing PZ content. This clearly excludes any localized increase in the number of viscous lossy units at MPB, as each defect of the same kind is contributing by the same amount to the viscous losses. Under such an assumption, it can be concluded that the increase of the intrinsic and reversible coefficient, d_0 at MPB (Figure 6.2) is essentially due to increased intrinsic response, as the potential well parameters have no reason to show an anomaly at this composition. Furthermore, the increase of f_0 distribution function parameter close to MPB (Figure 6.3) is certainly related to an increase in each switching unit average response which corresponds to extended contributions from each defect. As suggested by the comparison between extrinsic contributions in tetragonal and rhombohedral phases (see Figure 6.3 and its interpretation), these extended contributions may originate from the low spontaneous strain around MPB (0.43 % and 1.5 % respectively for the rhombohedral and the tetragonal phases [6]) which decreases the pinning defects efficiency on non-180° DW.

6.3 TEMPERATURE DEPENDENCE OF PIEZOELECTRICITY IN PNN-PZT

After exploring the MPB effect as a function of composition for PZT, one may take advantage of the temperature dependent MPB observed in Chapter III in PNN-PZT to avoid poling-induced effects as temperature only is changed for one given sample. Moreover, temperature variation measurements permit to use an easier-to-control variable than in compositional experiments. Thus, in this section, the evolution of the piezoelectric behavior will be monitored as a function temperature for a PNN-PZT composition undergoing a morphotropic transition.

6.3.1 Experimental

The composition chosen for testing the variation of the piezoelectric properties across the temperature dependent MPB is indicated on the phase diagram of Figure 6.7.

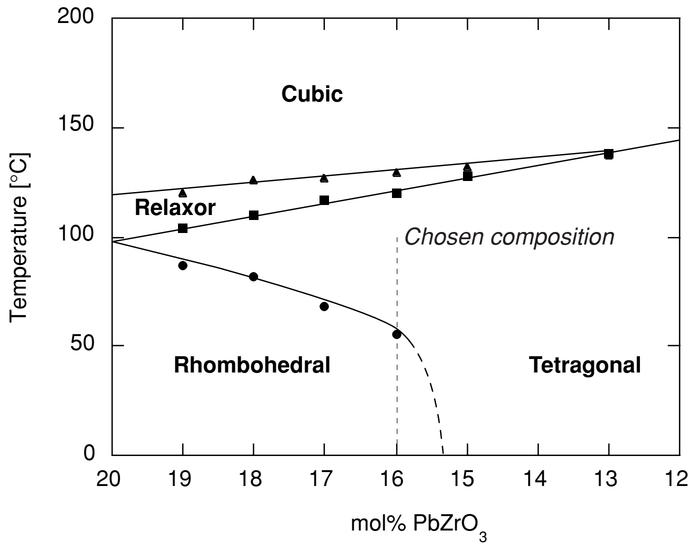

Figure 6.7: *Phase diagram for the 50PNN-50PZT compositions with the composition chosen for the temperature dependent measurements.*

Upon heating the selected 50PNN-16PZ-34PT composition undergoes a rhombohedral to tetragonal transition around 55°C. To prevent depoling effects due to temperature increase, the measurements were performed upon cooling. Moreover, as the piezoelectric measurements are conducted at constant temperature, the expected static transition temperature is different from the dynamic one. It can be obtained by dynamic heating and cooling measurements performed at the same temperature change rate, as presented for pyroelectric measurements in Figure 6.8. In this case, the morphotropic transition is expected at 45.2°C (i.e. the mathematical average of 54°C and 36.4°C) for ideally static measurements. It is noteworthy that each MPB crossing causes a slight loss in the total polarization, as illustrated by the peak in pyroelectric current. Hence, the poling level of the tested sample is lower than ideal (i.e. with a higher DW density) and decreases during experiment.

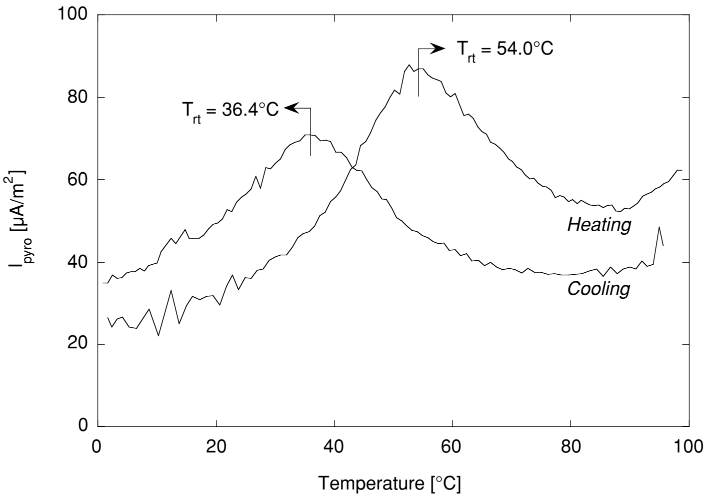

Figure 6.8: *Pyroelectric current density for 50PNN-16PZ-34PT poled at 25°C upon heating and cooling through morphotropic phase transition.*

Concerning the actual piezoelectric characterization, the sample was poled at 25°C with 20 kV/cm applied during 15 min. After placing it in the piezoelectric press, it was heated to 100°C and stabilized at this temperature for 1 hour. Afterwards, a large stress signal in bias and amplitude ($\sigma_{=}$ = 3.4 MPa and σ_0 = 1.7 MPa) was applied for stabilization during 2 hours. Yet, it was kept at lower values than in PZT to prevent too pronounced depoling. Then, piezoelectric measurements as a function of both stress amplitude and bias were performed at 1 Hz every 15°C. To insure stable conditions, the sample was kept for one hour at each temperature step before measuring. Moreover, stress stabilization was performed at each temperature by applying the maximum stress signal during 20 min before the actual measurements. The overall piezoelectric coefficients were calculated in the same way as for

PZT (see section 6.2.1). Finally, note that if one considers the spontaneous strain as an indicator of the MPB distance, the effective structural variation obtained in such a temperature-dependent measurement (from 100°C to 25°C) is much lower than what was presented for PZT immediately above (see e.g. temperature dependent XRD for 40PNN-60PZT in Figure 3.12 and compare the peak distortions with those of Figure 2.3). Hence, using this method, MPB effects monitoring is much finer than in compositional investigations.

6.3.2 Nonlinear characteristics across MPB

A typical overall piezoelectric coefficient dependence on stress amplitude is displayed in Figure 6.9. It can be seen that in the stress amplitude range used in this experiment, the nonlinear piezoelectric behavior is essentially Rayleigh-like (i.e. linearly dependent on the stress amplitude). This was observed at all temperatures. A slight quadratic behavior can yet be observed in Figure 6.9 as in most of the results. However, the use of a second order polynomial to characterize the piezoelectric nonlinear behavior induced too much dispersion in the final parameters. Thus, the obtained d_{33} stress amplitude dependences were all fitted with a linear expression and the basic Rayleigh law ($d_{33} = d_0 + \alpha \sigma_0$) was assumed to be approximately correct in the considered experimental range. This assumption implies that the Rayleigh parameter, α, obtained here is only an apparent parameter and may be dependent on the bias stress in the same way as in section 4.3.4.

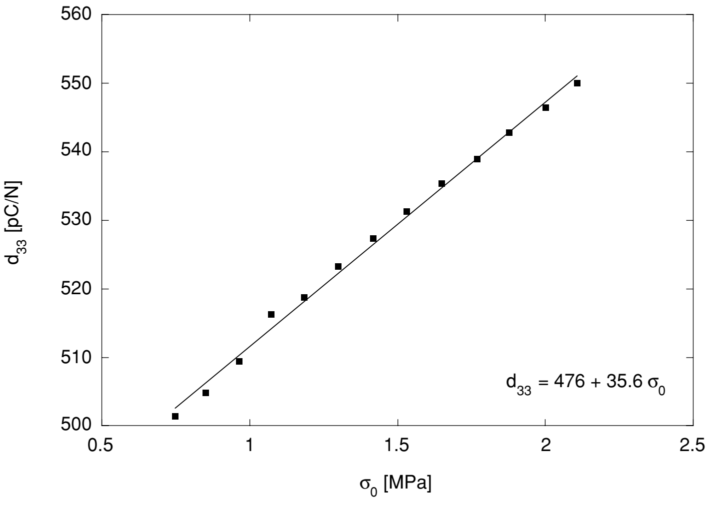

Figure 6.9: *Typical d_{33} vs. stress amplitude, σ_0 dependence for the 50PNN-16PZ-34PT at 40°C for 1 Hz. The line represents the best linear fit ($d_{33} = d_0 + \alpha\sigma_0$) to the data points. Such a linear dependence was observed for all temperatures.*

At each temperature, a series of d_{33} vs. σ_0 dependences was obtained for various bias stresses. The intrinsic and reversible contributions coefficients, d_0, extracted for the bias stresses were then averaged for each temperature. They are presented in Figure 6.10.

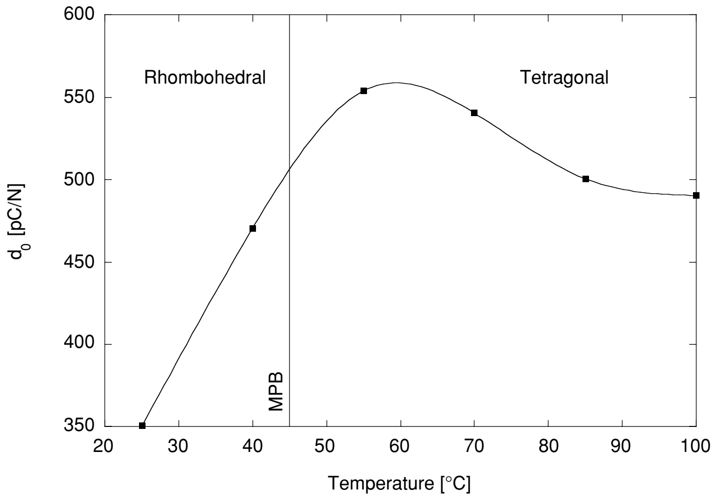

Figure 6.10: *Temperature dependence of the intrinsic and reversible piezoelectric contributions,* d_0 *(measured at 1 Hz) for 50PNN-16PZ-34PT.*

Similarly to PZT, the d_0 coefficients are presenting a maximum close to the supposed MPB position (at slightly higher temperatures than expected, ca 55°C). Note that such a maximum on tetragonal side of the MPB is observed in the compositional properties dependence of PNN-PZT at low field (see Figure 2.18 and Table 2.3). The temperature shift of the maximum may be related to the depoling effects at the morphotropic transition, leading to a decrease of the intrinsic response at the actual MPB position (inducing the d_0 drop below 55°C). The peak cannot be related to an increase in the available polarization directions as no poling electric field is applied during cooling. Hence, this increase can be either due to intrinsic phenomenological effects or to reversible extrinsic contributions. The latter increase may in turn arise from either an increase in the contributing defects number or from a change of pinning efficiency (i.e. the restoring force getting lower).

If the Rayleigh behavior observed on the d_{33} vs. σ_0 dependences were truly related to a flat distribution function (see Equation (4.12) and section 4.3.3), the bias stress dependence investigations would yield bias stress independent nonlinear parameter, α (cf. Equation (4.4) and Equation (4.12) with $\alpha = f_0$). However, here, the Rayleigh law might just be a good approximation of the general piezoelectric nonlinear behavior over a limited range of stress amplitudes and, hence, α may vary with bias stress. A typical Rayleigh parameter, α dependence on bias stress is presented in Figure 6.11.

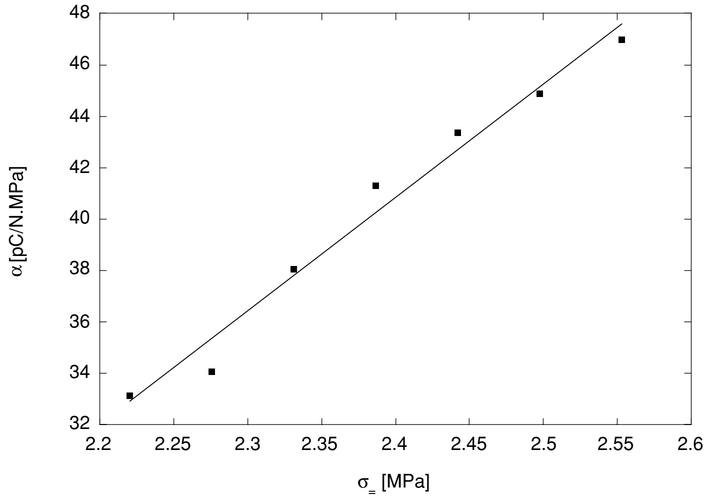

Figure 6.11: *Typical bias stress, $\sigma_=$ dependence of the nonlinear parameter, α for 50PNN-16PZ-34PT at 70°C. The solid line represents a linear fit to the data points. Qualitatively, a similar dependence was observed for all temperatures.*

For all the tested temperatures, the nonlinear parameter, α is indeed not independent of $\sigma_=$. Moreover, it exhibits some “inverted” roof-like dependence along the internal stress axis as α increases with $\sigma_=$ (compare with Figure 4.20). Such a behavior is mathematically compatible with the roof-like distribution and also leads to a quadratic stress amplitude dependence as shown in Equation (4.19):

$$\Delta d_{33} \propto f_0 \sigma_0 + \frac{1}{3}(g + k)\sigma_0^2 \tag{6.2}$$

with a positive g parameter. If k is staying negative, then the total quadratic coefficient may decrease significantly and hence the overall piezoelectric behavior look like a linear one (i.e. Rayleigh-like) over the tested range of stress amplitudes. Furthermore, a roof-like distribution function exhibiting a positive g parameter cannot be normalized, thus such a distribution can be considered as a local one only (it might be similar to the low $\sigma_=$ side of Figure 4.20). Since the same behavior was observed independently of the measuring temperature, it can be considered that the fitted values of α at a given bias stress are representative of the extrinsic contributions level. Hence, the α values for a bias tress of 2.5 MPa are plotted as function of temperature in Figure 6.12.

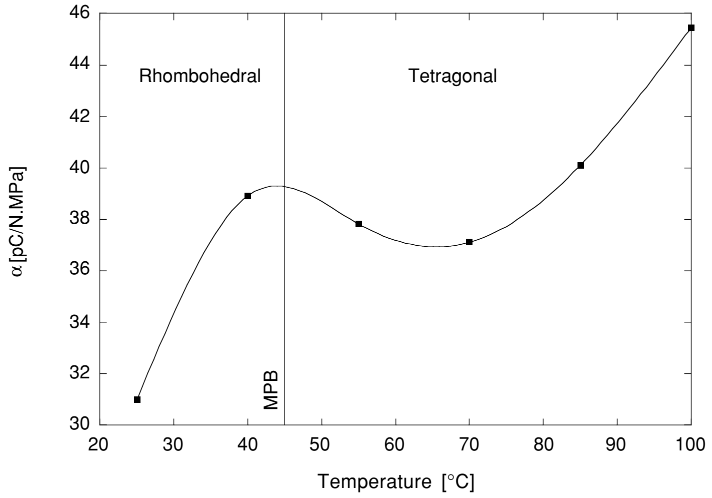

Figure 6.12: *Temperature dependence of the nonlinear parameter, α (measured at 1 Hz) for a 50PNN-16PZ-34PT for $\sigma_{=}$ = 2.5 MPa.*

The nonlinear parameter, α is globally decreasing with temperature and presents a clear local maximum at the MPB temperature. At the end of the temperature interval, there is only one point but it is confirmed by the measurements performed at different bias stresses. Moreover, several distinct characterizations on similar samples have yielded the same behavior for α. The overall temperature decrease is probably not specific to the morphotropic transition as shown for the high temperature values (≥ 70°C) in Figure 6.12. Indeed, some partial depoling may occur at each temperature step due to the repeated loading of the samples. Unfortunately, the test of such an hypothesis is difficult due to the fact that pyroelectric measurements cannot be performed directly in the piezoelectric press. Thus, the temperature dependence of the nonlinear parameter was rather measured with the application of a small external electric field (2 kV/cm) between each measurement (i.e. from bias stress unloading to the next loading after cooling) to prevent depoling effects. The resulting α parameter dependence on temperature is presented in Figure 6.13. To insure equivalent poling conditions an initial depoling procedure at high stress was performed for one hour at each temperature before the actual measurement.

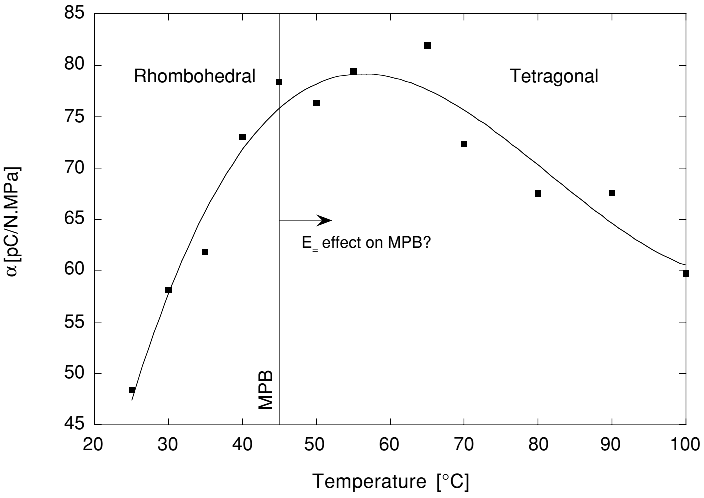

Figure 6.13: *Temperature dependence of the nonlinear parameter, α (measured at 1 Hz, with 2 kV/cm field applied at each temperature change) for 50PNN-16PZ-34PT for* $\sigma_=$ *= 3.2 MPa.*

When depoling effects are removed by the application of a small electric field between the measurements, the α dependence on temperature shows a clear maximum (similarly to f_0 in PZT, cf. Figure 6.3) situated slightly above the expected MPB temperature. This temperature offset of the peak (similar to the one observed for d_0 in Figure 6.10) can be interpreted in two compatible ways. It can be due to some effect causing the tetragonal phase to have higher extrinsic contributions than the rhombohedral one. However, this is not what is suggested by the observations on PZT (see Figure 6.3). More seemingly, the electric field applied during cooling is shifting the actual morphotropic transition to higher temperatures as illustrated in Figure 3.20. Nevertheless, the overall α behavior clearly indicates that extrinsic contributions reach a maximum in the MPB vicinity similarly to PZT. Finally, the shape of the extrinsic contributions peak in PNN-PZT is different from the one observed in PZT (cf. Figure 6.3). For PNN-PZT, the extrinsic contributions are higher in the tetragonal phase than in the rhombohedral one, whereas the spontaneous strain in PNN-PZT is expected to vary across MPB in the same way as in PZT. This may be due to an increase of DW mobility at high temperatures, especially if the DW motion is related with nucleation and growth mechanisms [20].

The viscous loss tangents, tg δ_V, were extracted from the loops using the mixed Rayleigh-viscous method developed in section 5.1. The Equation (5.13) (with the simple Rayleigh loop) was chosen over Equation (5.20) (with the elaborated non-linear loop) as the overall piezoelectric behavior is much closer to the Rayleigh one than to a more complex model. The viscous losses obtained at each temperature for the various bias stresses are reported in Figure 6.14.

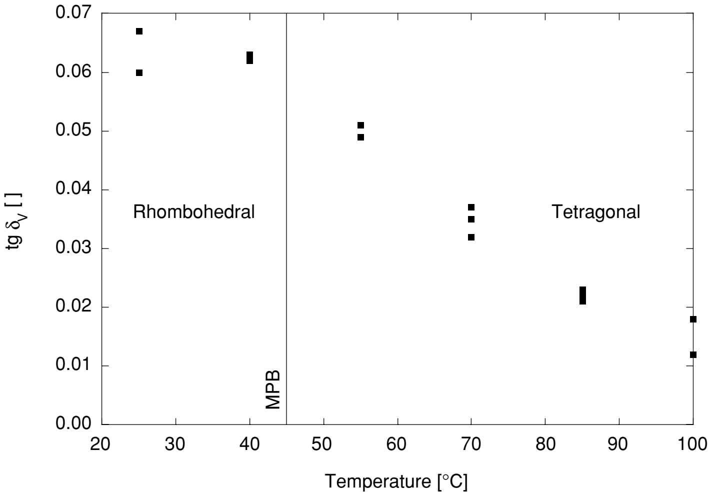

Figure 6.14: *Viscous loss tangent as a function of temperature for 50PNN-16PZ-34PT at 1 Hz.*

The viscous losses show no significant anomaly at the MPB, alike PZT. They increase with decreasing temperature by the same factor as in PZT (≈ 3 times) but over a much smaller spontaneous strain variation range. Again, from this even loss variation, it can be concluded that the peak in extrinsic contributions observed in Figure 6.13 is related to unit response extension rather than appearance of new contributing defects. Moreover, this also indicate that the maximum of reversible contributions observed in Figure 6.10 close to MPB is most probably related to intrinsic contributions.

In summary, although the PNN-PZT piezoelectric behavior is influenced by thermal effects (e.g. the nonlinear parameter, α, being greater in the PNN-PZT tetragonal phase contrary to PZT), the piezoelectric response in PNN-PZT as a function of temperature is quite similar to the one observed for PZT as a function of composition. Hence, a general interpretation of the MPB effects on the piezoelectric response based on both PZT and PNN-PZT results can be proposed in the next section.

6.4 THE PIEZOELECTRIC RESPONSE ACROSS A MPB

Considering the quite similar results obtained for PZT and PNN-PZT piezoelectric behavior across MPB, our approach gives the following general picture of the various contributions dependence on crystallography:

Intrinsic contributions: they are indeed increasing significantly at MPB, as expected from single crystal phenomenology [5] and from the greater number of polarization directions available during poling [7, 8]. For poled PZT samples, they lead to a strong peak for d_0 at MPB with no associated peak of the viscous losses (see Figure 6.2).

Reversible extrinsic contributions: they are probably increased at MPB, even though it is impossible to strictly separate intrinsic effects from reversible contributions (cf. Figure 6.10). As no contributing defects density change occurs at MPB, such an increase may arise from the presence of IDW in this region. Indeed, as stated in section 3.5.2, an intermediate monoclinic phase between rhombohedral and tetragonal phases would increase the IDW thickness relatively to regular DW, leading to a lower pinning [21]. Hence, the observed d_0 maximum at MPB is supposedly due to the superimposed peaks of intrinsic response and reversible contributions.

Irreversible extrinsic contributions: they are reaching a maximum at MPB. However, this maximum does not correspond to appearance of new defects but rather to extended contributions from the existing ones, as confirmed by the absence of anomaly in the viscous losses for both PZT and PNN-PZT (see Figures 6.6 and 6.14). Such a peak may be related to a decrease of the pinning efficiency correlated to the minimal spontaneous strain in the MPB region [6] (as observed when comparing PZT extrinsic contributions for rhombohedral and tetragonal phases in Figure 6.3). Moreover, IDW may also contribute more because of their increased thickness.

Note that the here-above proposed mechanisms where chosen as the ones making the lowest number of assumptions. More elaborated interpretations are certainly possible if more complex mechanisms are postulated (such as considering that viscous losses are not proportional to the number of defects). Hence, at MPB, increased intrinsic contributions arise for phenomenological reasons and from the greater number of polarization directions. Moreover, extrinsic contributions are enhanced in the same region due to a decrease of pinning efficiency at MPB related to the lower spontaneous strain. The latter interpretation suggests that the main pinning defects are elastic ones, in agreement with the ideal model of electrically neutral non-180° DW contributions. Such a hypothesis could be tested if a significant decrease of the mechanical defects density could be obtained in these materials, as it should be accompanied with enhanced extrinsic contributions. Furthermore, assuming this strain-related mechanism, the higher properties observed in the relaxor-PZT compositions compared to regular PZT can be explained by a lower spontaneous strain leading to increased reversible and irreversible contributions to the total piezoelectric response. Finally, for similar electrostrictive coefficients, new soft piezoelectric materials should be searched in the compounds presenting the lowest spontaneous strains (as in rhombohedral PZN-PT single crystals).

6.5 SUMMARY

In this chapter, the advanced nonlinear description tools developed in Chapters IV and V were used to tentatively characterize the piezoelectric behavior of MPB-crossing systems (PZT vs. composition and PNN-PZT vs. temperature). Those systems exhibited similar dependences for intrinsic and extrinsic contributions which permitted to interpret the piezoelectric response peak as composed of a peak of both types of contributions. The intrinsic contributions were indeed reaching a maximum at MPB due to the greater number of available polarization directions and to phenomenological effects. It was also shown that the extrinsic contributions peak at the morphotropic phase boundary was not due to an increased number of contributing defects which would have also affected the viscous losses, but are rather related to a global decrease in the pinning interactions throughout the material linked to the low spontaneous strain in this region. This permitted to suggest an explanation of the piezoelectric superiority of the relaxor-ferroelectric compositions over PZT as due to a lower spontaneous strain associated with comparable electrostrictive coefficient.

6.6 REFERENCES

1. B. Jaffe, R.S. Roth, and S. Marzullo, *Piezoelectric properties of lead zirconate-lead titanate solid-solution ceramics.* J. Appl. Pys., (1954) **25** p. 809-10.
2. B. Jaffe, R.S. Roth, and S. Marzullo, *Properties of piezoelectric ceramics in the solid-solution sereies lead titanate - lead zirconate - lead oxide : Tin oxide and lead titanate - lead hafnate.* J. Res. Natl. Bur. Stds., (1955) **55** [5] p. 239-54.
3. V.A. Isupov, *Dielectric polarization of* $PbTiO_3$-$PbZrO_3$ *solid solutions.* Sov. Phys. Solid State, (1970) **12** [5] p. 1084-8.
4. K. Carl and K.H. Härdtl, *On the origin of the maximum in the electromechanical activity in* $Pb(Zr_xTi_{1-x})O_3$ *ceramics near the morphotropic phase boundary.* Phys. Stat. Sol. A, (1971) **8** p. 87-98.
5. M.J. Haun, E. Furman, S.J. Jang, and L.E. Cross, *Thermodynamic theory of the lead zirconate-titanate solid solution system, Part V: Theoretical calculations.* Ferroelectrics, (1989) **99** p. 27-44.
6. M.R. Soares, A.M.R. Senos, and P.Q. Mantas, *Phase coexistence region and dielectric properties of PZT ceramics.* J. Eur. Ceram. Soc., (2000) **20** [3] p. 321-24.
7. W. Heywang, *Ferroelktrizität in perowskitischen Systemen und ihre technischen Anwendungen.* Z. angew. Phys., (1965) **19** [5] p. 473-81.
8. V.A. Isupov, *Properties of* $Pb(Zr,Ti)O_3$ *piezoelectric ceramics and nature of their orientational dielectric polarization.* Sov. Phys. Solid State, (1968) **19** [4] p. 989-91.
9. L. Benguigui, *Thermodynamic theory of the morphotropic phase transition tetragonal-rhombohedral in the perovskite ferroelectrics.* Solid State Com., (1972) **11** p. 825-828.
10. G.A. Smolenskii, V.A. Bokov, V.A. Isupov, N.N. Krainik, R.E. Pasynkov, and A.I. Sokolov, *Ferroelectrics and Related Materials*. Ferroelectricity and Related Phenomena, ed. G.W. Taylor. Vol. 3. 1984, New York: Gordon and Breach Science Publishers.
11. L.E. Cross, *Ferroelectric Ceramics: Tailoring Properties for Specific Applications*, in *Ferroelectric Ceramics (tutorial reviews, theory, processing, and applications)*, N. Setter and E.L. Colla, Editors. 1993, Birkhäuser Verlag: Basel.
12. S. Li, W. Cao, R.E. Newnham, and L.E. Cross, *Electromechanical nonlinearity of ferroelectric ceramics and related non-180° domain wall motions.* Ferroelectrics, (1993) **139** p. 25-49.
13. B.A. Strukov and A.P. Levanyuk, *Ferroelectric Phenomena in Crystals: Physical Foundations*. 1998, Berlin: Springer.

14. B. Noheda, J.A. Gonzalo, L.E. Cross, R. Guo, S.E. Park, D.E. Cox, and G. Shirane, *Tetragonal to monoclinic phase transition in a ferroelectric perovskite: The structure of* $PbZr_{0.52}Ti_{0.48}O_3$. Phys. Rev. B, (2000) **61** [13] p. 8687-95.

15. M. Demartin, *Influence de l'élaboration et de la microstructure sur le déplacement des parois de domaine et les propriétés électro-mécaniques de céramiques de* $Pb(Zr,Ti)O_3$ *et* $BaTiO_3$, in *Materials Dept.* 1996, Swiss Federal Institute of Technology Lausanne: Lausanne, Switzerland.

16. D.V. Taylor, *Dielectric and piezoelectric properties of sol-gel derived* $Pb(Zr,Ti)O_3$ *thin films*, in *Materials Dept.* 1999, Swiss Federal Institute of Technology Lausanne: Lausanne, Switzerland.

17. S. Hiboux, P. Muralt, and T. Maeder, *Domain and lattice contributions to dielectric and piezoelectric properties of* $Pb(Zr_x,Ti_{1-x})O_3$ *thin films as a function of composition.* J. Mater. Res., (1999) **14** [11] p. 4307-19.

18. D. Damjanovic, *Stress and frequency dependence of the direct piezoelectric effect in ferroelectric ceramics.* J. Appl. Phys., (1997) **82** [4] p. 1788-97.

19. G. Bertotti, *Application of the Preisach model of hysteresis.* Mater. Sci. Forum, (1999) **302-3** p. 43-52.

20. R.C. Miller and G. Weinreich, *Mechanisms for the sidewise motion of 180° domain walls in barium titanate.* Phys. Rev., (1960) **117** [6] p. 1460-6.

21. T. Nattermann, Y. Shapir, and I. Vilfan, *Interface pinning and dynamics in random systems.* Phys. Rev. B, (1990) **42** [13] p. 8577-86.

CHAPTER VII
CONCLUSIONS AND PERSPECTIVES

The present work attempted to enhance the understanding of the high properties in PZT and relaxor-PZT compositions focusing on extrinsic contributions to the piezoelectric response. These issues were first approached by developing an efficient nonlinearities and hysteresis description framework based on the Preisach model for ferromagnetics and then by studying the effects of a morphotropic phase boundary on the properties. Innovative processing solutions for relaxor-ferroelectric were also designed, permitting a rigorous properties examination.

In the following, the main achievements will be summarized starting with the extrinsic contributions model based on the Preisach formalism. Then, the results about morphotropism and its relation with the piezoelectric properties will be recalled. Finally, the questions unveiled by this work will be briefly presented along with the further studies that may be conducted on the basis of this thesis.

7.1 HIGH PERFORMANCE PIEZOELECTRICS NONLINEARITY AND HYSTERESIS

The Preisach model was successfully applied to the description of the piezoelectric coefficient nonlinearity and response hysteresis. This description is based on the existence of distributed bistable units in the hysteretic system. It was first shown that appropriate distribution functions for the bistable units can account for the main observed piezoelectric coefficient nonlinearities, such as linear field dependence, and threshold fields. Moreover, the quadratic field dependence of the piezoelectric coefficient, the most widely observed nonlinear case, could be related to a roof-like topography of the distribution function in the Preisach plane. Furthermore, appropriate experimental techniques were developed to fully characterize the parameters of the distribution function for a piezoelectric exhibiting such a quadratic nonlinearity.

Besides its nonlinearity description abilities, the Preisach formalism intimately links the piezoelectric coefficient field dependence with the response hysteresis description. Hence, it was here possible to propose a new type of loop description for the piezoelectric response including both Preisach and viscous contributions. Using this model, rigorous loss characterization could be performed on the main types of lead-containing piezoelectrics, i.e. PT, PZT, and relaxor-PZT. Moreover, based on the distribution function designed for the nonlinear description, it was shown that distribution parameters can be directly extracted from the experimental loops, hence demonstrating that a full piezoelectric extrinsic contributions characterization could be in principle obtained from a single hysteresis. Finally, the versatility of the hysteresis Preisach modeling was illustrated by the derivation of the first analytical expression for a pinched ferroelectric loop. The initial distribution function shape was justified by the mechanisms usually postulated as leading to the appearance of such constricted loops in acceptor doped ferroelectrics.

In conclusion, the Preisach formalism provided a way to describe and average the microscopic extrinsic contributions to the piezoelectric response. This method is very promising compared to the classical macroscopic ones (like thermodynamics) as it truly helps to gain alternative insight in the microscopical physical mechanisms responsible for the piezoelectric nonlinearity and hysteresis.

7.2 PIEZOELECTRICITY AROUND THE MORPHOTROPIC PHASE BOUNDARY

The crystallographic issues in high performance piezoelectrics were approached by treating the morphotropic phase boundary (MPB) effects on properties. First, a general composition-temperature phase diagram was proposed for the PNN-PZT compositions. It exhibits a curved MPB which was shown to be crystallographically equivalent to the quasi-vertical one of PZT. The effects of various temperature and electric field treatments on the MPB were tested with the PNN-PZT compositions. They show that the MPB position can be significantly altered by the thermo-electric history.

Then, the extrinsic contributions around the morphotropic phase boundary were studied in the Preisach framework, for both temperature-dependent and composition-dependent morphotropic phase boundaries. Extrinsic contributions were found to peak at the MPB. Such an increase was interpreted as due to a decrease of the efficiency of the pinning defects, rather than by an increase in the concentration of the contributing defects (such as domain walls). This efficiency decrease was related to the decreasing spontaneous strain at MPB which governs elastic pinning. The appearance of interphase domain walls, separating tetragonal and rhombohedral structures in the same grain, was also correlated to this extrinsic contribution increase. Indeed, following the recent studies on intermediate phases in PZT supported by our own results for PNN-PZT, such interphase boundaries are probably thicker than regular domain walls and hence less subject to pinning in general.

Thus, this study permitted to propose an explanation for the superior properties of relaxor-ferroelectric solid solutions as such compositions present a lower spontaneous deformation. This may cause a decrease of the pinning defects efficiency and hence induce a significant increase in both reversible and irreversible extrinsic contributions responsible for the higher properties of such compositions.

7.3 PERSPECTIVES

As this study presents the first implementation of the Preisach model for piezoelectricity, numerous issues remain open. Among them, the introduction of vectorial modeling is probably one of the most interesting, as piezoelectricity is intrinsically a tensorial process. In particular, it may permit to analyze more precisely the crystallographic influence on piezoelectricity. Then, the extension of the present time-dependent models existing for the after-effect in ferromagnetic materials to the frequency dependence of piezoelectricity would be of great practical interest. The rigorous correlation of low energy level bistable units with the relaxation behavior of piezoelectrics should permit to increase significantly the accuracy of actuator control and sensor monitoring by integrating frequency and amplitude issues in one single description. Furthermore, the implementation of the obtained minimal distribution functions into a feed-forward actuator control may reduce significantly the number of numerical operations at each control step and hence permit to reach higher controlling frequencies.

Another future challenge is the identification of the microscopical mechanisms of the extrinsic piezoelectric contributions. Unfortunately, there are only a few studies on such mechanisms and most of them are not able to account for the irreversible (nonlinear) extrinsic contributions. It is suggested that direct optical observations of domain wall motion under field may lead to renewed interpretations for the Preisach bistable units. Statistical characterization of the pinning energy field should also be considered as it may permit to link microscopic mechanisms with the macroscopic piezoelectric response. Finally, the identification of the true physical nature of the pinning field(s) causing the Preisach-like behavior in piezoelectrics would be of great fundamental interest, as little work exists on the thermodynamics of energetically unconjugated variables (such as stress and dielectric displacement or electric field and deformation) as in piezoelectricity. Such studies will certainly permit to increase the physical understanding of the processes related to the spreading devices which are converting into an electrical signal thermodynamical variables such as temperature or stress.

Table of Symbols

α	Rayleigh nonlinear piezoelectric coefficient ($d_{33} = d_0 + \alpha\sigma_0$)
β	Second order nonlinear piezoelectric coef. ($d_{33} = d_0 + \alpha\sigma_0 + \beta\sigma_0^2$)
d	Piezoelectric coefficient ($d = \partial D / \partial\sigma = \partial u / \partial E$)
d_0	Intrinsic and reversible part of the piezoelectric coefficient
d_{31}	Transverse piezoelectric coefficient
d_{33}	Longitudinal piezoelectric coefficient
d_∞	Non-relaxing part of the piezoelectric coefficient
d^*	Apparent piezoelectric coefficient (complex number)
D	Dielectric displacement
Δ	Polarizing power difference (cf. equation 3.1)
Δd	Relaxing part of the piezoelectric coefficient
e	Electronic charge ($1.60\ 10^{-19}$ C)
E	Electric field ($E_=$: bias field, E_0 : field amplitude)
ε	Dielectric permittivity ($\varepsilon = \kappa / \varepsilon_0$), usually measured at 1 kHz
ε_0	Free space permittivity ($8.85\ 10^{-12}$ F/m)
f_0	First-order parameter of the roof-like distribution
$\mathcal{F}$	Generalized field ($\mathcal{F}_=$: bias field, $\mathcal{F}_0$: field amplitude)
g	Second-order parameter of the roof-like distribution
G	Gibbs free energy
G_p	Pinning energy profile
γ	Apparent piezoelectric viscosity
η	Mechanical viscosity

I_{pyro}	Pyroelectric current
j	Third-order parameter of the corrected roof-like distribution
k	Second-order parameter of the roof-like distribution
k_p	Planar coupling coefficient
k_t	Thickness coupling coefficient
k_{33}	Longitudinal coupling coefficient
κ	Dielectric susceptibility
p	Pyroelectric coefficient
P_{pyro}	Spontaneous polarization measured by Byer-Roundy method
P_s	Spontaneous polarization
r	Ionic radius
$\mathcal{R}$	Generalized response
ρ	Absolute density, usually in [g/cm^3]
s	Elastic compliance
S	Entropy density
σ	Stress ($\sigma_=$: bias stress, σ_0 : stress amplitude)
$\mathrm{tg}\,\delta$	Loss tangent, defined as $\mathrm{tg}\,\delta = \mathrm{Im}(\varepsilon, d, s)/\mathrm{Re}(\varepsilon, d, s)$
$\mathrm{tg}\,\delta_R$	Rayleigh-related piezoelectric loss tangent
$\mathrm{tg}\,\delta_V$	Viscous piezoelectric loss tangent
$\mathrm{tg}\,\delta_\Delta$	Experimental minus Rayleigh piezoelectric loss tangent
T	Temperature
T_C	Curie temperature
T_m	Maximum of permittivity temperature, usually measured for 1 kHz
T_{NR}	Temperature of normal to relaxor ferroelectric transition

T_{rt}	Temperature of morphotropic (rhombohedral-tetragonal) transition
u	Mechanical deformation
ψ	Piezoelectric viscosity
X	Domain wall position in pinning potential
Z	Ionic valence number
ζ	Dielectric viscosity

Table of Abbreviations

AF	Anti-Ferroelectric
BJ	Barkhausen Jump
BT	Barium Titanate
DW	Domain Wall
FWHM	Full Width at Half Maximum
HT	High Temperature
IDW	Interphase Domain Wall
JCPDS	Joint Committee on Powder Diffraction Standards
LGD	Landau Ginzburg Devonshire
LT	Low Temperature
MPB	Morphotropic Phase Boundary
OU	Ornstein-Uhlenbeck stochastic process
PLZT	Lead Lanthanum substituted Zirconate Titanate, $(Pb,La)(Zr,Ti)O_3$
PMN	Lead Magnesium Niobate, $Pb(Mg_{1/3}Nb_{2/3})O_3$
PNN	Lead Nickel Niobate, $Pb(Ni_{1/3}Nb_{2/3})O_3$
PSN	Lead Scandium Niobate, $Pb(Sc_{1/2}Nb_{1/2})O_3$
PST	Lead Scandium Tantalate, $Pb(Sc_{1/2}Ta_{1/2})O_3$
PT	Lead Titanate, $PbTiO_3$
P_xN_{2y}	General formulation for pyrochlores, $Pb_xNb_{2y}O_{x+5y}$
PZ	Lead Zirconate, $PbZrO_3$
PZN	Lead Zinc Niobate, $Pb(Zn_{1/3}Nb_{2/3})O_3$
PZT	Lead Zirconate Titanate, $Pb(Zr,Ti)O_3$
SEM	Scanning Electron Microscopy

WL	Wiener-Lévy stochastic process
XRD	X-Ray Diffraction (Debye-Scherrer method)

Curriculum Vitae

Gilles Robert
né le 13 octobre 1973, célibataire, de nationalité suisse.

1997-2001	*Doctorat ès Sciences* au Laboratoire de Céramiques, Département de Matériaux, Ecole Polytechnique Fédérale de Lausanne.
1995-1996	*Diplôme d'Etudes Approfondies* en “Métallurgie spéciale et matériaux”, Université de Paris-XI Orsay et Commissariat à l'Energie Atomique.
1993-1994	Année de 2ème cycle, Materials Science and Engineering Department, Carnegie-Mellon University (Pittsburgh PA, USA)
1991-1996	*Diplôme d'Ingénieur en Sciences des Matériaux*, Ecole Polytechnique Fédérale de Lausanne.
1988–1991	*Maturité Fédérale type C*, Gymnase Cantonal de Neuchâtel

Publications

1. G. Robert, M. Demartin, and D. Damjanovic, *Phase diagram for the $0.4Pb(Ni_{1/3}Nb_{1/3})O_3$-$0.6Pb(Zr,Ti)O_3$ solid solution in the vicinity of a morphotropic boundary.* J. Am. Ceram. Soc., (1998) **81** [3] p. 749-53.

2. G. Robert, D. Damjanovic, and N. Setter, *Temperature dependence of piezoelectric properties for relaxor-ferroelectric solid solutions undergoing a rhombohedral to tetragonal phase transition.* Ferroelectrics, (1999) **224** p. 97-104.

3. G. Robert, D. Damjanovic, and N. Setter, *Separation of nonlinear and friction-like contributions to the piezoelectric hysteresis.* ISAF 2000, (2000).

4. G. Robert, D. Damjanovic, and N. Setter, *Preisach modeling of ferroelectric pinched loops.* Appl. Phys. Lett., (2000) **77** [25] p. 4413-5.

5. G. Robert, D. Damjanovic, N. Setter, and A.V. Turik, *Preisach modeling of piezoelectric nonlinearity in ferroelectric ceramics.* accepted in J. Appl. Phys. (2001).

6. G. Robert, M. Demartin, D. Damjanovic, and N. Setter, *Synthesis of lead nickel-niobate zirconate titanate solid solutions by a B-site precursor.* submitted to J. Am. Ceram. Soc. (2001).

7. G. Robert, D. Damjanovic, and N. Setter, *Piezoelectric hysteresis analysis and loss separation.* submitted to J. Appl. Phys. (2001).

8. S. Gentil, G. Robert, N. Setter, P. Tissot, and J.P. Rivera, *Growth and properties of transparent $Pb(Zn_{1/3}Nb_{2/3})O_3$-$PbTiO_3$ single crystals with a cubic habitus.* Jap. J. Appl. Phys., (2000) **39** [5A] p. 2732-5.

Acknowledgements

Même s'il ne porte le nom que d'un seul auteur, ce travail n'est pas le fruit d'une traversée en solitaire. J'aimerais ici exprimer ma gratitude à tous ceux qui ont contribué à cette étude. Tout d'abord, ma reconnaissance va à la Prof. Nava Setter, ma directrice, qui a su trouver le juste équilibre entre contrôle et encouragements, tout en me permettant de travailler dans une infrastructure optimale. L'apport du Dr. Dragan Damjanovic, mon superviseur, a été déterminant tant au niveau scientifique qu'humain. J'aimerais le remercier de sa disponibilité, de son soutien et de sa finesse qui m'ont permis de toujours trouver chez lui opinions éclairées, nouveaux défis et compréhension lors de passages plus difficiles. Mes talents actuels en synthèse de poudres céramiques doivent beaucoup au Dr. Marlyse Demartin-Maeder ainsi qu'à Jacques Castano. Ils furent mes Pygmalions dans les méandres du broyage, de la calcination et du frittage. Merci à Marlyse de son sens pédagogique et à Jacques pour la préparation de tant de poudres “selon la méthode X ou Y”. J'ai aussi grandement bénéficié des discussions, parfois animées, avec les Dr. Sacha Tagantsev et Enrico Colla. Merci à ces physiciens de n'avoir jamais voulu épargner l'ingénieur et de l'avoir aidé à découvrir les joies d'un raisonnement rigoureux, parfois judicieusement assaisonné d'équations. J'ai également eu la chance de bénéficier de l'aide de nombreuses personnes pour la caractérisation de mes compositions. Merci au Dr. Brahim Dkhil pour les mesures XRD à haute définition, au Dr. Pedro Moeckli pour l'identification des mes précurseurs, au Dr. David Taylor pour ses explications intarissables sur “l'art de la mesure” et à Guy Raeber pour ses réparations “just-in-time”. Ma reconnaissance va également aux membres de mon jury les Prof. J.-A. Manson, M. Gijs, P. Gonnard, P. Stadelmann et A.V. Turik qui ont généreusement accepté de réfléchir aux résultats de mon travail et de les critiquer avec discernement. Finalement, j'aimerais remercier tous les membres du laboratoire de céramiques de l'EPFL qui par leur sens de la communauté et leur inextinguible bonne humeur ont significativement contribué à faire de cette thèse une des périodes les plus privilégiées de mon existence.